Multi-scale approaches to tire grip on wet roads

Matheus de Lorenzo Oliveira

To cite this version:

Matheus de Lorenzo Oliveira. Multi-scale approaches to tire grip on wet roads. Mechanical engineering [physics.class-ph]. Institut Polytechnique de Paris, 2024. English. NNT : 2024IPPAX038 . tel-04735887

HAL Id: tel-04735887
https://theses.hal.science/tel-04735887v1

Submitted on 14 Oct 2024

INSTITUT
POLYTECHNIQUE
DE PARIS

NNT : 2024IPPAX038

Thèse de doctorat

Multi-scale approaches of tire adherence on wet roads

Thèse de doctorat de l'Institut Polytechnique de Paris
préparée à a l'École polytechnique

École doctorale n°626 de l'Institut Polytechnique de Paris (EDIPP)
Spécialité de doctorat : Mécanique des fluides et des solides, acoustique

Thèse présentée et soutenue à Palaiseau, le 12 juin, par

MATHEUS DE LORENZO OLIVEIRA

Composition du Jury :

Mme. Julie DIANI Directrice de recherche, LMS, École polytechnique	Président
M. Alexander LION Professor, Universität der Bundeswehr München	Rapporteur
M. Vladislav YASTREBOV Chargé de recherche, Centre des Matériaux, MINES Paris, PSL	Rapporteur
M. Oscar LOPEZ-PAMIES Professor, Newmark Civil Engineering Laboratory	Examinateur
M. Patrick LE TALLEC PR, LMS, École polytechnique	Directeur de thèse
Eric BERGER Expert performance, Michelin Technological Center of Ladoux	Invité
Philippe BUSSETTA Chercheur scientifique, Michelin Technological Center of Ladoux	Invité

To my loving family

Acknowledgement

This research was conducted during my time as a PhD student at the *Laboratoire de Mécanique des Solides* at the *Institut Polytechnique de Paris* and during my tenure at the research facility of Michelin in Ladoux. Many contributed significantly to this work, and without their support, this dissertation would not have come to fruition.

I would like to express my deepest gratitude to my doctoral supervisor, Prof. Patrick Le Tallec. His unwavering support, guidance, and encouragement allowed me to pursue this research with focus and determination. I am especially thankful for the enriching discussions and the intellectual environment he fostered, which greatly enhanced my research experience. His mentorship has been invaluable, and I will always hold fond memories of the collaborative and stimulating atmosphere he provided.

Secondly, I also thank all the members and participants from the laboratory. Kostas Danas, Julie Diani, Vincent De Greef, Simon Hallais for the pertinent remarks, sharing of pertinent bibliography and assistance in the understanding of different subjects. Also, I express my gratitute do the other PhD students that, regardless of topics, were essential for the incorporation of a curious and thoughtfull mind.

I also give my sincere thanks to all the members and participants of the laboratory. Special thanks to Kostas Danas, Vincent De Greef, and Simon Hallais for their insightful feedback, the sharing of pertinent literature, and their assistance in navigating various complex topics. My gratitude extends to my fellow PhD students, whose curiosity and thoughtfulness contributed greatly to nurture a collaborative environment.

I am particularly grateful to the members of my thesis jury: Julie Diani, Oscar Lopez-Pamies, Alexander Lion, and Vladislav Yastrebov, for their just evaluation, constructive feedback, and contributions during pivotal moments of my research. Their expertise and input were instrumental in refining and enhancing the quality of this work.

Finally, I am thankful for the support and training I received during my time at Michelin. I extend my heartfelt thanks to Eric Berger, Adrien Di-Pasquale, Simon Nuytten, Philippe Busseta, Matthieu Papi and Arbia Ben khodja for their guidance and for generously sharing their expertise, both broad and specific, which significantly enriched this thesis. I also wish to thank the Michelin Adherence, Wear, and Test team for providing the opportunities to implement experimental and numerical methodologies related to this research.

Abstract

This research investigates the prediction of tangential forces generated during the relative sliding of an industrial rubber mix material with a complex geometry, such as tread patterns, on a wet rough road surface. A multi-scale contact model is built, incorporating material characteristics, contact interactions, and geometrical contributions. The development of each part of the model is evaluated against a series of experiments with increasing complexity. The final result demonstrates both reasonable qualitative and quantitative correlations with tribological data. The research can be divided into two central investigations: the development of the mechanical problem from the centimeter to millimeter scale, and the implementation of an effective local friction model taking into account contributions from the millimeter to micrometer scale. These two parts are then assembled into a final multi-scale framework, also verified experimentally.

The initial phase of the research focuses on developing the constitutive model primarily based on filled rubber mix characteristics. For such, mechanical tests such as Dynamic Mechanical Analysis (DMA) and uniaxial loading/unloading were employed to extract the viscoelastic properties of industrial-filled rubber. This data is used to characterize a proposed finite non-linear viscoelastic material law with a novel formulation for its viscosity. The constitutive model captures effects like non-linear stiffness and a large range in strain magnitude and strain rate sensitivity.

The second phase examines the combined effects of material properties and contact interactions via an experimental landing-sliding contact campaign with smooth, lubricated surfaces. The setup considers a treadless rubber specimen and a substrate composed of rigid spheres coated with dry lubricant, immersed in a temperature-controlled water tank. The experiment design and protocol attempt to minimize adhesion and temperature effects, emphasizing viscoelastic dissipation caused by the indenters at the centimeter to millimeter scale. Numerical simulations using Finite Element Modeling (FEM) were performed to capture the non-homogeneous deformations, utilizing the proposed non-linear viscoelastic model and a simpler viscoelastic formulation, for comparison. A reasonable correlation is obtained and unique tribological trends are captured by the non-linear viscoelastic model.

The third stage identifies the geometrical characteristics of the road surface from millimeter to micrometer scales using confocal microscopy. The study introduces a novel multi-depth descriptor to assess the texture's aggressiveness, identifying polished zones and revealing phase-related information loss when utilizing Gaussian ground reconstructions. Based on these findings, a viscoelastic half-space approach called Continuous-Convolution Fast-Fourier-Transform is implemented to model the dissipative contribution of these smaller scales. From this local model, a proposed effective local friction as a function of pressure and velocity is generated.

The final phase integrates all first-order effects, including non-linear material properties, complex rubber geometry, and contact interactions covering the full-scale range from centimeters to micrometers. Experimentally, rubber mix samples with and without simplified tread patterns, were slid against rough ground surfaces in wet conditions. FEM simulations were used to reconstruct the sliding process, with two approaches for frictional contact: a constant ad hoc local friction and effective functional friction sensitive to local pressure and local sliding velocity. Both approaches displayed strong correlations with experimental data, particularly regarding key deformation trends like Leading Edge curling/snailing and tread block self-contact. Unlike the constant ad-hoc local friction, the functional local friction does not require tribological experiments for its identification only the ground's profile and viscoelastic properties, while still offering similar predictive quality.

Keywords: friction, tire, tread-pattern, viscoelasticity, non-linear, roughness, multiscale, FEM.

Résumé

Cette étude porte sur la prédiction des forces tangentielles générées lors du glissement relatif d'un mélange de caoutchouc industriel à géométrie complexe, telles que les bandes de roulement, sur une surface routière rugueuse et mouillée. Un modèle de contact multi-échelle est construit, incorporant les caractéristiques des matériaux, les interactions de contact et les contributions géométriques. Le développement de chaque partie du modèle est évalué par rapport à une série d'essais expérimentaux de complexité croissante. Le résultat final démontre des corrélations qualitatives et quantitatives raisonnables avec les données tribologiques. La recherche peut être divisée en deux parties principales : le développement du problème mécanique de l'échelle centimétrique à l'échelle millimétrique, et la mise en œuvre d'un modèle de frottement local efficace prenant en compte les contributions de l'échelle millimétrique à l'échelle micrométrique. Ces deux parties sont ensuite assemblées dans un modèle multi-échelle, également vérifié expérimentalement.

La phase initiale de la recherche se concentre sur le développement du modèle constitutif principalement basé sur les caractéristiques des mélanges chargé industriel. Pour ce faire, des essais mécaniques tels que l'analyse mécanique dynamique (DMA) et les essais de charge/décharge uniaxiale ont été utilisés pour extraire les propriétés viscoélastiques du caoutchouc industriel. Ces données sont utilisées pour caractériser une loi de matériau viscoélastique non linéaire finie, proposée avec une nouvelle formulation pour sa viscosité. Le modèle constitutif capture des effets tels que la rigidité non linéaire et une large gamme dans l'amplitude de la déformation ainsi que la sensibilité à la vitesse de déformation.

La deuxième phase examine les effets combinés des propriétés des matériaux et des interactions de contact avec une campagne expérimentale d'atterrissage-glissement sur des surfaces lisses et lubrifiées. L'expérience porte sur un échantillon de caoutchouc sans bande de roulement et sur un substrat composé de sphères rigides enduites de lubrifiant sec, immergées dans un réservoir d'eau à température contrôlée. La conception et le protocole de l'expérience visent à minimiser les effets d'adhésion et de température, en mettant l'accent sur la dissipation viscoélastique causée par les sphères à l'échelle du centimètre ou du millimètre. Des simulations numériques utilisant la Modélisation par Éléments Finis (MEF) ont été réalisées pour capturer les déformations non homogènes, en utilisant le modèle viscoélastique non linéaire proposé et une formulation viscoélastique plus simple, à des fins de comparaison. Une corrélation raisonnable est obtenue, et les tendances tribologiques uniques sont saisies par le modèle viscoélastique non linéaire.

La troisième étape identifie les caractéristiques géométriques de la surface de la route à l'échelle du millimètre et du micromètre à l'aide de la microscopie confocale. L'étude introduit un nouveau descripteur multi-profondeur pour évaluer l'agressivité de la texture, en identifiant les zones polies et en révélant la perte d'information liée à la phase lors de l'utilisation de reconstructions gaussiennes du sol. Sur la base de ces résultats, une approche viscoélastique du demi-espace appelée transformée de Fourier rapide à résolution continue est mise en œuvre pour modéliser la contribution dissipative de ces petites échelles. À partir de ce modèle local, une proposition de frottement local effectif en fonction de la pression et de la vitesse est générée.

La phase finale intègre tous les effets de premier ordre, y compris les propriétés non linéaires des matériaux, la géométrie complexe du caoutchouc et les interactions de contact couvrant la gamme complète de centimètres à micromètres. Expérimentalement, des échantillons de mélange de caoutchouc avec et sans motif de bande de roulement simplifié ont été glissés sur des surfaces rugueuses dans des conditions humides. Des simulations avec MEF ont été utilisées pour reconstituer le processus de glissement, avec deux approches pour le contact frictionnel : un frottement local ad hoc constant et un frottement fonctionnel efficace sensible à la pression locale et à la vitesse de glissement locale. Les deux approches ont montré de fortes corrélations avec les données expérimentales, en particulier en ce qui concerne les tendances clés de la déformation comme l'enroulement du bord d'attaque et l'auto-contact des blocs de la bande de roulement. Contrairement au frottement local ad hoc constant, le frottement local fonctionnel ne nécessite pas d'essais expérimentaux tribologiques pour son identification, seulement le profil du sol et les propriétés viscoélastiques, tout en offrant une qualité prédictive similaire.

Mots-clés : friction, pneu, bande-de-roulement, viscoélasticité, non-linéaire, rugosité, multi-échelle, MEF.

Contents

List of Figures

List of Tables

Chapter 1

Introduction

1.1 Motivation

The performance of a tire in breaking conditions when it is in contact with wet rough road surfaces is one of the key elements raised to ensure the safety of vehicle users.

Predicting wet grip requires the accounting of the specific behavior of the tread materials (viscoelastic characteristics and complex geometry), the characterization of the road roughness (spatial scales ranging from cm to μm), and also their contact interactions (tire-tire, tire-road). Due to the multi-scale and multi-physical nature of this frictional interaction, developing a model faces important challenges. Global macro-scale experiments require appropriate measures to isolate parameters of interest since many coupled effects might strongly change the final result. On the other hand, very local experiments must be sufficiently accurate to be representative.

From a numerical perspective, the use of the Finite Element Method (FEM) seems appropriate considering the complexity of such a model (tire tread self-interaction, complex surface geometry, non-linear viscoelastic properties), however, accessible processing options limit the possibility to gather, in a single simulation, all the spatial scales present in a reasonable running time. It is thus necessary to develop a coupled/hybrid approach that runs directly the interactions generated with the sculpture and the surface on the macro-scale (cm to mm) and associate it with coherent homogenized tribological laws for the smaller scales (mm to μm).

The mix of appropriated numerical simulations and homogenized local contributions, both being supported with global and local experimental verification is a promising offer to gain a deeper understanding of the rubber friction process at breaking conditions. This could potentially help in the conception of novel tire designs and potentially reduce the number of traffic fatalities.

1.2 Objectives and chronogram

Our central problem is the prediction of tangential forces generated by the relative sliding of a rubber mix material with a complex geometry (tread pattern) on a wet road surface.

Given the viscoelastic character of the tire material and the complex texture of the road surface, their interaction is associated with a multi-frequency excitation, resulting globally in a grip performance. Therefore, a model of this problem must account for different time and space scales. However, as mentioned in the previous section, to overcome the huge computational cost of a numerical simulation involving all scales of interest, one must carefully identify the bigger scales to be directly simulated and extract the first-order physical mechanisms that need to be kept.

For this reason, the objective of the thesis is threefold:

- The development and numerical implementation of a well-posed model of the mechanical problem, taking into account native roughness of the order of millimeters to centimeters and the associated tread pattern of the tire found on this scale range;
- The development of a hybrid friction law resulting from the homogenization of the behavior at the smallest scales from micrometer to millimeter and associated with additional experimental calibrations;
- The experimental validation of the developed friction law, and the calibration of the constitutive parameters of this law from various tribological tests run in the laboratory.

1.3 Object of study

The thesis participates in a project called Dual Grip, whose main goal is to propose a modeling approach for the friction coefficient during the stabilized dynamic sliding of the tire.

Directing the attention to a single tire where the referential is its center, a longitudinal breaking condition of the tire in contact with a wet rough surface is the condition considered (no turning takes place). Assuming there is no intermittent breaking due to Anti-lock Breaking Systems (ABS), considering only the horizontal contributions, a commonly used quantity to evaluate this interaction is the slipping rate, $G\%$ defined as

$$G\% = \frac{V_R}{V_S} = \frac{\omega_T R_T - V_S}{V_S} \tag{1.3.1}$$

where V_S the road surface velocity, R_T and ω_{Tire} represent the radius and the angular velocity of the tire and V_R is the relative speed between the tire and surface dynamic contributions. When breaking sliding is taking place, $G\% \leq 0$ and for many practical cases, V_R is between 0.5 m/s and 2 m/s.

Since different characteristics configure the tread sculpture of a tire, the macro-scale of interest will not consider the entire tire, but a portion of its sculpture. In addition, since a variety of tread patterns exists currently on the market, provided by Michelin, the sculptures will be simplified as lamelizations consisting of a row of tread blocks along the direction of the sliding) (Figure 1.1).

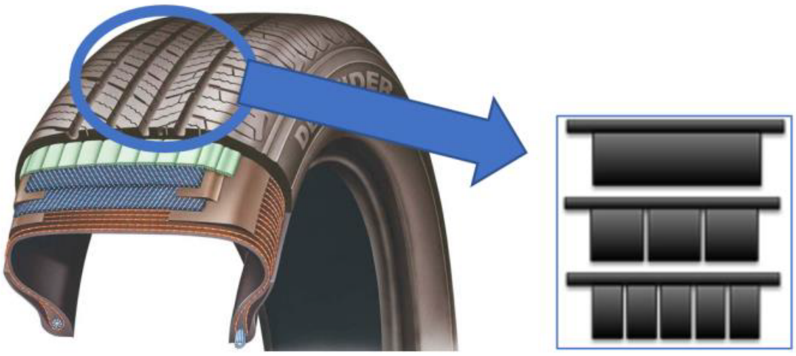

Figure 1.1: Schematic representation of a fraction of the tire surface with different lamelizations (courtesy of Michelin).

Longitudinal breaking is a transient condition that evolves in time, the velocity of the vehicle reduces until a full stop is reached. The tread pattern region is divided into a shearing and a slipping part, as observed in Figure 1.2.

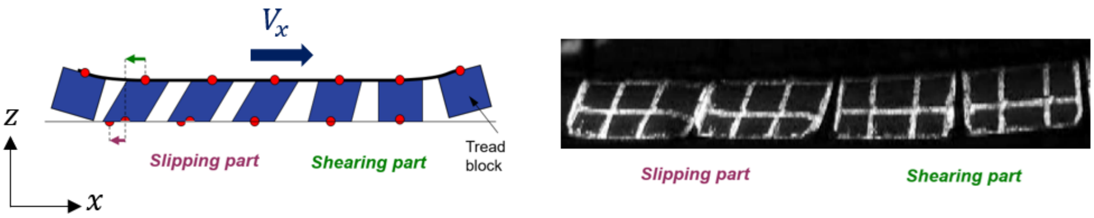

Figure 1.2: Schematic representation of the state of tread blocks upon sliding (left). Experimental imagery of a simplified tread pattern sliding on a smooth surface (right, courtesy of Michelin).

As the vehicle continues to decelerate, most tread blocks will eventually start to slide. A key global parameter describing this state is the friction coefficient defined by Amontons-Coulomb law as

$$\mu = \frac{F_T}{F_N}, \tag{1.3.2}$$

where F_T is the tangential resistance force parallel and opposite to the vehicle's movement and F_N is the normal reaction force to the vehicle's load. The tangential resistance force is higher when most of the tread blocks are shearing, then when some of the tread blocks start to slide, its magnitude lowers and stabilizes when most tread blocks (at least 90% of the rubber mix area in contact with the road) are in sliding condition. The friction value does not change greatly in time in this sliding phase, as shown in Figure 1.3. This study will focus on this stabilized state of interest, which will now be called the Stabilized Dynamic Phase (SDP). This state is also called stationary friction.

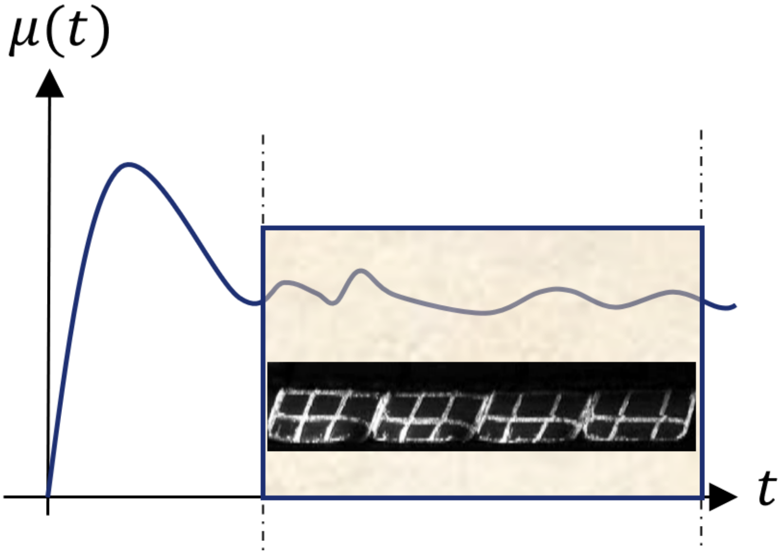

Figure 1.3: Schematic representation of friction evolution in time. Stabilized region highlighted with correspondent state of tread blocs from experimental imagery (courtesy of Michelin).

Lastly, three additional constraints will be added to our study. First, the radial disposition of the tread pattern (due to the geometry of the tire) in the contacting zone of interest will be considered flattened. Second, on SDP conditions, the horizontal velocity imposed (responsible for the sliding) will be imposed as a constant, invariant in time. Lastly, the temperature conditions will be considered within the range of 7°C and 15°C.

To keep consistency with real experiments, those simplifications will be considered in the modeling part as well as supported by equivalent tribological experiments (more details will be presented in section 4.1) for appropriate validation. Those simplifications are reasonable, given that Michelin already has transfer functions from this simplified condition to more complex cases. More details will be described further in this section 4.1.

1.4 Organization of the thesis

This document is organized as follows:

Chapter 2 introduces the physical mechanisms associated with rubber friction, the state-of-the-art concerning different friction model approaches, and the most relevant conclusions and challenges for the object of study.

Chapter 3 develops the fundamental notation and the general mechanical framework to be used in the study, together with a description of its numerical implementation within a Finite Element framework.

Chapter 4 Describes the research framework within the Dual Grip Michelin project. Moreover, this chapter introduces a new form of evaluating the complexities of the rough surface across its scales. Lastly, previous results obtained before the thesis are discussed to justify subsequent actions.

Chapter 5 focuses on the constitutive models to be used herein. It describes and analyzes the experimental data, which are available or were obtained during this work. It reviews in detail the two classes of models to be used. It then presents the detailed calibration strategy that had to be implemented to identify the proper values of the mechanical parameters used in these models. In that process, the chapter also proposes a generalization of the non-linear model to better handle the experimental results.

Chapter 6 relies on the foundations built in Chapter 3 and Chapter 5 by implementing the non-linear model in a numerical reconstruction of an original experimental setup using smooth spheres as substrate sliding against the rubber mix without the presence of sculptures. This part of the study attempts to minimize potential multi-scale effects expected for classical sliding contact with rough surfaces and better investigate how the non-linear viscosity affects tribological response.

Chapter 7 invokes multi-scale models described in Chapter 2, extending and contextualizing some principles to a complex tribological contact with rough surfaces. The necessary formulations within each scale are defined and discussed.

Chapter 8 implements the strategy introduced in Chapter 7 as a numerical reconstruction of the experimental protocol from Chapter 4. The key aspects from simulations are recovered and compared with experimental data.

Chapter 2

Theoretical background

2.1 Methodology of review

In order to identify which context the tread pattern specificities for rubber mix friction was taken by the scientific community, the initial portion of the research was dedicated to review two main subjects:

- Physical mechanisms present for rubber sliding friction on rigid rough surfaces;
- Multi-scale friction approaches for viscoelastic models.

as presented in Figure 2.1.

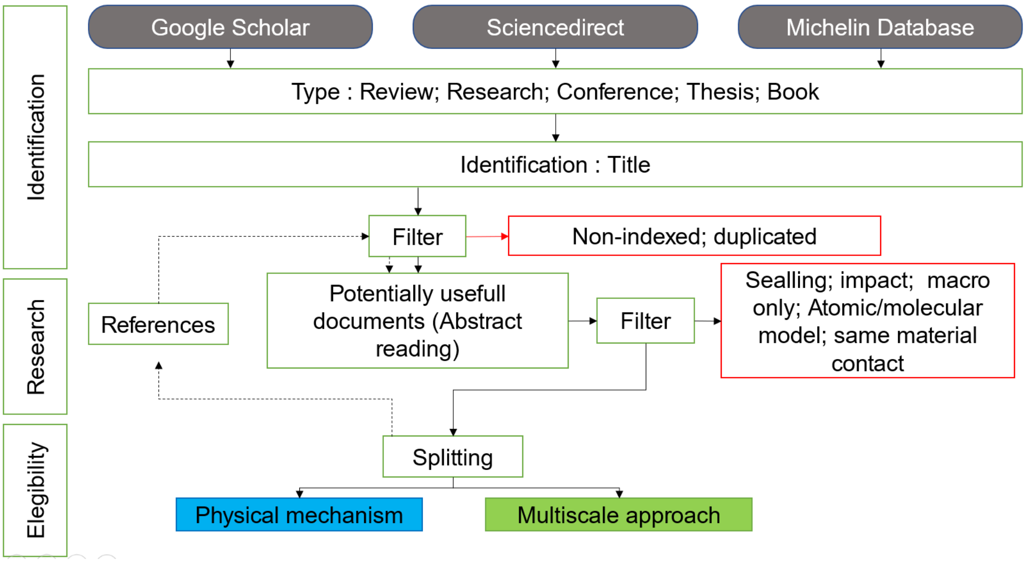

Figure 2.1: Bibliographic review planning.

Both Michelin's internal conclusions and external documentation were taken into account for the research.

This document will present a contextualization of the principal scientific works and main contributions. Concerning the physical mechanisms, only topics necessary for further understanding of the efforts made will be described in more detail.

2.2 Mechanical properties of rubber

2.2.1 General characteristics

Elastomers play an important role in many tribological applications in the industrial sector and standard routine activities. As a special case of polymers, it is composed of long molecular chains, formed of covalent bonded atoms coiled within themselves. Those chains are a repetition of a small chemical molecule structure called monomers [54].

One of the main characteristics of natural rubber elastomers is their ability to undergo large deformations. If mechanical stress is applied, due to their weak inter-chain interactions, the polymer molecules begin to untangle/uncoil to an extended configuration. Differently from "usual" elastic materials, its equilibrium state is related primarily to the maximum entropy (minimum free energy) of a network of chains [83].

Generally, the properties of natural rubber are not adequate for most industrial applications, so in order to prevent complete untangling, the rubber chains are connected to each other via sulfur bonds/bridges. When sufficient thermal energy is added, a cross-linking of the polymer matrix can occur, reducing the free volume by bringing adjacent chains closer. This may prevent a permanent flow under tensile stress. A schematic representation of cross-linked chains is shown in Figure 2.2. This process is called *vulcanization*, developed by Charles Goodyear in 1839.

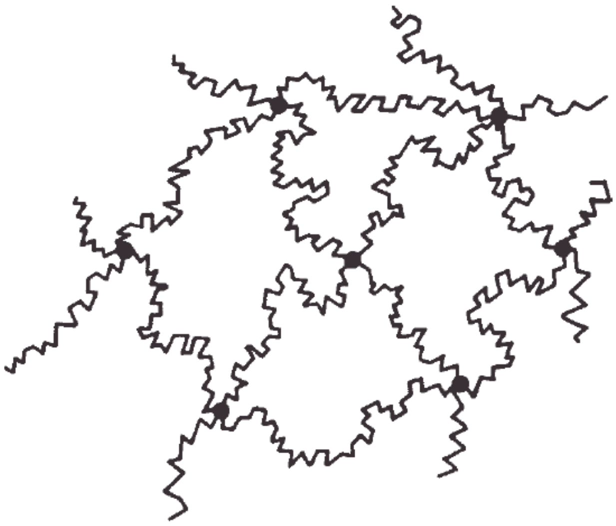

Figure 2.2: Schematic representation of a cross-linked portion of the polymer chain network (from [54]).

When a rubber is stretched, once the tensile application ceases, the polymer-chains tends to coil again in the direction of maximum entropy of the network chains. However, this process is not instantaneous neither completely reversible. From a mechanical standpoint, the stress-strain relationship is highly non-linear and irreversible. When stressed, the initially coiled long molecular chains are forced to rearrange themselves, in doing so, kinetic energy is dissipated and the chaotic structure do not allow the return to its original position when stress is removed. This behaviour is related to a characteristic feature of polymers: its possibility to display an intermediate range of properties between an elastic solid and a viscous fluid. This combined form of response is termed viscoelasticity [54].

2.2.2 Linear viscoelastic properties

Phenomenological models of viscoelasticity do not have necessarily a direct relation with a chemical composition. A classical simplification hypothesis is to assume linear viscoelasticity so that the total deformation can be considered as a sum of independent elastic and viscous contributions. Boltzmann superposition principle (proposed by Boltzmann in 1876) proposes a time-dependent mechanical response, where a change in stress is a function of the entire past strain history of the specimen [50].

$$\sigma(t) = \int_{-\infty}^{t} G(t-\tau)\dot{\epsilon}(\tau)\, d\tau \tag{2.2.1}$$

where σ is the stress history and $\dot{\epsilon}$ is the deformation rate and τ is an auxiliary variable to help account for previous contributions. $G(t)$ is known as the relaxation modulus, whereas is typical shape is plotted through time in Figure 2.3. The plots show qualitatively that when rubber is stressed over a short period, its modulus is very high (glassy region), while for a long period of application, it tends to relax and becomes softer (rubbery region). The intermediate/transition region and its pertinence will be accessed later in this section.

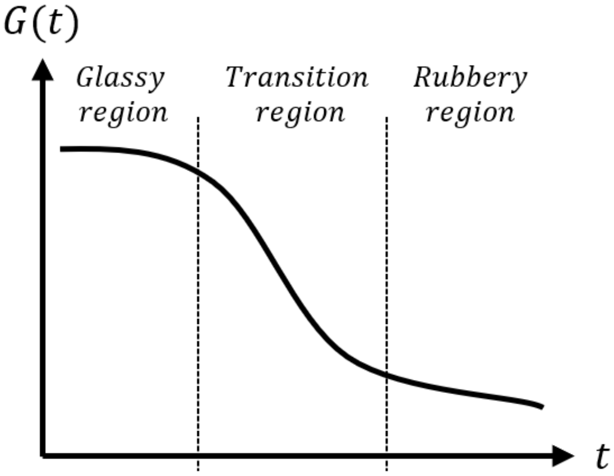

Figure 2.3: Schematic plot of the rubber shear modulus against time.

If a periodic deformation is taken into account, as in Dynamic Mechanical Analysis (DMA) experiments, the strain history can be imposed in the form $\epsilon(t) = \epsilon_0 \sin(\omega t)$. If this signal is inserted into (2.2.1), stress is written as

$$\sigma(t) = \epsilon_0 \sin(\omega t) \left[\omega \int_{0}^{\infty} G(t') \sin(\omega t')\, dt'\right] + \epsilon_0 \cos(\omega t) \left[\omega \int_{0}^{\infty} G(t') \cos(\omega t')\, dt'\right] \tag{2.2.2}$$

where the substitution $t' = t - \tau$ is considered, ϵ_0 is the amplitude of the sinusoidal deformation history and ω its angular frequency. The first term of (2.2.2) is in phase with the imposed deformation signal, while the second term is out of phase by $\pi/2$. The first term inside the brackets is frequently termed storage modulus, usually represented as $G'(\omega)$ (or $G_{Prime}(\omega)$), and the second term in brackets loss modulus represented as $G''(\omega)$ (or $G_{Second}(\omega)$). The terms "storage" and "loss" can be understood when the energy variation per cycle, ΔE, is shown for the same imposed strain history and the stress from (2.2.2)

$$\Delta E = \oint \sigma(t)\, d\epsilon = \int_0^{\frac{2\pi}{\omega}} \epsilon_0 \left[G'(\omega)\sin(\omega t) + G''(\omega)\cos(\omega t)\right] \epsilon_0 \omega \cos(\omega t)\, dt = \epsilon_0^2 \pi G''(\omega) \tag{2.2.3}$$

where it is seen that the energy associated to the storage modulus, $G'(\omega)$, is recovered elastically, while the energy associated to the loss modulus $G''(\omega)$ is not.

For many rubber materials, as long as the strain magnitudes are small, the stress response can be considered similar to the strain history with an intermediate mismatch, $0 \leq \delta \leq \pi/2$ [50], as represented in Figure 2.4, so that

$$\sigma(t) = \sigma_0 \sin(\omega t + \delta) = \sigma_0 \cos(\delta)\sin(\omega t) + \sigma_0 \sin(\delta)\cos(\omega t) \tag{2.2.4}$$

.

with

$$G' = \frac{\sigma_0}{\epsilon_0}\cos(\delta) \quad , \quad G'' = \frac{\sigma_0}{\epsilon_0}\sin(\delta) \quad \text{and} \quad \tan(\delta) = \frac{G''}{G'}. \tag{2.2.5}$$

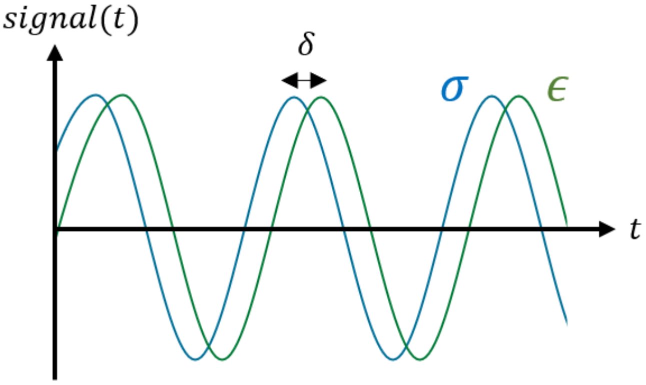

Figure 2.4: Schematic plot of the periodic strain signal and the correspondence stress response in time. Both magnitudes are normalized.

It is also convenient to represent them as the real and imaginary parts of a complex shear modulus

$$G^*(\omega) = G'(\omega) + iG''(\omega) \tag{2.2.6}$$

which, can also be used as a relation between the frequency-dependent form of the stress, σ^*, and strain, ε^*

$$\sigma^*(\omega) = G^*(\omega)\varepsilon^*(\omega). \tag{2.2.7}$$

The tangent of the phase angle between stress and strain is expressed as the ratio between the imaginary and real parts of the complex shear modulus. Therefore, the tangent of the phase angle is a measure of the mechanical energy loss due to the material's viscoelasticity. For a better visualization, generalized curves of a range of frequencies for the storage modulus, the loss modulus and the loss tangent are presented for a periodic strain with constant amplitude in Figure 2.5

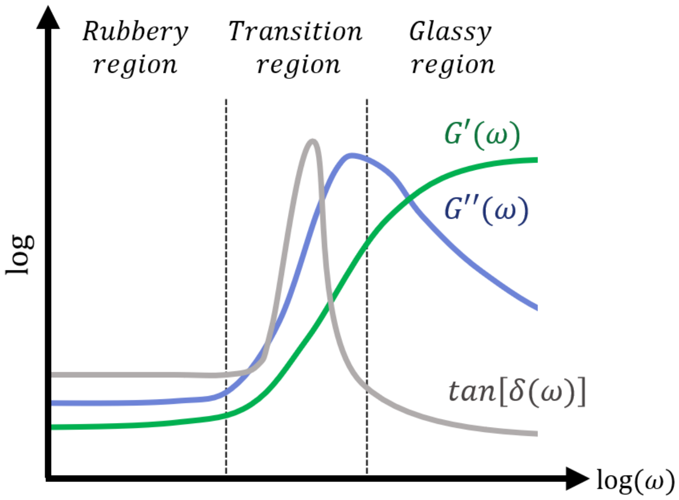

Figure 2.5: Schematic plot of storage and module and loss tangent against the logarithm of the frequency (based on constatations from [50]).

2.2.3 Time-temperature equivalence

Polymers in general, have a strong relationship with temperature since rubber deformations are associated with changes in molecular conformation. For example, in the glassy stage, stiffness is expected to relate to changes in the stored elastic energy, due to small perturbation of the molecules from their equilibrium positions. On the other hand, the rubbery state is expected to present network changes with considerable flexibility. To this end, with some degree of success, relations between conformational freedom (in terms of molecular motion) are associated with a temperature rise [54].

Remarkably, in 1955 a phenomenological procedure that assumes a relation between time scale and temperature was proposed by William, Landel, and Ferry [5]. It is stated that the effect of changing temperature is equivalent to the application of a multiplication factor a_T to the load frequency, where

$$\log(a_T) = \frac{-C_1(T - T_{ref})}{C_2 + (T - T_{ref})} \tag{2.2.8}$$

which is usually termed the WLF equation. T is the temperature in question, T_{ref} is usually chosen as the glass transition, ${T_g}^1$, of the material. C_1 and C_2 are constants, which can be obtained by using experimentally recovered shift factors to (2.2.8) within the still feasible range of frequency that can be reproduced by the experiment.

With the WLF transform, it is possible to characterize the material behavior at very high frequencies, simply by doing subsequent DMA tests over a limited frequency range at many different temperatures. The horizontal shifting gives a simple superposed curve, called the master curve, covering the behavior for a large frequency range. A schematic depiction is shown in Figure 2.6, building the superposition by shifts $G'(\omega, T_i) \rightarrow G'(\omega a_{T,i}, T_i)$ for the recovery of the storage modulus as a master curve.

2.2.4 Non-linear properties

In the tire industry, for a better control of mechanical properties like stiffness response, dissipation and transition region/state placement (as shown in Figure 2.5 and 2.3), fillers

---

[1] or $T_g + 50$, but the best choice of T_{ref} depends on the considered material.

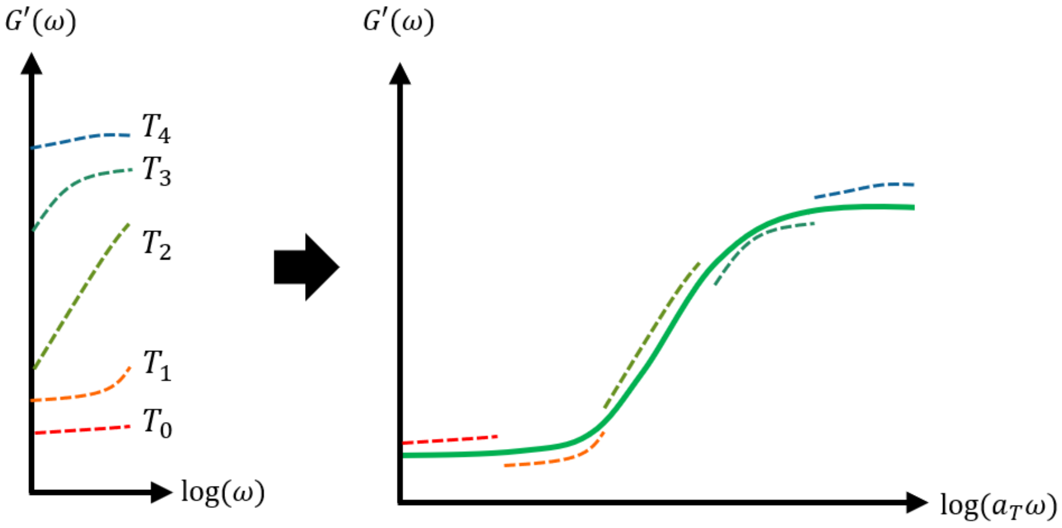

Figure 2.6: Schematic reconstruction of storage modulus in frequency as a master curve with WLF approach, where $T_{i+1} < T_i$ (based on [50], [54], [83]).

like Carbon-Black and Silica are introduced in the vulcanization process [41]. Usually filled elastomers show a dependency to the stress-strain path. With it, two phenomena are usually discussed in the literature: the Mullins and Payne effect.

Mullins effect is usually described as a stress-softening behaviour induced by strain. Consider a virgin filled rubber subjected to a cyclic loading history, a high stress response is mostly observed during the first loading cycle, followed by lower stress values upon recycling [2]. One proposition to justify the initial high value is an increase on the local state of deformation of the rubber matrix, due to the physical presence of filler [12], [14], while the softening behaviour is explained by the micro-mechanical breakage of those hard filler clusters [7]. It is usually assumed to be an irreversible occurrence at moderate/room temperatures [8]. This effect is also present in unfilled elastomers, although more pronounced in filled rubber [93].

Payne effect is also described as a stress-softening effect, now induced by an increase in dynamic strain amplitude [9], [10]. As a dynamic effect, looking at the dynamic parameters presented on the previous section (but now considered in terms of the sinusoidal strain amplitude at a given frequency). With increasing strain amplitude, the Payne effect decreases the storage modulus and produces a sigmoidal path for the loss modulus [84], as shown schematically in Figure 2.7. On a molecular level, one possible explanation to the Payne effect can be attributed to dynamic reversible breakdown and recovery process of the structural aggregates made by the fillers [18], being a reversible process associated to filled elastomers [18].

Considerations of non-linear stress-strain dependencies contained in this document will be presented on the next chapters, when appropriated observations and hypothesis are built. Nevertheless, the object of study, that is tire sculptures in contact with the rough surface during stabilized sliding conditions, as discussed in section 1.3, so that the first non-linear cycles effects associated with Mullins softening effect won't be considered. Therefore, for all experiments, the samples will be preconditioned before testing, so that Mullins effect is not expected to be prevalent.

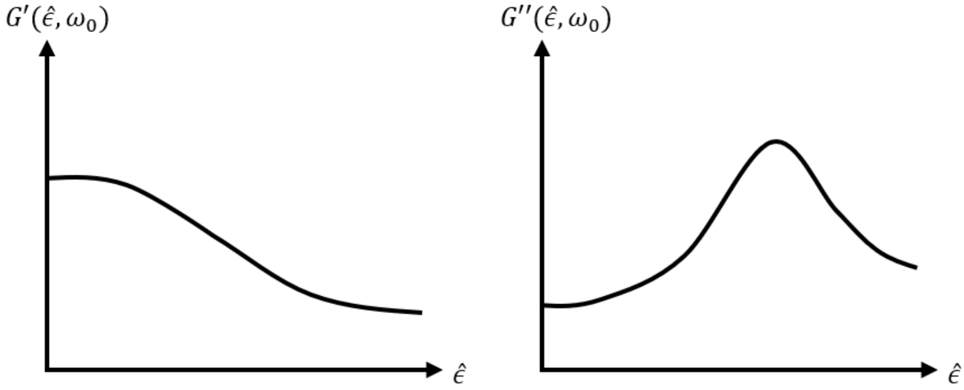

Figure 2.7: Typical storage and loss modulus dependency on frequency and dynamic strain amplitude.

2.3 Mechanisms of rubber friction

There is an extensive range of mechanisms that were found to contribute in the frictional response of rubber. Some effects are more prevalent than others and they can be interdependent from one another. Due to the potential risk of an excessive large scope of research, some of those effects will be prioritized, with respect to the context presented in section 1.3.

2.3.1 General characteristics and contact

The application of friction for technological purposes, in a broader sense, can be traced to at least one thousand years. A deeper analysis can be found a few hundred years ago from Leonardo da Vinci (1495) investigations, later on, verified experimentally for many materials by Guillaume Amontons (1736) and then Charles-Augustin de Coulomb (1806). Amontons and Coulomb defined the linear proportionality connection between a normal reaction force and a perpendicular resistance force as the coefficient μ introduced in equation (1.3.2), which is recurrently termed in Amontons-Coulomb friction law.

Later on, Bowden and Tabor, in 1949, were the first to advise the importance of the surface roughness to the bodies in contact. Their proposition explains the origin of kinetic friction between pure metallic surfaces through the formation of cold-weld junctions. When two bodies are pressed together, depending on the texture of the surface, a very small portion of one surface comes into close contact with another, while for the rest of the area, the distance between the bodies is so large that any atomic interactions and friction contributions can be neglected. This introduced two important concepts: (1) the small ratio value between true contact area, A_T, and nominal/apparent area, A_0; (2) if sliding is taking place, constant shear stress, τ_c, is necessary to shear a cold-weld junction, so that the total friction force is given by

$$F_T = \tau_c A_T \tag{2.3.1}$$

The theory proposes that Frictional force depends on the true contact area (although independent from apparent/nominal area), via a constant shear stress at the interface. An important consequence is that if the Amontons-Coulomb proportionality area is true and a constant coefficient, μ, exists, it must be that

$$F_T \propto F_N \tag{2.3.2}$$

to which, by inserting eq. (2.3.1) in (2.3.2) one finds that

$$\tau_c \propto \frac{F_N}{A_T} \tag{2.3.3}$$

Considering metallic contact, when shear stress τ_c is considered to be constant, a linear proportionality between true contact area provides one of the most common explanations[2], for the Amontons-Coulom law that the friction force is proportional to normal load and independent of apparent surface area [53], [131].

Before, in 1882, Hertz solved analytically the problem of contact between two elastic bodies with curved surfaces, which allowed to explicit the contact pressure field. For an elastic sphere in contact with a continuous rigid half-space, a relationship between the normal load, F_N, and true contact area, A_T, resulted as $A_T \propto F_z^{\frac{2}{3}}$. However, this result did not agree with experimental observations [4] and the conclusion from Bowden and Tabor with Amontons-Coulomb law.

Archard, in 1957, was the first to demonstrate a linear relation between normal load and true contact area for simplified surfaces composed of multiple overlapped spherical protuberances of recursively smaller radius spheres [6]. When Hertz contact theory is used with an increasing number of length scales (recursive spheres superposition), the relations are

(a) $A_T \propto F_z^{\frac{2}{3}}$ (b) $A_T \propto F_z^{\frac{8}{9}}$ (c) $A_T \propto F_z^{\frac{26}{27}}$ (d) $A_T \propto F_z^{\frac{4}{5}}$ (e) $A_T \propto F_z^{\frac{14}{15}}$ (f) $A_T \propto F_z^{\frac{44}{45}}$ as shown schematically in Figure 2.8.

This recursive configuration of a sphere of smaller radii was one of the first multi-scale approaches for elastic contact that presented good qualitative sense, not only with Amontons-Coulomb law but also for the importance of roughness to its enforcement. The validation of the Amontons-Coulomb law (for the case where this is found experimentally to be true) is one of the ways to evaluate the quality of the contact proposal of future multi-scale contact models. This is pertinent because some multi-scale friction models (which later evolved to include rubber contact) are usually supported by those contact theories.

A few years later, instead of working with uniformly distributed surface roughness, Greenwood and Williamson proposed another contact model with stochastically rough surfaces, where spherical asperities heights are statistically distributed for an average center-plane height [13]. Their work (also called GW-Theory) considers the case of exponential and Gaussian height probability densities. Using Hertzian theory when a contact occurs, it was found that this distribution returned a linear proportionality between true contact area and load. This theory gives reasonable results for the contact of hard elastic solids, like steel plates. Later, Bush, Gibson, and Thomas extended GW-Theory (usually called BGT-Theory), by allowing statistical distribution of heights and radii in both horizontal directions (effectively using ellipsoids and not spheres) [19]. In addition, they used important parameters discussed by Nayak, concerning not only the RMS distribution of height but also its gradient and the curvature of the rough peaks [16]. Later on, Greenwood also simplified the BGT-theory, although similar predictions reduced the surface information necessary for meaningful results [60]. Still, current multi-scale Hertzian-based theories also found linear relations between load and true contact area.

---

[2] This scenario is extremely simplified and considered within the framework, theory, and experimental case studies of Amontons, Coulomb and Da Vinci, Bowden and Tabor, whose proposals are only valid for some elastic contacts and load ranges. Considering current understanding, simple elastic-plastic models are not always valid, since the metal microstructure may affect significantly the contact behavior [70] and/or very soft materials might fill the asperities cavities, creating a non-linear inverse proportionality between friction and load [122]. This asymptotic linear relation of multi-asperity contact theories turns out to be mostly used as an academic result, recurrently considered as a validation of elastic contact theories.

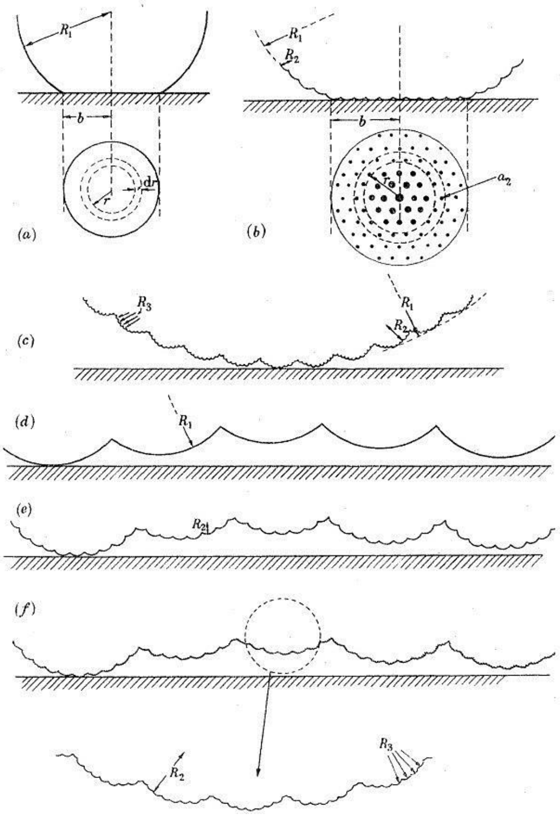

Figure 2.8: Archard contact model (from [6]).

The developments discussed above possess three important assumptions that are intrinsic to Hertzian contact theory: (1) loads applied are relatively low; (2) contacts are elastic; and (3) the true contact area is much smaller than the apparent/nominal (or geometric) area. From 2001 onward, Persson developed his contact theory, which considers a fully three-dimensional surface, assuming two surfaces completely compressed against each other (large true contact area is large) by a certain pressure expressed as a Dirac delta function [46], [65] at macro-scale. The author establishes a relation between statistical properties of the vertical position of the surface and the inter-facial pressure distribution, by relating it with a Gaussian distribution. The evolution of this distribution across the scales follows a diffusion-type equation (pressure acts as the "concentration" parameter), as seen represented in Figure 2.9.

Both BGT and Persson's theories are multi-scale and statistical in nature. For this reason, *in situ* experiments are difficult to produce with reasonable precision and statistical representation, also, not all types of rubber-surface contact can be evaluated [103], [127]. In this context, complete numerical simulations studies are crucial to evaluate the predicting capabilities between the last version of the Hertzian-based contact model (i.e. BGT-theory) and the current Persson's contact model [48], [51], [70], [71], [81], [122], [123]. The main points brought forward by those researches are: Persson's model predicts adequate qualitative growth of contact area with increasing nominal pressure until full contact is reached. However, for moderate loads, the simulated true contact area evolves slightly non-linearly, being below the asymptotic prediction of Hertzian-based multi-scale approaches and above Persson's theory. A more recent review on the topic showed that the contact area growth depends not only on the gradient of the surface, but also weakly on the Nayak parameters. The most meaningful results from Carbone and Bottigione [70] and Yastrebov, Anciaux, and Molinary regarding relative contact evolution are shown in Figure 2.10.

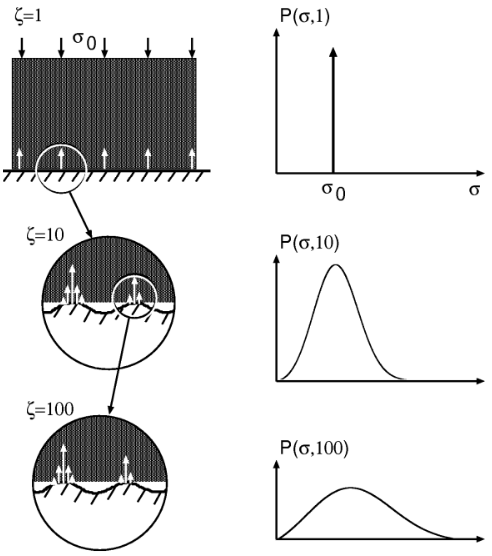

Figure 2.9: Persson contact model (from [52]).

Carbone and Bottigione (left plot in Figure 2.10) studied the validity between Persson theory and the BGT-Theory (named on the study simply by Bush, one of the authors) [70]. Their work also considered the asymptotic results (infinitesimal pressure) of contact area fraction to evaluate how long linearity is maintained. BGT-Theory was considered to maintain a linear relation between true contact area and the load for very small load values with a small contact area fraction, A/A_0 (less than 0.01% of nominal contact area). On the other hand, Persson's theory was considered to hold this proportionality up to 10–15%. They also showed a strong sensibility of BGT-Theory to one of Nayak's parameters spectrum breadth, α [16], to which Persson's model is insensitive.

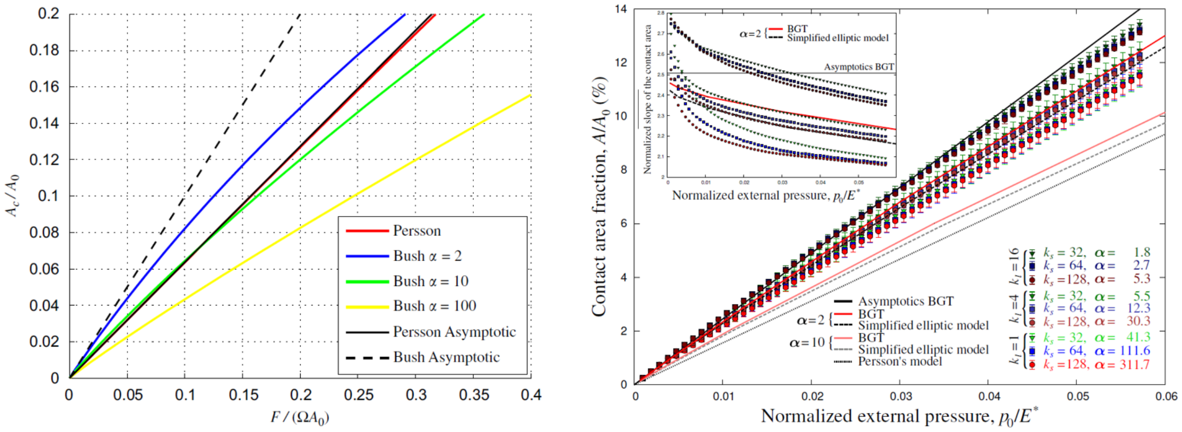

Figure 2.10: Left: Evolution of the contact area fraction and Nayak parameter sweep with normalized normal load for Persson, BGT/Bush-theory (from [70]). Right: Evolution of the contact area fraction and Nayak parameter sweep with normalized normal load for Persson, BGT/Bush-theory, and different numerical magnifications and cutoffs (from [122]). The slope of the contact area growth is also depicted.

Yastrebov, Anciaux, and Molinary (right plot in Figure 2.10) [122] added to the current understanding by using a FFT-based boundary element method which the results are averages of 50 statistically equivalent realizations of rough surfaces with different magnification surface ranges, k_l/k_s and the associated Nayak parameter, α. Their observations demonstrate that although there is a numerical sensibility to the Nayak parameter, this consideration is overestimated by BGT-theory, especially for high pressures, since it is an asperity-based model. Nonetheless, Persson's theory still has valid *qualitative* evolution, where its absolute value improves asymptotically with pressure, since its theory was derived from a saturated contact, as shown in Figure 2.11.

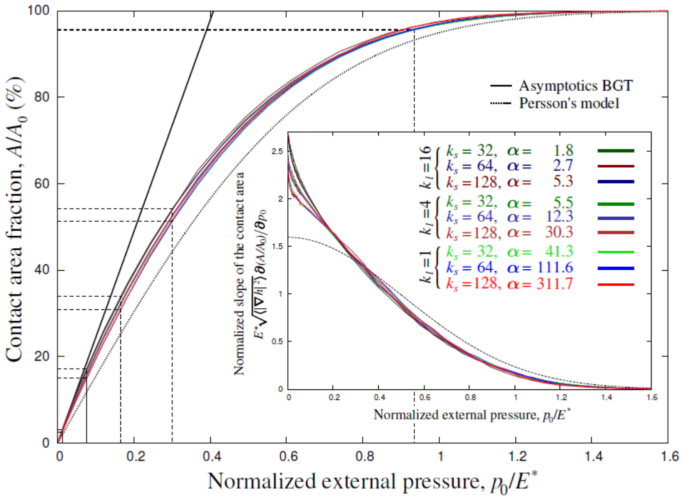

Figure 2.11: Evolution of the contact area fraction up to full saturation and Nayak parameter sweep with normalized normal load for Persson, BGT/Bush-theory, and different numerical magnifications and cutoffs. Marked pressures and corresponding areas refer to topographies depicted in Fig. 7,8. from [105].

Numerical observations are "brute-force computing" that makes no uncontrolled approximations to the assigned mathematical models. Their results show that for light nominal load, the linear proportionality between contact area and load is due to an increasing number of contact zones, while for higher pressure, the increase in contact area is associated with the expansion of the existing contacting spots [105], [122]. This increase can expand and merge contact spots (coalescence). Some propositions attempt to consider junction effects, however, they operate in a deterministic framework and not a statistical one, which is impractical in a complete analytical approach across scales [52], [128].

The use of the Hertzian-based contact theories is not restricted to vanishingly small areas, but can also be used for higher loads, at which the area evolves non-linearly with the load, and depends on the Nayak parameter [128]. On another hand, Persson models can lead to good qualitative predictions, but its model usually has difficult implementation [147].

2.3.2 Rough surfaces

Three important assumptions are normally considered when characterizing surfaces across the scales: (1) translational invariance; (2) isotropy; and (3) self-affinity.

Real surfaces found on the road consist of a plethora of asperities with different geometries, sizes, and distributions. Mathematically one could represent a surface as a height signal across a x-y plane, $z(\mathbf{x})$ (where $\mathbf{x} = (x, y)$). Exact measures of a rough surface across all scales require complex and time-consuming strategies of measure. However, due to its considerable geometrical complexity, it is convenient to represent the road surface by its statistical properties instead of its exact morphology [42].

Besides the mean height, another important descriptor is the variance σ^2, which measures the fluctuations around the mean height

$$\sigma^2 = \langle [z(\mathbf{x}) - \langle z(\mathbf{x}) \rangle]^2 \rangle \tag{2.3.4}$$

where if the average plane is conveniently placed at the origin, so that $\langle z(\mathbf{x}) \rangle = 0$, then $\sigma^2 = \langle z^2 \rangle$. In addition, other statistical properties of a generic random surface can be identified via the height-difference correlation function, given by

$$\Gamma_{HDC}(\mathbf{x}, \mathbf{x}_0) = \langle [z(\mathbf{x}_0 + \mathbf{x}) - \langle z(\mathbf{x}_0) \rangle]^2 \rangle \tag{2.3.5}$$

An alternative scale-sensitive analysis can be implemented via the use of another function called height-correlation, defined as

$$\Gamma_{HC}(\mathbf{x}, \mathbf{x}_0) = \langle z(\mathbf{x}_0 + \mathbf{x}) z(\mathbf{x}_0) \rangle - \langle z(\mathbf{x}_0) \rangle^2 \tag{2.3.6}$$

The correlation functions are related via $\Gamma_{HDC} = 2(\sigma^2 - \Gamma_{HC})$. Now, two new assumptions are presented when considering rough surfaces. The first is termed translational invariance, where the correlation functions do not depend on the choice of $\mathbf{x}_0$, so that their values are only associated with the in-plane distance vector $\mathbf{x}$ [52]. The second is called isotropy, so that the correlation functions do not depend on the direction along which the point $(\mathbf{x}_0 + \mathbf{x})$ is chosen [42].

Persson calculates $\langle z(\mathbf{x}_0 + \mathbf{x}) z(\mathbf{x}_0) \rangle$ as the spatial average of the height profile measurements taken over the area of interest, say $A = L^2$,

$$\langle z(\mathbf{x}_0 + \mathbf{x}) z(\mathbf{x}_0) \rangle = \int_0^L \int_0^L z(x_0 + x, y_0 + y) z(x_0, y_0) \, dxdy \tag{2.3.7}$$

This assumes that the largest asperity wavelength is much smaller than the characteristic size of L.

Power Spectral Density of rough surfaces

Except for the factor 2π (due to the radian terminology of frequency), the Fourier transform of $\langle z(\mathbf{x}_0 + \mathbf{x}) z(\mathbf{x}_0) \rangle$ can be defined as the surface Power Spectral Density density (PSD), $C(q)$ [52] so that

$$C(\mathbf{q}) = \frac{1}{(2\pi)^2} \iint\limits_{-\infty}^{\infty} \langle z(\mathbf{x}_0 + \mathbf{x}) z(\mathbf{x}_0) \rangle e^{-i(\mathbf{q} \cdot \mathbf{x})} \, dxdy \tag{2.3.8}$$

where $\mathbf{q}$ is termed wave-vector, a counterpart of $\mathbf{x}$ in the frequency domain (but spatial). When isotropy is considered, the PSD is a function of the magnitude of the wave-vector, $q = |\mathbf{q}|$

$$C(q) = \frac{1}{(2\pi)^2} \iint\limits_{-\infty}^{\infty} \langle z(\mathbf{x}) z(\mathbf{0}) \rangle e^{-i(\mathbf{q} \cdot \mathbf{x})} \, dxdy \tag{2.3.9}$$

Persson demonstrated via the Wiener–Khintchine theorem [52] that the PSD from eq. (2.3.9) can be directly calculated as

$$C(q) = \frac{1}{(2\pi)^2 A} |Z(q)|^2 \tag{2.3.10}$$

where $Z(q)$ is the Fourier transform of $z(\mathbf{x})$. This is a simpler form to be considered numerically via the use of the Fast Fourier Transform (FFT). One important remark is that the power spectra lose the phase information of the signal, which might have an impact upon the *skewness* of the roughness towards the peak or at the bottom of the surface.

Self-affinity

In a first-order approximation, most road surfaces can be considered to be nearly self-affine fractal [52], [66], [103], [129], [131]. This property refers to invariance of the surface statistical properties when a magnification by a factor ζ in the xy-plane and ζ^H in the perpendicular z is applied, so that

$$\langle z(\mathbf{x}) z(\mathbf{0}) \rangle = \langle \zeta^H z(\zeta \mathbf{x}) \zeta^H z(\mathbf{0}) \rangle \tag{2.3.11}$$

where H ($0 \leq H \leq 1$) is known as the Hurst exponent. It is related to the local fractal dimension D of the surface, via $D = \delta - H$ (where δ is the dimension of the Euclidean embedding space). In general, road surfaces tend to have $D \approx 2.2$ [45]. Sayles and Thomas demonstrated that for several surfaces the PSD could be represented by a power law [22], which was also identified for the case studies of Persson when eq. (2.3.11) is inserted in eq. (2.3.8) [52], rendering a power spectra that decreases as $q^{-2(H+1)}$. Still, for some cases, two scaling regimes identified with two distinct Hurst exponents (H_1 and H_2) can be a better description [72].

The schematic representation of both power law forms for the PSD is presented in Figure 2.12 and described by the following system

$$C(q) = \begin{cases} C_0 & \text{if } q_L \leq a < q_0 \\ \text{If single power law} & \\ C_0 \left(\frac{q}{q_0}\right)^{-2(H+1)} & \text{for } q_0 \leq a < q_1 \\ \text{If two-fold power law} & \\ C_0 \left(\frac{q}{q_0}\right)^{-2(H_1+1)} & \text{for } q_0 \leq a < q_1 \\ C_0 \left(\frac{q_1}{q_0}\right)^{-2(H_1+1)} \left(\frac{q}{q_1}\right)^{-2(H_2+1)} & \text{for } q_1 \leq a < q_2 \end{cases} \tag{2.3.12}$$

The smallest wave number, q_L, corresponds to the biggest length scale measured, above which the PSD remains constant until the wave number reaches what is called the roll-off frequency, q_0, with length $\lambda_0 = 2\pi/q_0$. This plateau persists as long as two heights in a certain scale remain uncorrelated, as previously discussed. The largest frequency, q_1 (or q_2 depending on the power-law considered), is called a cut-off wave number and although its value is associated with the smallest component of the dataset, its recovery is not easy and the correct estimation of this value remains a topic of research [103], [113], [118], [136].

For cases where the mean of the signal is zero,and in the case of translational invariance, using the inverse Fourier transform of eq. (2.3.8) yields

$$\langle z(\mathbf{x}_0 + \mathbf{x}) z(\mathbf{x}_0) \rangle \approx \langle z^2 \rangle = \iint\limits_{-\infty}^{\infty} C(\mathbf{q}) e^{i(\mathbf{q} \cdot \mathbf{x})} \, dq_x \, dq_y = 2\pi \int_{-\infty}^{\infty} q C(q) \, dq \tag{2.3.13}$$

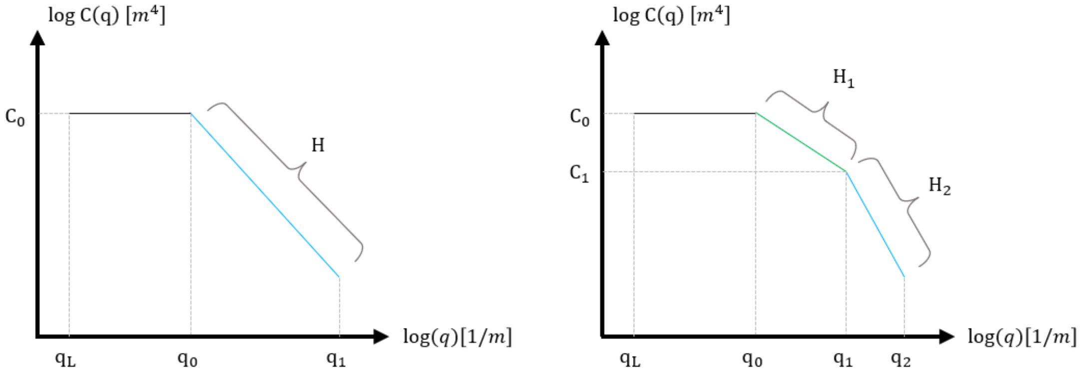

Figure 2.12: Single (left) and two-fold (right) power law representations of the Power Spectral Density density.

Beyond q_0, higher order moments of the PSD (associated with Nayak's parameters) like the average slope, (gradient) or curvature are dominated by shorter wave-length components [52], [118].

2.3.3 Hysteresis and adhesion

An important contribution to the understanding of rubber friction in dry surfaces was made by the seminar work of Grosch in 1963 [11]. The Author measured the friction force of rubber compounds sliding over a series of surfaces with different roughness. Each test was carried out at a constant temperature and at a very low sliding speed to keep the frictional heating low. Then, the run was repeated for many temperatures, so that a master curve could be defined with the WLF equation [5], as discussed in section 2.2.3. Figure 2.13 presents the master curves of friction for two rough surfaces, one without the presence of dust (clean silicon carbide) and one with a thin coating of magnesia powder (dusted silicon carbide).

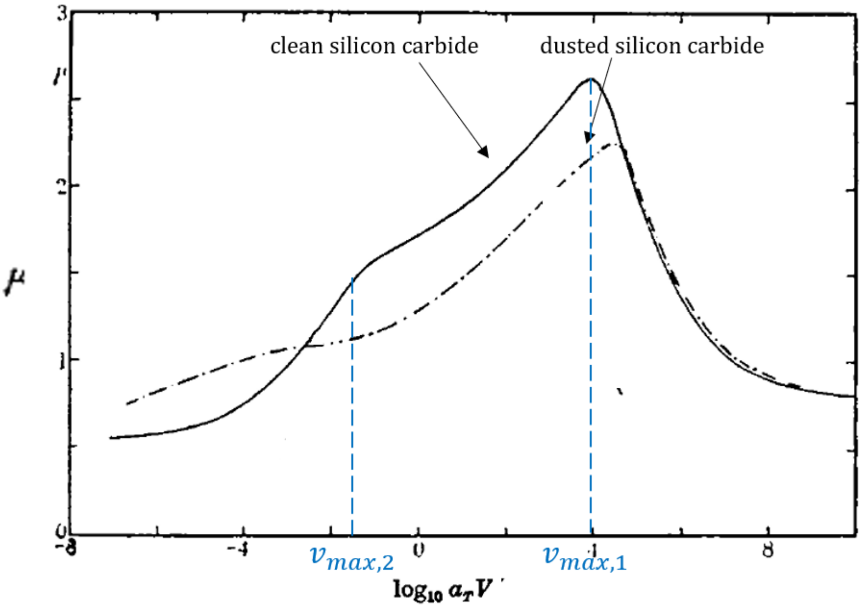

Figure 2.13: Master curve for the coefficient of friction of styrene-butadiene on three different surfaces (from [11]).

Grosh observed that, for the same surface substrate, the ratio between the velocity where friction value is maximum, $v_{max,1}$ and the frequency (in Hz), where the loss tangent is its highest, $f_{max,1} = \omega_{max,1}/(2\pi)$, was constant irrespective of the rubber, as shown in the wave speed equation

$$\frac{v_{max,1}}{f_{max,1}} = 1.5 \cdot 10^{-4} m. \tag{2.3.14}$$

As for the left bump present on the clean silicon carbide surface, its associated ratio was also found to be constant as long the surface was the same

$$\frac{v_{max,2}}{f_{max,2}} = 6 \cdot 10{-}9m. \tag{2.3.15}$$

Replacing the surface will modify the value of the ratios. From those relations, the friction coefficient for each rubber compound was associated with its own bulk viscoelastic properties. Moreover, the two peaks from Figure 2.13 are respectively related to two types of friction contributions: adhesion (first hump in clean silicon carbide surface) and hysteresis (second/max peak independent of clean or dusted silicon carbide) for the curve associated to clean silicon carbide in Figure 2.13.

Adhesion is generally described as an “intimal contact” between two surfaces so that inter-molecular and intra-molecular surface forces can be accounted for [128]. From a molecular point of view, it is believed to be associated with inter-molecular forces of bonding and de-bonding due to inter-molecular forces (i.e. Van Der Waals) [53] in the contact layer between the rubber material and the road surfaces [132]. Since the peak of the loss modulus precedes the entering to the glassy state, higher speeds than $v_{max,2}$ reduce its contribution. Another indicator of “intimal contact“ interpretation comes from the disappearance of the first peak when an intermediate separation, like magnesia powder, is added. Lastly, from Eq. (2.3.15) the order of this “effective” wavelength is much smaller than the one obtained from Eq. (2.3.14), justifying the position of the adhesion peak on the left of the hysteresis peak, since, for a lower speed, the frequency necessary to reach $f_{max,2}$ is achieved earlier for the smallest molecular scales.

Hysteresis is also known as “internal friction” or “internal cohesion”. It is related to the volumetric deformations imposed on the rubber by cyclic loading and unloading caused by the asperities of the surface, which in turn causes viscoelastic energy dissipation in the bulk of the material. For this reason, it is understandable to find the relationship in 2.3.14 for the loss tangent, as it concerns the transition zone where the viscoelastic dissipation is maximum. Moreover, the addition of magnesia powder changed slightly the maximum friction coefficient magnitude, as a fine layer still could slightly change the surface roughness as well.

Those two mechanisms can be contextualized to the interaction of rubber with a single asperity, as presented in Figure 2.14. The adhesion component relates to molecular chain stretch, caused by cohesion and decohesion at the rubber-surface interface, generating an opposing force to the relative motion of this close contact interface. It is a local mechanism sensitive to roughness and intermediate media like fluids and particles, as it reduces the true contact area [42]. In the case of hysteresis, as the rubber bumps against the left side of the asperity (Figure 2.14), the imposed deformation creates a reaction from the material. However, since a portion of the energy provided is lost, the rubber does not completely recover itself to interact with the right side of the asperity, as would be the case for a perfectly elastic material. This generates an asymmetry in the contact pressure distribution, resulting in a net tangential force component opposite to the sliding [42].

Since the recovery/lowering of the rubber on the right side, the asperity (Figure 2.13) is not instantaneous, the contact area is also asymmetric, which is a characteristic behavior

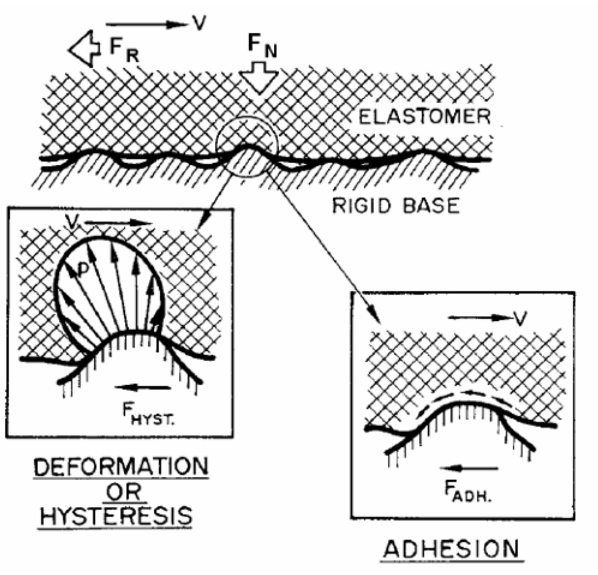

Figure 2.14: Hysteresis and Adhesion contributions representation for interaction between rubber and single asperity (from [21], [68]).

from the transition state. On the other hand, in Figure 2.15, for the lowest and highest speeds, the contact area seems to be almost as symmetric as a Hertz contact case. This is not surprising, as in very low and very high frequencies the rubber operates on its rubbery and glassy state, where low dissipation is expected (far from the maximum value of $\tan(\delta)$, in Figure 2.5) [17]. The non-instantaneous covering of the rubber around the asperity also justifies the smaller area on the high-speed case, since the rubber does not have time to greatly relax on either side. This is important if geometric or rheological non-linearities are considered [132] or even adhesion contribution.

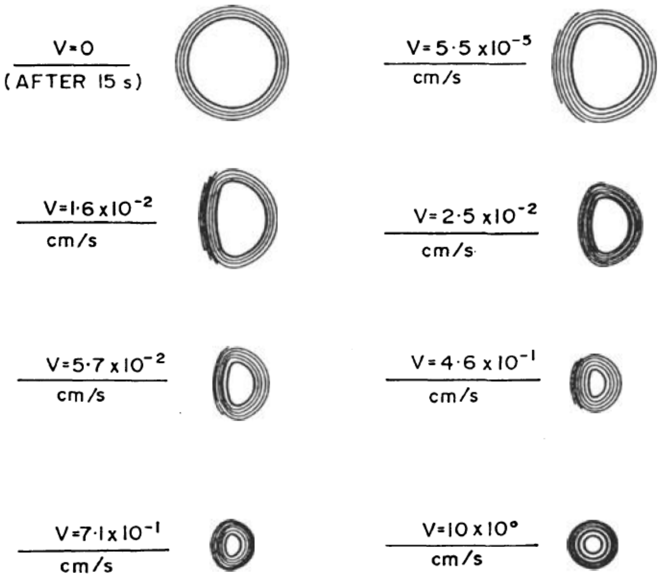

Figure 2.15: Experimental observation of a glass ball rolling at different speeds on epoxy resin. (from [17]).

2.3.4 Further effects

For applications in tire-road contacts, hysteresis and adhesion generally contribute the most to the friction response. Still, in light of additional geometrical considerations (multi-scale, sculpture), not only their interactions may vary, but also additional mechanisms might come into play in a coupled manner.

Lubricant in a rough surface

One of the first roles of lubricant was raised by Bowden and Tabor as a direct inhibitor of intimate contact between surfaces and an intermediate media between contact.

The capacity of the lubrication fluid to influence friction is recurrently represented via an empirical curve, today called Stribeck curve [53], represented in Figure 2.16. It demonstrates the evolution of the friction coefficient with Hersey number, $H = \eta V/P$, a dimensionless lubrication parameter defined by the fluid viscosity, η, applied pressure, P, and the sliding velocity, V. The horizontal axis could also be obtained in terms of the film thickness ratio, $\lambda_{film} = h_{film}/h_{RMS}$, composed by the height of the fluid layer, h_{film}, and combined root mean square of the surface roughness of the contacting surfaces.

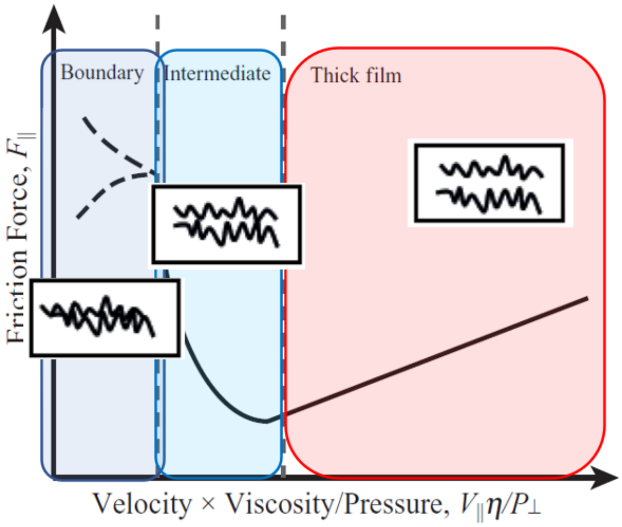

Figure 2.16: Schematic representation of a Stribeck curve. (from [17]).

What the curve in Figure 2.16 highlights is the evolution of the friction in three lubrication regimes [53], [147]:

- Boundary lubrication regime (on the left): Involves a single mono-layer of lubricant molecules, which are absorbed onto each of the surfaces during sliding ($\lambda_{film} \leq 1$).
- Hydrodynamic lubrication regime (on the right): Thick or very viscous films behaving as a barrier between interfaces, with friction force related to the viscous characteristics of the fluid ($\lambda_{film} \geq 3$).
- Intermediate/mixed lubrication regime (in the middle): Partial separation occurs, but not enough to hide completely the mechanical indentation perceived of the rubber promoted by the hard asperities ($1 \leq \lambda_{film} \leq 3$).

While adhesion has a considerable effect on dry friction, the presence of lubricant at the interface can prevent the rubber from coming into intimate contact with the counter surface, so that its contribution to overall friction can be sometimes neglected [55], [128].

On an even further argument, one of the indications for these strong inter-molecular forces not to dominate the frictional response, as observed by Grosch, lies in the low true contact area when surfaces are rough. For dry contact case, previous experimental investigations have been carried out at low rates of separation (v < mm/s) and showed that a roughness in the order of 1 μm was sufficient to reduce the adhesion to a low-level [20]. The true contact area is considered to be in the order of $\tilde{1}$% in comparison with the nominal contact area for tires on the road, and pure hysteretic models were found to indicate this statement [55]. However, the study cases considered were found to be restrictive and today adhesion is no longer considered to be negligible for rough dry surfaces [103], [113].

Unfortunately, due to the current empirical understanding of adhesion, it is not straightforward to argue that when a rough surface is lubricated, adhesion can be ignored. Indeed, for very sharp asperities and thin water films, partial adhesion is believed to occur due to dewetting effects [33], where the water is wiped away due to a *squeeze-out* phenomena, so that the lubricant between substrate and rubber may not remain in sealed off regions within the contact, producing dry patches [142].

The complications presented above are mostly related to small velocities (around mm/s) under boundary or mixed lubrication. When higher velocities are employed, high-end mixed lubrication or hydrodynamic regime behaviors become prevalent, so that a complete separation between the rough surface and the rubber is expected with no adhesion contributions [53]. On the other hand, complex fluid dynamic interactions should be considered. Fortunately, some pertinent simplifications with meaningful success and accessible implementation exist [43], [102], [108]. In addition, when the rough surface stiffness is much higher than the stiffness of the substrate (like rubber), even with complete fluid separation, the softer material is still partially deformed due to the influence of the rigid asperities, creating a convoluted hysteretic interaction with a “smoothed” roughness profile [108], [119]. This type of behavior is also called an Elastohydrodynamic regime, also found for elastic contact under high pressures. This last effect could also be considered within multi-scales scope, in addition to sealing effects, where small water pockets can be considered to be sealed off, serving as a cut-off of even smaller scales (usually below 1 μm) that will not be “observed” (as a hysteretic contribution) by the rubber anymore [55], [103], [129].

All the above contributions do not regard a direct tangential contribution of the fluid, but mainly its interaction with the most pro-eminent ones: hysteresis and adhesion. However, when the film of water is very thin (usually bellow 1 μm), viscosity can become non-negligible, and tangential contributions related to the shear of the film might exist [53]. Since the relative velocity of this work is considerably high, the water field is not believed to be *squeezed-out* to this extent, so this contribution is outside the scope of the research.

Wear

Wear occurs when the rubber material interacts with the rough road substrate. When the sliding velocity increases, the local stress at the contact point between the rubber and road surface also increases near the sharp asperities. This high stress at the contact point reduces the linkage between the rubber molecules and causes some rubber material to be detached [53].

Some qualitative characteristics can be considered from the visual inspection of the worn-out surface: for rough and sharp surfaces, the cutting and plowing of rubber by high local stresses applied by tips of asperities results in abrasion lines parallel to the sliding, while for smooth and clean surfaces, the adhesive wear results in a ripple perpendicular to the sliding direction, also known as ridge pattern. If sharp edges can be detected on the surface, it also indicates that the rubber materials are worn off by crack propagation and tearing (mechanical damage), while soft edges indicate material decomposition, due to high local temperature and stress, also known as thermo-chemical and mechano-chemical wear [24], [53].

A very important parameter to quantify this mechanism is wear rate, usually expressed in volume, or weight-loss per sliding distance. This descriptor is sensible to material proprieties, the surface topography of two bodies in contact, sliding velocity, squeezing load, and as well as environmental conditions, such as temperature and humidity [53]. Its physical effects on the rubber may create repercussions that indirectly affect friction, especially in long-term analysis (in this context, long sliding distances). For dry surfaces, over relatively long run-in phases (around 32 meters of sliding), the shape of the rubber may change, resulting generally in a different contact area, a more uniform temperature, and contact pressure distributions [114].

In addition, the interaction between filled rubbers (usually carbon or silica particles) and the rough surface may result in wear processes where the hard filler particles scratch the counter-surface (usually resulting in polishing of the counter-surface) [103]. For wet surfaces, a coupled effect of wear and lubrication might happen for charged/filled rubber with silica particles, whereas abrasive rubber exposes the silica particles on the compound surface, resulting in breaking down of thin water film, promoting the nucleation of dry patches [74].

Although long-term effects are more evident, in the case of short-time evaluations, studies relating wear and friction are relatively recent, with few physics-based wear models [63], [125]. Since hysteresis and adhesion still are the main contributors to rubber friction, for short sliding distances, abrasion contribution is usually neglected, except if there is a clear indication that it could be a piloting mechanism.

Flash-temperature

As previously discussed, a viscoelastic material presents a temperature dependence to which some applications can be derived, like the time-temperature equivalence, as presented in section 2.2.3. In another argument, in sliding conditions, the temperature can also increase in the contact area as a result of friction energy dissipation. This second effect can be coupled with the first if the temperature rise is high enough to affect the rheological properties of the material which, in turn, will also affect its friction result.

In tribology, this interplay is commonly called flash temperature, and its prevalence is tightly related to the interplay between local heat formation and its diffusion to the bulk of the rubber. Persson presented a rule-of-thumb that for road surfaces and velocities below 0.01 m/s [76], the temperature increase is negligible because of heat diffusion, above this value, local heating may result in stick-slip instabilities, affecting tire-road friction.

From it, other coupled effects could be related, like an increase in wear-rate [114] and, in more extreme cases, thermomechanical damage [24]. In addition, the change in surface also greatly affects the adhesion contribution, if present. On the other hand, a temperature regulation due to the presence of water might counterbalance these phenomena [108].

Interlocking

An important geometrical effect that is frequently observed but not thoroughly discussed for tread patterns is the interlocking between the rubber and the surface, where the rubber block hits with its front/leading edge asperities of the rough road surface and causes a horizontal resistance force. Sometimes, this cyclic interlocking is characterized by time-dependent stick-slip transitions at the macroscopic scales, here denominated as *mechanical gearing*, a condition occurring at the leading edge of the rubber block [129],

[138]. This is depicted in Figure 2.17 for a rubber immersed in water sliding over a rough surface at 0.1 m/s towards the left direction.

This effect can become involved in other mechanisms acting as a trigger to many of the previous points discussed. From a purely hysteretic interpretation on macro scales, each rubber block sometimes gets stuck against a macro-asperity (little or no slip in the contact area) and shears off very strongly until the contact breaks. This leads to very large strains values located near the contact edges [93], [128].

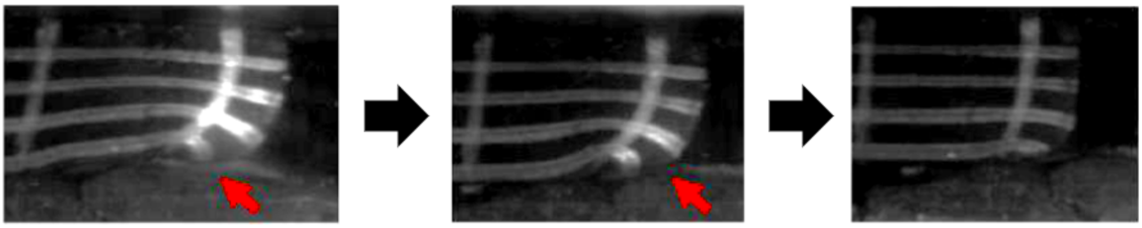

Figure 2.17: Tribological measurement (compression @2bar / shear/slip @0.1m/s) of a tread element on a wet rough surface (courtesy of Michelin).

2.4 Rubber friction approaches

The discussion presented so far fundamentally presents two important topics: contact with a pertinent choice of surface roughness across scales and potential physical effects related to the frictional behavior of rubber. True contact studies are one branch of tribology and not exclusive to elastomer materials and although important physical effects were identified, except for hysteresis, most other effects for rubber are conditionally dependent on the characteristics of the sliding conditions: lubrication, temperature, filler on elastomer material, distance and duration of sliding, velocity, rubber geometry, and others.

Those difficulties reflect on the current state of friction laws proposed in the literature for rubber in rough surfaces [128]. Multi-scale propositions are more recent than single-scale approaches and, therefore do not share the same level of coupling with different physical effects, and if they do, they usually are made via some empirical addition [42], [129], [136]. For this reason, although most topics in tribology are not mutually exclusive, they are not at the same point of theoretical, experimental, and implementation maturity. For this reason, this section is not an exhaustive listing of proposed frictional law, but instead a classification of the most important approaches and contextualizes their case to the current study.

2.4.1 Analytical models

Analytical models stem from theoretical assumptions with some level of experimental validation to construct an approximation of a phenomenon. When an adequate analytical model is properly characterized and the conditions to be evaluated are within the reach of its assumptions, it could be used as a stand-alone predictor.

For the frictional contact case, it is proposed a classification between two groups of analytical friction models: empirical (or semi-empirical) analytical models and physical-based analytical models. The difference between each will be clarified during the discussion.

Empirical models

Empirical models were developed to predict the friction coefficient at the contact interface as a certain function of the different parameters. They can be quite straightforward to construct and are usually implemented as local *ad hoc* friction values in numerical simulations. Some typical propositions are presented in Table 2.1.

Its characterization depends mostly on tribological tests and, although efficient in obtaining the result, they lack generality for different types of rubber and surfaces, causing an over-fitting of some particular result or requiring multiple tribological experiments tests to have a reasonable level of representativeness.

Proposed by	**Friction Law**	
Schallamach [3]	$\mu = \mu_0 \left(p/p_0\right)^{-\frac{1}{3}}$	(2.4.1)
Savkoor [26]	$\mu = \mu_s + (\mu_s - \mu_s) \exp\left[-h^2 \log^2\left(v/v_{peak}\right)\right]$	(2.4.2)
Huemer [75]	$\mu = \left(\alpha \lvert p \rvert^{n-1} + \beta\right) / \left(a + b/\lvert \mathbf{v} \rvert^{\frac{1}{m}} + c/\lvert \mathbf{v} \rvert^{\frac{2}{m}}\right)$	(2.4.3)
Radó [30]	$\mu = \mu_p \exp\left[-\left(\log(v/v_{peak})/C\right)^2\right]$	(2.4.4)
Lorentz [88]	$\mu_{adh} = (\tau_0/\sigma_0) \exp\left[\left(-c \log(v/v_{peak})^2\right)\right] P(q)$	(2.4.5)
Löwer [144]	$\mu = \mu_\infty - (\mu_\infty - \mu_0) \exp\left(-\lambda \bar{p}\right)$	(2.4.6)

Table 2.1: Typicla empirical friction models

In a sense, those approaches return a homogenized response of the contribution from all scales and the viscoelastic response by considering that tribological tests have all the necessary information.

Physical-based models

The goal of this review is to properly identify the possibilities of multi-scale physical-based friction laws. However, their development is usually long and considerably convoluted. Since the application/development of a specific friction law is not expected for this stage of the research, but a proper understanding of the models is still necessary. Thus, a simple case that uses contact theory Greenwood & Williamson [13] and linear viscoelastic material is developed and discussed based on Popov's work [131]. This example serves as a bridge to properly relate to more involved models and clarify their limitations for further purposes.

Considering the case of contact between a rigid sphere and a half space made of a linearly elastic material undergoing small deformation, as shown schematically in Figure 2.18.

Hertzian theory provides three important relations

$$a^2 = Rd \quad ; \quad F = \frac{4}{3} E^* R^{\frac{1}{2}} d^{\frac{3}{2}} \quad ; \quad A = \pi a^2 = \pi d R \tag{2.4.7}$$

where F is the normal force in the contact interface, R is the radius of the sphere, d is the associated penetration and $E^* = E/(1-\nu^2)$ is the effective (or reduced) Young modulus

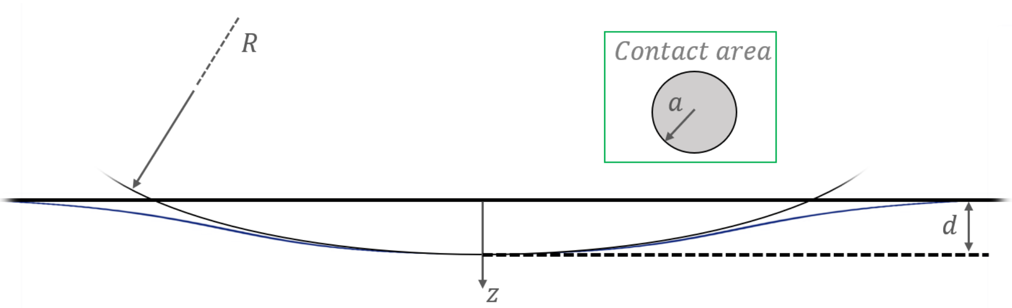

Figure 2.18: A rigid sphere in contact with an elastic half-space.

for the contact pair. The contact area, A, is circular with a as its radius. In addition to the assumptions made so far, for the relations to be valid in small deformation, d should be small compared to R.

Although not straightforward, one can easily identify this circular contact for the case between a rigid half-space and an elastic sphere, as its solution is equivalent to the current example.

Earlier GW contact theories considered a surface composed of asperities of the same size and curvature, with the *caveat* that the height distribution is stochastically distributed around a mean plane. If contacting asperities are sufficiently far from each other, their deformations are independent, allowing a convenient application of Hertzian contact.

Within this framework, Figure 2.19 displays a more complex scenario with a rough rigid surface of spheres of the same radii and vertical position stochastically distributed around a mean placed in the origin $z = 0$ and an elastic half-space distanced from this mean plane by h_0.

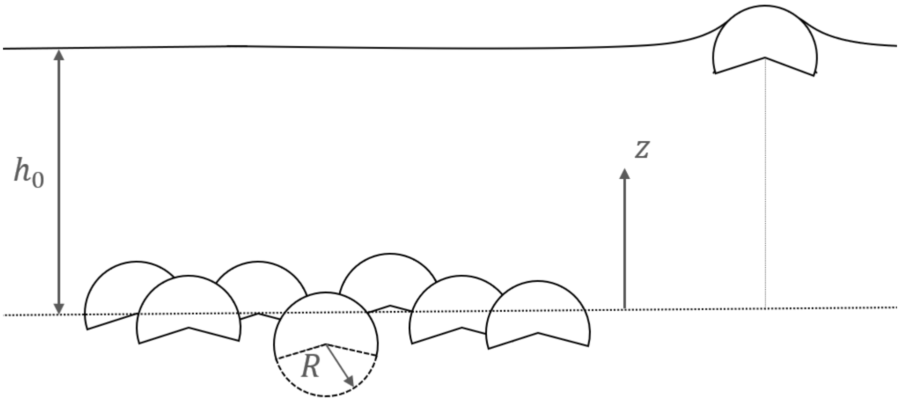

Figure 2.19: Model of a stochastic surface according to Greenwood and Williamson (based on [13]).

Contact only exists when a certain asperity vertical position is above the separation between the mean plane and the elastic half-space ($z > h_0$), therefore a slight change in notation is used to predict the load and contact area from the equations (2.4.7) as

$$\Delta F = \frac{4}{3} E^* R^{\frac{1}{2}} (z - h_0)^{\frac{3}{2}} \quad ; \quad \Delta A = \pi (z - h_0) R \tag{2.4.8}$$

To describe the height distribution (in the vertical direction as z), a probability density function, $\phi(z)$, is considered so that the probability of an asperity to have a height within the interval $[z; z + dz]$ is $\phi(z)dz$. Considering the distribution to be normal, $\phi(z)$ becomes

$$\phi(z) = \sqrt{\frac{1}{2\pi l^2}} e^{-\frac{z^2}{2l^2}} \tag{2.4.9}$$

where $l = \sqrt{\langle z^2 \rangle}$ is the root mean square of the height distribution and $\langle \cdot \rangle$ in this chapter represents the mean value. For this document, it represents the first proposition of a descriptor to characterize the *roughness* of a surface.

If the total number of asperities is N_0, then the number, of asperities residing within this same differential height interval is $N_0 \phi(z) dz$. If the interest is for all the contact cases above h_0 then

$$N = \int_{h_0}^{\infty} N_0 \phi(z)\, dz \tag{2.4.10}$$

As the induced elastic deformations are supposed to be independent, the total contribution of the N individual true contact areas and loads are in terms of true contact area

$$A = \int_{h_0}^{\infty} N_0 \phi(z) \pi (z - h_0) R\, dz \tag{2.4.11}$$

and in terms of total contact force

$$F = \int_{h_0}^{\infty} N_0 \phi(z) \frac{4}{3} E^* R^{\frac{1}{2}} (z - h_0)^{\frac{3}{2}}\, dz. \tag{2.4.12}$$

To make further progress, we introduce dimensionless quantities $\xi = z/l$ ad $\xi_0 = h_0/l$. Then, the total contact area, A and average contact area $\langle \Delta A \rangle$ per asperity can be written as follows

$$A = \int_{h_0}^{\infty} N_0 \phi(z) \pi (z - h_0) R\, dz = N_0 R l \sqrt{\frac{\pi}{2}} \int_{\xi_0}^{\infty} e^{-\frac{\xi^2}{2}} (\xi - \xi_0)\, d\xi \tag{2.4.13}$$

and

$$\langle \Delta A \rangle = \pi R l \left[\frac{\int_{\xi_0}^{\infty} e^{-\frac{\xi^2}{2}} (\xi - \xi_0)\, d\xi}{\int_{\xi_0}^{\infty} e^{-\frac{\xi^2}{2}}\, d\xi} \right]. \tag{2.4.14}$$

When the macroscopic normal load is increased, the mean asperity plane and the elastic half-space are expected to get closer, reducing ξ_0. Popov demonstrated that for an interval of normalized separation $[0; 5]$ quantities associated with the total area vary 7 orders of magnitude while the “mean local area per asperity only triples, as shown in Figure 2.20

Values close to $\xi_0 = 0$ represent very high loads, such that the true contact area is around 50% of the nominal contact area. For $\xi_0 \geq 4$ the contact is unrealistic, with very few contacting spots. Therefore, for a more realistic range of $[2.5; 3.5]$ is noticed that $\langle \Delta A \rangle / (\pi R l) \approx 0.3$. A good approximation for the average area of an asperity is, therefore

$$\langle \Delta A \rangle \approx R l \tag{2.4.15}$$

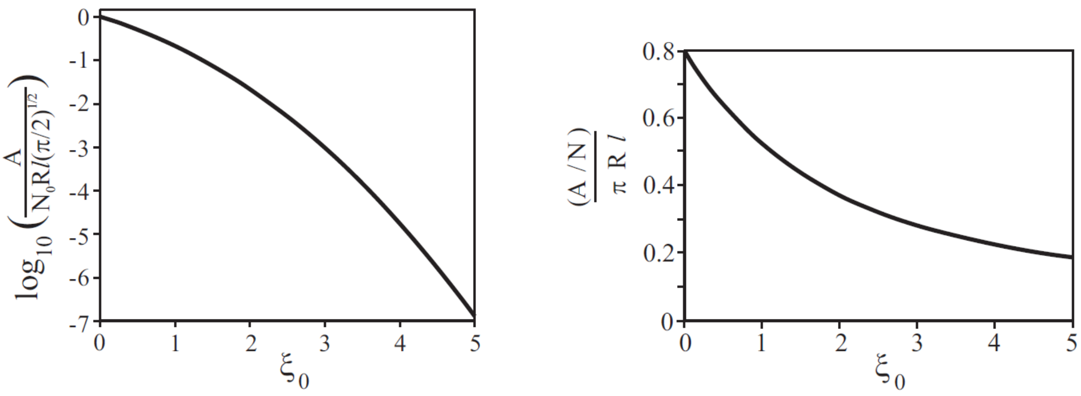

Figure 2.20: Dependence of the contact area and the average contact area of a single micro-contact on the separation variable (by [131]).

This shows that the average value of the microscopic contact area remains practically constant when the load varies by a few orders of magnitude. For the same range of $[2.5; 3.5]$ for ξ_0 the ratio between total contact area and load is also almost unchanged

$$\frac{A}{F} = \sqrt{\frac{R}{l}}\frac{3\pi}{4E^*}\left[\frac{\int_{\xi_0}^{\infty} e^{-\frac{\xi^2}{2}}(\xi - \xi_0)\, d\xi}{\int_{\xi_0}^{\infty} e^{-\frac{\xi^2}{2}}(\xi - \xi_0)^{\frac{3}{2}}\, d\xi}\right] \tag{2.4.16}$$

which the term in brackets can be approximated as a constant for a reasonable range of ξ_0. The average pressure, $\langle p \rangle$, applied on the true contact surface can be defined as

$$\langle p \rangle \approx \frac{F}{A} \approx k^{-1} E^* \sqrt{\frac{l}{R}} \tag{2.4.17}$$

recreating the linear relationship discussed in previous sections between true contact area and load. For a bit more generality, if the RMS and curvature are taken as the average of a sufficient large horizontal sample of the surface, and with the relation of the curvature with the second derivative of the surface signal, $1/R = -z''$, one has that

$$\sqrt{\frac{l}{R}} \to \sqrt{\langle z z'' \rangle} = \sqrt{\langle z'^2 \rangle} = \sqrt{\langle (\nabla z)^2 \rangle} \tag{2.4.18}$$

with $\sqrt{\langle (\nabla z)^2 \rangle}$ representing the root mean square of the gradient of the surface profile. Substituting (2.4.18) in (2.4.17) returns

$$\langle p \rangle \approx k^{-1} E^* \sqrt{\langle (\nabla z)^2 \rangle} \tag{2.4.19}$$

where for most elastic contact cases $k \approx 2$.

The friction force, F_f, can be calculated either by direct calculation of the horizontal component of the pressure force or by the energy loss caused by the material. For viscoelastic materials, if energy is being dissipated per second per unit surface in the sliding area as the power $\dot{W}$ at constant sliding velocity, v, then, from a macroscopic point of view, the total energy loss can be considered as being dissipated only by friction forces [52], [103], [131], [132]. By also using (1.3.2) and the newfound average contact pressure

$$\dot{W} = F_f v \to F_f = \frac{\dot{W}}{v} \to \mu = \frac{\dot{W}}{\langle p \rangle v} \tag{2.4.20}$$

The volumetric dissipation for a viscoelastic material was already derived in (2.2.3). After substituting the frequency in radians, ω, to the frequency in Hertz, $\tilde{\omega} = \omega/(2\pi)$, the power is given by

$$\dot{W}(\tilde{\omega}) = \frac{1}{2} r \tilde{\omega} \varepsilon_0^2 G''(\tilde{\omega}) \tag{2.4.21}$$

where it is assumed that the power dissipated to friction has been dissipated on average over a depth r equal to the characteristic diameter of the roughness. Since $\varepsilon^* = \varepsilon_0 e^{iwt}$, because the magnitude $||e^{iwt}|| = 1$, from eq. (2.2.7) the oscillation amplitudes of the stress and deformation are connected by the magnitude of the complex shear modulus so that

$$\sigma_0^2 = ||G^*(\tilde{\omega})||^2 \varepsilon_0^2 \quad ; \quad \frac{\sigma_0^2}{||G^*(\tilde{\omega})||^2} = \varepsilon_0^2 \tag{2.4.22}$$

Then, to associate σ_0 to the approximated contact pressure $\langle p \rangle$ description from eq. (2.4.19), incompressibility is assumed ($\nu \approx 0.5$)

$$E^*(\tilde{\omega}) \approx 4G^*(\tilde{\omega}) \tag{2.4.23}$$

so that eq. (2.4.19) becomes

$$\langle p \rangle \approx 4k^{-1} ||G^*(\tilde{\omega})|| \sqrt{\langle (\nabla z)^2 \rangle}. \tag{2.4.24}$$

Lastly, by substituting (2.4.24) into $(2.4.22)_2$ and subsequently in (2.4.21), this new form of the dissipated power can then enter on the friction equation from $(2.4.19)_3$, giving

$$\mu = \frac{\dot{W}}{\langle p \rangle v} = \kappa^* \frac{\tilde{\omega} r}{v} \sqrt{\langle (\nabla z)^2 \rangle} \frac{G''(\tilde{\omega})}{||G^*(\tilde{\omega})||} \tag{2.4.25}$$

with κ^* being a dimensionless coefficient on the order of unity.

The frequency of oscillation is assumed to be the ratio of the horizontal velocity v by the diameter r of the asperity, yielding

$$\tilde{\omega} = \frac{v}{r} \tag{2.4.26}$$

Doing the substitution and multiplying the friction equation by r renders the power dissipated per unit area so

$$\mu = \kappa^* \sqrt{\langle (\nabla z)^2 \rangle} \frac{G''(\tilde{\omega})}{||G^*(\tilde{\omega})||} = \kappa^* \sqrt{\langle (\nabla z)^2 \rangle} \frac{G''(v/r)}{||G^*(v/r)||} \tag{2.4.27}$$

From eq. (2.2.6), it is possible to conclude that $G''/G^* \leq 1$. Therefore, if adhesion contribution is not considered, the coefficient of friction cannot be larger than the average gradient of the surface $\mu \leq \sqrt{\langle (\nabla z)^2 \rangle}$.

One point of necessary caution regarding the above friction law is the limitation of the model caused by its assumptions. The friction law considers the GW-theory, which in itself is based on Hertzian contact theory. However, Hertz contact is also an approximation, whose theory implements a fundamental solution attributed to Boussinesq (1885) [82]. The solution consists of a superposition principle to an arbitrary pressure distribution $p(x, y)$ across elastic the half-space to yield the displacement field, $w(x, y)$, given as

$$w(x,y) = \frac{1}{\pi E^*} \int_{-\infty}^{\infty} \int_{-\infty}^{\infty} \frac{p(x', y')}{\sqrt{(x-x')^2 + (y-y')^2}} \, dx' \, dy'. \tag{2.4.28}$$

For the solution to be valid, two assumptions must hold. The first considers the surface gradient, $\sqrt{(\nabla z)^2}$, to be small in the relevant area of the given contact problem in the non-deformed and deformed state, usually termed *half-space approximation*. It is an important condition for the superposition principle. The second hypothesis is the linearity of the material with infinitesimal deformation behavior, which allows the superposition approach within the mapping of the pressure field to a displacement field. Those assumptions were also termed geometrical and rheological linearities within the context of rubber friction [132]. Those aspects will be discussed further in this document.

One final limitation to the example above is that the asperities had the same size and curvature across the whole surface, not representing a multi-scale physical-based friction law. This challenge has been addressed, among others, by Klüppel and Heinrich [41] and by Persson [45], which are reference works in this field. They are based on the same global use of the work caused by the dissipation of the viscoelastic model from eq. (2.4.20) and the consideration of a normal contact pressure based on a certain contact theory.

Persson's friction model [45] attempts to predict the hysteresis contribution to sliding friction between rubber and random rough surfaces across scales via a single equation

$$\mu = \frac{1}{2} \int_{q_0}^{q_1} q^3 P(q) C(q) \left\{ \int_0^{2\pi} \cos(\varphi) Im \left(\frac{2G^*(qv\cos(\varphi))}{\sigma_z (1-\nu)} \right) d\varphi \right\} dq. \tag{2.4.29}$$

Part of the terminology introduced by the equation was presented in section 2.3.2, where q_0 and q_1 are the roll-off and cut-off wave numbers respectively, and $C(q)$ is the Power Spectral Density Density (PSD) of the surface from eq. (2.3.9) or (2.3.10). The imaginary part of complex shear modulus, G^*, is considered. The normal stress, σ_z, was in some cases simplified by Persson as a uniform pressure distribution, σ_0. The quantity φ is the angle between the orientation of the local surface tangent and the sliding direction.

One additional term in equation (2.4.29) is the factor $P(q)$ representing the ratio between the contact area in a certain scale q and the macroscopic nominal contact area at $q = q_L$ (as defined in section 2.3.2 and represented in Figure 2.12). This term is considered to enforce a partial (and not saturated) contact since for most running conditions, the rubber usually never fills the cavities in a road across the whole contact region. A more detailed description of this particular parameter will follow later on in this section.

Persson's friction law is based on a contact theory developed by himself [45], and as previously discussed in section 2.3.1, the contact area ratio $P(q)$ has direct proportionality with normal stress and μ has an inverse proportionality to the nominal load. The normal load will then disappear from the expression, which, at least according to Persson, is proof that rubber friction is weak/independent on load [42], [52]. A weak dependence was also found for the derived eq. (2.4.27). In reality, a reduction in friction can be found for an increasing load [3], [39], but some consider this to be a thermal effect disguised as a load effect [76], [114].

Klüppel and Heinrich theory [41], [72], on the other hand, is a multi-scale friction law that is an extension of the Greenwood & Williamson contact theory [13] and a self-affine surface, their equation also describes the hysteresis contribution to friction [106]

$$\mu = \frac{\langle z_p \rangle}{2\pi\sigma_z} \int_{q_0 v}^{q_1 v} \frac{q}{\lambda^2} C_{1D}(q) Im\left(G^*(qv)(1+\nu)\right) \, d\varphi \, dq. \tag{2.4.30}$$

where λ is the associated wavelength of interest, and $\langle z_p \rangle$ is an average penetration depth of the rubber into the road surface and $C_{1D}(q)$ is a one dimensional PSD. Eq. (2.4.30) is a modified form from the original to better compare with Persson eq. (2.4.29) [41], [106].

Original Greenwood and Williamson theories [13] operate under the assumption of vanishing interaction between contact spots, which is adequate for small loads and/or distant contacting asperities. However, as shown in eq. (2.4.17), the local average contact pressure is quite insensitive for small loads [131], for high enough gradients, its magnitude gets closer to the modulus order [45], having a higher probability of large and/or complete penetration. A more recent extension of GW-theory [60] consider a second-order interaction between asperities for smaller scales [13] This last proposition presents a weak dependence on nominal/macro-scale normal load.

Another difference comes from the use of one-dimensional PSD (of unity m^3) so that the Fourier transform of the auto-correlation function from eq. (2.3.9) is considered only on the dimension of the sliding path.

$$C_{1D}(q) = \frac{1}{2\pi} \int_{-\infty}^{\infty} \langle z(x) z(0) \rangle e^{-i(qx)} \, dx. \tag{2.4.31}$$

As a consequence the one-dimensional PSD does not differentiate a sinusoidal surface from a two-wave surface as presented in table 2.2. Since both models are associated with the dissipated energy to the system, neglecting such additional cyclic loading on the rubber can influence friction prediction.

Signal	$C_{1D}(q)$	$C(q)$
$z_0 \cos(q_0 x)$	$\frac{z_0^2}{2}\delta(q-q_0)$	$\frac{z_0^2}{2}\delta(q-q_0)$
$z_0 \cos(q_0 x)\cos(q_0 y)$	$\frac{z_0^2}{2}\delta(q-q_0)$	$\frac{z_0^2}{2}\delta(q-q_0)\delta(q-q_0)$

Table 2.2: Comparison between the different strategies

Despite the distinctions presented so far, both theories agree quite well concerning the load dependency of rubber friction. In addition, both Klüppel and Heinrich or Persson's laws present qualitative correlation with some experimental cases [103], [113] or with numerical simulations [70], [122], [123]. The main debate revolves around the underlying multi-scale contact model considered, which was introduced in section 2.3.1, and current challenges are exemplified in Figure 2.10 and remain an open problem [123].

Limitations

Concerning non-linearities associated with the effects of filled rubbers, Persson, Tolpekina, and Pyckhout-Hintzen argue that in the analytical treatment of sliding friction, it is nearly impossible to include non-linearity in a completely rigorous way [133]. The usual approach assumes a linear relation between stress and strain in the theoretical derivations, but instead of using a small shear modulus, $G^*(\omega)$, an effective shear modulus $G^*(\omega, \epsilon)$ is considered for a typical strain ϵ involved in the problem of interest [52]. This is corroborated by other approaches found to add non-linear effects on rubber with Klüppel and Heinrich framework [124].

To further progress the current research, one way to identify the capabilities of physical-based friction laws is to relate what are the assumptions they both have in common: linear viscoelastic material law and small surface gradient $\langle(\nabla z)^2\rangle$.

For Klüppel and Heinrich's approach, a small RMS slope and a linear relationship between displacement and stress comes from its underlying Hertz contact theory, which is required for the Boussinesq solution from eq. (2.4.28) to hold and the integral from eq. (2.4.30) to still be valid.

In the case of Persson friction law, the evaluation is not trivial. Its contact framework already considers self-affine surfaces with $\sqrt{\langle z^2\rangle / R} \approx 1$ which is the gradient (from eq. (2.4.18)), which can be associated to high local contact pressure values (from eq. (2.4.19)) and a local strain to be as large as 100% [45]. The *caveat* is that the framework also acknowledges that, on smaller scales, the values and range of local contact pressures are so diverse and large that for analytical purposes they should be represented statistically. Persson tackles this by proposing a probability density function of stress that evolves through magnification in a diffusion-like manner, which seems to be a good qualitative representation of contact evolution [70], [103], [122]. This magnification framework imposes the use of a linear viscoelastic model so that its Fourier transform frequency excitation directly connects with the magnification variable.

Although finite strains are expected for smaller scales, it is believed to be highly *localized* around the tips of asperities. Ueckermann *et al* [104] measured the skid resistance of tires using the Wehner/Schulze test and suggested that an average strain of 8% better represents a contact patch. One possible interpretation of why this smaller average value does approximate well is considered. According to Persson, the probability density function presented in Figure 2.9 from section 2.3.1 relates to contact area fraction via

$$\frac{A(\zeta)}{A_0} = \frac{\sigma_0 \int_0^\infty P(\sigma, \zeta)\, d\sigma}{\int_0^\infty \sigma P(\sigma, \zeta)\, d\sigma} \tag{2.4.32}$$

where σ_0 is the nominal normal stress (contact pressure). Persson demonstrated [45] that

$$\sigma_0 = \int\limits_0^\infty \sigma P(\sigma, \zeta)\, d\sigma \tag{2.4.33}$$

which is expected as the mean value (expected value) of the normal stress at different length scales should equal the nominal pressure if equilibrium exists [125]. This also shows that $P(\sigma, \zeta)$ is not truly a probability density function for $\sigma \in (0, \infty)$, and its integration over this interval represents the ratio of the actual contact area to the nominal area which evolves with magnification

$$\frac{A(\zeta)}{A_0} = \int\limits_0^\infty P(\sigma, \zeta)\, d\sigma. \tag{2.4.34}$$

The exact determination of $P(\sigma, \zeta)$ requires a knowledge of σ relation with strain, which Persson considered to be linear. Since the objective of this construction is to gain insight without the exact definition of the stress, the qualitative behavior is related to Figure 2.9. By considering a stress $\sigma_N > \sigma_0$ that fully saturates the contact, it is noticed that two things can bring the distribution closer to σ_N: the increase of σ_0 which pushes the distribution $P(\sigma, \zeta)$ to higher values of σ and an increase in the magnification ζ that is directly related to the variance of $P(\sigma, \zeta)$ and a reduction of the overall integral from eq. (2.4.34). This leaves a small contact area ratio for those scales [98].

One additional insight is that on large magnifications, $P(\sigma, \zeta)$ is much flatter than distributions in bigger scales, which results in an integral from eq. (2.4.34) that is weakly sensitive to nominal pressure, corroborating with the behavior previously shown in Figure 2.20. It is important to remember that although nominal contact pressure σ_0 does not greatly impact the local contact area, a certain local contact spot area is sensitive to its correspondent local contact pressure. It is the large variety of local contact pressure across the whole surface that is represented statistically through $P(\sigma, \zeta)$.

Even if on smaller scales, the variance is large enough to present a portion of the distribution in $\sigma \geq \sigma_N$ (bigger probability of having saturated contact), its accountability is represented only through a very small contact area fraction value due to the reduction of the overall integral over magnification as seen in eq. (2.4.34). So an important aspect to follow is how "quickly" the variance would increase through magnification. Manners and Greenwood evaluated Persson's elastic contact theory [62] demonstrating that in full contact, the variance, V, is proportional to the average squared slope

$$V = \frac{1}{4} E^{*2} \langle (\nabla z)^2 \rangle \tag{2.4.35}$$

highlighting the connection that a high enough $\langle (\nabla z)^2 \rangle$ can potentially create an incorrect prediction of $A(\zeta)/A_0$. Surprisingly, in some cases, friction is not strongly affected by this. One of the possible reasons is due to compensating effects as [98], [132]: (1) the underestimation of deformation (through small contact area fraction) is compensated by an overestimated value of linear viscoelastic stiffness; (2) the high penetrations also occurs in high frequencies where rubber is usually in its glassy state with small contact area as shown experimentally by Figure 2.15; (3) in the full contact case, but still within linear assumptions, the linear contributions of each roughness length scale of a surface become effectively uncorrelated in the Fourier space [132].

In the work of Lorentz *et al* [88], a validation between the friction law and experimental observations was found only when the cut-off wave number, q_1, was truncated such that $\langle (\nabla z)^2 \rangle \approx 1.3$. This is not considered a solved problem but instead a "free parameter" which seems to derive good agreement with experiments [97], [136]. The reality behind this correspondence is probably in the middle: there is a good qualitative agreement in most of the models, but when one tries to be quantitative, the number of effects is so large that only a certain choice of the fitting parameters in the models, makes the answer reasonable, within the limited and well-specified range of experiments to be modeled.

Following the terminology of Yastrebov *et al* [122], the physical-based multi-scale friction laws are backed up by two principal "uncontrolled" approximations to connect surface and rheological information: small average slope (gradient) and linear stress-strain relationship. In Persson's theory, although finite deformations contributions (viewed as the contact area fraction) are seemingly restrained and counterbalanced in contrast to the overall effective dissipation of the system, the presence of strong non-linear stress-strain relationship and high enough surface gradients can compromise this delicate balance of compensations [98], [132].

As of now, the recipe of physical-based models is defined by three principal characteristics:

- The friction law is composed of geometrical information of the surface and rheological characteristics of the viscoelastic material;
- The connection between geometrical and rheological information is possible via the work/power equation caused by frictional forces, which are directly associated with the dissipation of the viscoelastic model;
- The chosen contact theory with the additional roughness assumptions (in this example, stochastic height distribution) will reflect on the resultant geometrical surface descriptor.

2.4.2 Numerical models

Pure numerical observations are "brute-force computing" that makes little to no a priori approximations. However, when direct numerical simulations are considered in contact analysis, the implementation of all scales simultaneously via explicit modeling of the surface roughness (from mm to μm) can be computationally long or even unfeasible, which imposes the use of multi-scale techniques with a priori coupling assumptions.

Multi-scale numerical modeling of material behavior is a vast subject that is not exclusive to friction-related research. In fact, in the context of the analysis of heterogeneous media, a frequently used classification of multi-scale methods is based on the underlying problem formulation (continuum or discrete) methods [116].

- Concurrent methods: In this method, two (or more) scales are simultaneously addressed in the problem formulation. In general, different lengths and time scales can be used in a single domain and different methodologies may be used on different parts of the domain;
- Hierarchical methods: In this case, the scales are linked in a hierarchical manner, which implies that distinct scales are considered and coupled in the same part of a domain;
- Hybrid methods: Interplay of previous classes (a combination between concurrent and hierarchical methods or a combination of two different concurrent (or hierarchical) methods).

From a tribological standpoint, Persson's [45] and Klüppel and Heinrich [41] friction models could be considered as concurrent methods, which are made tractable through a priori approximations of their proposed mathematical models.

A simple and general multi-scale approach in rolling contact is the use of *ad hoc* friction laws as local tangential contributions to the numerical framework. In other words, the whole rubber-surface system is explicitly calculated up to a certain scale and the smallest contributions are considered locally via an effective law. The friction law can be empirical in nature as the ones presented in Table 2.1 or physically based. This combination works best if: (1) the global numerical model can produce the necessary inputs for the friction function (i.e. pressure, relative velocity, temperature, etc); (2) The numerical local conditions respect the assumptions of the designated *ad hoc* law (i.e. homogeneous pressure distribution for Persson's friction law); (3) The contribution of all smaller scales than the numerical resolution can be treated as an effective tangential stress

Boundary methods

When rubber friction can be calculated in the framework of linear viscoelasticity with infinitesimal deformations and if the average square slope $\langle(\nabla z)^2\rangle$ is smaller than one, its numerical implementation requires solving the problem only for surface degrees of freedom, to which different techniques exist, namely: Green's Function Molecular Dynamics (GFMD) [57], Boundary Element Method (BEM) [91], Smart Block Molecular Dynamic (SBMD) [153], Multilevel Multi-Integration Method (MLMIM) [43] and FFT-based BEM (FFT-BEM) [31], [37], [137].

Those surface discretization techniques are less demanding than Finite Element Methods (FEM). Moreover, in multi-scale approach, many works incorporate FFT-based or MLMIM half-space techniques due their ability to consider all (or at least most) of the involved roughness length scales at once with reduced computational time [92], [95], [100]–[102], [111], [149]. Those approaches, like analytical laws, are also a form of concurrent method. Nonetheless, even if both operate within the half-space approximations, three pivotal advantages are gained: (1) The contributions of all scales are considered explicitly and not by simple superposition; (2) Coalescence (fusion) of contact spots with increasing load is present (3) The use of a discretized surface that contains characteristics outside the scope of convenient simplifications (non-Gaussian, non-self-affine, translational variant, etc) is possible since, in general, the surface Power Spectral Density does not necessarily contains all the necessary topographical information to describe a single surface. This notion is to be further discussed in Section 4.3.

Another strong advantage of using half-space contact problems is the maturity to which Elastohydrodynamics conditions are accounted for (as presented in section 2.3.4). Based on the previous studies on transient rough contact problems, the relation between the surface roughness deformation and operating conditions was considered through the "Amplitude Reduction Theory" [36], [56], later on, extended [59] and validated [87] for rough surfaces. This technique considers a correction of surface roughness amplitude due to the presence of fluid and soft material deformation across scales through a master curve as shown in Figure 2.21. This theory was later extended and applied to viscoelastic contact problems [43], [102], [108].

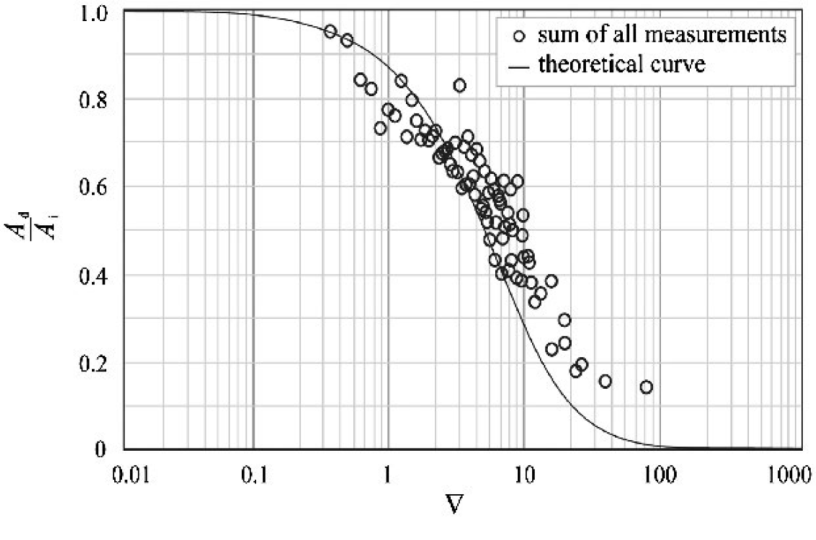

Figure 2.21: Relative amplitude as a function of the dimensionless wavelength parameter ∇. A_i and A_d are the amplitude of surface roughness and deformed surface, respectively. Continuous line is theoretical curve from [56] compared with experimental results from [87].

In terms of validity, linear models based on the viscoelastic half-space theory do predict the friction coefficient by accounting for all length scales of surface roughness, however, they are most accurate for root mean square slope values lower than one [111], [132], otherwise displaying slight overestimation in friction for large values of true contact area

[146]. The Amplitude Reduction Theory, although validated experimentally, is only valid for small average mean slopes of the surface as well [87], which also restraints this method to half-space approximation cases.

Finite element method

For soft viscoelastic materials, not only does the system operate under finite kinematics, but also the material itself contributes to the non-linearities of the overall problem. Those challenges bring forth the Finite Element Method as a very adequate approach due to its versatility. They require a discretization of the volumes of the contacting bodies and an appropriate treatment of their contact interaction [66]. The absence of restrictions on the material models and on the geometries of contacting solids makes this method a multipurpose engineering tool. However, this is possible at the cost of high computational complexity as compared to discretized half-space techniques [122], [128].

When contextualized to multi-scale analysis, the proper capture of the stress field in the vicinity of a contact zone requires a very dense spatial discretization. For the current study case, if a resolution up to 1 μm^2 is truly expected, the surface interface would require at least 10^7 cells to cover 1 cm^2 area. For this reason, FEM is justified if the problem at hand cannot be solved within the assumptions of half-space approximations, and even in this case, the use of concurrent methods might not be the best solution. As of now, the most mature non-linear numerical multi-scale approach for Finite Elements is the Hierarchical approach generally called *Contact Homogenization Technique* (CHT).

The CHT approach was first proposed by Wriggers and Temizer considering rigid particles embedded between a finitely deformable elastic solid and a rigid surface [73]. At this stage, the premise of the CHT approach model involved a repartition of surface roughness as a finite number of equivalent sinusoidal surfaces, to which from the smallest to the biggest, a FE simulation was made with a representative contact element (RCE) to recover a homogenized friction value. Then, this result is imposed recursively as local friction values to the next bigger scale. Later on, this approach was further developed: (1) to consider viscoelasticity [77]; (2) to define appropriate criteria for the RCE [94]; (3) to consider partitioned rough signal instead of equivalent sinusoidal signal [129]. It was also compared to linear kinematic approaches [132], [146] and to experimental results [126].

To give a clearer understanding as to why this method classifies as a Hierarchical approach, the principal steps and features are discussed for a simpler case with single "macro" and "micro" scale coupling, represented in Figure 2.22 and described as follows:

(A) A macroscopic calculation is used to determine local contact pressure values $p_{1,c}$ of all time steps and contact elements. In this step the contact is set to be friction-less and only the partitioned surface associated with this macro-scale is considered;

(B) Based on recurrence, a contact pressure distribution $n(p_{1,c})$ is built;

(C) The previous information is used to construct a field of boundary conditions allocating a finite number of relative velocities, $v_{2,i}$, and pressures, $p_{2,i}$. The subdivision and refinement of this field depends on $n(p_{1,c})$, as very high pressures occur less often and fewer points are considered;

(D) A periodic macroscopic representation of finite element setup is constructed and various friction-less calculations are performed for $v_{2,i}$ and $p_{2,i}$. Notice that, even in smaller scales, finite strain, and non-linear material models can be introduced here without greater issues;

(E) The micro-scale total tangential force, F_T can be obtained via the recovered energy dissipation (seen in $(2.4.20)_3$). The micro-scale total normal force F_N is found through balancing the surface reaction forces, enabling the computing of a coefficient of friction (as per the Amontons-Coulomb friction law defined in (1.3.2)). After a transition phase, a homogenized response of the friction can be obtained via

$$\bar{\mu} = \frac{1}{\Delta t} \int_{t_0}^{t_1} \mu(t)\, dt; \tag{2.4.36}$$

(F) The homogenized values of friction via eq. (2.4.36) are assembled as a discrete field $\mu_2(p_{2,i}, v_{2,i})$;

(G) The macroscopic calculation is calculated again, but this time with a local tangential value $\mu_2(p_{2,i}, v_{2,i})$ where any in-between inputs of pressure and/or velocity are interpolated for this discrete friction field.

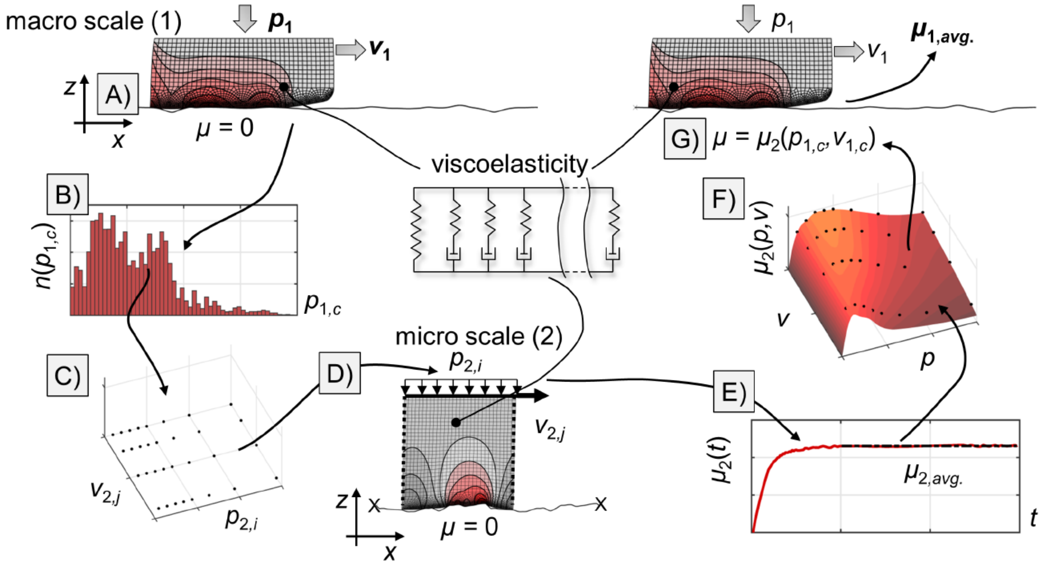

Figure 2.22: Schematic representation of two-scale CHT procedure step from A to G (by [129]).

The positive characteristics of this method are (1) Preservation of Finite Element formulation versatility across scales (no need for small strains, linear viscoelasticity and half-space considerations); (2) Although the coupling of scales is not as strong as a complete simulation encompassing all scales, it still surpasses a pure superposition of independent friction contributions across scales since, in this method, the local tangential forces from the smaller scales will interfere in the dissipation of the bigger scales.

The method also has clear challenges to address: (1) The friction field is based on an estimation defined from an initial friction-less macro-scale simulation, since local tangential forces can affect the macro dissipation to some degree, a strong deviation of the initial estimated friction field range might require a secondary loop of the whole procedure; (2) Although smaller scale dissipations do interfere with bigger scales, this interference is considered *as an effective tangential force*, only valid if the ratio between partitioned scales is high enough to ignore more elaborated ways the smaller dissipation can affect the bigger [94], [129]; (3) As more hierarchical scales are considered, the computational time can become large very quickly

In general terms, this approach still requires more validation. Most of the publications deal with dry contact and consider mainly hysteresis-based multi-scale approaches and, even if adhesion is considered, its contribution remains largely empirical. Some frameworks do exist to account for adhesion [64], [117], [145]. Lastly, although finite strains are an inherent part of this interaction, most studies do not consider non-linear viscoelastic materials.

Other perspectives

The choice between FEM or discretized half-space techniques is not trivial. The latter, when valid, is extremely efficient and has useful strategies to deal with lubrication, but in case their assumptions are compromised, FEM must be considered. Pure FEM approaches are complex and their computation time can quickly become impractical.

A more recent study made by Scaraggi, Comingio *et al* [110] evaluated the influence of geometrical and rheological non-linearity of rubber sliding over a Westergaard geometry (single asperity contact). Their study evaluated friction, true contact area, and pressure distribution for a range of velocities and pressures for different numerical techniques: (1) BEM, with linear rheology, linear kinematics, and small-slope roughness assumptions; (2) Finite Element with linear rheology and non-linear kinematics; (3) Finite Element with non-linear rheology (through a neo-hookean hyperelastic contribution) and non-linear kinematics. The main conclusions are: that the small deformations and small surface gradient assumptions of the discrete half-space techniques lead to quantitative deviations from the non-linear kinematic and rheological FE results in terms of contact area and contact pressure distribution. Remarkably, both techniques converge in terms of resulting friction as long $\sqrt{\langle(\nabla z)^2\rangle} \leq 1$. In addition, the contact area and pressure distribution in FEM and half-space simulations can converge for very high velocities since high-frequency asperity excitation operates in the glass state of the rubber (as shown in Figure 2.15) so that contact occurs only at the top of the asperity where both numerical scenarios and geometric non-linearities contributions are small.

The above conclusions are also related to Hybrid approaches where FEM and BEM are coupled into FEM-BEM solvers for the solution of three-dimensional contact problems [86], [132], [146]. The principle is to apply CHT techniques with Finite Elements only to scale ranges where $\sqrt{\langle(\nabla z)^2\rangle} > 1$ (usually found for the smallest scale) while half-space techniques could be potentially implemented for the remaining scales. Still, this proposition must be considered with caution, as a very simple non-linear rheological model was evaluated and experimental validations are, to current knowledge, yet to be made.

2.5 Concluding remarks

The present chapter reviewed central aspects of viscoelastic theory, concerning their linear and non-linear properties. These concepts were used as foundations to review concepts of sliding rubber friction, discussing: (i) rough ground characterization; (ii) physical mechanisms in place and (iii) the evolution of different contact models (analytical and numerical) and their differences.

The review outlines the scale of the problematic at hand and the risk of tackling all the problematic within a limited time-frame, since this is an active line of study being slowly filled by different lines of research and many experts in their own fields across the century. Therefore, in order to bring meaningful contributions to this research field, a prioritization is made when contextualized to the present object of study, producing the following highlights:

- Non-linear viscoelastic effects should not be overlooked due to the high filling content of industrial tire rubber mix;

- For tread patterns, its zone of influence and interaction exists beyond the interfacial road-rubber contact zone. Thus, a Finite Elements Method environment is preferable for this behaviour, at least for micro-scales;
- The relative velocity range of interest ($0.6 - 2$ $[m/s]$) is larger than the ranges where neglecting adhesion and lubrication effects could impact the output. This suggest, for the micro-scale:
  - The possibility of accounting for contributions with simplified approaches that prioritize hysteresis contribution with cut-off length scales of 1 $[\mu m]$;
  - The use of numerical and/or physical-based friction laws over empirical laws, due to their generality.

As of now, the decision of the friction law is yet to be made, as they require an adequate interconnection between experiments and numerical results already obtained on the macro-scale.

Chapter 3

Generic model

3.1 Basics of continuum mechanics

3.1.1 Kinematics

This section introduces the fundamental geometrical quantities for the identification of a material body, Ω, as a set of particles, P, and its different configurations when occupying parts of a three-dimensional Euclidean space, $\mathbb{E}^3$, in a certain moment in time. As large deformations are considered in this document, it is important to distinguish between the *reference* configuration (defined here as being the initial state at time $t = 0$) and a transformed time-dependent configuration termed *current*. Following the literature, the terms in the reference configuration are described here as capital letters, while the current configuration as small letters.

The position vector of a particle in the reference configuration is denoted as $\mathbf{X}$ and $\mathbf{x}$ for the current configuration, with both belonging to the three-dimensional Euclidean vector space, $\mathbb{V}^3$. The used basis system of unit vectors $\mathbf{E}_i$ and $\mathbf{e}_i$ is denoted utilizing the Einstein summation convention for both configurations

$$\mathbf{X} = X_i \mathbf{E}_i \quad ; \quad \mathbf{x} = x_i \mathbf{e}_i \tag{3.1.1}$$

nevertheless, since Cartesian coordinates were chosen for both configuration, in this particular case the base vectors are made identical, so that $\{\mathbf{E}_i\} = \{\mathbf{e}_i\}$.

As presented in Figure 3.1, motion and deformation are portrayed as a time-dependent coordinate (in this case Cartesian for both configurations) transformation/mapping between the reference and current configuration

$$\mathbf{x} = \varphi(\mathbf{X}, t). \tag{3.1.2}$$

When a field value is described in terms of position $\mathbf{X}$, the description is called Lagrangian or material. Conversely, when $\mathbf{x}$ is used, it is termed Eulerian or spatial description. The body in the reference configuration is defined as Ω_0, while its boundary, $\partial\Omega_0$, is partitioned into two parts: Γ_t with imposed surface traction and Γ_u with prescribed displacements. Their counterparts in the current configuration are, respectively, $\Omega(t)$, γ_t, γ_u and γ_c as indicated in Figure 3.1 such that

$$\Gamma_t \cup \Gamma_u = \partial\Omega_0 \quad ; \quad \Gamma_t \cap \Gamma_u = \emptyset \tag{3.1.3}$$

and

$$\gamma_t \cup \gamma_u = \partial\Omega(t) \quad ; \quad \gamma_t \cap \gamma_u = \emptyset \tag{3.1.4}$$

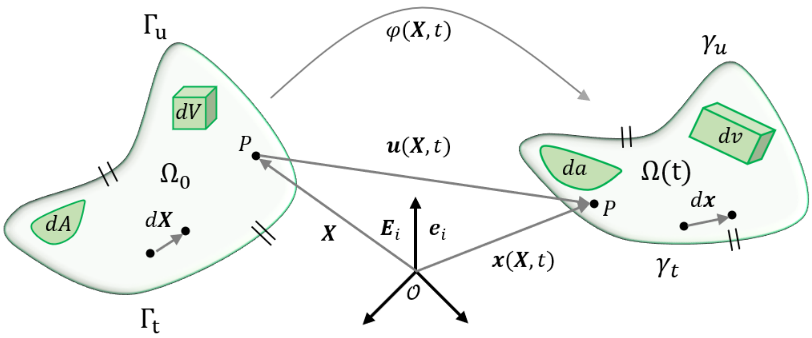

Figure 3.1: Kinematics of a solid body including surface, line and volume elements.

The displacement vector, $\mathbf{u}$ is the difference between the reference and current position vectors

$$\mathbf{u}(\mathbf{X},t) = \varphi(\mathbf{X},t) - \mathbf{X} = \mathbf{x}(\mathbf{X},t) - \mathbf{X} \tag{3.1.5}$$

while the time derivative of the current position vector describes the velocity $\mathbf{V}(\mathbf{X},t)$ and its second time derivative, the acceleration $\mathbf{A}(\mathbf{X},t)$

$$\mathbf{V}(\mathbf{X},t) = \frac{d\mathbf{u}}{d\mathbf{t}}(\mathbf{X},t) = \frac{d\mathbf{x}}{d\mathbf{t}}(\mathbf{X},t) = \dot{\mathbf{x}}(\mathbf{X},t) \tag{3.1.6}$$

$$\mathbf{A}(\mathbf{X},t) = \frac{d^2\mathbf{x}}{dt^2} = \frac{d\mathbf{V}}{d\mathbf{t}}(\mathbf{X},t) = \ddot{\mathbf{x}}(\mathbf{X},t). \tag{3.1.7}$$

The deformation gradient tensor $\mathbf{F}$ maps a line element, $d\mathbf{X}$, from the initial configuration to the current configuration as $d\mathbf{x}$ during a deformation process so that

$$d\mathbf{x} = \mathbf{F}d\mathbf{X} \quad ; \quad \mathbf{F} = \frac{\partial\mathbf{x}}{\partial\mathbf{X}} = \nabla\varphi = \nabla\mathbf{x}. \tag{3.1.8}$$

From a physical interpretation, two points should not collapse to the same position, neither pass through themselves, therefore we should have a transformation $\mathbf{F}$ such that

$$det(\mathbf{F}) = J > 0 \tag{3.1.9}$$

where J is called Jacobian. This also reflects on the mapping between the current and reference infinitesimal volumes

$$dv = JdV. \tag{3.1.10}$$

Lastly, surface elements can be mapped with Nanson's formula

$$\mathbf{n}da = J\mathbf{F}^{-T}\mathbf{N}dA \tag{3.1.11}$$

with $\mathbf{n}$ and $\mathbf{N}$ being the normal vector of the considered surface element in current and reference configuration.

The deformation induced strains inside the body can be described using the squares of the lengths of the differential elements $d\mathbf{x}$ and $d\mathbf{X}$

$$|d\mathbf{x}|^2 = d\mathbf{X} \cdot \mathbf{F}^T\mathbf{F}d\mathbf{X} = d\mathbf{X} \cdot \mathbf{C}d\mathbf{X} \tag{3.1.12}$$

and

$$|d\mathbf{X}|^2 = d\mathbf{x} \cdot \mathbf{F}^{-T}\mathbf{F}^{-1}d\mathbf{x} = d\mathbf{x} \cdot \mathbf{B}^{-1}d\mathbf{x} \tag{3.1.13}$$

with $\mathbf{C}$ being called the right Cauchy-Green deformation tensor in the reference configuration and $\mathbf{B} = \mathbf{F}\mathbf{F}^T$ the left Cauchy-Green deformation tensor in the current configuration.

Another important strain measure is related to the differences in the squares of the undeformed and deformed lengths, $d\mathbf{x}$ and $d\mathbf{X}$, where three relations are of importance in this document: the Green-Lagrange strain tensor, $\mathbf{E}$, Euler-Almansi strain tensor, $\mathbf{e}$, and Hencky/true strain tensor, $\mathbf{E}_0$

$$\mathbf{E} = \frac{1}{2}(\mathbf{C} - \mathbf{I}) \quad ; \quad \mathbf{e} = \frac{1}{2}(\mathbf{I} - \mathbf{B}^{-1}) \quad ; \quad \mathbf{E}_0 = \frac{1}{2}\log(\mathbf{C}). \tag{3.1.14}$$

where $\mathbf{I}$ is the identity tensor.

As previously mentioned, the deformation gradient transformation accepts an inverse, $\mathbf{F}^{-1}$. From the polar decomposition theorem, the tensor can be decomposed into an orthogonal tensor and a positive definite symmetric tensor

$$\mathbf{F} = \mathbf{R}\mathbf{U} = \mathbf{V}\mathbf{R} \tag{3.1.15}$$

where, $\mathbf{R} \in Orth^+$ ($\mathbf{R}\mathbf{R}^T = \mathbf{R}^T\mathbf{R} = \mathbf{I}$ and $det(\mathbf{R}) = 1$). The tensors $\mathbf{U}$ and $\mathbf{V}$ are called right stretch tensor and left stretch tensor, having both the properties of being positive definite (i.e. $\mathbf{q} \cdot \mathbf{U}\mathbf{q} > 0$ for non-zero $\in \mathbb{R}^3$) and symmetric (i.e $\mathbf{V}^T = \mathbf{V}$). By using the polar decomposition on the right and left Cauchy-Green deformation tensor, one finds that

$$\mathbf{C} = \mathbf{U}^T\mathbf{U} = \mathbf{U}^2 \quad ; \quad \mathbf{B} = \mathbf{V}\mathbf{V}^T = \mathbf{V}^2 \tag{3.1.16}$$

Lastly, an important relation is the time derivative of the deformation tensor. By making use of the mapping $\mathbf{x}(\mathbf{X}, t)$, the velocity and acceleration can be recast as

$$\mathbf{V}(\mathbf{X}, t) = \dot{\mathbf{x}}(\mathbf{X}, t) = \mathbf{v}\{\mathbf{x}(\mathbf{X}, t), t\} \tag{3.1.17}$$

$$\mathbf{A}(\mathbf{X}, t) = \ddot{\mathbf{x}}(\mathbf{X}, t) = \mathbf{a}\{\mathbf{x}(\mathbf{X}, t), t\} \tag{3.1.18}$$

so that

$$\dot{\mathbf{F}} = \frac{\partial}{\partial t}\frac{\partial \mathbf{x}}{\partial \mathbf{X}} = \frac{\partial \dot{\mathbf{x}}}{\partial \mathbf{X}} = \frac{\partial \mathbf{V}}{\partial \mathbf{X}} = \frac{\partial \mathbf{v}}{\partial \mathbf{X}} = \frac{\partial \mathbf{v}}{\partial \mathbf{x}}\frac{\partial \mathbf{x}}{\partial \mathbf{X}} = \mathbf{L}\mathbf{F} \quad ; \quad \mathbf{d} = \frac{1}{2}(\mathbf{L} + \mathbf{L}^T) \quad ; \quad \mathbf{w} = \frac{1}{2}(\mathbf{L} - \mathbf{L}^T) \tag{3.1.19}$$

where $\mathbf{L} = \partial\mathbf{v}/\partial\mathbf{x}$ is called spatial velocity gradient, $\mathbf{d}$ and $\mathbf{w}$ are, respectively, their symmetric and anti-symmetric/skew portion. $\mathbf{d}$ is effectively a measure of deformation rate for large deformations, while $\mathbf{w}$ is a measure of the rate of rotation of the material.

3.1.2 Stress and general principles

Cauchy's theorem postulate state that the traction per unit surface, $\mathbf{t}$, depends linearly to the outward normal $\mathbf{n}$ of the differential area, da, considering it is is continuous through $\mathbf{x}$. If true, there is a second-order tensor called Cauchy-Stress tensor, $\boldsymbol{\sigma}$, such that

$$\mathbf{t}(\mathbf{x}, \mathbf{n}, t) = \boldsymbol{\sigma}(\mathbf{x}, t)\mathbf{n}. \tag{3.1.20}$$

By using Nanson's formula form (3.1.11), one may write

$$\boldsymbol{\sigma}\mathbf{n}da = J\boldsymbol{\sigma}\mathbf{F}^{-T}\mathbf{N}dA \tag{3.1.21}$$

which allows us to define another second-order tensor called First-Piola Kirchhoff (1-PK), $\mathbf{P}$

$$\mathbf{P} := J\boldsymbol{\sigma}\mathbf{F}^{-T} \tag{3.1.22}$$

forming another type of traction density, $\mathbf{T}$, acting in the differential areas of the reference (also could be contextualized to undeformed) configuration

$$\mathbf{T} = \mathbf{P}\mathbf{N} \tag{3.1.23}$$

so that we have $\mathbf{t}da = \mathbf{T}dA$. The operation presented for stress in (3.1.22) is a push-forward (reference to current configuration fields) and pull-back (current to reference configuration fields) operation. This manipulation play an important role in many theoretical derivations and practical applications, for example, to ensure objectivity. Another concept of pull-back (to the rotated configuration) can be employed to define a rotated stress tensor, $\boldsymbol{\sigma}$ defined via

$$\boldsymbol{\sigma} := \mathbf{R}^T\boldsymbol{\sigma}\mathbf{R}. \tag{3.1.24}$$

Conservation of mass

If mass, m, do not change in time, one might express over the domain of the body, by considering the mass density $\rho = \rho(\mathbf{x}, t) \geq 0$, that

$$\frac{dm}{dt} = \frac{d}{dt}\int_{\Omega(t)} \rho \, dv = 0. \tag{3.1.25}$$

If that is true then,

$$\int_{\Omega(t)} \rho \, dv = \int_{\Omega_0} \rho_0 \, dV \tag{3.1.26}$$

where $\rho_0 = \rho_0(\mathbf{X})$ represents the mass density on the reference configuration. By using (3.1.10) it further follows that

$$\int_{\Omega_0} J\rho \, dV = \int_{\Omega_0} \rho_0 \, dV \tag{3.1.27}$$

so that

$$\rho = J^{-1}\rho_0. \tag{3.1.28}$$

By taking the material time derivative (or Lagrangian time derivative) given as

$$\frac{D\langle\cdot\rangle}{Dt} = \frac{\partial\langle\cdot\rangle}{\partial t} + \left(\frac{\partial\langle\cdot\rangle}{\partial t} \cdot \nabla\langle\cdot\rangle\right) \tag{3.1.29}$$

of eq (3.1.28) renders

$$\dot{\rho} = \frac{\partial\rho}{\partial t} + \frac{\partial\rho}{\partial \mathbf{x}} \cdot \mathbf{v} = -\frac{1}{J^2}\dot{J}\rho_0 = -\frac{1}{J}\mathbf{F}^{-T} \cdot \dot{\mathbf{F}}\rho_0 \tag{3.1.30}$$

By using the first statement form eq. (3.1.19) the last expression can be recast as

$$\frac{\partial\rho}{\partial t} + div(\rho\mathbf{v}) = 0. \tag{3.1.31}$$

where $div\langle\cdot\rangle = \partial\langle\cdot\rangle/\partial\mathbf{x}$. This form is also called the *continuity equation.*

Balance of linear momentum

The time derivative of the linear momentum of a body in the current configuration must equals the sum of the applied external forces forming the balance equation

$$\frac{d}{dt}\int_{\Omega(t)} \rho\mathbf{v} \, dv = \int_{\Omega(t)} \rho\mathbf{b} \, dv + \int_{\partial\Omega(t)} \mathbf{t} \, da \tag{3.1.32}$$

where $\mathbf{b} = \mathbf{b}(\mathbf{X}, t)$ is a body force per unit mass acted on the body, and $\mathbf{t} = \mathbf{t}(\mathbf{X}, t)$ the force previously described, and $\mathbf{v} = \mathbf{v}(\mathbf{x}, t)$ the spatial description of velocity, from (3.1.17). By implementing the conclusions from (3.1.31) on the left term, decomposing the traction using Cauchy's theorem and then invoking Gauss theorem for the surface integral to be exchanged by a volume integral, (3.1.32) becomes

$$\int_{\Omega(t)} div(\boldsymbol{\sigma}) \, dv + \int_{\Omega(t)} \rho\mathbf{b} \, dv = \int_{\Omega(t)} \rho\dot{\mathbf{v}} \, dv \tag{3.1.33}$$

so that locally

$$div(\boldsymbol{\sigma}) + \rho\mathbf{b} = \rho\dot{\mathbf{v}} = \rho\ddot{\mathbf{x}}. \tag{3.1.34}$$

By using (3.1.22) and the conservation of mass and the change in the coordinates as done in (3.1.17), the balance of linear momentum, (3.1.34), can be pushed back as

$$Div(\mathbf{P}) + \rho_0\mathbf{B} = \rho_0\dot{\mathbf{V}} \tag{3.1.35}$$

considering that $\mathbf{B}(\mathbf{X}, t) = \mathbf{b}\{\mathbf{x}(\mathbf{X}, t)\}$ and $Div\langle\cdot\rangle = \frac{\partial\langle\cdot\rangle}{\partial\mathbf{X}}$.

Balance of angular momentum

This balance is formulated with respect to a fixed point $\mathbf{x}_0$ as a reference. So, the time derivative of angular momentum in the current configuration equals the sum of applied external moments

$$\frac{d}{dt}\int_{\Omega(t)} (\mathbf{x} - \mathbf{x}_0) \times \rho\dot{\mathbf{v}}\, dv = \int_{\Omega(t)} (\mathbf{x} - \mathbf{x}_0) \times \rho\mathbf{b}\, dv + \int_{\partial\Omega(t)} (\mathbf{x} - \mathbf{x}_0) \times \mathbf{t}\, da \tag{3.1.36}$$

Using the Gauss theorem, the conservation of mass, and the balance of linear momentum just obtained, it can be shown that the Cauchy stress tensor has to be symmetric, so that

$$\boldsymbol{\sigma} = \boldsymbol{\sigma}^T. \tag{3.1.37}$$

By also inserting (3.1.22) on this relation, one also finds the result in terms of the First Piola-Kirchhoff stress tensor

$$\mathbf{P}\mathbf{F}^T = \mathbf{F}\mathbf{P}^T. \tag{3.1.38}$$

Balance of energy

From the first law of thermodynamics, the sum of applied mechanical power, M and non-mechanical power (like thermal), P must equals the time derivative of the total energy, which can also be decomposed into a kinetic part, K and an internal energy part, I. From it

$$\frac{d}{dt}(K + I) = M + P \tag{3.1.39}$$

By introducing local quantities as the specific internal energy per unit mass, $e(\mathbf{x}, t)$, heat source per unit mass, $r(\mathbf{x}, t)$ and a heat flux per unit area (in the current configuration), $h(\mathbf{x}, t)$ such that

$$h(\mathbf{x}, t) = -\mathbf{q}(\mathbf{x}, t) \cdot \mathbf{n} \tag{3.1.40}$$

equation (3.1.36) is conveniently written in integral form with respect to the current volume and area similar to the previous balances

$$\frac{d}{dt}\int_{\Omega(t)} \rho\left(e+\frac{1}{2}\mathbf{v}\cdot\mathbf{v}\right)dv = \int_{\Omega(t)} \rho\left(\mathbf{b}\cdot\mathbf{v}+r\right)dv + \int_{\partial\Omega(t)} \mathbf{t}\cdot\mathbf{v}-\mathbf{q}\cdot\mathbf{n}\,da \tag{3.1.41}$$

Similarly, the use of the Gauss theorem and (3.1.34) yields the local form

$$\rho\dot{e} = \rho r + \boldsymbol{\sigma}:\mathbf{L} - div(\mathbf{q}) \tag{3.1.42}$$

with the spatial velocity gradient, $\mathbf{L}$ taken from (3.1.19). And the double dot is the contracted product, with the property that since Cauchy-Stress was found to be symmetric on (3.1.37), we also have that

$$\rho\dot{e} = \rho r + \boldsymbol{\sigma}:\mathbf{d} - div(\mathbf{q}) \tag{3.1.43}$$

Equivalently, inserting (3.1.22) in (3.1.42) and defining the following relations

$$E(\mathbf{X},t) = e\{\mathbf{x}(\mathbf{X},t),t\} \tag{3.1.44}$$

$$R(\mathbf{X},t) = r\{\mathbf{x}(\mathbf{X},t),t\} \tag{3.1.45}$$

$$\mathbf{Q}(\mathbf{X},t) = J\mathbf{q}\{\mathbf{x}(\mathbf{X},t),t\}\mathbf{F}^{-T} \tag{3.1.46}$$

the balance of energy can be expressed as

$$\rho\frac{\partial E}{\partial t} = \rho R + \mathbf{P}:\dot{\mathbf{F}} - Div(\mathbf{Q}) \tag{3.1.47}$$

Entropy inequality

Considering the existence of two additional quantities: the entropy per unit mass $\eta(\mathbf{x},t)$ and the absolute temperature $\theta(\mathbf{x},t)$, we can introduce the second principle of thermodynamics

$$\frac{d}{dt}\int_{\Omega(t)} \rho\eta\,dv \geq \int_{\Omega(t)} \frac{\rho r}{\theta}\,dv - \int_{\partial\Omega(t)} \frac{1}{\theta}\mathbf{q}\cdot\mathbf{n}\,da. \tag{3.1.48}$$

Making use of the conservation of mass, (3.1.48) can be written locally as

$$\rho\theta\dot{\eta} \geq \rho r - div(\mathbf{q}) + \frac{1}{\theta}\mathbf{q}\cdot grad(\theta) \tag{3.1.49}$$

where *grad* is the gradient in the current configuration.

Additionally, this inequality can be rewritten in terms of the energy available to do work, the Helmholtz free energy, $\psi(\mathbf{x},t)$

$$\psi = e - \theta\eta \tag{3.1.50}$$

returning after use of the energy conservation Eq. (3.1.43)

$$\boldsymbol{\sigma} : \mathbf{L} - \rho(\dot{\psi} - \eta\dot{\theta}) - \frac{1}{\theta}\mathbf{q} \cdot grad(\theta) \geq 0. \tag{3.1.51}$$

This last relation is also called Clausius-Duhem inequality (or the reduced dissipation inequality). As achieved previously, this inequality can also be pushed-back by introducing

$$\Theta(\mathbf{X}, t) = \theta\{\mathbf{x}(\mathbf{X}, t), t\} \tag{3.1.52}$$

$$N(\mathbf{X}, t) = \eta\{\mathbf{x}(\mathbf{X}, t), t\} \tag{3.1.53}$$

from those, the Helmholtz free energy can also be represented with the same reference

$$\Psi = E - \Theta N \tag{3.1.54}$$

therefore

$$\rho_0 \left(\frac{\partial \Psi}{\partial t} - N \frac{\partial \Theta}{\partial t} \right) + \frac{1}{\Theta}\mathbf{Q} \cdot Grad(\Theta) - \mathbf{P} : \dot{\mathbf{F}} \leq 0 \tag{3.1.55}$$

where *Grad* is the gradient in the reference configuration.

3.2 Material model

3.2.1 Framework

The balance equations leave the system undetermined. To reach a complete set of equations, it is necessary to provide additional equations that describe the mechanical behavior of the material that the body is made of. Such equations are called constitutive equations.

This section consists of two parts. In the first part, some material characteristics of rubber are described qualitatively and represented mathematically in order to narrow down the appropriate material model option. The second part presents two different constitutive equations used throughout this work: one already available within the chosen finite element software and another proposed model.

Rubber characteristics - homogeneity

The filler introduced to the material can cause complications during the production process, where the particles tend to agglomerate during mixing such that the resulting material can become rather inhomogeneous [84]. However, in order to avoid this, Michelin processes add further chemical additives to rubber mix which hinder agglomeration.

Furthermore, considering the contributions originated from short wavelength excitations (smaller scales), a homogeneous assumption might not be sufficient. Some interpretations consider that if the shortest perturbing wavelength are larger than the filler particle (with typical size of order of 100 nm), and the densely packed clusters with typical size around 1 μm, then material scales excited by bigger wavelengths could be approximated as being homogeneous [42], [52]. This scale is reasonable for the cut-off of smallest scales in lubricated contact (also ≈ 1 μm) [101], [103], [129].

Although local considerations must be observed with care, for the macro-scale, the material is assumed to be homogeneous.

Rubber characteristics - isotropy

As mentioned in section 4.2, the three filled-rubber materials evaluated experimentally have considerable high filling PHR (parts per hundred of rubber). Then, one must be careful before considering isotropy. However, the samples from uniaxial and shear experiments (tribological and purely mechanical) do not have a protocol to prioritize directions of the cut to their respective geometries. The tendencies observed when solicitating those samples were of higher importance for the problematic discussed in section 4.4.3 than the dispersion associated to the repetition, where different specimens would have different orientations.

Up to this stage of the research and also due to the large scope of it, isotropy was adopted in this work.

Rubber characteristics - hyper-elasticity

As observed in section 4.4 especially for contact areas, the rubber undergoes visible levels of deformations. In addition, more controlled uniaxial tests from 5.1.2 solicited all the materials of interest to operating points where the small deformation hypothesis are no longer valid, with considerable recovery and no apparent fracture.

It was concluded that the inclusion of hyperelastic behaviours is necessary for the case study.

Rubber characteristics - viscoelasticity

The DMA experiments observe different levels of dissipation (by observing the hysteretic cycle) when frequency is changed, showing a clear dependence upon the rate of deformation. This is within the scope of linear viscoelasticity.

However, non-linear coupling between deformation magnitude and deformation rate were observed for the polarized DMA case study. Since all DMA result data comes from already accommodated samples and the coupling is still present upon repetition, this reversible non-linearity is assumed to be associated with the Payne effect in contrast with Mullins effect.

Rubber characteristics - thermal effects

Tribological tests used in this work were conditioned to minimize temperature effects. The slide distances are short (around 200 mm), each run is alternated with a waiting time (of 30 or 60 seconds), immersed in water with controlled temperature (at 7°C or 15°C), so that, at least for the macro-scale, temperature contacts are small and homogeneous throughout the sample.

So for the considerations of macro-scale (cm to mm) the material is considered to be isothermal. However, those measures do not ensure flash temperature effect are negligible for smaller scales (mm to μm).

Rubber characteristics - compressibility

The resistance of elastomers to the volume-changing deformation is large. Rubber is considered as a nearly incompressible material. No changes in density can be remarked on uniaxial loading. For future numerical implementation a nearly incompressible material model is to be developed.

3.2.2 Two-potential framework

Invoking the principles existent for the two-potential framework described, among others, by Kumar and Pamies, Le Tallec and Rahier and Kaiss or Reese and Govindjee [27], [34], [107] (described in more detail in 8.4) the material constitutive response can be described by a stress-deformation relation, (3.2.1), involving internal variables and an evolution equation for those same internal variables, (3.2.2):

$$\mathbf{P} = \frac{\partial \hat{\Psi}}{\partial \mathbf{F}}(\mathbf{F}, \mathbf{\Lambda}) \tag{3.2.1}$$

$$\frac{\partial \varphi}{\partial \dot{\mathbf{\Lambda}}}(\mathbf{F}, \mathbf{\Lambda}, \dot{\mathbf{\Lambda}}) + \frac{\partial \Psi}{\partial \mathbf{\Lambda}}(\mathbf{F}, \mathbf{\Lambda}) = 0, \tag{3.2.2}$$

where φ is convex in $\dot{\mathbf{\Lambda}} = \frac{d\mathbf{\Lambda}}{dt}$ such that $argmin_{\dot{\mathbf{\Lambda}}} \varphi(\mathbf{F}, \mathbf{\Lambda}, \dot{\mathbf{\Lambda}}) = 0$ [107]. According to the second principle, the following requirement must hold

$$\frac{\partial \varphi}{\partial \dot{\mathbf{\Lambda}}} : \dot{\mathbf{\Lambda}} \geq 0. \tag{3.2.3}$$

To specialize the above constitutive framework to rubber viscoelasticity, three considerations are applied:

- Taking as reference simpler viscoelastic rheological models, the internal variable is associated to a deformation gradient, $\mathbf{F}^v$ associated with the dissipative part of the deformation;

$$\mathbf{\Lambda} := \mathbf{F}^v \tag{3.2.4}$$

- The free energy is decomposed into an energy associated to thermodynamic equilibrium states of the elastomer, Ψ^{Eq}, which do not depend on $\mathbf{F}^v$, and an additional energy storage at non-equilibrium states, Ψ^{NEq};

$$\Psi(\mathbf{F}, \mathbf{F}^v) = \Psi^{Eq}(\mathbf{F}) + \Psi^{NEq}(\mathbf{F}, \mathbf{F}^v). \tag{3.2.5}$$

- A multiplicative split (as schematically shown in Figure 3.2) decomposes the deformation gradient, $\mathbf{F}$, into an elastic and viscous part (internal variable) of the deformation gradient.

$$\mathbf{F} = \frac{\partial \varphi_e}{\partial \mathbf{x}_v} \frac{\partial \varphi_v}{\partial \mathbf{X}} = \mathbf{F}^e \mathbf{F}^v \tag{3.2.6}$$

  Both $\mathbf{F}^v$ and $\mathbf{F}^e$ are non observable processes, however $\mathbf{F}$ is. Equation (3.2.6) allows to chose one of the representations in Ψ^{NEq}

$$\Psi^{NEq}(\mathbf{F}, \mathbf{F}^v) = \Psi^{NEq}(\mathbf{F}^e) = \Psi^{NEq}(\mathbf{F}\mathbf{F}^{v-1}) \tag{3.2.7}$$

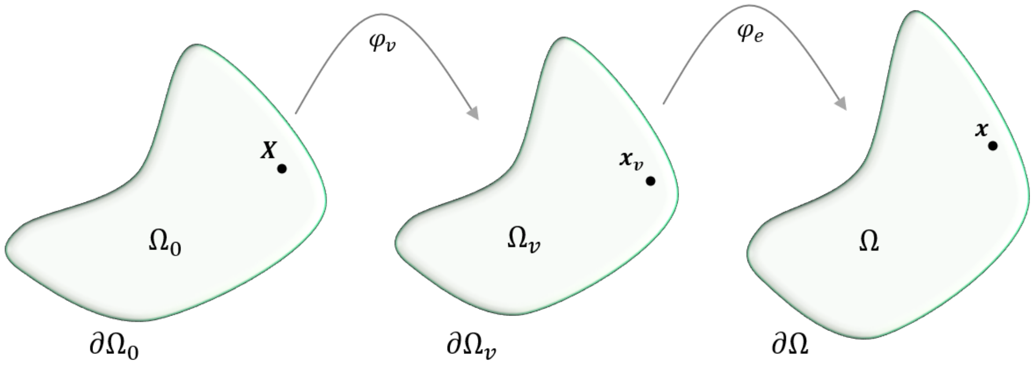

Figure 3.2: Representation of mapping of material points $\mathbf{X}$ to the undeformed reference configuration Ω_0 their spatial position $\mathbf{x}$ in the current deformed configuration Ω, and the assumed decomposition.

It is of interest to associate the energy function to the energy (conserved and dissipated) of the material when it is deformed, as such, this energy should be independent of a generic change of the observer (objectivity). The motion presented in Equation (3.1.2) could be viewed from another reference frame denoted via the superscript $*$, which can be related to the original spatial frame as

$$\mathbf{x}^* = \mathbf{Q}\mathbf{x} + \mathbf{c} \quad ; \quad \mathbf{F}^* = \mathbf{Q}\mathbf{F} \tag{3.2.8}$$

where $\mathbf{Q} \in Orth^+$ and $\mathbf{c} \in \mathbb{V}^3$. If the thermodynamic potentials are objective then $\Psi^* = \Psi$ and $\varphi^* = \varphi$. However, since $\mathbf{Q}$ is applied after the transformation, and the deformation field φ_v is not connected to the current configuration, $\mathbf{F}^{v*} = \mathbf{F}^v$, therefore objectivity can be expressed as

$$\Psi^{Eq}(\mathbf{Q}\mathbf{F}) = \Psi^{Eq}(\mathbf{F}) \quad ; \quad \Psi^{NEq}(\mathbf{Q}\mathbf{F}, \mathbf{F}^v) = \Psi^{NEq}(\mathbf{F}, \mathbf{F}^v) \tag{3.2.9}$$

and

$$\varphi(\mathbf{Q}\mathbf{F}, \mathbf{F}^v, \dot{\mathbf{F}}^v) = \varphi(\mathbf{F}, \mathbf{F}^v, \dot{\mathbf{F}}^v). \tag{3.2.10}$$

If the polar decomposition from (3.1.15) is inserted in $\mathbf{F}$ (although no such decomposition is made for the internal variable $\mathbf{F}^v$), then from the objectivity principle one may reach that

$$\Psi^{Eq}(\mathbf{R}\mathbf{U}) = \Psi^{Eq}(\mathbf{U}) \quad ; \quad \Psi^{NEq}(\mathbf{R}\mathbf{U}, \mathbf{F}^v) = \Psi^{NEq}(\mathbf{U}, \mathbf{F}^v) \tag{3.2.11}$$

and

$$\varphi(\mathbf{R}\mathbf{U}, \mathbf{F}^v, \dot{\mathbf{F}}^v) = \varphi(\mathbf{U}, \mathbf{F}^v, \dot{\mathbf{F}}^v). \tag{3.2.12}$$

In addition, for mathematical convenience the potential functions could also be represented in terms of the right Cauchy-Green deformation tensor, $\mathbf{C}$,

$$\Psi^{Eq}(\mathbf{F}) = \Psi^{Eq}(\mathbf{C}); \quad \Psi^{NEq}(\mathbf{F}, \mathbf{F}^v) = \Psi^{NEq}(\mathbf{C}, \mathbf{F}^v) = \Psi^{NEq}(\mathbf{C}^e) \tag{3.2.13}$$

and

$$\varphi(\mathbf{F},\mathbf{F}^v,\dot{\mathbf{F}^v}) = \varphi(\mathbf{C},\mathbf{F}^v,\dot{\mathbf{F}^v}) \tag{3.2.14}$$

where $\mathbf{C}^e = \mathbf{F}^{eT}\mathbf{F}^e = \mathbf{F}^{v-T}\mathbf{C}\mathbf{F}^{v-1}$. If the material is considered to be isotropic, the thermodynamic potentials can only depend on their invariants

$$\begin{cases} I_1(\mathbf{C}) = tr(\mathbf{C}) \\ I_2(\mathbf{C}) = \frac{1}{2}\{[tr(\mathbf{C})]^2 - tr(\mathbf{C}^2)\} \\ I_3(\mathbf{C}) = J(\mathbf{C}) = \sqrt{det(\mathbf{C})} \end{cases} \tag{3.2.15}$$

The non equilibrium potential Ψ^{NEq} is not required to be an isotropic function. Still, some models consider this to be the case [32], to which, invariants that are analogous to (3.2.15) are considered

$$\Psi^{Eq}(\mathbf{C}) = \Psi^{Eq}(I_1, I_2, J); \quad \Psi^{NEq}(\mathbf{C}^e) = (I_1^e, I_2^e, J^e) \tag{3.2.16}$$

where

$$\begin{cases} I_1^e = I_1(\mathbf{C}^e) = tr(\mathbf{C}^e) \\ I_2^e = I_2(\mathbf{C}^e) = \frac{1}{2}\{[tr(\mathbf{C}^e)]^2 - tr(\mathbf{C}^{e2})\} \\ I_3^e = I_3(\mathbf{C}^e) = J(\mathbf{C}^e) = \sqrt{det(\mathbf{C}^e)} \end{cases} \tag{3.2.17}$$

One may also have another invariant representation where

$$\begin{cases} I_1^v = I_1(\mathbf{C}^v) = tr(\mathbf{C}^v) \\ I_2^v = I_2(\mathbf{C}^e) = \frac{1}{2}\{[tr(\mathbf{C}^v)]^2 - tr(\mathbf{C}^{v2})\} \\ I_3^v = I_3(\mathbf{C}^v) = J(\mathbf{C}^v) = \sqrt{det(\mathbf{C}^v)} \end{cases} \tag{3.2.18}$$

Although seemingly restrictive, the above laid-out two-potential constitutive relations are general enough to describe viscoelastic solids and fluids, viscoplastic solids, phase transforming materials and other types of dissipative materials [107].

3.2.3 Finite non-linear viscoelasticity

The model to be used as reference in this work was proposed by Kumar and Pamies [107] in an attempt to account for at least five features recognized for the rubber:

- The storage of energy is governed by changes in entropy of the underlying polymer network (as it was also mentioned in section 2.2)
- The dissipation of energy is primarily governed by friction among neighboring polymer chains (termed as "internal friction" as seen in 2.3.3)
- When all forces are removed after an arbitrary loading path, elastomers creep to their original configuration
- When subjected to relaxation and creep loading conditions, elastomers exhibit a transient response that then evolves into an equilibrium state of deformation and stress

- When subjected to loading conditions of the same type but different loading rate, elastomers exhibit different responses

The model proposed by Kumar and Pamies is related to other thermodynamically consistent propositions as Le Tallec *et al* [27] and Bergström and Boyce [32]. Both propositions can be seen as special cases for the laid-out Two-Potential framework. The model accounts for the non-Gaussian elasticity of elastomers, as well as for the deformation-enhanced shear thinning of their viscous dissipation governed by the rotational motion of the underlying polymer chains [107].

The free energy potential is separated into a thermodynamical equilibrium (Eq) and a non-equilibrium (NEq) part as

$$\Psi(\mathbf{F},\mathbf{F}^v) = \Psi^{Eq}(\mathbf{F}) + \Psi^{NEq}(\mathbf{F}^e) = \Psi^{Eq}(\mathbf{F}) + \Psi^{NEq}(\mathbf{F}\mathbf{F}^{v-1}) \tag{3.2.19}$$

The dissipation potential is restricted without seemingly loss of generality in the following quadratic form in $\dot{F^v}$

$$\varphi(\mathbf{F},\mathbf{F}^v,\dot{\mathbf{F}^v}) = \varphi(\mathbf{F},\mathbf{F}^e,\dot{\mathbf{F}^v}) = \frac{1}{2}\mathbf{L}^v : \mathcal{A}(\mathbf{F},\mathbf{F}^e)\mathbf{L}^v \tag{3.2.20}$$

where $\mathbf{L}^v = \dot{\mathbf{F}}^v\mathbf{F}^{v-1}$ and recalling that $\mathcal{A}(\mathbf{F},\mathbf{F}^e)$ is still required to fulfill previously required conditions as ensuring a positive dissipation and

$$\mathcal{A}(\mathbf{QFK},\mathbf{QF}^e) = \mathcal{A}(\mathbf{F},\mathbf{F}^e) \tag{3.2.21}$$

Originally, the free-energy potential characterized by the equilibrium and non-equilibrium portions are I_1-based stored energy functions [80] and impose incompressibility via an unbounded energy value when compressible conditions take place. This effect is represented in the following notation

$$\Psi^{Eq}(\mathbf{F}) = \begin{cases} \frac{3^{1-\alpha_1}}{2\alpha_1}\mu_1[I^{\alpha_1} - 3^{\alpha_1}] + \frac{3^{1-\alpha_2}}{2\alpha_2}\mu_2[I^{\alpha_2} - 3^{\alpha_2}] & \text{if } J = 1 \\ +\infty & \text{otherwise} \end{cases} \tag{3.2.22}$$

$$\Psi^{NEq}(\mathbf{F}^e) = \begin{cases} \frac{3^{1-a_1}}{2a_1}m_1[I^{ea_1} - 3^{a_1}] + \frac{3^{1-a_2}}{2a_2}m_2[I^{ea_2} - 3^{a_2}] & \text{if } J^e = 1 \\ +\infty & \text{otherwise} \end{cases} \tag{3.2.23}$$

In these expressions μ_r, α_r, m_r and a_r (for $r = 1, 2$) are real-valued material parameters associated with the non-Gaussian statistical distribution of the underlying polymer chains. A quadratic form is also proposed for the dissipation potential

$$\mathcal{A}_{ijkl}(\mathbf{F},\mathbf{F}^e) = 2\eta_k(I_1^e, I_2^e, I_1^v)\mathcal{K}_{ijkl} + 3\eta_J\mathcal{J}_{ijkl} \tag{3.2.24}$$

where

$$\eta_k(I_1^e, I_2^e, I_1^v) = \eta_\infty + \frac{\eta_0 - \eta_\infty + k_1[I_1^{v\beta_1} - 3^{\beta_1}]}{1 + (k_2 J_2^{NEq})^{\beta_2}} \tag{3.2.25}$$

$$J_2^{NEq} = \left(\frac{I_1^{e2}}{3} - I_2^e\right)\left(\sum_{r=1}^{2} 3^{1-a_r} m_r I_1^{ea_r - 1}\right)^2 \tag{3.2.26}$$

$$\eta_J = +\infty \tag{3.2.27}$$

In the above expressions, $\eta_0 \geq \eta_\infty$, $\beta_r \geq 0$, $K_r \geq 0$ (for $r = 1, 2$) are real-valued material parameters that associated with reptation dynamics. η_J is an unbounded value to force incompressibility on the non-equilibrium part. $\mathcal{K}$ and $\mathcal{J}$ represent the fourth order orthogonal projection tensors onto the set of deviatoric and spherical second order tensors respectively, given in Einstein summation notation by

$$\mathcal{K}_{ijkl} = \frac{1}{2}(\delta_{ik}\delta_{jl} + \delta_{il}\delta_{jk} - \frac{2}{3}\delta_{ij}\delta_{kl}) \quad ; \quad \mathcal{J}_{ijkl} = \frac{1}{3}\delta_{ij}\delta_{kl} \tag{3.2.28}$$

A key ingredient in such models is the non-linearity of the viscosity coefficient η_k. Two important characteristics may be highlighted here:

- The viscosity function η_k is an increasing function of I_1^v (as defined in (3.2.18)). that is of the irreversible part of the deformation;
- J_2^{NEq} is a increasing function representing the second invariant of the stress deviator $\mathbf{T}_{dev}^{NEq}$, which, is proportional to $\dot{\mathbf{F}}^v$. Therefore its presence in the denominator in the viscosity coefficient ensures that the viscosity will be a decreasing function of the irreversible deformation rate.

Those sensitivities are termed in the work of Kumar and Pamies as *enhanced shear thinning*, which is of high pertinence to the non vanishing deformation field created by the curling observed in the tread blocks Leading Edge and for the hysterestic sensitivity to difference sliding velocities (therefore different frequencies excitations from the rough surface) as discussed in section 4.4.

By inserting (3.2.24) into (3.2.20) the dissipation potential reads

$$\varphi(\mathbf{F}, \mathbf{F}^e, \dot{\mathbf{F}^v}) = \frac{1}{2}\mathbf{L}^v : [2\eta_k(I_1^e, I_2^e, I_1^v)\mathcal{K} + 3\eta_J\mathcal{J}]\,\mathbf{L}^v \tag{3.2.29}$$

Upon inserting the dissipation potential into (3.2.2), after some algebraic manipulation the evolution equation may be written in terms of the internal variable $\mathbf{C}^v$

$$\dot{\mathbf{C}^v} = \frac{\sum_{r=1}^{2} 3^{1-a_r} m_r (\mathbf{C} : \mathbf{C}^{v-1})^{a_r - 1}}{\eta_k(I_1^e, I_2^e, I_1^v)} \left[\mathbf{C} - \frac{1}{3}(\mathbf{C} : \mathbf{C}^{v-1})\mathbf{C}^v\right] \tag{3.2.30}$$

A very important action is to verify that not only should $J^v = 1$ but also $\dot{J^v} = 0$ where it is seen that for it to be true it must be that $\dot{\mathbf{C}^v} : \mathbf{C}^{v-1} = 0$. By rewriting the equation above to this form, one finds that this condition is automatically verified.

To obtain the stress-deformation equation, (3.2.19) is derived with respect to the gradient deformation tensor as shown in (8.4.8)

$$\mathbf{P} = \frac{\partial \Psi}{\partial \mathbf{F}}(\mathbf{F}, \mathbf{F}^v) = \frac{\partial \Psi^{Eq}}{\partial \mathbf{F}}(\mathbf{F}) + \frac{\partial \Psi^{NEq}}{\partial \mathbf{F}}(\mathbf{F}\mathbf{F}^{v-1}) \tag{3.2.31}$$

From here forth, two modifications will be made in parallel with the derivations that differs from the original constitutive model proposed in 2016 by Kumar Pamies [107]: (1) the constitutive model will be written so that the model is not incompressible, but instead almost-incompressible for numerical applications; (2) the evolution equation will be manipulated so that its implementation is optimized.

To idealize resistance to change in volume types of deformation, introduce a volumetric sensitive free energy $\Psi^{Vol}(\mathbf{F}) = \mathcal{C}(\mathbf{F})$ so that the relation reads

$$\mathbf{P} = \frac{\partial \Psi}{\partial \mathbf{F}}(\mathbf{F}, \mathbf{F}^v) = \frac{\partial \Psi^{Eq}}{\partial \mathbf{F}}(\mathbf{F}) + \frac{\partial \Psi^{NEq}}{\partial \mathbf{F}}(\mathbf{F}\mathbf{F}^{v-1}) + \frac{\partial \mathcal{C}}{\partial \mathbf{F}}(\mathbf{F}) \tag{3.2.32}$$

Similar to the previous model the choice of $\mathcal{C}(\mathbf{F})$ is associated to a quasi-incompressible model, where different arrangements can be found in the literature. The decomposition into isochoric and volumetric is not considered in this case, instead, the last term of the right-hand side of the above equation (also called compressible term) should be such that, when linearized, the model should collapse to its intended rheological model in the limit of small deformations. For the model of Kumar and Pamies the linearized result is the compressible form of the so-called Standard Linear Solid model (Maxwell representation).

The two initial terms of the right-hand side are derived

$$\mathbf{P} = \left[\sum_{r=1}^{2} 3^{1-\alpha_r} \mu_r I_1^{\alpha_r - 1}\right] \mathbf{F} + \left[\sum_{r=1}^{2} 3^{1-a_r} m_r (\mathbf{C} : \mathbf{C}^{v-1})^{a_r - 1}\right] \mathbf{F}\mathbf{C}^{v-1} + \frac{\partial \mathcal{C}}{\partial \mathbf{F}}(\mathbf{F}) \tag{3.2.33}$$

The necessary value for the stated conditions to be met is when

$$\Psi^{Vol}(\mathbf{F}) = \mathcal{C}(\mathbf{F}) = \frac{\Lambda}{2}(J-1)^2 - \sum_{r=1}^{2}(\mu_r + m_r)\log(J) \tag{3.2.34}$$

where

$$\frac{\partial \mathcal{C}}{\partial \mathbf{F}}(\mathbf{F}) = \left[\Lambda J(J-1) - \sum_{r=1}^{2}(\mu_r + m_r)\right] \mathbf{F}^{-T} \tag{3.2.35}$$

so that

$$\mathbf{P} = \left[\sum_{r=1}^{2} \mu_r \left(\frac{I_1}{3}\right)^{\alpha_r - 1}\right] \mathbf{F} + \left[\sum_{r=1}^{2} m_r \left(\frac{\mathbf{C} : \mathbf{C}^{v-1}}{3}\right)^{a_r - 1}\right] \mathbf{F}\mathbf{C}^{v-1} + \left[\Lambda J(J-1) - \sum_{r=1}^{2}(\mu_r + m_r)\right] \mathbf{F}^{-T}. \tag{3.2.36}$$

In the limit of small deformations as $\mathbf{F} \to \mathbf{I}$, the stress-deformation response and evolution equation linearize properly as they reduce asymptotically to

$$\mathbf{P} = \boldsymbol{\sigma} = 2\left[\sum_{r=1}^{2} \mu_r\right] \mathbf{E} + 2\left[\sum_{r=1}^{2} m_r\right] (\mathbf{E} - \mathbf{E}^v) + \Lambda tr(\mathbf{E})\mathbf{I} \tag{3.2.37}$$

as the same approach is done for the evolution equation one finds

$$\dot{\mathbf{E}}^v = \frac{\left[\sum_{r=1}^{2} m_r\right]}{\eta_0} (\mathbf{E} - \mathbf{E}^v) \tag{3.2.38}$$

with $\mathbf{E}$ and $\mathbf{E}^v$ approximated at the small deformation limit as

$$\mathbf{E} \approx \frac{1}{2}(\mathbf{F} + \mathbf{F}^T - 2\mathbf{I}) \quad ; \quad \mathbf{E}^v \approx \frac{1}{2}(\mathbf{F}^v + \mathbf{F}^{vT} - 2\mathbf{I}) \tag{3.2.39}$$

By introducing then the following internal variable

$$\mathbf{D}^v := \mathbf{C}^{v-1} \tag{3.2.40}$$

the evolution equation and the stress-deformation equation may be written as

$$\mathbf{P} = \left[\sum_{r=1}^{2} \mu_r \left(\frac{I_1}{3}\right)^{\alpha_r - 1}\right] \mathbf{F} + \left[\sum_{r=1}^{2} m_r \left(\frac{\mathbf{C} : \mathbf{D}^v}{3}\right)^{a_r - 1}\right] \mathbf{F}\mathbf{D}^v + \\ \left[\Lambda J (J-1) - \sum_{r=1}^{2} (\mu_r + m_r)\right] \mathbf{F}^{-T}. \tag{3.2.41}$$

$$\dot{\mathbf{D}}^v = \frac{\sum_{r=1}^{2} 3^{1-a_r} m_r (\mathbf{C} : \mathbf{D}^v)^{a_r - 1}}{\eta_k (I_1^e, I_2^e, I_1^v)} \left[\frac{1}{3} (\mathbf{C} : \mathbf{D}^v) \mathbf{D}^v - \mathbf{D}^v \mathbf{C} \mathbf{D}^v\right] = \mathbf{G}(\mathbf{D}^v, t) \tag{3.2.42}$$

It is also possible to represent the stress-deformation equation in the current configuration by using (3.1.22), being

$$\boldsymbol{\sigma} = \frac{1}{J} \left[\sum_{r=1}^{2} \mu_r \left(\frac{I_1}{3}\right)^{\alpha_r - 1}\right] \mathbf{F}\mathbf{F}^T + \frac{1}{J} \left[\sum_{r=1}^{2} m_r \left(\frac{I_1^e}{3}\right)^{a_r - 1}\right] \mathbf{F}\mathbf{D}^v \mathbf{F}^T + \\ \left[\Lambda (J-1) - \frac{1}{J} \sum_{r=1}^{2} (\mu_r + m_r)\right] \mathbf{I}. \tag{3.2.43}$$

3.2.4 Finite linear viscoelasticity

This class of constitutive laws is of very classical use in rubber modelling. For example, this type of constitutive law is a default model proposed by the IMPETUS software for the computation of viscoelastic problems. It can be related to a two potential formulation in small strains, but not for large strains.

As in [34], it is based on a splitting of the stress tensor as the sum of an equilibrium hyperelastic part and of a viscoelastic added stress. The equilibrium hyperelastic part is simply given by a compressible Mooney-Rivlin law described in the current configuration as

$$\boldsymbol{\sigma}^{Eq} = \mu_1 J^{-\frac{5}{3}} \left(2\mathbf{B} - \frac{2 I_1}{3} \mathbf{I}\right) + \mu_2 J^{-\frac{7}{3}} \left(2 I_1 \mathbf{B} - 2\mathbf{B}^2 - \frac{4 I_2}{3} \mathbf{I}\right) + \Lambda \left(J - 1\right) \mathbf{I} \tag{3.2.44}$$

based on the reduced invariants $J^{-2} I_1$ and $J^{-4} I_2$ for the isochoric part of the free energy and a volumetric energy

$$\Psi^{Eq,Vol}(J) = \frac{\Lambda}{2} (J-1)^2. \tag{3.2.45}$$

In small strains, the viscoelastic added stresses are associated to k Maxwell Rheological models (prony series), and thus, satisfy the differential equations already contextualized from section 2.2.2 with

$$\boldsymbol{\sigma}_k^v = \mu_k \left(\boldsymbol{\varepsilon}_{dev} - \boldsymbol{\varepsilon}_k^v\right) \quad ; \quad \dot{\boldsymbol{\varepsilon}}_k^v = \frac{1}{\tau_k} \left(\boldsymbol{\varepsilon}_{dev} - \boldsymbol{\varepsilon}_k^v\right) \tag{3.2.46}$$

where $\tau_k = \eta_k/\mu_k$ correspond to the relaxation/characteristic time and μ_k is the shear stiffness of the branch. The elimination of $\boldsymbol{\varepsilon}_k^v$ renders the differential form of the model as

$$\dot{\boldsymbol{\sigma}}_k^v + \frac{1}{\tau_k}\boldsymbol{\sigma}_k^v = \mu_k \dot{\boldsymbol{\varepsilon}}_{dev}^v. \tag{3.2.47}$$

From eq. (3.2.44) the stress is defined as

$$\boldsymbol{\sigma} = \boldsymbol{\sigma}^{Eq} + \sum_{k=1}^{m} \boldsymbol{\sigma}_k^v \tag{3.2.48}$$

The model is extended of large strains by a co-rotational approach through $\boldsymbol{\sigma}_k^v = \mathbf{R}\tilde{\boldsymbol{\sigma}}_k^v\mathbf{R}^T$ so that

$$\dot{\tilde{\boldsymbol{\sigma}}}_k^v + \frac{1}{\tau_k}\tilde{\boldsymbol{\sigma}}_k^v = \mu_k \dot{\mathbf{E}}_{dev}. \tag{3.2.49}$$

with $\mathbf{R}$ corresponding to the rotational matrix associated to the polar decomposition from eq. (3.1.15). $\dot{\mathbf{E}}_{dev}$ is the deviatoric part of the objective strain rate tensor. It can be obtained from the also objective rate of deformation tensor, $\mathbf{d}$, which is the symmetric part of the velocity gradient as defined in eq. (3.1.19) (section 3.1.1) [67].

This differential constitutive law is objective by construction and can easily be fitted in DMA experiments handling a large spectrum of relaxation times. However, as observed in [99], there is no guarantee that this law does satisfy the second principle from eq. (3.1.51) as written in the co-rotational configuration.

3.3 Generic Initial-Boundary-Value-Problem

3.3.1 Strong form of equilibrium

From the developments of the general principles, kinematics and forces, an important part of the description of any model is the structuring of the set of equations that represents the mechanical response of the system of interest. This group of equations are referred to as the Initial-Boundary-Value-Problems (IBVPs). This description considers the case of the body represented in Figure 3.1 with the exception of the boundary associated with contact, Γ_c, which will be included later on. Still, all the previous points discussed so far are included.

The boundary value problem may be summarized as follows: Considering the following constitutive relation

$$\mathbf{P}(\nabla\mathbf{x}, \mathbf{D}^v) = \frac{\partial \Psi^{Eq}}{\partial \mathbf{F}}(\nabla\mathbf{x}) + \frac{\partial \Psi^{NEq}}{\partial \mathbf{F}}(\nabla\mathbf{x}, \mathbf{D}^v) + \frac{\partial \Psi^{Vol}}{\partial \mathbf{F}}(\nabla\mathbf{x}) \tag{3.3.1}$$

where $\nabla\mathbf{x}(\mathbf{X}, t) = \mathbf{F}(\mathbf{X}, t)$, for all material points $\mathbf{X} \in \Omega_0$ at any given time $t \in (0, T]$, find the motion field $\varphi(\mathbf{X}, t)$ that satisfies with $\mathbf{P}$ given by eq. (3.3.1):

$$
\begin{cases}
\textit{Balance of linear momentum} & \\
Div\left[\mathbf{P}(\nabla\mathbf{x},\mathbf{D}^v)\right] + \rho_0\mathbf{B}(\mathbf{X},t) = \rho_0\ddot{\mathbf{x}}(\mathbf{X},t) & \forall(\mathbf{X},t)\in\Omega_0\times(0,T] \\
\textit{Compressibility constraint} & \\
det\left[\nabla\mathbf{x}(\mathbf{X},t)\right] > 0 & \forall(\mathbf{X},t)\in\Omega_0\times(0,T] \\
\textit{Boundary conditions} & \\
\left[\mathbf{P}(\nabla\mathbf{x},\mathbf{D}^v)\right]\mathbf{N} = \bar{\mathbf{T}}(\mathbf{X},\mathbf{x},\nabla\mathbf{x},t) & \forall(\mathbf{X},t)\in\Gamma_t\times(0,T] \\
\mathbf{x}(\mathbf{X},t) = \bar{\mathbf{x}}_u(\mathbf{X},t) & \forall(\mathbf{X},t)\in\Gamma_u\times(0,T] \\
\textit{Initial conditions} & \\
\mathbf{x}(\mathbf{X},t_0) = \bar{\mathbf{X}} & \forall\mathbf{X}\in\Omega_0 \\
\dot{\mathbf{x}}(\mathbf{X},t_0) = \dot{\bar{\mathbf{v}}}_u(\mathbf{X}) & \forall\mathbf{X}\in\Omega_0 \\
\textit{Additional constitutive constraints} & \\
\dot{\mathbf{D}}^v(\mathbf{X},t) = \mathbf{G}(\mathbf{D}^v,t) & \forall(\mathbf{X},t)\in\Omega_0\times(0,T] \\
\dot{\mathbf{D}}^v(\mathbf{X},t_0) = \mathbf{I} & \forall\mathbf{X}\in\Omega_0
\end{cases}
\tag{3.3.2}
$$

The balance of angular momentum is automatically satisfied if the constitutive equation proposed is objective. When the IBVP is solved, the deformation field $\mathbf{x}(\mathbf{X},t)$ is determined, from which all the other relevant fields can be determined. Observe that because we assume isothermal conditions, we do not need to introduce the energy conservation equation.

3.3.2 Weak form of equilibrium

In order to solve the partial differential equation resulting from the balance of linear momentum, weak forms are derived for the later introduced Finite element method. The developments here are based on the description of Laursen [47].

A variational form based on the principle of virtual work of the Initial Boundary Value Problem is formulated by first defining solution spaces, $\mathcal{C}_t$, of kinematically admissible transformation (corresponding to each $t\in(0,T]$) and a weighting space, $\mathcal{V}$. These spaces are vector valued and can be written as

$$
\mathcal{C}_t := \{\mathbf{x}_t\in\mathcal{H}_1(\Omega)\mid\mathbf{x}_t=\bar{\mathbf{x}_t}(\mathbf{X},t)\quad\text{for}\quad(\mathbf{X},t)\in\Gamma_u\times(0,T]\}
\tag{3.3.3}
$$

$$
\mathcal{V} := \{\hat{\mathbf{x}}\in\mathcal{H}_1(\Omega)\mid\hat{\mathbf{x}}=\mathbf{0}\quad\text{for}\quad\mathbf{X}\in\Gamma_u\}
\tag{3.3.4}
$$

where $\mathcal{H}_1(\Omega)$ consists of all vector valued functions over Ω_0 whose values and first derivatives are square integrable. The weighting function, $\hat{\mathbf{x}}\in\mathcal{V}$, is an admissible value inserted while keeping the same solution to the system from the strong form. By operating in the Balance of Linear momenta with Einstein summation notation in the reference configuration, and multiplying by a test function $\hat{\mathbf{x}}\in\mathcal{V}$ we get

$$
\int_{\Omega_0}\Big[Div(\mathbf{P})+\rho_0\mathbf{B}-\rho_0\dot{\mathbf{V}}\Big]\cdot\hat{\mathbf{x}}dV = \int_{\Omega_0}Div(\mathbf{P})\cdot\hat{\mathbf{x}}dV + \int_{\Omega_0}\rho_0\mathbf{B}\cdot\hat{\mathbf{x}}dV - \int_{\Omega_0}\rho_0\dot{\mathbf{V}}\cdot\hat{\mathbf{x}}dV = 0.
\tag{3.3.5}
$$

Knowing from the divergence theorem that

$$
Div(\mathbf{P})\cdot\hat{\mathbf{x}} = Div(\mathbf{P}\cdot\hat{\mathbf{x}}) - \mathbf{P}:\frac{\partial\hat{\mathbf{x}}}{\partial\mathbf{X}}
\tag{3.3.6}
$$

one can rewrite to the following form

$$\int_{\partial\Omega_0} \mathbf{T}\cdot\hat{\mathbf{x}}dA + \int_{\Omega_0} \rho_0\mathbf{B}\cdot\hat{\mathbf{x}}dV - \int_{\Omega_0} \mathbf{P} : \frac{\partial\hat{\mathbf{x}}}{\partial\mathbf{X}}^T dV - \int_{\Omega_0} \rho_0\dot{\mathbf{V}}\cdot\hat{\mathbf{x}}dV = 0 = G^b(\mathbf{x}_t, \hat{\mathbf{x}}) \quad (3.3.7)$$

where $\mathbf{T}$ is the traction density, acting in the reference configuration differential areas as per Eq. (3.1.22).The boundary can be partitioned into a displacement and traction part. However, from (3.3.4), $\mathcal{V}$ renders

$$\int_{\Gamma_t} \mathbf{T}\cdot\hat{\mathbf{x}}dA + \int_{\Omega_0} \rho_0\mathbf{B}\cdot\hat{\mathbf{x}}dV - \int_{\Omega_0} \mathbf{P} : \frac{\partial\hat{\mathbf{x}}}{\partial\mathbf{X}}^T dV - \int_{\Omega_0} \rho_0\dot{\mathbf{V}}\cdot\hat{\mathbf{x}}dV = 0 = G^b(\mathbf{x}_t, \hat{\mathbf{x}}) \quad (3.3.8)$$

The above equation is the weak form of the balance of linear momentum. The equation can be pushed forward to the current configuration

$$\int_{\gamma_t(t)} \mathbf{t}\cdot\hat{\mathbf{x}}da + \int_{\Omega(t)} \rho\mathbf{b}\cdot\hat{\mathbf{x}}dv - \int_{\Omega(t)} \boldsymbol{\sigma} : \frac{\partial\hat{\mathbf{x}}}{\partial\mathbf{x}}^T dv - \int_{\Omega(t)} \rho\dot{\mathbf{v}}\cdot\hat{\mathbf{x}}dv = 0 = g^b(\mathbf{x}_t, \hat{\mathbf{x}}) \quad (3.3.9)$$

3.4 Numerical implementation

This section will briefly describe some of the main characteristics of the chosen numerical software.

3.4.1 General characteristics

The software being used during the research is called IMPETUS Afea, a non-linear explicit finite element solver.The software uses slightly modified (optimised) quadratic and cubic shape functions and is capable of running contact problems with those higher order interpolations with good stability, being one of the main characteristics for its use.

IMPETUS has both internal and external documentation, but these are limited to general concepts necessary for implementation. Specific treatments solutions, smoothing controls contact search strategies and others are not available to the public. Therefore, the following description is based on benchmarks made directly with IMPETUS Afea team or it is based on the works of Benson [67].

3.4.2 Spatial discretization

In finite elements the domain is subdivided into a number of element subdomains, Ω^e, where $\{e\}$ refers to a certain element in the mesh, as shown schematically in Figure 3.3.

In 3D Impetus uses second order hexahedron or second order tetrahedron, by associating a shape function, N_i, to a certain node n_i to do the domain discretization, we define $N_i(\mathbf{X}) \in \mathcal{C}_t$ with $i = 1, 2, ...m$ as being linearly independent functions that form a base of a subspace $\mathcal{C}_t^h$ of $\mathcal{C}_t$. In other words

$$\mathbf{x}_t^h = \sum_{i=1}^{n_{np}} N_i(\mathbf{X})\mathbf{d}_i(t) \therefore \mathbb{N}^T(\mathbf{X})\cdot\mathbb{D}(t) \quad (3.4.1)$$

where $\mathbf{d}$ is (in general) a vector with unknown coordinates of nodal points $\{i\}$ at a certain time t. The notation used at the right-hand side is a schematic representation of an

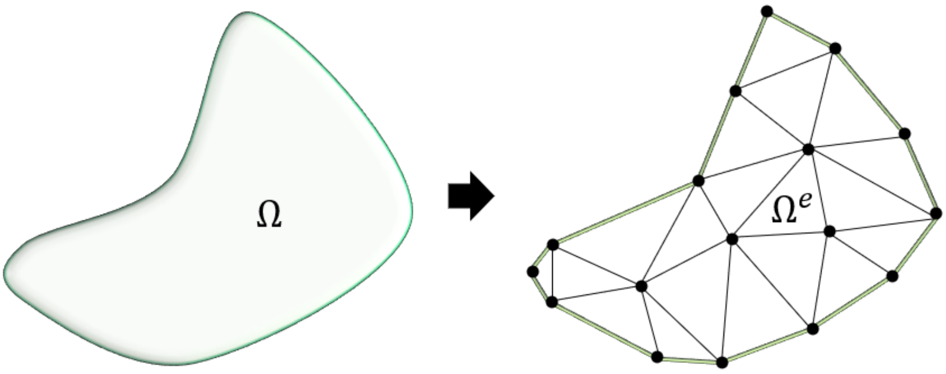

Figure 3.3: General notation for finite element discretization of the domain.

assembly of element level contributions[1]. With a set of a nodal shape function, the finite discrete solution space $\mathcal{C}_t^h$ is defined as

$$\mathcal{C}_t^h := \left\{ \mathbf{x}_t^h = \sum_{i=1}^{n_{np}} N_i(\mathbf{X})\mathbf{d}_i(t) \mid \mathbf{x}_t^h \approx \bar{\mathbf{x}}_t(\mathbf{X},t) \quad \text{for} \quad (\mathbf{X},t) \in \Gamma^u \times (0,T] \right\} \tag{3.4.2}$$

Similarly, a representation of the discrete velocity could be made since the shape function do not depend on time

$$\mathbf{v}_t^h = \sum_{i=1}^{n_{np}} N_i(\mathbf{X})\mathbf{v}_i(t) \therefore \mathbb{N}^T(\mathbf{X}) \cdot \mathbb{V}(t) \tag{3.4.3}$$

Although not necessary, Galerkin method implements the same set of shape functions to approximate the weighting space, $\mathcal{V}$, as well so that

$$\hat{\mathbf{x}}^h = \sum_{j=1}^{n_{np}} N_j(\mathbf{X})\hat{\mathbf{x}}_i^h \therefore \mathbb{N}^T(\mathbf{X}) \cdot \hat{\mathbb{D}} \tag{3.4.4}$$

where $\hat{\mathbf{x}}^h$ is a vector with (in general) nodal constants $\{j\}$. The finite weighting space, $\mathcal{V}^h$, can be expressed as

$$\mathcal{V}^h := \left\{ \sum_{j=1}^{n_{np}} N_j(\mathbf{X})\hat{\mathbf{x}}_i^h \mid \hat{\mathbf{x}}^h = \mathbf{0} \quad \text{for} \quad (\mathbf{X}) \in \Gamma^u \right\} \tag{3.4.5}$$

By writing (3.3.9) in this discrete form, one finds

$$\begin{aligned} &\int_{\partial\Omega(t)} \mathbf{t} \cdot \mathbb{N}^T(\mathbf{X}) \cdot \hat{\mathbb{D}} da + \int_{\Omega(t)} \rho\mathbf{b} \cdot \mathbb{N}^T(\mathbf{X}) \cdot \hat{\mathbb{D}} dv - \\ &\qquad \int_{\Omega(t)} \boldsymbol{\sigma} : \nabla\mathbb{N}^T(\mathbf{X}) \cdot \hat{\mathbb{D}} dv - \int_{\Omega(t)} \rho \left[\mathbb{N}^T(\mathbf{X}) \cdot \dot{\mathbb{V}}(t)\right] \cdot \left[\mathbb{N}^T(\mathbf{X}) \cdot \hat{\mathbb{D}}\right] dv = 0 \end{aligned} \tag{3.4.6}$$

Since $\hat{\mathbb{D}}$ is arbitrary, for non-zero values, the rest of the terms in evidence must be identically to zero, yielding

---

[1] In order to keep the generality of options to implement in Finite Element while highlighting the integration scheme of interest in this work.

$$\int_{\partial\Omega(t)} \mathbf{t} \cdot \mathbb{N}^T(\mathbf{X}) da + \int_{\Omega(t)} \rho\mathbf{b} \cdot \mathbb{N}^T(\mathbf{X}) dv - \\ \int_{\Omega(t)} \mathbb{B}^T(\mathbf{X}) : \boldsymbol{\sigma} dv - \int_{\Omega(t)} \rho\mathbb{N}(\mathbf{X})\mathbb{N}^T(\mathbf{X}) dv \dot{\mathbb{V}}(t) = 0 \quad (3.4.7)$$

where

$$\nabla\mathbb{N}^T(\mathbf{X}) = \mathbb{B}^T(\mathbf{X}) \quad (3.4.8)$$

By defining the integrals in a more compact representation

$$\begin{cases} \mathbb{M} = \int_{\Omega(t)} \rho\mathbb{N}(\mathbf{X}) \cdot \mathbb{N}^T(\mathbf{X}) d\mathbf{v} \\ \mathbb{F}_{int} = \int_{\Omega(t)} \mathbb{B}^T(\mathbf{X}) : \sigma dv \\ \mathbb{F}_{ext} = \int_{\partial\Omega(t)} \mathbf{t} \cdot \mathbb{N}^T(\mathbf{X}) dv + \int_{\Omega(t)} \rho\mathbf{b} \cdot \mathbb{N}^T(\mathbf{X}) dv \end{cases} \quad (3.4.9)$$

one may write the non-linear equation as

$$\mathbb{M}\dot{\mathbb{V}}(t) + \mathbb{F}_{int}\left[\mathbb{D}(t)\right] - \mathbb{F}_{ext}(t) = 0 \quad (3.4.10)$$

Where $\dot{\mathbb{V}}(t)$ can also be termed as an acceleration $\mathbb{A}(t)$.

The relations from eq.(3.4.9) presents the assembled representation of the weak form of eq. (3.3.9)

3.4.3 Time stepping procedure

The time stepping scheme to be used for the time integration of the non-linear momentum from eq. (3.4.10) is of second order accuracy. It is an explicit central difference method also termed *Leap-Frog* integration scheme. For notation, the time-step indexing is represented as a superscript on the left.

Herein, the approximation of the time derivative of a time-dependent function, f, is obtainable via a Taylor expansion

$$^{n+\frac{1}{2}}f\left(t + \frac{^{n+1}\Delta t}{2}\right) = {}^{n+\frac{1}{2}}\Delta t\, {}^{n}f'(t) + {}^{n-\frac{1}{2}}f\left(t + \frac{^{n}\Delta t}{2}\right) \quad (3.4.11)$$

to which the stepping procedure is represented schematically through Figure 3.4

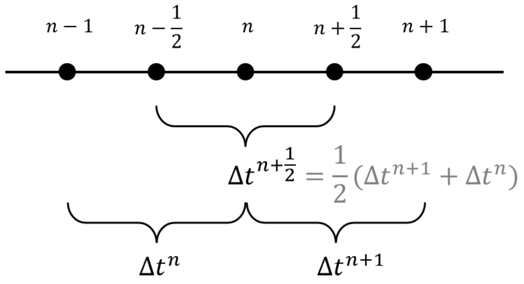

Figure 3.4: Schematic representation of time step indexing.

Given initial conditions $^{n}\mathbf{x}$, $^{n-\frac{1}{2}}\mathbf{v}$ and $^{n}\sigma$ the central difference update follows.

$$\mathbb{M}\,{}^{n}\mathbb{A}(t) = \mathbb{M}\left[\frac{{}^{n+\frac{1}{2}}\mathbb{V}(t) - {}^{n-\frac{1}{2}}\mathbb{V}(t)}{\frac{1}{2}\left({}^{n+1}\Delta t + {}^{n}\Delta t\right)}\right] = \mathbb{F}_{ext}({}^{n}\mathbf{x}, {}^{n-\frac{1}{2}}\mathbf{v}, {}^{n}t) - \mathbb{F}_{int}({}^{n}\mathbf{x}, {}^{n-\frac{1}{2}}\mathbf{v}, {}^{n}\sigma\, {}^{n}t) \quad (3.4.12)$$

The updated of velocity takes the form

$${}^{n+\frac{1}{2}}\mathbb{V} = {}^{n+\frac{1}{2}}\Delta t \mathbb{M}^{-1}\left[\mathbb{F}_{ext} - \mathbb{F}_{int}\right] + {}^{n-\frac{1}{2}}\mathbb{V} = {}^{n+\frac{1}{2}}\Delta t\, {}^{n}\mathbb{A} + {}^{n-\frac{1}{2}}\mathbb{V} \quad (3.4.13)$$

where ${}^{n}\mathbb{A}$ is the acceleration. The obtained velocity, ${}^{n+\frac{1}{2}}\mathbb{V}$, can be implemented to define the position next step as

$${}^{n+1}\mathbb{D} = {}^{n}\mathbb{D} + {}^{n+1}\Delta t\, {}^{n+\frac{1}{2}}\mathbb{V} \quad (3.4.14)$$

With this update, the stress at time ${}^{n+1}t$ can potentially be determined. Three recurrent inputs are used for this update: a state variable, ${}^{n+1}\mathbf{\Lambda}$, the velocity gradient, ${}^{n+\frac{1}{2}}\mathbf{L} = \mathbf{B}\,{}^{n+\frac{1}{2}}\mathbf{v}$, and the time step between n and $n+1$, ${}^{n+1}\Delta t$ and the deformation gradient calculated at time ${}^{n+1}t$ by differentiating Eq.(3.4.14) in space.

To keep a second order accuracy, rate terms are always within the half step indexing $n + 1/2$, while other quantities are in $n + 1$ and lastly state/history variables are in n but also updated directly to $n + 1$.

An important characteristic of the explicit time integration is their conditional stability. Stability, in the roughest sense, requires that the numerical solution remains bounded for all time. The conditionality for explicit methods requires the time step to be less than a critical limit. This limit is sometimes called Courant stability limit and its shown as follows

$$\Delta t \leq \frac{2}{\omega_{max}} \quad (3.4.15)$$

where ω_{max} is the highest modal frequency in the mesh. This frequency can be estimated (in a way that is conservative for *linear* systems) that

$$\omega_{max} \approx 2\left(\frac{c_{mat}}{h_{mesh}}\right)_{max} \quad (3.4.16)$$

with c_{mat} corresponding to the wave speed of the medium and h_{mesh} the characteristic mesh size. For the values to be maximum, the smallest h_{mesh} and maximum c_{mat} must be considered [47].

In an unbound isotropic continuum the fastest wave is usually the longitudinal with a propagation speed, c_L, of

$$c_L = \sqrt{\frac{\lambda_{mat} + 2\mu_{mat}}{\rho_{mat}}} \quad (3.4.17)$$

where λ_{mat} and μ_{mat} are the first and second Lamé parameters, respectively and ρ_{mat} is the density of the material. The limit in the time step increment. Combining eq. (3.4.16) and (3.4.17) into (3.4.15) renders

$$\Delta t \leq \frac{h_{mesh}}{\sqrt{\frac{\lambda_{mat}+2\mu_{mat}}{\rho_{mat}}}} \quad (3.4.18)$$

The first Lamé parameter is given by

$$\lambda_{mat} = \frac{E\nu}{(1+\nu)(1-2\nu)} \quad (3.4.19)$$

where E is the Young's modulus and ν is the Poisson's ratio. For rubbers, Poisson's Ratio is considered as $\nu = 0.5$ due to incompressibility assumptions. However this state is undefined in Courant's. This is one of the reasons to why the constitutive relation was adapted to be quasi-incompressible but not completely incompressible so that numerically $\nu = 0.49$.

3.4.4 Local time integration of constitutive laws

In addition to the time stepping procedures that are necessary in connection with this dynamic problem, additional time integration procedures are necessary when the constitutive models utilized are written in terms of evolution equations in time. In other words, in order to calculate $\mathbb{F}_{int}$ while advancing the solution requires an algorithmic approach to update the state variables when the stress is also being updated.

One integration procedure is defined for each constitutive law.

Finite non-linear viscoelasticity stepping

Similar to the previous model, within a Finite Element framework, the time dependent integral can be solved between the steps where the stress must be updated. Here there is only one evolution equation to be solved in the fixed reference configuration. Since the evolution equation (3.2.42) is non-linear, an explicit solution do not exist, from which Pamies proposed an explicit fifth-order Runge–Kutta scheme with extended region of stability.

Within the time internal $\Delta t = (t^{n+1} - t^n)$, an updated algorithmic internal variable can be defined as

$$\mathbf{D}^v(t^{n+1}) = \mathbf{D}^v(t^n) + \frac{\Delta t}{90}(7k_1 + 32k_3 + 12k_4 + 32k_5 + 7k_6) \tag{3.4.20}$$

with

$$\begin{cases} k_1 = \mathbf{G}(\mathbf{D}^v(t^n), t^n) \\ k_2 = \mathbf{G}(\mathbf{D}^v(t^n) + k_1\frac{\Delta t}{2}, t^n + \frac{\Delta t}{2}) \\ k_3 = \mathbf{G}(\mathbf{D}^v(t^n) + (3k_1 + k_2)\frac{\Delta t}{16}, t^n + \frac{\Delta t}{4}) \\ k_4 = \mathbf{G}(\mathbf{D}^v(t^n) + k_3\frac{\Delta t}{2}, t^n + \frac{\Delta t}{2}) \\ k_5 = \mathbf{G}(\mathbf{D}^v(t^n) + 3(-k_2 + 2k_3 + 3k_4)\frac{\Delta t}{16}, t^n + 3\frac{\Delta t}{4}) \\ k_6 = \mathbf{G}(\mathbf{D}^v(t^n) + (k_1 + 4k_2 + 6k_3 - 12k_4 + 8k_5)\frac{\Delta t}{7}, t^n + \Delta t) \end{cases} \tag{3.4.21}$$

Since this is an explicit approach, for the current constitutive law, an appropriated choice of time step, Δt would be such that the following holds

$$\frac{\eta_k(I_1^e, I_2^e, I_1^v)}{\sum_{r=1}^{2} m_r} \geq 10\Delta t \tag{3.4.22}$$

This ensures that the relaxation time is ten times larger than the time step, ensuring proper computing of the explicit fifth-order Runge–Kutta scheme.

Finite Linear viscoelasticity time stepping

The finite linear viscoelastic model has been written in terms of the co-rotational added stress in eq. (3.2.47). The updated form is represented as

$$
{}^{n+1}\boldsymbol{\sigma} = {}^{n+1}\boldsymbol{\sigma}^{Eq} + \sum_{k=1}^{m} {}^{n+1}\mathbf{R}\ {}^{n+1}\tilde{\boldsymbol{\sigma}}_k^v\ {}^{n+1}\mathbf{R}^T \tag{3.4.23}
$$

where the objective stress, $\boldsymbol{\sigma}_k^v$ obeys

$$
\dot{\boldsymbol{\sigma}}_k^v + \frac{1}{\tau_k}\boldsymbol{\sigma}_k^v = \mu_k \dot{\mathbf{E}}_{dev}. \tag{3.4.24}
$$

The update approach considered in IMPETUS assumes a constant stretch rate, therefore

$$
{}^{n+\frac{1}{2}}\dot{\mathbf{E}}_{dev} = {}^{n+\frac{1}{2}}\mathbf{L}_{Sym} - \frac{1}{3}\left({}^{n+\frac{1}{2}}\mathbf{L}_{Sym} : \mathbf{I}\right)\mathbf{I} \tag{3.4.25}
$$

with the velocity gradient given as ${}^{n+\frac{1}{2}}\mathbf{L} = \mathbf{B}\,{}^{n+\frac{1}{2}}\mathbf{v}$ and its symmetric part previously defined in eq. (3.1.19). As the stretch rate is an objective quantity, its result is considered in the the exact integration of the co-rotational viscoelastic contribution of stress within the time interval $[t^n, t^{n+1}]$ via

$$
{}^{n+1}\tilde{\boldsymbol{\sigma}}_k^v = {}^{n+1}\tilde{\boldsymbol{\sigma}}_k^v \exp\left(\frac{{}^{n}t - {}^{n+1}t}{\tau_k}\right) + \mu_k \tau_k\, {}^{n+\frac{1}{2}}\dot{\mathbf{E}}_{dev}\left[1 - \exp\left(\frac{{}^{n}t - {}^{n+1}t}{\tau_k}\right)\right] \tag{3.4.26}
$$

which is the updated formula used in the time integration of eq. (3.4.23).

3.4.5 Mesh construction and numerical integration

All the numerical evaluations were built in a 3D space with tetrahedral and hexahedral elements. Structured grids were built internally (with hexahedral elements) for very simple geometries while more complex geometries using unstructured grids (with tetrahedral elements) were imported from external sources.

A local refinement of the mesh is also made internally (In IMPETUS interface), resulting in a refined hexahedral grid which can be controlled locally. Although the exact scheme is not precised, if a refinement is applied in a tetrahedral grid, the tetrahedral elements selected for refined are split into four hexahedral elements (Schneider's pyramid, possibly via a four split scheme) as presented in Figure 3.5 [58]

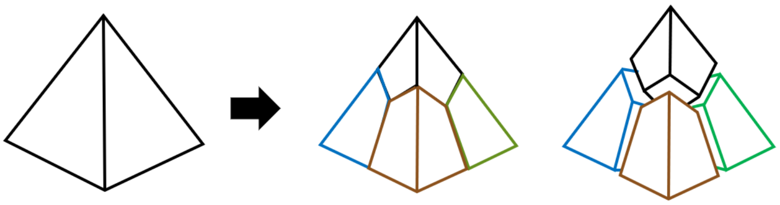

Figure 3.5: Schematic representation of Hex meshing of Schneider's pyramid for tetrahedral to hexahedral conversion.

Concerning the family of shape/interpolation functions considered, only linear and quadratic elements were considered in this work.

The integration over the entire domain can be decomposed into a discrete sum where the smooth integration still lies for each element (suffix e)

$$\mathbb{F}_{int} = \sum_{e} \int_{\Omega_e} \mathbb{B}_e^T(\mathbf{X}_e) : \sigma_e dv_e \tag{3.4.27}$$

which after numerical integration results

$$\mathbb{F}_{int} = \sum_{e} \sum_{\mathbf{X}_e^p} \omega_e^p \left(\mathbb{B}_e^T : \sigma_e\right)(\mathbf{X}_e^p) \tag{3.4.28}$$

where ω_e^p is the weight scalar and $\mathbf{X}_e^p$ are the integration points. The quantity and values for weights and integration points depends on the type of element being evaluated its correspondent degree (if the interpolation function is polynomial).

Although the exact numerical scheme is not accessible, IMPETUS do not use reduced numerical integration. Therefore, no hourglass controls are implemented on its routine and, as a consequence, there is no plane strain framework available.

One last resource that is a command called *frequency cut-off.* The primary purpose of this command is to allow for larger time steps. This is achieved by suppressing angular frequencies $\omega \leq 2/\Delta t_{target}$. The exact procedure is approximate and frequencies below the threshold value will, to some extent, be affected. If used with care, the command is applied to increase the time step size in dynamic events that are dominated by the lowest natural frequencies.

3.5 Basics of contact Mechanics

The case of contact will be built upon the framework established for the case without contact presented in section 3.1. Now the attention is directed to the case presented in Figure 3.6, where large deformation and large motion frictional contact involving two bodies should be considered. In the figure, the superscripts $\langle\cdot\rangle^{(i)}$ with $i = 1, 2$ makes reference with one of the two bodies over an interval of time $(0, T]$. Both bodies in the reference configuration are defined as $\Omega_0^{(i)}$, while its boundary, $\partial\Omega_0^{(i)}$, is partitioned into three parts: Γ_t with imposed surface traction, Γ_u with prescribed displacements and Γ_c for surfaces in potential contact. Their counterparts in the current configuration are, respectively, $\Omega(t)$, γ_t, γ_u and γ_c. Such that

$$\Gamma_t^{(i)} \cup \Gamma_u^{(i)} \cup \Gamma_t^{(i)} = \partial\Omega_0^{(i)} \quad ; \quad \Gamma_t^{(i)} \cap \Gamma_u^{(i)} = \Gamma_t^{(i)} \cap \Gamma_c^{(i)} = \Gamma_u^{(i)} \cap \Gamma_c^{(i)} = \emptyset \tag{3.5.1}$$

and

$$\gamma_t^{(i)} \cup \gamma_u^{(i)} \cup \gamma_t^{(i)} = \partial\Omega_0^{(i)} \quad ; \quad \gamma_t^{(i)} \cap \gamma_u^{(i)} = \gamma_t^{(i)} \cap \gamma_c^{(i)} = \gamma_u^{(i)} \cap \gamma_c^{(i)} = \emptyset \tag{3.5.2}$$

Some fundamental descriptions and further discussions can be found in the works of Wriggers [66], Laursen [47] and Zhong [28].

3.5.1 Kinematics

Positions belonging to $\Omega^{(i)}(t)$ are called $\mathbf{x}^{(i)}$ (in the reference configuration, $\mathbf{X}^{(i)}$). It is assumed that an unique correspondence between $\mathbf{x}^{(1)}$ and $\mathbf{x}^{(2)}$ exists. More precisely, for each position $\mathbf{x}^{(1)} \in \gamma_c^{(1)}$ there is one related position $\hat{\mathbf{x}}^{(x)} \in \gamma_c^{(2)}$ that can be obtained. This

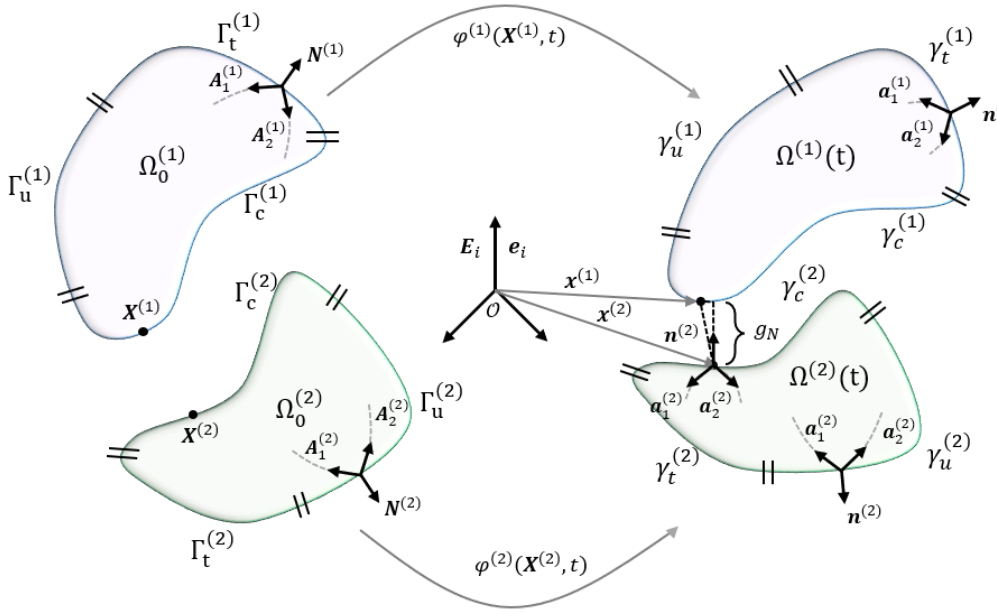

Figure 3.6: Kinematics of a solid body including potential contacting surfaces in reference and current configuration.

association is contextualized to what potentially would be contact *per se*. To make further progress, a parametrization of the surface (2) is defined via the mapping $\Psi^{(2)} : \mathcal{B}^{(2)} \to \mathbb{E}^3$, with a reference case, $\Psi_0^{(2)}$, and current case, $\Psi^{(2)}(t) = \Psi_t^{(2)}$, so that

$$\Psi_0^{(2)}(\mathcal{B}^{(2)}) = \Gamma_c^{(2)} \quad ; \quad \Psi_t^{(2)}(\mathcal{B}^{(2)}) = \gamma_c^{(2)} \tag{3.5.3}$$

where $\mathcal{B}^{(2)} \subseteq \mathbb{E}^2$ and mappings are assumed smooth in continuum case. This manipulation is represented in Figure 3.7.

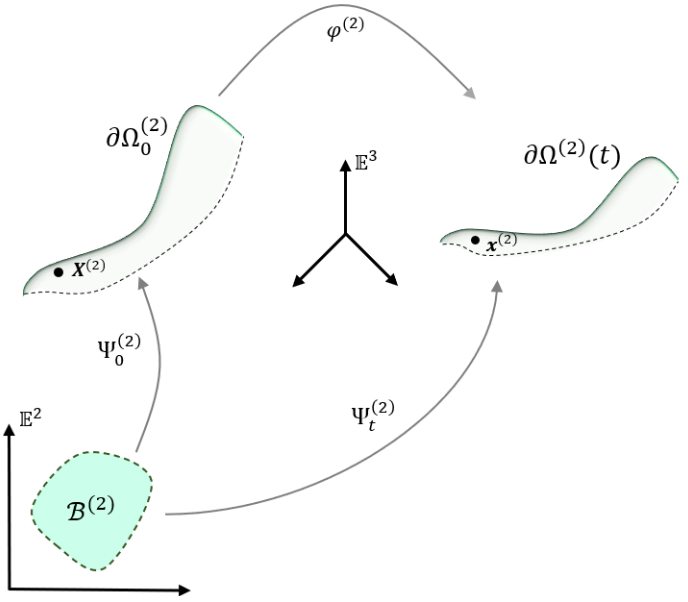

Figure 3.7: Schematic of the parametrization of the contact surface.

Moreover, once a one-to-one association between surface (2) with a reference surface (1) is defined, ultimately $\xi_\alpha = \xi_\alpha(\mathbf{X}^{(1)}, t)$.

The association use the tangential and normal vectors of the boundary (Figure 3.6). Tangential vectors $\mathbf{a}_\alpha^{(2)}$ for $\alpha = 1, 2$ and the normal vector, $\mathbf{n}^{(2)}$ of the surface position can be written as

$$\mathbf{a}_\alpha^{(2)} = \frac{\partial \mathbf{x}^{(2)}}{\partial \xi_\alpha} = \mathbf{x}_{,\alpha}^{(2)} \quad ; \quad \mathbf{n}^{(2)} = \frac{\mathbf{a}_1^{(2)} \times \mathbf{a}_2^{(2)}}{||\mathbf{a}_1^{(2)} \times \mathbf{a}_2^{(2)}||} \tag{3.5.4}$$

where $\mathbf{x}_{,\alpha}^{(2)}$ represents the tangential components of a position $\mathbf{x}^{(2)}$. The *closest point projection* of $\mathbf{x}^{(1)}$ minimizes the distance, $d(\mathbf{x}^{(1)}, \xi_\alpha)$, between $\mathbf{x}^{(1)}$ and $\mathbf{x}^{(2)}(\xi_\alpha)$

$$d(\mathbf{x}^{(1)}, \xi_\alpha) = ||\mathbf{x}^{(1)} - \mathbf{x}^{(2)}(\xi_\alpha)|| \tag{3.5.5}$$

At the minimum in ξ_α, we should have

$$\frac{\partial d(\mathbf{x}^{(1)}, \xi_\alpha)}{\partial \xi_\alpha} = \frac{\mathbf{x}^{(1)} - \mathbf{x}^{(2)}(\xi_\alpha)}{||\mathbf{x}^{(1)} - \mathbf{x}^{(2)}(\xi_\alpha)||} \cdot \mathbf{x}_{,\alpha}^{(2)} = 0 \tag{3.5.6}$$

implying orthogonality between the distance vector, $\mathbf{x}^{(1)} - \mathbf{x}^{(2)}(\xi_\alpha)$, and the tangent vector and $\mathbf{a}_\alpha^{(2)} = \mathbf{x}_{,\alpha}^{(2)}$. Once the nearest position in surface (2) is found, this quantity will be denoted with a hat marking above the symbol, indicating that for a certain position $\mathbf{x}^{(1)} \in \gamma_c^{(1)}$, the unique closest position in $\gamma_c^{(2)}$ is referred as $\hat{\mathbf{x}}^{(2)}$.

Subsequently, a projected normal gap function is defined, seen in Figure 3.6, from the three quantities just obtained

$$g_N := (\mathbf{x}^{(1)} - \hat{\mathbf{x}}^{(2)}) \cdot \mathbf{n}^{(2)} \tag{3.5.7}$$

with negative value when penetration of the body occurs.

By now considering the potential frictional response, the primary kinematic variable of interest is the relative velocity. Moreover, two cases should be identified: (1) stick state, where two bodies stick together and no *relative* movement in the tangential direction occurs, which can be formulated as

$$\dot{\hat{\xi}}_\alpha = \frac{\partial \hat{\xi}_\alpha}{\partial t} = 0 \tag{3.5.8}$$

within a large deformation framework in the current configuration. It imposes a non-linear constraint equation on the motion in the contact interface. On the other hand (2), a slip/sliding state between the $\mathbf{x}^{(1)}$ and $\mathbf{x}^{(2)}$ leads to the relative motion of the two points in the tangential direction along the contact interface. The incremental relationship of the tangential relative displacement vector is

$$d\mathbf{g}_T = \hat{\mathbf{a}}_\alpha^{(2)} d\hat{\xi}_\alpha = \hat{\mathbf{x}}_{,\alpha}^{(2)} \dot{\hat{\xi}}_\alpha dt \quad \rightarrow \quad \dot{\mathbf{g}_T} = \hat{\mathbf{x}}_{,\alpha}^{(2)} \dot{\hat{\xi}}_\alpha \tag{3.5.9}$$

with $\dot{\mathbf{g}_T}$ denoting the tangential relative velocity.

To determine $\dot{\hat{\xi}}_\alpha$, we use the orthogonality condition (3.5.6)

$$\left(\mathbf{x}^{(1)} - \hat{\mathbf{x}}^{(2)}\right) \cdot \hat{\mathbf{x}}_{,\alpha}^{(2)} = 0 \tag{3.5.10}$$

which is true when $\mathbf{x}^{(2)} = \hat{\mathbf{x}}^{(2)}$. By taking the material (or Lagrangian) time derivative of eq. (3.5.10) one gets

$$\begin{aligned}
\frac{D}{Dt}\left[\left(\mathbf{x}^{(1)} - \hat{\mathbf{x}}^{(2)}\right) \cdot \hat{\mathbf{x}}^{(2)}_{,\alpha}\right] &= \frac{D}{Dt}\left(\mathbf{x}^{(1)} - \hat{\mathbf{x}}^{(2)}\right) \cdot \hat{\mathbf{x}}^{(2)}_{,\alpha} + \left(\mathbf{x}^{(1)} - \hat{\mathbf{x}}^{(2)}\right) \cdot \frac{D}{Dt}\left(\hat{\mathbf{x}}^{(2)}_{,\alpha}\right) \\
&= \left(\mathbf{v}^{(1)} - \hat{\mathbf{x}}^{(2)} - \hat{\mathbf{v}}^{(2)}_{,\beta}\dot{\hat{\xi}}_\beta\right) \cdot \hat{\mathbf{x}}^{(2)}_{,\alpha} + \left(\mathbf{x}^{(1)} - \hat{\mathbf{x}}^{(2)}\right) \cdot \left(\hat{\mathbf{x}}^{(2)}_{,\alpha} + \hat{\mathbf{x}}^{(2)}_{,\alpha\beta}\dot{\hat{\xi}}_\beta\right) \\
&= \left(\mathbf{v}^{(1)} - \hat{\mathbf{v}}^{(2)}\right) \cdot \hat{\mathbf{x}}^{(2)}_{,\alpha} + g_N \mathbf{n}^{(2)} \cdot \hat{\mathbf{x}}^{(2)}_{,\alpha} + (g_N \mathbf{n}^{(2)} \cdot \hat{\mathbf{x}}^{(2)}_{,\alpha\beta} - \hat{\mathbf{x}}^{(2)}_{,\beta} \cdot \hat{\mathbf{x}}^{(2)}_{,\alpha})\dot{\hat{\xi}}_\beta \\
&= 0
\end{aligned} \tag{3.5.11}$$

The above equation can be rearranged as

$$A_{\alpha\beta}\dot{\hat{\xi}}_\beta = \left(\mathbf{v}^{(1)} - \hat{\mathbf{v}}^{(2)}\right) \cdot \hat{\mathbf{x}}^{(2)}_{,\alpha} + g_N \mathbf{n}^{(2)} \cdot \hat{\mathbf{x}}^{(2)}_{,\alpha} \tag{3.5.12}$$

where the components of the metric tensor, $\hat{m}_{\alpha\beta}$, and the components of the surface curvature, $\hat{k}_{\alpha\beta}$, are identified

$$A_{\alpha\beta} = \hat{m}_{\alpha\beta} + g_N \hat{k}_{\alpha\beta} = \hat{\mathbf{x}}^{(2)}_{,\alpha} \cdot \hat{\mathbf{x}}^{(2)}_{,\beta} - g_N \mathbf{n}^{(2)} \cdot \hat{\mathbf{x}}^{(2)}_{,\alpha\beta} \tag{3.5.13}$$

Considering a dual or reciprocal basis as $\hat{\mathbf{x}}^{(2),\alpha} = \hat{m}^{\alpha\beta}\hat{\mathbf{x}}^{(2)}_{,\beta}$, when a perfect sliding is considered, where $g_N = \dot{g}_N = 0$ then eq. (3.5.12) simplifies to

$$\dot{\hat{\xi}}_\alpha = \left(\mathbf{v}^{(1)} - \hat{\mathbf{v}}^{(2)}\right) \cdot \hat{\mathbf{x}}^{(2),\alpha} \tag{3.5.14}$$

3.5.2 Balance equations

In order to properly define the equilibrium, two considerations must be clarified. First, with $g_N = 0$, a traction vector is exchanged between $\mathbf{x}^{(1)}$ and $\mathbf{x}^{(2)}(\xi_\alpha)$. In the current and reference configuration the traction acts on both surfaces, obeying the third Newton's law

$$\mathbf{t}^{(1)} = -\mathbf{t}^{(2)} \tag{3.5.15}$$

allowing the traction to be quantified with respect to a single surface $\gamma_c^{(2)}$ (or $\Gamma_c^{(2)}$).

The Eulerian description is as follows

$$\mathbf{t}^{(2)} = \mathbf{t}^{(2)}_N + \mathbf{t}^{(2)}_T \quad ; \quad \mathbf{t}^{(2)}_N = t^{(2)}_N \hat{\mathbf{n}}^{(2)} \quad ; \quad \mathbf{t}^{(2)}_T = t^{(2),\alpha}_T \hat{\mathbf{x}}^{(2)}_{,\alpha} = t^{(2)}_{T,\alpha}\hat{\mathbf{x}}^{(2),\alpha} \tag{3.5.16}$$

3.5.3 Contact constraints

Normal direction

In contact, the relation between $t_N^{(2)}$ and g_N in $\gamma_c^{(2)}$ can be defined through a set of well-posed restrictions. Those constrains present themselves in three forms: (1) penetration is not allowed; (2) contact normal stresses are of compressive nature; (3) contact normal stress vanishes when gap is open and is negative when the gap is closed.

Those conditions are represented by

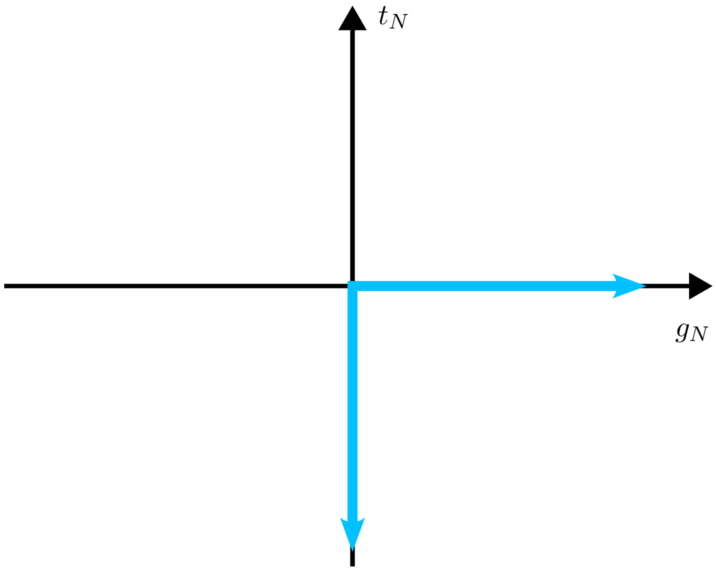

Figure 3.8: Schematic illustration of tangential contact constraint.

$$g_N \geq 0 \quad ; \quad t_N \leq 0 \quad ; \quad t_N g_N = 0 \tag{3.5.17}$$

which are usually termed Hertz-Signori-Moreau contact conditions [43]. Figure 3.8 gives a schematic representation of the admissible combinations of g_N and t_N.

It is observed that the contact stress is a non-smooth and non-linear implicit function of g_N, it is also multi-valued at $g_N = 0$.

Tangential direction

By connecting stick-slip behaviour with a local interpretation of Amontons-Coulomb law presented in eq. (1.3.2), classical laws of frictions can be stated: (1) the tangential stress vector acts in the opposite direction to the relative sliding velocity

$$\hat{\mathbf{x}}^{(2)}_{,\alpha} = -\frac{\dot{\mathbf{g}}_T}{||\dot{\mathbf{g}}_T||}; \tag{3.5.18}$$

(2) stick condition happens when the magnitude of the tangential stress do not exceed the tangential frictional stress transmitted through Amontons-Coulomb law

$$||\mathbf{t}^{(2)}_T|| \leq \mu |t^{(2)}_N| \quad \textit{if} \quad \dot{\mathbf{g}}_T = \mathbf{0}; \tag{3.5.19}$$

(3) slip conditions happens when the frictional stress is equal, and not higher, than the tangential frictional stress transmitted through Amontons-Coulomb

$$\mathbf{t}^{(2)}_T = \mu |t_N| \frac{\dot{\mathbf{g}}_T}{||\dot{\mathbf{g}}_T||} \quad \textit{if} \quad \dot{\mathbf{g}}_T \neq \mathbf{0}; \tag{3.5.20}$$

Figure 3.9 gives a schematic representation of the admissible combinations of kinetics and load interaction

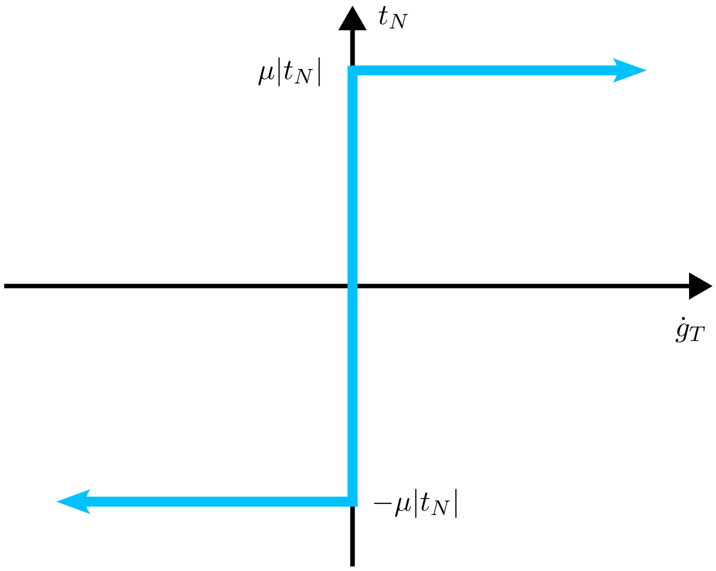

Figure 3.9: Schematic illustration of tangential contact constraint.

The same remark made for the normal contact can be found here, where the inequalities generate non-smooth, non-linear and multi-valued states, being usually termed unconstrained/unregularised/exact coulomb friction law. By observing Figure 3.9, one sees that the behaviour is analogous to a rigid-perfectly plastic constitutive description. For this reason a very common exploitation is to define the constraint through a elasto-plasticity framework. First, a criteria within Amontons-Coulomb law is defined by means of a slip function

$$f_s(\mathbf{t}_T^{(2)}) = ||\mathbf{t}_T^{(2)}|| - \mu|t_N^{(2)}| \leq 0 \tag{3.5.21}$$

Moreover, the tangential slip, $\mathbf{g}_T$ is split into an elastic (stick) and a plastic (slip) part as

$$\mathbf{g}_T = \mathbf{g}_T^e + \mathbf{g}_T^p. \tag{3.5.22}$$

Above $\mathbf{g}_T^{stick}$ can be interpreted as micro displacements in the contact interface and be treated in simpler cases via an isotropic linear elastic relation, with an elastic constant, c_T

$$\mathbf{t}_T^{(2)} = c_T \mathbf{g}_T^e = c_T(\mathbf{g}_T - \mathbf{g}_T^p) \tag{3.5.23}$$

Similar to previous constitutive equations, the plastic tangential slip, $\mathbf{g}_T^p$, can be viewed as governed by a dissipation

$$\mathcal{D}^{slip} = \mathbf{t}_T^{(2)} \cdot \dot{\mathbf{g}}_T^p \geq 0 \tag{3.5.24}$$

through the evolution equation (analogous for plastic slip studies)

$$\dot{\mathbf{g}}_T^p = \dot{\gamma}\frac{\partial f_s}{\partial \mathbf{t}_T^{(2)}}(\mathbf{t}_T^{(2)}) = \dot{\gamma}\frac{\partial}{\partial \mathbf{t}_T^{(2)}}\left[\sqrt{\left(\mathbf{t}_T^{(2)}\right)^2} - \mu|t_N^{(2)}|\right] = \dot{\gamma}\frac{\mathbf{t}_T^{(2)}}{||\mathbf{t}_T^{(2)}||} = \dot{\gamma}\mathbf{n}_T^{(2)} \tag{3.5.25}$$

where $\dot{\gamma}$ is denominated slip rate to be determined via the Kuhn-Karush-Tucker statements [47], [66]:

$$f_s \leq 0 \quad ; \quad \dot{\gamma} \geq 0 \quad ; \quad \dot{\gamma} f_s = 0 \tag{3.5.26}$$

The first statement concerns stick conditions, while the second to slip conditions. The last is analogous to the third statement for the normal contact, which is a complementary condition to avoid simultaneous conditions of stick and slip. The difference of this plastic-analogy representation to a more direct Amontons-Coulomb description is that the co-linearity between slip and frictional stress is properly written in rate form, changing the frictional law into an evolutionary type. This new friction law do not assume a true sticking state but still has two sliding states elastic (stick) and plastic (slip).

A numerical benefit of this analogy is that friction equations can be written in terms of vectors or as the surface mapping presented in section 3.5.1.

3.5.4 Strong form of equilibrium

With obvious simplification of our previous notation, the boundary value problem may be summarized as follows: considering the constitutive relation

$$\mathbf{P}(\mathbf{F}, \mathbf{D}^v) = \frac{\partial \Psi}{\partial \mathbf{F}}(\mathbf{F}, \mathbf{D}^v); \tag{3.5.27}$$

to be valid for both bodies, find the motion field $\varphi(\mathbf{X}^{(i)}, t)$ that satisfies:

$$\left\{ \begin{array}{ll}
\textit{Balance of linear momentum} & \\
Div\left(\mathbf{P}^{(i)}\right) + \rho_0^{(i)} \mathbf{B}^{(i)} = \rho_0^{(i)} \ddot{\mathbf{x}}^{(i)} & \forall (\mathbf{X}^{(i)}, t) \in \Omega_0^{(i)} \times (0, T] \\
\textit{Compressibility constraint} & \\
det\left(\mathbf{F}^{(i)}\right) > 0 & \forall (\mathbf{X}^{(i)}, t) \in \Omega_0^{(i)} \times (0, T] \\
\textit{Boundary conditions} & \\
\mathbf{P}^{(i)} \mathbf{N}^{(i)} = \bar{\mathbf{T}}^{(i)} & \forall (\mathbf{X}^{(i)}, t) \in \Gamma_t^{(i)} \times (0, T] \\
\mathbf{x} = \bar{\mathbf{x}}_u & \forall (\mathbf{X}^{(i)}, t) \in \Gamma_u^{(i)} \times (0, T] \\
\textit{Initial conditions} & \\
\mathbf{x}^{(i)} = \mathbf{X}^{(i)} & \forall \mathbf{X}^{(i)} \in \Omega_0^{(i)} \\
\dot{\mathbf{x}}^{(i)} = \dot{\bar{\mathbf{x}}}_u^{(i)} & \forall \mathbf{X}^{(i)} \in \Omega_0^{(i)} \\
\textit{Initial Constitutive conditions} & \\
[\mathbf{D}^v]^{(i)} = \mathbf{I} & \forall \mathbf{X}^{(i)} \in \Omega_0^{(i)} \\
\textit{Contact conditions} & \\
g_N \geq 0 & \forall (\mathbf{X}^{(1)}, t) \in \Gamma_c^{(1)} \times (0, T] \\
t_N \leq 0 & \forall (\mathbf{X}^{(1)}, t) \in \Gamma_c^{(1)} \times (0, T] \\
g_N t_N = 0 & \forall (\mathbf{X}^{(1)}, t) \in \Gamma_c^{(1)} \times (0, T] \\
f_s = ||\mathbf{t}_T^{(2)}|| - \mu |t_N^{(2)}| \leq 0 & \forall (\mathbf{X}^{(1)}, t) \in \Gamma_c^{(1)} \times (0, T] \\
\dot{\mathbf{g}}_T^p = \dot{\gamma} \frac{\mathbf{t}_T^{(2)}}{||\mathbf{t}_T^{(2)}||} & \forall (\mathbf{X}^{(1)}, t) \in \Gamma_c^{(1)} \times (0, T] \\
\dot{\gamma} \geq 0 & \forall (\mathbf{X}^{(1)}, t) \in \Gamma_c^{(1)} \times (0, T] \\
\dot{\gamma} f_s = 0 & \forall (\mathbf{X}^{(1)}, t) \in \Gamma_c^{(1)} \times (0, T] \\
\textit{Constitutive conditions} & \\
\left[\dot{\mathbf{D}}^v\right]^{(i)} = \mathbf{G} & \forall (\mathbf{X}^{(i)}, t) \in \Omega_0^{(i)} \times (0, T]
\end{array} \right. \tag{3.5.28}$$

3.5.5 Weak form of equilibrium

By working with respect to both bodies (i), a solution and a weighting space are with potential solutions and admissible variations defined previously for eq. (3.3.3) and (3.3.4)

$$\mathcal{C}_t^{(i)} := \{\mathbf{x}_t^{(i)} \in \mathcal{H}_1(\Omega) \mid \mathbf{x}_t^{(i)} = \bar{\mathbf{x}}_t^{(i)} \quad \text{for} \quad (\mathbf{X}^{(i)}, t) \in \Gamma_u^{(i)} \times (0, T]\}$$

$$\mathcal{V}^{(i)} := \{\hat{\mathbf{x}}^{(i)} \in \mathcal{H}_1(\Omega) \mid \hat{\mathbf{x}}^{(i)} = \mathbf{0} \quad \text{for} \quad \mathbf{X}^{(i)} \in \Gamma_u^{(i)}\}$$

Following the same arguments made for a single deformable body in eq. (3.3.8) (reference configuration) the weak form is given via

$$\begin{aligned} G(\mathbf{x}_t, \hat{\mathbf{x}}) &:= \sum_{i=1}^{2} \left\{ G^{b,(i)}(\mathbf{x}_t^{(i)}, \hat{\mathbf{x}}^{(i)}) \right\} \\ &= \sum_{i=1}^{2} \left\{ \begin{array}{l} \int_{\Omega_0^{(i)}} \mathbf{P}^{(i)} : \frac{\partial \hat{\mathbf{x}}^{(i)}}{\partial \mathbf{X}^{(i)}}^T dV + \int_{\Omega_0^{(i)}} \rho_0^{(i)} \dot{\mathbf{V}}^{(i)} \cdot \hat{\mathbf{x}}^{(i)} dV \\ - \int_{\Omega_0^{(i)}} \rho_0^{(i)} \mathbf{B}^{(i)} \cdot \hat{\mathbf{x}}^{(i)} dV - \int_{\Gamma_t^{(i)}} \mathbf{T}^{(i)} \cdot \hat{\mathbf{x}}^{(i)} dA \end{array} \right\} \\ &- \sum_{i=1}^{2} \left\{ \int_{\Gamma_c^{(i)}} \mathbf{T}^{(i)} \cdot \hat{\mathbf{x}}^{(i)} dA \right\} = 0 \\ &\equiv G^{int,ext}(\mathbf{x}_t, \hat{\mathbf{x}}) + G^{c}(\mathbf{x}_t, \hat{\mathbf{x}}) \end{aligned} \tag{3.5.29}$$

which must hold for all weighting virtual quantity $\hat{x}$ in $\mathcal{V} = \mathcal{V}^{(1)} \times \mathcal{V}^{(2)}$. The notation $G^{int,ext}(\mathbf{x}_t, \hat{\mathbf{x}})$ represents the sum of the internal and external power, while $G^{c}(\mathbf{x}_t, \hat{\mathbf{x}})$ is the virtual work correspondent to the contact forces.

The contact virtual work contains two integrals. The differential contact traction induced on body (1) surfaces equal and opposite to that produced on body (2) surface, therefore

$$G^{c}(\mathbf{x}_t, \hat{\mathbf{x}}) = \int_{\Gamma_c} \left(T_N^{(2)} \hat{\mathbf{n}}^{(2)} + T_{T,\alpha}^{(2)} \hat{\mathbf{x}}^{(2),\alpha} \right) \cdot \left(\hat{\mathbf{x}}^{(1)} - \hat{\mathbf{x}}^{(2)} \right) dA \tag{3.5.30}$$

3.5.6 Numerical implementation contact

Enforcement of constraints

Contact problems are characterized by the constraints, described in section 3.5.3, that must be imposed on contact boundaries. By looking at the already discretized equation (3.4.10) for the continuum case and the weak form of eq. (7.5.17) when contact is considered, if similar discretization procedure is followed for the contact case, the result have a portion, $\mathbb{F}_c$, associated to contact as an external force contribution[2]

$$\mathbb{M}\dot{\mathbb{V}} + \mathbb{F}_{int} - \mathbb{F}_{ext} + \mathbb{F}_c = 0 \tag{3.5.31}$$

The contact term, $\mathbb{F}_c(t)$, represents extra unknowns that cannot be solved without invoking contact conditions. For this reason, the fundamental challenge lies in calculating the contact forces themselves.

A conceptional straightforward way to determine contact forces is to take them as primary unknowns and enforce the kinematic constraints exactly. New unknowns are introduced and at the same time as many new equations are obtained. This enforcement

---

[2] Although the procedure was not yet presented, the formulation is just from previous developments in the literature [66]. The early description allows to better contextualize the enforcement of constraints as it is deeply related to the numerical implementation.

corresponds to the so-called Lagrange multiplier method. An alternative strategy to allow penetrations in the contacting boundaries and then calculate contact forces as functions of the penetrations, therefore, no new unknowns are introduced. This enforcement corresponds to the so-called penalty method [28]. There are other methods, like Augmented Lagrange, Nitsche, Perturbed Lagrange, Cross Constraint and others. An overview can be found in the works of Wriggers [66] and Laursen [47].

In general, Finite Element approaches that are capable of treating contact problems must: detect contact, construct an update of the potential contact portion of the boundary, insert this update in the discretized (and possibly linearized) weak form to resolve the problem [66]. In an implicit integration scheme, the contact portion should be identified/created before a contact occurs and, if needed, removed and recreated at each solution step. In the case of explicit integration, generally, the searching step just needs to detect already occurred penetrations [96].

IMPETUS Afea utilises an explicit integration scheme for the motion, as presented in section 3.4.3. and a penalty method for contact as in [28], [66].

Penalty methods have the particular advantage of removing the constraints explicitly from the variational formulation. The penalty method considering frictional contact can be defined as

$$G^{c,slip} = \int_{\Gamma_c} \left(\epsilon_N g_N \delta g_N + \epsilon_T \mathbf{g}_T \cdot \delta \mathbf{g}_T\right) dA, \quad \epsilon_N, \epsilon_T \geq 0 \tag{3.5.32}$$

where ϵ_N and ϵ_T represent penalty stiffness parameters. The penalty terms are only added when penetration is detected ($g_N \leq 0$) and the normal traction is computed directly as $T_N^{(2)} = \epsilon_N g_N$. In case penetration is confirmed, it is still necessary to define if it is at the state of stick or slip.

As previously defined, a modification in the classical friction law was made via an analogy with the rigid-perfect plastic constitutive behaviour. Although no true sticking state exists, it is still necessary to distinguish between two different states (elastic/"stick" and plastic/"slip"). Numerically, the use of a *trial state* is common, for which the description is listed as follows:

1. Assuming that the solution is known at a time, ${}^{n}\boldsymbol{t}$. In addition, considering an explicit scheme step, the displacements and traction are obtained for ${}^{n+1}\boldsymbol{t}$;

2. The sliding state is fixed as being elastic/"stick", following the evolution equation (3.5.23) a trial update is computed

$$ {}^{n+1}\mathbf{t}_T = c_T \, {}^{n+1}\mathbf{g^e}_T = c_T \left({}^{n+1}\mathbf{g}_T - {}^{n}\mathbf{g^p}_T \right) $$

   where if there was no slip on the previous time step $c_T \, {}^{n+1}\mathbf{g}^{\boldsymbol{e}}_{\boldsymbol{T}} = c_T \, {}^{n+1}\mathbf{g}_{\boldsymbol{T}}$;

3. The normal force trial update is determined

$$ {}^{n+1}\mathbf{t}_N = \epsilon_N \, {}^{n+1}\mathbf{g}_N $$

4. The slip function is evaluated

$$ {}^{n+1}f_s = || \, {}^{n+1}t_T || - \mu | {}^{n+1}t_N | $$

5. The confirmation or not of the previous inequality returns the branching

$$
{}^{n+1}t_T = \begin{cases} {}^{n+1}t_T & \text{if } {}^{n+1}f_s \leq 0 \\ \mu|{}^{n+1}t_N|\frac{{}^{n+1}\boldsymbol{t}_T}{||{}^{n+1}\boldsymbol{t}_T||} & \text{otherwise} \end{cases} \tag{3.5.33}
$$

Figure 3.10 presents a schematic representation of the admissible combinations of kinetics and load interaction when penalty enforcement method is considered.

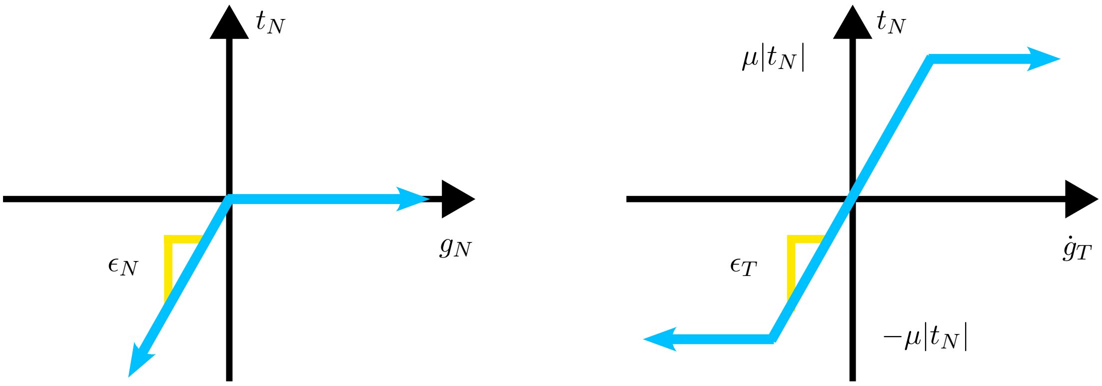

Figure 3.10: Schematic illustration of normal and tangential constraint when enforced by a penalty method.

The use of penalty methods are very practical. However, some limitations must be remarked: (1) The no penetration condition can be only be ensured when $\epsilon_N \rightarrow \infty$. However, due to numerical ill-conditioning, it is not possible in practice so that usually an exact response cannot be achieved [28]. (2) The penalty stiffness is problem-dependent, a low parameter value allows strong penetrations returning non realistic results. A high stiffness compared to the surrounding stiffness of the Finite Elements will lead to small time steps [66].

Spatial discretization

As previously mentioned, a portion of the solution process requires an identification of which part of the boundary is actively in contact. When using Finite Elements, a contacting node or element from one body can interact with several other elements. The current software in three dimensions uses the Node-To-Surface (NTS[3]) strategy.

The concept of master-slave is first presented. In the NTS strategy the slave is a node belonging to $\Gamma_c^{(1)}$ and a surface portion belonging to $\Gamma_c^{(2)}$ is the master surface. Some level of caution must be taken into account, since contact pressures are transferred from the slave node to the master surface as a concentrated force, which leads to violations of the balance moments at the element level, which affects the value of contact pressure levels [78].

By using the developments from Wriggers [66], starting with the weak form of the contact contribution, the integral contribution can be discretized with respect to the n_s slave nodes that penetrate into the master surface as

$$
G^{c,slip} = \int_{\Gamma_c} (\epsilon_N g_N \delta g_N + \epsilon_T \mathbf{g}_T \cdot \delta \mathbf{g}_T)\, dA = \sum_{s=1}^{n_s} (\epsilon_N g_{N,s} \delta g_{N,s} + \epsilon_T \mathbf{g}_{T,s} \cdot \delta \mathbf{g}_{T,s})\, A_s \tag{3.5.34}
$$

---

[3] Not to be confused with Node-To-Segment approach, which is the case for two dimensional case

where A_s is associated with the slave nodes. It is determined via a projection from the current master surface. The nodes considered in the sum are also called *active nodes.*

The discretized weak form for $G^{int,ext}(\mathbf{x}_t, \hat{\mathbf{x}})$ was already presented in section 3.4.2, the same formulation is considered now with contact contribution

$$\boldsymbol{\eta}^T \left[\mathbb{M}\dot{\mathbb{V}}(t) + \mathbb{F}_{int}\left[\mathbb{D}(t)\right] - \mathbb{F}_{ext}(t) + \mathbb{F}_c\left[\mathbb{D}(t)\right]\right] = \mathbf{0} \tag{3.5.35}$$

In addition to the contact contribution, $\mathbb{F}_c$, another difference is that the equation represents a coupled system with one subsystem of equations for each body.

Explicit solution procedure

For a generalization of contact with friction, the following notation is introduced: one set, $\mathcal{F}_{sl}$, represents the contact nodes that are in slipping conditions, while another, $\mathcal{F}_{st}$, holds the set of nodes that are in stick conditions. Both sets form the total set, $\mathcal{J}_A$, of the previously defined *active nodes* so that

$$\mathcal{F}_{sl} \cup \mathcal{F}_{st} = \mathcal{J}_A \quad ; \quad \mathcal{F}_{sl} \cap \mathcal{F}_{st} = \emptyset \tag{3.5.36}$$

In addition, stored slots will be represented by an over-line $\bar{\langle \cdot \rangle}$, temporary storage wont have his highlight. The following description considers that in the first step no contact takes place. A case which is within the scope of all contact analysis made so far.

```
Initialization set parameters ${}^nt = 0$; ${}^n\bar{\mathbf{x}} = {}^0\mathbf{x}$; ${}^{n-\frac{1}{2}}\bar{\mathbf{v}} = {}^0\mathbf{v}$; ${}^n\bar{\boldsymbol{\Lambda}} = {}^0\bar{\boldsymbol{\Lambda}}$; ${}^n\bar{\boldsymbol{\sigma}} = {}^0\bar{\boldsymbol{\sigma}}$
    WHILE: ${}^nt \leq T$
        IF ${}^nt = 0$
            Define ${}^n\Delta t = {}^{n+1}\Delta t = \Delta t$
            Assemble $\mathbf{M}$, calculate $\mathbf{M}^{-1}$
            Calculate ${}^0\mathbf{A} = \mathbf{M}^{-1}\left[{}^n\mathbf{F}_{ext}({}^n\bar{\mathbf{x}}, {}^{n-\frac{1}{2}}\bar{\mathbf{v}}, {}^nt) - {}^n\mathbf{F}_{int}({}^n\bar{\mathbf{x}}, {}^{n-\frac{1}{2}}\bar{\mathbf{v}}, {}^n\bar{\boldsymbol{\sigma}}, {}^nt)\right]$
            Calculate ${}^{n+\frac{1}{2}}\mathbf{v} = \Delta t\,{}^0\mathbf{A} + {}^{n-\frac{1}{2}}\bar{\mathbf{v}}$
            Calculate ${}^{n+1}\mathbf{x} = \Delta t\,{}^{n+\frac{1}{2}}\mathbf{v} + {}^n\bar{\mathbf{x}}$
            Define ${}^nt = \Delta t$
        ELSE
            Calculate ${}^{n+1}\boldsymbol{\sigma}\left[{}^{n+1}\boldsymbol{\Lambda}({}^n\bar{\boldsymbol{\Lambda}}, {}^n\bar{\mathbf{x}}, {}^{n+1}\mathbf{x}), {}^n\bar{\mathbf{x}}, {}^{n+1}\mathbf{x}, {}^{n+\frac{1}{2}}\mathbf{v}, {}^{n+1}\Delta t\right]$
            Store ${}^n\bar{\mathbf{x}} = {}^{n+1}\mathbf{x}$; ${}^{n-\frac{1}{2}}\bar{\mathbf{v}} = {}^{n+\frac{1}{2}}\mathbf{v}$;${}^n\bar{\boldsymbol{\sigma}} = {}^{n+1}\boldsymbol{\sigma}$;${}^n\bar{\boldsymbol{\Lambda}} = {}^{n+1}\boldsymbol{\Lambda}$;${}^n\bar{\Delta}t = {}^{n+1}\Delta t$
            Calculate ${}^n\mathbf{F}_{ext}({}^n\bar{\mathbf{x}}, {}^{n-\frac{1}{2}}\bar{\mathbf{v}}, {}^nt)$, ${}^n\mathbf{F}_{int}({}^n\bar{\mathbf{x}}, {}^{n-\frac{1}{2}}\bar{\mathbf{v}}, {}^n\bar{\boldsymbol{\sigma}}, {}^nt)$
            Define ${}^{n+1}\Delta t$ (check Courant's criteria), calculate ${}^{n+\frac{1}{2}}\Delta t = \frac{{}^{n+1}\Delta t + {}^n\bar{\Delta}t}{2}$
            Check for contacting nodes $\in \mathcal{J}_a$: $g_{Ns} \leq 0$
            Set all active nodes to stick state: $\mathcal{F}_{st} = \mathcal{J}_a$
            Identify nodes $\in \mathcal{F}_{sl}$ via trial from eq. (3.5.33), calculate ${}^n\mathbf{F}_c$
            Calculate ${}^n\mathbf{A} = \mathbf{M}^{-1}\left({}^n\mathbf{F}_{ext} - {}^n\mathbf{F}_{int} - {}^n\mathbf{F}_c\right)$
            Calculate ${}^{n+\frac{1}{2}}\mathbf{v} = {}^{n+\frac{1}{2}}\Delta t\,{}^n\mathbf{A} + {}^{n-\frac{1}{2}}\bar{\mathbf{v}}$
            Calculate ${}^{n+1}\mathbf{x} = {}^{n+1}\Delta t\,{}^{n+\frac{1}{2}}\mathbf{v} + {}^n\bar{\mathbf{x}}$
            Calculate ${}^nt = {}^nt + {}^{n+1}\Delta t$
```

Reminding that ${}^n\mathbf{F}_c$ also contains the parameters ξ_α and relative motion and velocity quantities, which are implicitly considered in the *trial* procedure.

Further remarks

To conclude the discussion raised so far, some finishing aspects will be discussed. Those remarks are either specific treatments in the Finite Element software IMPETUS or conditions considered in the study cases.

As a subclass of the contact problem developed so far, one simplification commonly used is when a deformable body comes into contact with a rigid obstacle. This case is called in the literature the *Signori* problem [47], [66]. To solve this case, a reinterpretation of some variables are necessary. Although relative motions and velocities are still present in the weak form from of the virtual works (eq. (7.5.17)) there is no contribution of the rigid body. The master surface is an appropriated choice for the parametrization ($\mathcal{A}^{(2)}$) and for the rigid body from which the following variations simplify to

$$\delta g_N = \delta \mathbf{x}^{(1)} \cdot \hat{\mathbf{n}}^{(2)} \quad ; \quad \delta \hat{\xi}_\alpha = \delta \mathbf{x}^{(1)} \cdot \hat{\mathbf{x}}^{(2),\alpha} \tag{3.5.37}$$

so that the weighting parameter in the contact virtual work is

$$G^c(\mathbf{x}_t, \hat{\mathbf{x}}) = \int_{\Gamma_c} \left(T_N^{(2)} \hat{\mathbf{n}}^{(2)} + T_{T,\alpha}^{(2)} \hat{\mathbf{x}}^{(2),\alpha} \right) \cdot \hat{\mathbf{x}}^{(1)} dA \tag{3.5.38}$$

One important aspect that rises from the choice of the rigid body as the master is how the choice is made. In the case of a Node-To-Surface approach, as the bodies come into contact, the penetrations are detected and contact constraints are applied according to the constraint enforcement (in this case penalty method). In this scenario, the contact boundary will only resist to penetrations of slave nodes into master surfaces, while master nodes will go undetected (regardless of the reinforcement approach) as shown in Figure 3.11.

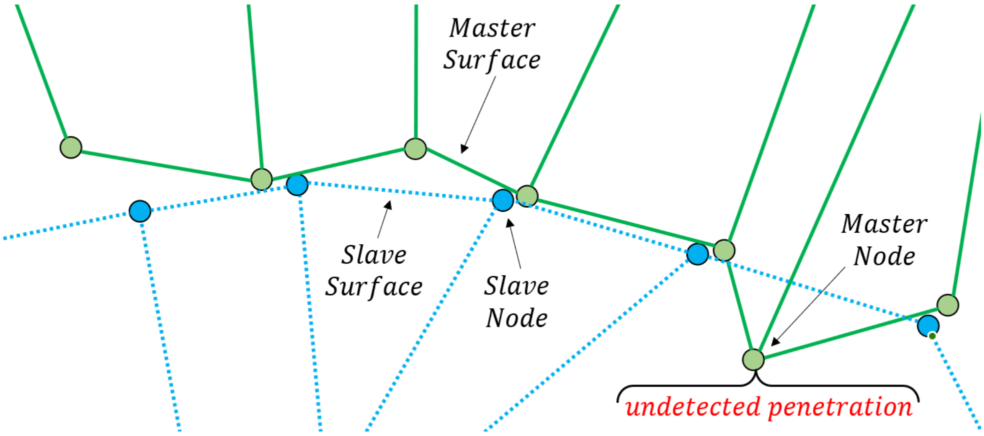

Figure 3.11: Schematic illustration of master node-surface penetration into the slave surface. The representation is made in 2D (Node-To-Segment) but a direct correlation can be made for 3D.

One of the solutions for this case is to refine the mesh of the slave surface.

When two bodies have comparable compliance, their results might not be the same depending on the the choice of master-slave pair. The accuracy of a result depends strongly on two things: (1) the integration scheme employed to numerically approximate the contact integral; (2) the discretization that is used in the simulation. Contacting surfaces of soft materials in contact during sliding can become distorted and the mismatching of elements causes discontinuity on the minimal distance functions calculated across time. This bias is stronger for penalty methods, due to the unchecked master node penetration [47].

To reduce this error, in the same loading increment it is possible to reverse the roles played by the bodies: the slave becomes the master and vice versa [25]. This method is usually called two-pass or balanced approach. However, Zavarize [35] and Laursen [47] remarked that the approach loses the physical interpretation of the traction forces to be evaluated at each contact node.

Another possibility is the removal of the *a priori* choice between master and slave via a symmetric treatment, where both states for both surfaces are considered simultaneously [44]. IMPETUS implements a symmetric approach unless stated to not do so. A symmetric master-slave formulation splits the virtual contact work into two parts, which are weighted by a coefficient θ which can depend on the mesh, geometry and stiffness of the material. The variational form of contact is then represented as

$$
\begin{aligned}
G^{Sym}(\mathbf{x}_t, \hat{\mathbf{x}}) &:= \sum_{i=1}^{2} \left\{ G^{b,(i)}(\mathbf{x}_t^{(i)}, \hat{\mathbf{x}}^{(i)}) \right\} \\
&= \sum_{i=1}^{2} \left\{ \begin{array}{l} \int_{\Omega_0^{(i)}} \mathbf{P}^{(i)} : \frac{\partial \hat{\mathbf{x}}^{(i)}}{\partial \mathbf{X}^{(i)}}^{T} dV + \int_{\Omega_0^{(i)}} \rho_0^{(i)} \dot{\mathbf{V}}^{(i)} \cdot \hat{\mathbf{x}}^{(i)} dV \\ - \int_{\Omega_0^{(i)}} \rho_0^{(i)} \mathbf{B}^{(i)} \cdot \hat{\mathbf{x}}^{(i)} dV - \int_{\Gamma_t^{(i)}} \mathbf{T}^{(i)} \cdot \hat{\mathbf{x}}^{(i)} dA \end{array} \right\} \\
&+ \theta \int_{\Gamma_c^{(1)}} \left(T_N^{(2)} \delta g_N^{(2)} + T_{T,\alpha}^{(2)} \delta \hat{\xi}_\alpha^{(2)} \right) dA \\
&+ (1-\theta) \int_{\Gamma_c^{(2)}} \left(T_N^{(1)} \delta g_N^{(1)} + T_{T,\alpha}^{(1)} \delta \hat{\xi}_\alpha^{(1)} \right) dA.
\end{aligned}
\tag{3.5.39}
$$

An advantage of the symmetric approach is that each of the bodies involved in the contact can be simultaneously master and slave, which preserves the physical meaning of the numerical contact traction forces. This implementation is necessary for the purposes of this research to consider contact between tread blocs.

One last complication is when a body interacts with itself. This case of self-contact corresponds to the observed curling effect on the Leading Edge. In addition to the need of symmetric treatment to reduce bias effect, another challenge lies in the identification of the self-contacting pair. Different algorithms exists to consider this effect. One example is the a *bucket sort* approach which subdivide the spatial domain into sub-spaces. The comparison of multiple buckets distances (therefore neighbour information is considered) is sufficient to identify the nearest contacting neighbour. Additional optimizations can be made by limiting the bucket spaces checked depending on different criteria which might or not be related to the problem in question. One possibility is the use of the convective coordinates ξ_α so that nearest Euclidean contacting pairs are only considered if they are not near neighbours with respect to this surface manifold, reducing computational time and avoiding inherent ”myopia”.

Chapter 4

Modelling tread pattern with a rough surface

4.1 Dual Grip project

Before discussing the numerical and experimental investigations, as briefly mentioned, the thesis also seeks to contribute to an ongoing Michelin project called Dual Grip, whose goal is to better understand the friction coefficient during the stabilized dynamic friction of the sliding tire. This chapter will describe the work performed in this framework by the author during the thesis, notably in the observation and analysis of the soil surface.

4.2 Sample geometry

Prior internal tribological investigations made for rubber blocks sliding on a rough surface identified two main interaction zones, which will be termed here as "Bulk" and "Leading Edge" (LE), as shown in Figure 4.1.

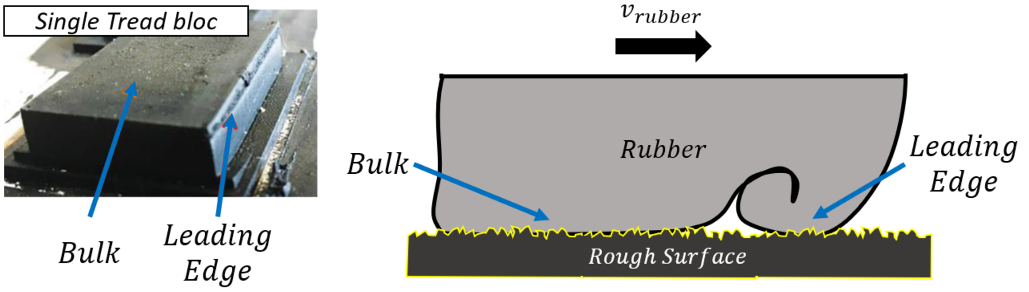

Figure 4.1: Definition of Bulk and Leading Edge Zones.

Although those zones belong to the same sample material, the operating conditions of the LE zone differ considerably from the Bulk portion. In the front of the block, the average contact pressure is usually higher [61], the "curling" effect promotes a non-vanishing field of tensile strain [138] and its geometry can potentially interlock with the asperities of the rough surface [129]. Those trends were already observed externally by some works [61], [121], [138], [144]. However, due to the complexity of its experimental and numerical reconstruction, the effect is not completely understood or quantified.

To further study the differences between those zones, two categories of specimens are proposed, to separate those portions (Bulk and LE). Those samples are appropriately called *Bulk Geometry/Sample* and *Leading Edge Geometry/Sample*.

4.2.1 Description of a bulk sample

When a single rubber block is considered, depending on its geometry aspect ratio, both LE and Bulk interaction states can occur (as shown in Figure 4.1). Therefore, to avoid the curling effect, the front corner of the block is rounded, as shown in Figure 4.2.

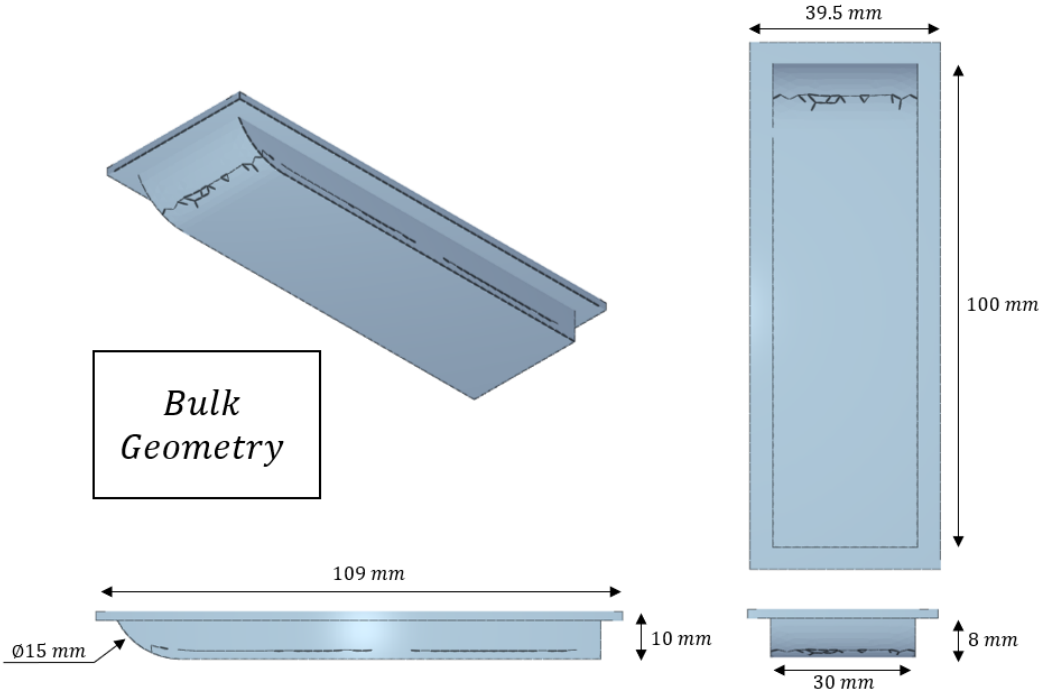

Figure 4.2: General geometric description of Bulk sample.

Although lateral curling can potentially occur, it is believed that most of the contribution stems from the front of the tread block in the direction of the sliding. This geometry is considered not only numerically, but also in experimental tribological protocol tests, where although the rounding can vary, fabrication constraints (mold dimensions) bound the geometry to a hexahedron with length, width, and height of $[L \times W \times H] = [100 \times 30 \times 8]$ [mm^3].

4.2.2 Description of a leading edge sample

An important work by Hofstetter *et al* [61] demonstrated numerically within finite strain framework that not only there is a higher contact pressure in the LE zone of the tread block, but also its distribution tends towards the front and disappear from the base as the number of lamelization[1] increases, as presented in Figure 4.3. The initial rubber block is sectioned into many tread blocks with a high aspect ratio, which bends more easily and pulls the contact toward the front. In addition, there is an inter-contact between tread blocks which plays a role in its degree of liberty and the resulting curling effect.

Those interactions occur far from the rubber-surface interface but influence the resulting contact area and pressure distribution, reiterating the importance of a FEM approach in contrast to BEM, at least in scales, where the tread pattern is relevant.

---

[1] Lamelization, in this context, correspond to the number of “sections” made on the original rubber block (zeroth lamelization)

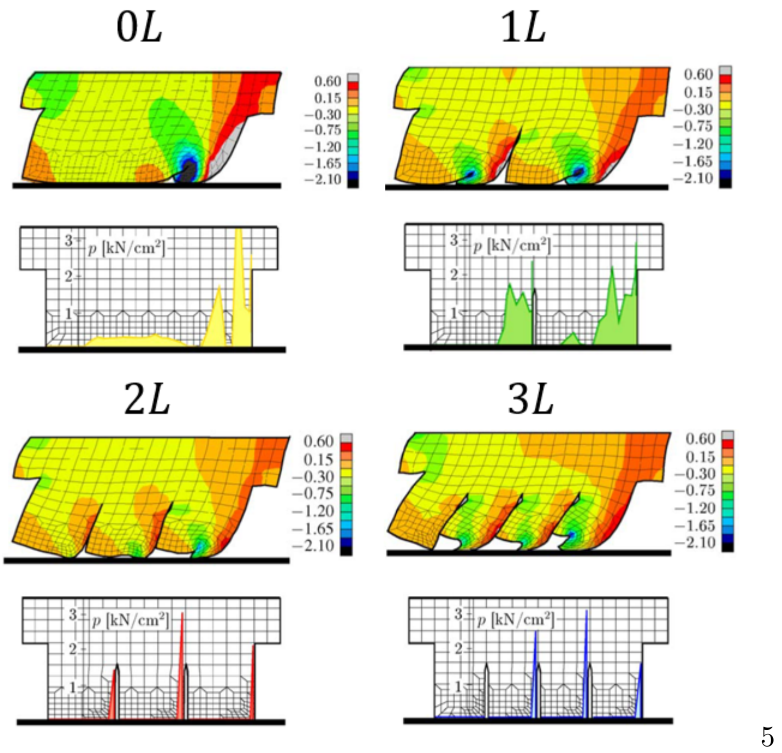

Figure 4.3: Rubber blocks with different block geometries in sliding state and their respective contact pressure distribution (from [61]).

Although this was observed numerically for a rubber material sliding on a smooth surface with an *ad hoc* empirical friction law, the same trend was qualitatively found in sliding friction experiments with rough surfaces, as shown in Figure 4.4.

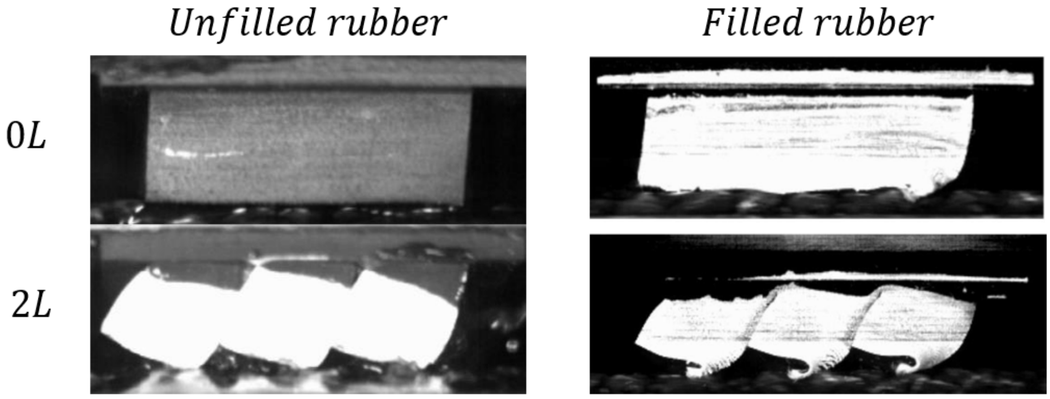

Figure 4.4: Profile videos with high speed camera (compression @3bar / shear/slip @1m/s) of a tread element on wet asphalt (MK2S, 2020) – linear material (left) non-linear material (right) (courtesy of Michelin).

Figure 4.4 also highlights the differences between a linear non-filled rubber material and a non-linear filled rubber material. Both cases present a bending of each tread block and their self-contact, however, for the non-linear material, a more pronounced curling effect occurs.

Motivated by those observations, the Leading Edge geometry to be used numerically and experimentally is presented in Figure 4.5. Like the Bulk geometry, this sample is also bounded in length, width, and height by $[L \times W \times H] = [100 \times 30 \times 8]$ $[\mathrm{mm}^3]$, however, its mold contains thin plates, here named *lamellae*, with a thickness of 0.6 [mm] that partitions the geometry base into individual tread blocks during fabrication.

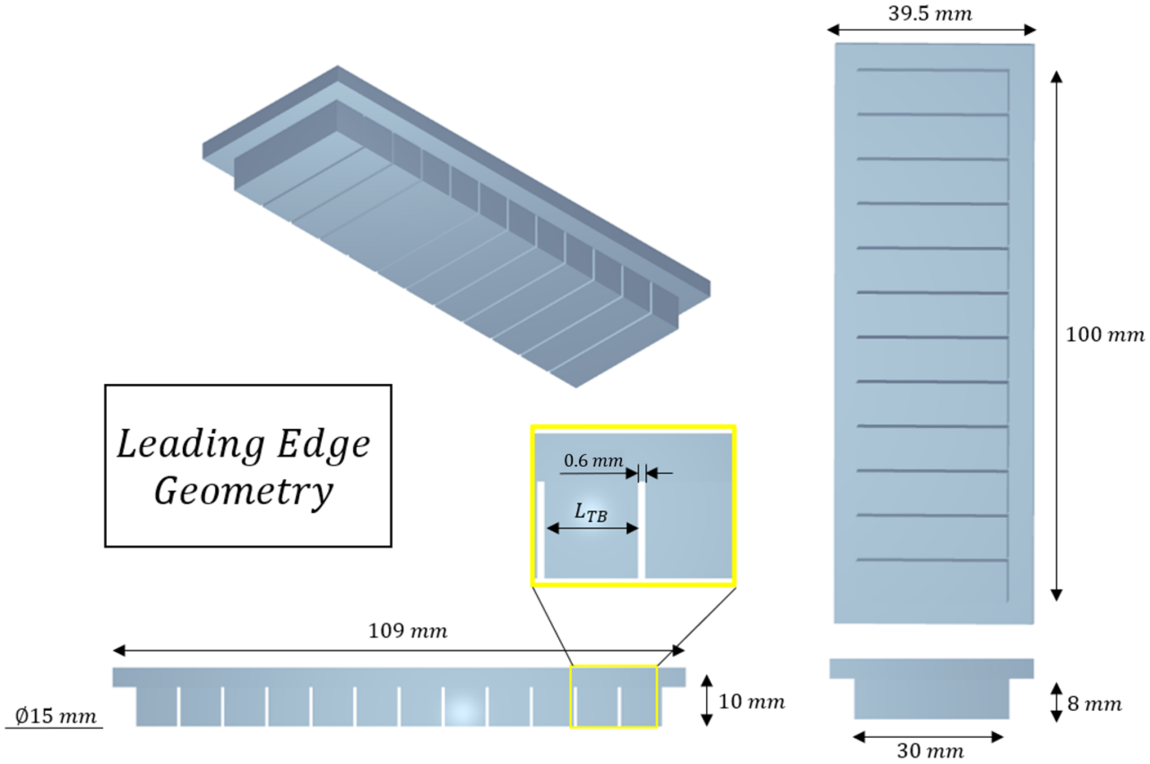

Figure 4.5: General geometric description of Leading Edge geometry. 11L lamelization sample example.

Different configurations are possible by changing the number of lamelizations, N_L. The thickness of the lamellae, t_L, and the total length, L, are kept fixed. Therefore, the length of the tread blocks L_{TB} is

$$L_{TB} = \frac{L - N_L t_L}{N_L + 1}, \tag{4.2.1}$$

whilst the number of tread block present is $N_{TB} = N_L + 1$. A selection of possible partitions is used in experimental evaluations, to be described in Section 4.4 and reconstructed numerically at the end of this work.

4.3 Geometry of a rough surface

Regardless of numerical or experimental application, within a multi-scale framework, there is always a trade-off between precision/resolution of the smaller scale and statistical relevance. Those aspects are essential not only for the measurements made by the author but also for the descriptors devised.

4.3.1 Measurement of soil profile

In the present work, the characterization of the profile of a solid was measured via profilometry, with specifications detailed in Table 4.1. Via a partnership with the enterprise Mahr the available profilometer (*MarSurf CM*) scans a region x8000 bigger than the chosen horizontal resolution. This large coverage is possible due to refined stitching techniques to increase even more the reconstructed range.

Measure	**Machine**	**Resolution xyz**	**Magnification**	**Stitching**
Profilometry	MarSurf CM	3.5x3.5x0.2 μm^3	x8000	~x3

Table 4.1: Measurements specifications of available machine for ground characterization.

The principle of confocal microscopy for the profilometer in question is summarized in the following steps (as seen in Figure 4.6):

1. Detection of a punctiform part of the sample through illumination from a small aperture;
2. Only the zones in focus have the highest signal strength. Those zones are recovered;
3. Numerical reconstruction of the in-focus points detected after the sweep

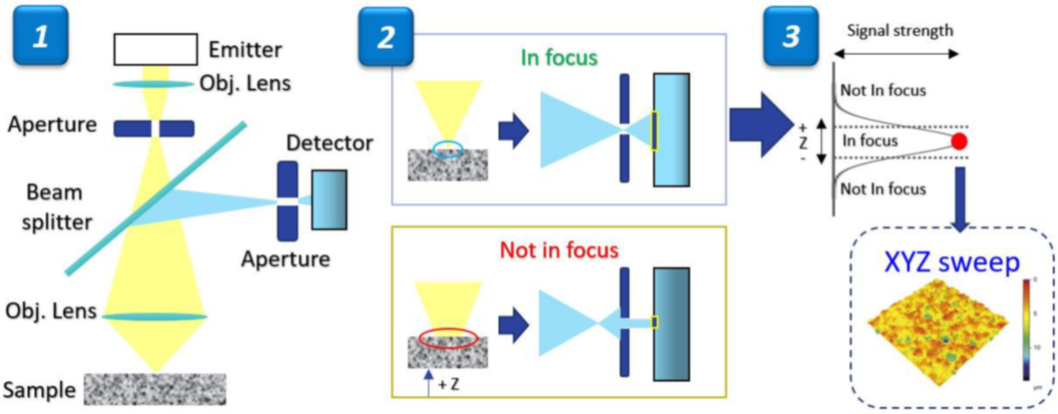

Figure 4.6: Schematic representation of confocal microscopy principle.

The measurements from two bituminous rough soils are available and are denominated hereafter as *Repro02* and *Repro08*. Each data output contains a regular grid (equally spaced in the directions perpendicular to vertical measure) with a resolution of 25 x 25 [μm^2], whereas the whole domain covers an area of 138 × 202 [mm^2]. The raw cloud data recovered for each surface is presented in Figure 4.7. The same two grounds measured by profilometry are also used in experimental tribological tests.

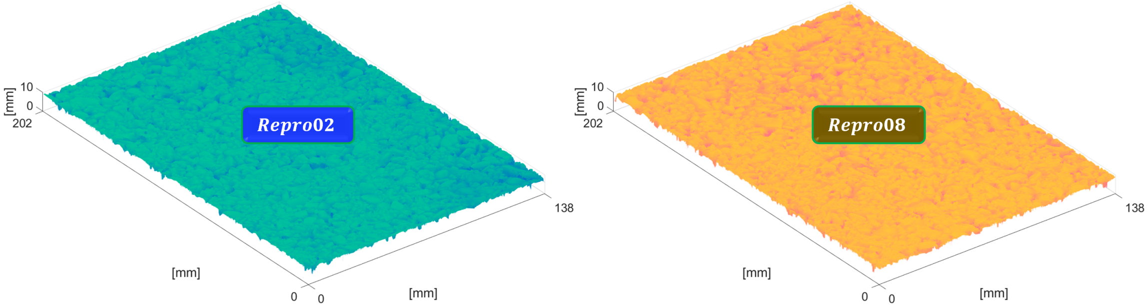

Figure 4.7: Measured cloud point for Repro02 (left) and Repro08 (right) surfaces.

The surface cloud point is transformed into a rigid domain slit discretized as a hexahedral mesh. Due to the large size of the rubber samples, a region of 40 x 150 [mm^2] is considered numerically, so that the stabilized sliding phase can still be reached. The current grid resolution still returns 70223 elements, thus a sub-sampling is applied leading to a final horizontal resolution of 300 x 300 [μm^2]. Figure 4.8 illustrates the steps made to transfer the measured surface into the IMPETUS environment.

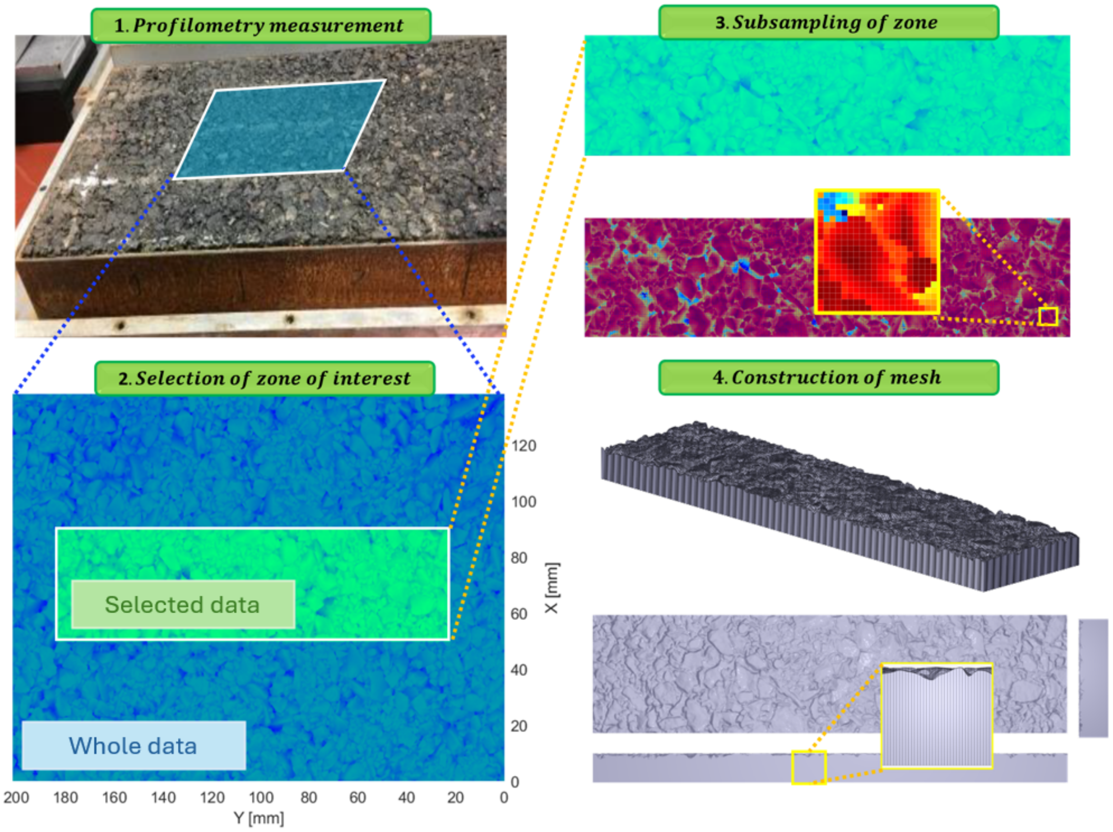

Figure 4.8: Main steps for the recovery of the rough surface from measured data and their transfer into the Finite Element software IMPETUS.

4.3.2 Characterization of a soil profile

In most cases, one descriptor is not able to uniquely represent the surface profile, so most approaches require multiple descriptors. A common strategy is to implement two types of descriptors together: fractal techniques and statistical parameters. Fractal techniques have as the main parameter a fractal dimension associated with the invariant statistical properties of asperities throughout the scales [109]. A prominent example is the power spectra density (PSD) used extensively in physical-based analytical friction models, described in Chapter 2. The main limitation of the PSD is the loss of phase information, so this descriptor is not unique to a single surface. Persson and others also remarked that the loss of phase removes important characteristics due to polishing effects where the top of the asperity might not have the same texture properties as the bottom, which is expected for realistic road surfaces [42], [52], [115], [141], [143].

To better understand the effective texture in-depth, without losing information across scales, a fractal technique is proposed, here denominated as *Lomb-Scargle Slope* (LSS). The method is based on the contributions of Lomb N. R. (1975) and Scargle J. (1983) with a good review made by VanderPlas [120]. The calculation of the slope is based on the Normalized Lomb-Scargle Periodogram, initially intended for astronomical and meteorological data, with potential use for road characterization of this analysis.

A profilometer has a fixed xy-plane displacement, its measurement results in an equally spaced grid for Repro02 or Repro08 cloud data points. Exploiting this characteristic, the surface is separated into line segments that extend in the direction of the sliding tests. Then, each horizontal line segment is sectioned into a number (in this case, four) vertical layers from its highest point to its lowest point, as seen schematically in Figure 4.9.

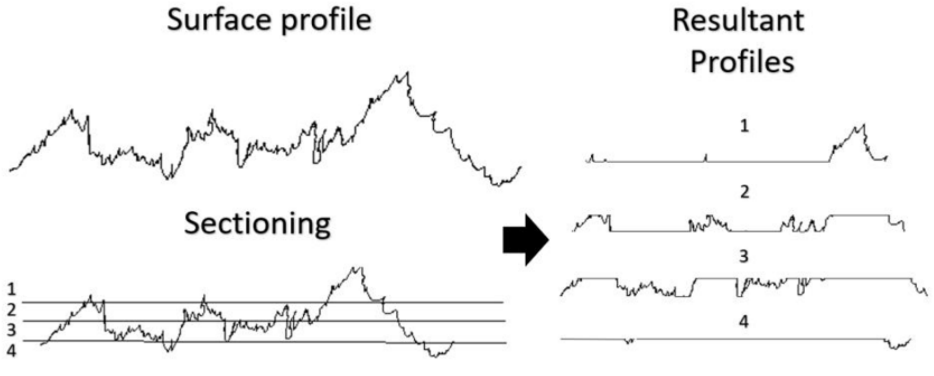

Figure 4.9: Schematic representation of surface partition.

The sectioning presented in Figure 4.9 creates "gaps" that would *a priori* interfere in the spectral representation of the signal of classical PSD techniques. To solve this, there are different strategies to remove (or at least reduce) possible artifacts from appearing from this approach:

- Linear interpolation or higher-order splines on the "gaps". However, these strategies often produce spurious bulges at low frequency when the gaps are long enough and frequency shifting due to spectral leakage;
- Windowing and overlapping noise treatment for each continuous "chunk" of data in between "gaps". Still, not all the segments of the data have enough points (some present only two data points) to ensure a good averaging between the contribution of each segment.

Spectral analysis for unevenly spaced data employing the Normalized Lomb-Scargle periodogram (or LS power spectra) weights data "per-point" basis instead of "per-time/space interval". The idea is to exploit this flexibility and analyze each layer of the surface individually with less spectral leakage due to the interference of the "gaps".

Polishing effects can occur at the smallest scales and then progressively climb up to bigger asperities for bituminous soil. For this reason, in deeper regions the expectation would be to find more aggressive (higher aspect ratio) asperities for a given wave number, thus a less steep slope. Since their high-frequency spectral magnitude does not reduce greatly when observed across scales, while smoother/polished surfaces would present a steeper slope, as shown in Figure 4.10, where only two slipes (A and B) as an exemplary comparison although for multiple layers would result in multiple curves.

The Lomb-Scargle Periodogram is intrinsically normalized, the important information is the slope of each layer, which is recovered through the following steps:

1. Each parallel line of the surface grid in the direction of sliding is sectioned by depth
2. A periodic signal with a shift parameter $\tau \in \mathbb{E}$ to ensure orthogonality is projected onto the signal to work with unevenly spaced data, its power spectra are calculated for each parallel sectioned Layer.
3. The slope of the power spectra obtained via least-squares for each depth Layer and the parallel results are averaged.

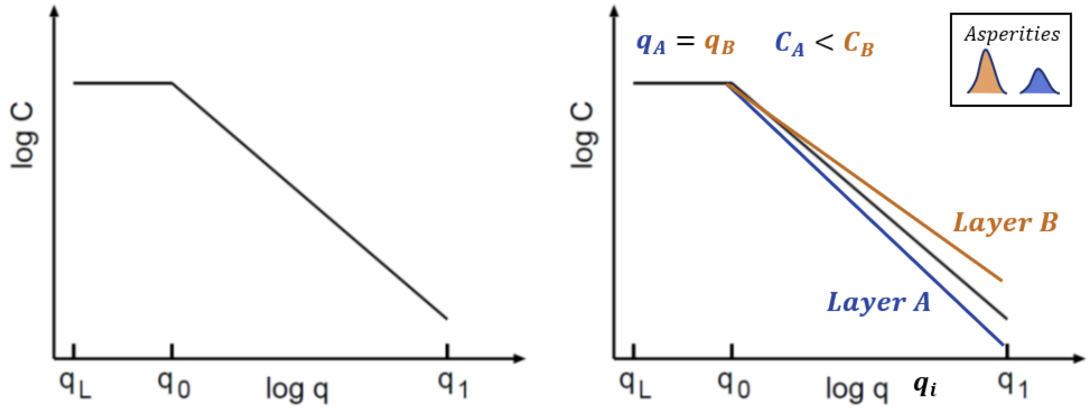

Figure 4.10: Left: Classical Power Spectra representation of a self-affine surface. Right: Power Spectra representation of two layers of a single surface using the Lomb-Scargle Periodogram.

For one-dimensional signal $s : \mathbb{R} \to \mathbb{R}$ (the parallel line of the surface grid) where the value of s is known for a certain space interval $[x_0, x_f]$ with $|x_f - x_0| = X$, the implementation made by the author goes as in three main steps:

1. Sampling wave-vector;
2. Defining offset;
3. Calculating Lomb-Scargle periodogram.

Sampling wave-vector

Linearly spaced wavevectors q_k, with $0 \leq k \leq M$ (where $M \in \mathbb{N}_0$) are defined. The number of components depends on the choice of the highest and smallest wave vector. By defining spatial frequency as $q_k = 2\pi f_k$, the lowest independent spatial frequency f_l is the inverse of the span of input data so $f_l = 1/X$ [69]. However, it is recommended to over-sample more finely than this interval [120] usually with an oversampling parameter $4 \leq c_o \leq 10$ so that

$$f_l = \frac{1}{c_o\, X}. \tag{4.3.1}$$

For the maximal spatial frequency, it is important to compute the periodogram to some well-motivated limiting frequency, usually a pseudo-Nyquist frequency, f_p, related to the parameter

$$c_h = \frac{f_p}{f_c} \tag{4.3.2}$$

where f_c is the Nyquist frequency given by $f_l = N/2X$, with $N \in \mathbb{N}_0$ representing the number of points of a discrete signal $s_n = s_n(x_n)$ on $0 \leq n \leq N-1$. The true Nyquist limit is advised if there is some information for the evenly-spaced data of the measure, and since the resolution of the measure is known, the Nyquist limit will be used, in other words, $c_h = 1$. Then, number of wavevectors, N_P, and the linearly spaced frequencies are defined by

$$N_P = \frac{f_p}{f_l} = \frac{c_o\, c_h}{2} N; \quad f_k = f_l + \frac{f_p - f_l}{N_P - 1} k, \tag{4.3.3}$$

with $0 \leq k \leq N_P - 1$.

Defining offset

To ensure orthogonality of sine and cosine at a sample of integration for each wavevector q_k a shift-factor τ_k is introduced

$$\sum_{n=1}^{N-1} \sin[q_k(x_n - \tau_k)] \cos[q_k(x_n - \tau_k)] = 0 \tag{4.3.4}$$

which holds if

$$\tau_k = \frac{1}{2q_k} \tan^{-1} \left[\frac{\sum_{n=1}^{N-1} \sin(2q_k x_n)}{\sum_{n=1}^{N-1} \cos(2q_k x_n)} \right] \tag{4.3.5}$$

Lomb-Scargle Periodogram

Lomb proposed the use of a basic model of a periodic signal as a sum of signals of different wavevectors, q_k, with the shift factor, τ_k

$$y(x_n) = \sum_{k=1}^{N_P-1} a_k \cos[q_k(x_n - \tau_k)] + b_k \sin[q_k(x_n - \tau_k)] \tag{4.3.6}$$

.

By "projecting" the signal onto this model, similar to how it is made to obtain a_k and b_k for the Fourier transform, since orthogonality of sine and cosine is ensured independent of the spacing between points at the integration interval. Lomb obtained the following values

$$a_k = \frac{\sum_{n=1}^{N-1} s_n \cos[q_k(x_n - \tau_k)]}{\sqrt{\frac{N}{2}} \sqrt{\sum_{n=1}^{N-1} s_n \cos^2[q_k(x_n - \tau_k)]}}; \quad b_k = \frac{\sum_{n=1}^{N-1} s_n \sin[q_k(x_n - \tau_k)]}{\sqrt{\frac{N}{2}} \sqrt{\sum_{n=1}^{N-1} s_n \sin^2[q_k(x_n - \tau_k)]}} \tag{4.3.7}$$

Lomb also defines the power spectral density, P_k, as

$$P_k = \frac{N}{4\sigma_0^2}(a_k^2 + b_k^2) \tag{4.3.8}$$

with σ_0^2 as the variation of the sample data. The form of the power spectra is proposed in such a way that at any individual frequency, this method gives the same power as a least-squares fit to sinusoids of that frequency.

It is advised to operate with the data as a difference from its mean, $s_n - \bar{s}_n$ to avoid bias in the case where the mean of the dataset mismatches the mean of the periodic projected model [79], so the usual formulation proposed for Lomb-Scargle periodogram is recovered, by inserting a_k and b_k into eq. (4.3.8)

$$\begin{aligned} P(q_k) = & \frac{1}{2\sigma_0^2} \frac{\{\sum_{n=1}^{N-1} (s_n - \bar{s}_n) \cos[q_k(x_n - \tau_k)]\}^2}{\sum_{n=1}^{N-1} \cos^2[q_k(x_n - \tau_k)]} \\ & + \frac{1}{2\sigma_0^2} \frac{\{\sum_{n=1}^{N-1} (s_n - \bar{s}_n) \sin[q_k(x_n - \tau_k)]\}^2}{\sum_{n=1}^{N-1} \sin^2[q_k(x_n - \tau_k)]} \end{aligned} \tag{4.3.9}$$

reminding that P_k is calculated for each $s(x_n)$, which in this case is a layer depth for each line segment.

Estimating the slope of a Lomb-Scargle periodogram for a ground height layer

Ideally, a consideration of each line segment to its corresponding layer would be of interest, but because of the heterogeneity of the surface, two layers of the same level but different line segments do not have the same number of points N, therefore, not having the same quantity of wavevectors N_P, so another strategy must be made.

Based on the data from Repro02, two Lomb-Scargle periodograms for two different layers are presented in Figure 4.11. It is noticeable that the spectral distribution frequencies higher than the roll-off plane (defined in section 2.3.2) behave similarly to self-affine surfaces (as in Figure 4.10) obtained through classical PSD calculation. Then their slope are obtained via least-square fit. The fact that the Lomb-Scargle periodogram is normalized for the lowest frequency is not considered a restriction, since low frequencies are attributed to bigger asperities, which aspect ratio is less sensitive to polishing than smaller asperities.

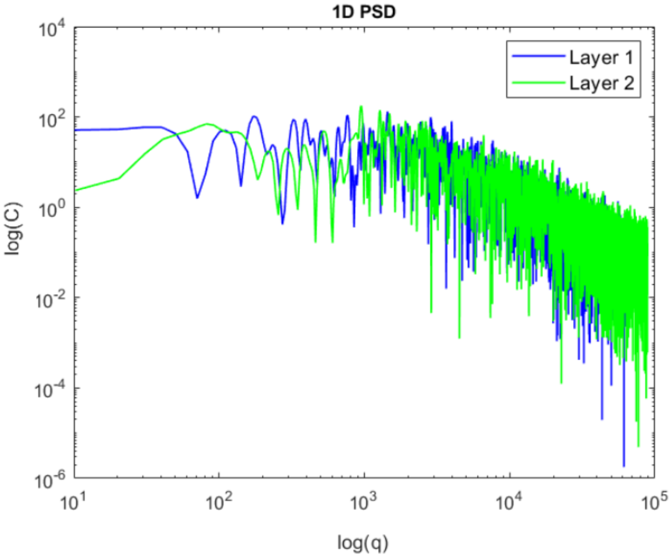

Figure 4.11: Result of two layers power spectra with LS periodogram.

To verify if the slope is related to bigger asperities in a certain depth, we introduce a sinus signal superposed with a random noise modulated in proportion to its "depth", as shown in Figure 4.12.

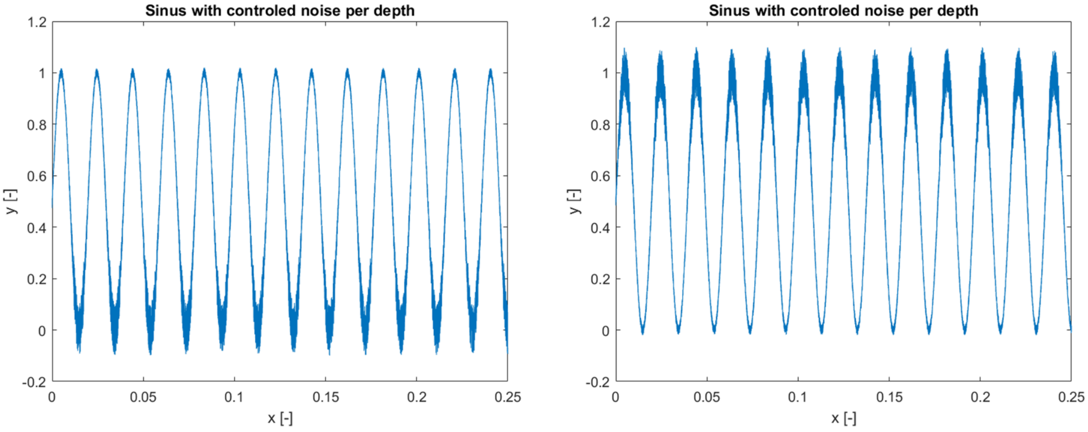

Figure 4.12: Sinus superposed with modulated Gaussian noise. Left: stronger noise in deeper zones. Right: Stronger noise in upper zones.

The result (Figure 4.13) presents a growing value (and reduction of slope inclination) per depth with the sinus with higher noise in the deeper layers, and the opposite for the sinus with high noise on the upper layers. The Layers are nothing more than maximum and minimum heights equally separated by the number of intended layers, where the largest value refers to the deepest interval.

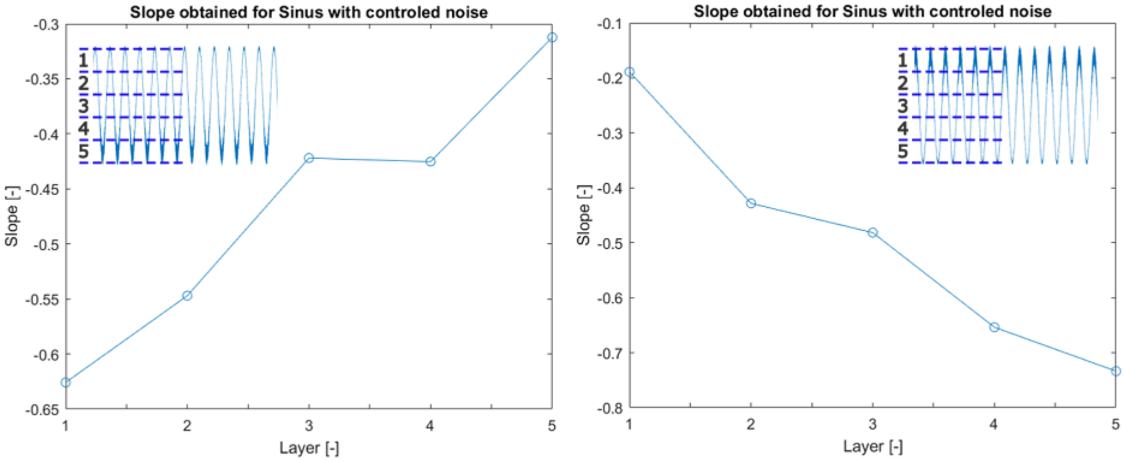

Figure 4.13: Slope per depth for sinus superposed with modulated noise.

Now to verify its applicability for soil surfaces, two important tools are also used for comparison and verification. The first tool was initially proposed by Persson [52] and its calculation procedure was further developed by Kanafi and Tuononen [115] in an attempt to describe the fractal content of used road surfaces. Due to a stronger polishing in the top asperities, when compared to the bottom, the surface presents a non-symmetric height distribution. The principle relies on the introduction of a top and a bottom power spectral density

$$C_T(q) = \frac{1}{(2\pi)^2} \iint_{-\infty}^{\infty} \langle z_T(\mathbf{x}) z_T(\mathbf{0}) \rangle e^{-i(\mathbf{q}\cdot\mathbf{x})}\, dxdy \tag{4.3.10}$$

$$C_B(q) = \frac{1}{(2\pi)^2} \iint_{-\infty}^{\infty} \langle z_B(\mathbf{x}) z_B(\mathbf{0}) \rangle e^{-i(\mathbf{q}\cdot\mathbf{x})}\, dxdy \tag{4.3.11}$$

where $z_T(\mathbf{x}) = z_T(\mathbf{x}) \forall z > 0$ (above mid-plane) and $z_T(\mathbf{x}) = z_T(\mathbf{x}) \forall z < 0$ (bellow mid-plane) as represented in Figure 4.14.

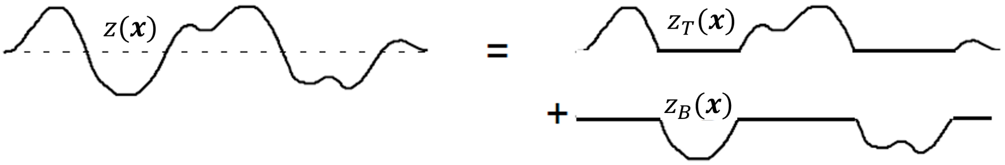

Figure 4.14: Surface profile decomposed into top and bottom profile (by [52] modified by the Author).

Kanafi and Tuononen proposed a correction of the form

$$C_B^* = \frac{C_B}{n_B} \quad ; \quad C_T^* = \frac{C_T}{n_T} \tag{4.3.12}$$

where $n_B = N_B/N$ and $n_T = N_T/N$ are the fractions of the nominal surface area projected over the medium plane. N represents the total number of data points and their partition over the medium plane for N_B and N_T. Persson described C_T as a Power Spectral Density resulting if the actual bottom profile was replaced by a mirrored top profile and vice-versa for C_B [52]. In reality, even though the generated top surface is not the same as the original topography, it gives the same perception of the statistical roughness properties of the original top profile.

One important limitation appears for any section that does not deal with medium xy-plane, leading to imprecise outputs [115]. Even though the correct scaling and short-scale roughness components are well preserved, if a very short Top section is taken (for instance, 5% of the data portion topography, instead of 50%), even if the top asperity is mirroring the surface, the spacing will not be taken into consideration. For this reason, when considering the data from Repro02 and Repro08, only the section made with 50% (top or bottom) will be used in this analysis.

Surface reconstruction

The second validation tool considered is to compare the periodograms of the original surface to the ones of a reconstructed surface. This reconstruction only uses the classical PSD of the measured surface data and is done with the following main steps [90]:

- Amplitude of each component of the Fourier Transform derived from the original PSD;
- Randomly generated phase values for each component;
- Inverse Fourier Transform is performed to have a surface in real space. From Repro02 and Repro08 two random surfaces were generated, which will be called Repro02Gen and Repro08Gen, respectively, as shown in Figure 4.15.

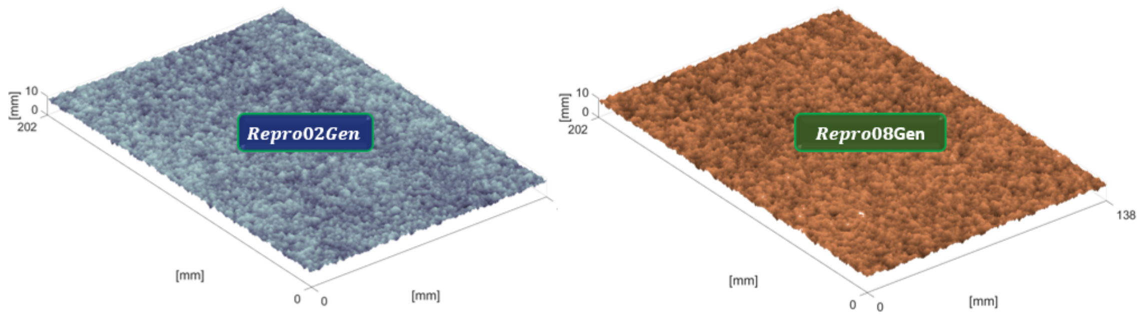

Figure 4.15: Generated cloud point for Repro02Gen (left) and Repro08Gen (right) surfaces.

A comparison between Repro02, Repro08, and their respective reconstructed counterparts Repro02Gen and Repro08Gen is presented in Figure 4.16. It is noticed that measured surfaces contain differences between the top (higher magnitude) and bottom (lower magnitude) evaluations across the whole spectrum. In contrast, this specificity is completely lost when classical PSD (with random phase) is considered, where top-bottom PSD contents for generated surfaces superpose. Moreover, a stronger difference is found for higher frequencies, which is expected, since larger asperities would be less sensitive to polishing, corroborating with internal observations of smaller asperities being impacted first by wear, creating an important connection with depth, polishing, and spectral content.

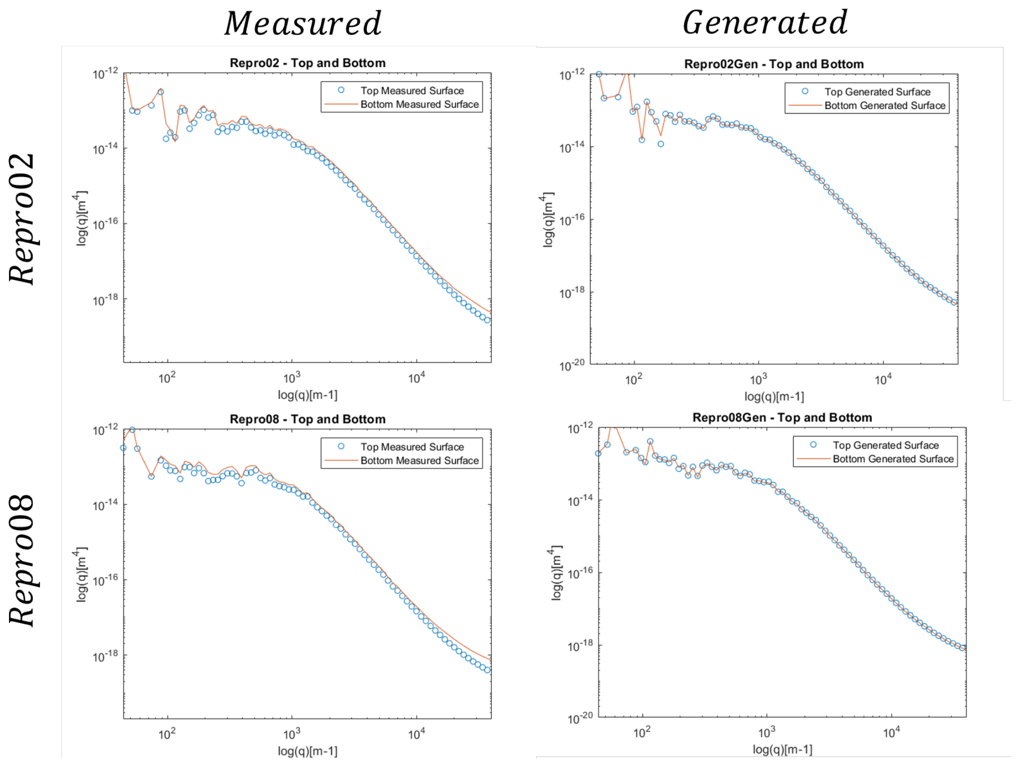

Figure 4.16: Top and Bottom Power Spectral Density of Repro02, Repro08 and their reconstructed counterparts Repro02Gen and Repro08Gen.

This framework, in addition to giving insight into the type of surface being studied, allows for the qualitative verification of the Lomb-Scargle Slope approach. The comparison between measured and generated surfaces is shown in Figure 4.17, where the surface is separated into five layers, where the first is the shallowest and the last is the deepest. In addition, the Figure also contains (on the right) the computation of classical PSD (as per eq. (2.3.10) from section 2.3.2) of Repro02 and Repro08.

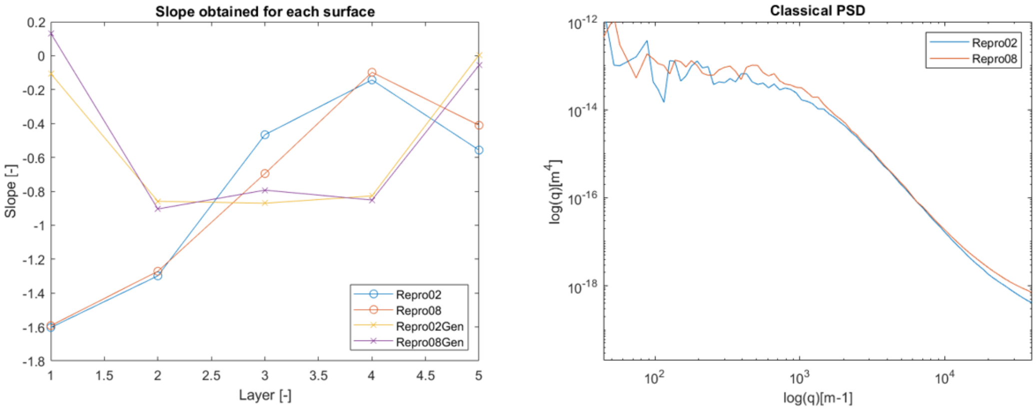

Figure 4.17: Evolution of LS PSD slope over deepness for all studied surfaces.

Starting from a qualitative point of view for the measured data, greater slope values found on deeper layers are in phase with previous observations and expectations, where smaller scales still preserve a high aspect ratio (Figure 4.10). To justify the strong slope value variation of this method, it is important to consider that, for self-affine surfaces, the mean square slope roughness is very sensitive to high-frequency content. Therefore, to compare this method with the top-bottom PSD approach, one should expect the Lomb-Scargle Slope to better agree with the high-frequency portion (and the gradient) of the power spectra, where the differences between polished and unpolished texture are most prevalent.

Another initially simple remark is the similar shape between the slope curve of Repro02 and Repro08. Albeit the curve of Figure 4.17 has an apparent simplicity, each point contains multi-scale information of asperity aspect-ratio. In other words, the method, if well executed, returns not only spectral information concerning roughness aggressivity, but also its distribution across macro-scale depth.

Directing attention to the generated surfaces, the presence of symmetry for the generated surface is in agreement with the loss of information per depth as it was found through the top-bottom PSD superposition. The reason why the smallest slopes are in the peaks and valleys for the generated surfaces seems not to be related to the Lomb-Scargle Slope method itself, but to how the curve was reconstructed, since its partition is made by depth (and not normalized by data points), therefore, the extreme layers tend to have more points a richer spectral content (which was randomly attributed by the phase) than the middle parts. One point of improvement would be to separate the surface for the number of data points, giving a better spectral content, but imposing a non-evenly distributed depth partitioning, which could compromise the analysis's initial objective.

4.4 Experimental tribological observations

To better characterize the two operating zones (Bulk and LE geometries) discussed at the beginning of this chapter, a learning base protocol was devised to evaluate the sculpture (lamelizations or their absence) and the rough soil in tribological contact. This evaluation uses both data from Finite Elements simulations to deliver the macro-mechanical aspects of the sculpture and experimental characterization of the dependence on pressure between the two zones.

This particular experimental result took place before the thesis. The hypothesis and questions that arose from it motivated the conception of the thesis.

4.4.1 Bulk/Leading Edge Protocol

Materials and methods

The test was performed using a High-Speed Linear Friction Tester (HSLFT, internally called MAPI) by Altracon company. The machine offers the possibility to determine the Amontons-Coulomb friction with a considerable range of operations conditions that encompass all tire load classes regarding their dynamic conditions, tread block design, and rough surface, as well as temperature control.

For the object of study of this research, the main quantity of interest is the stabilized dynamic friction coefficient, recovered employing the Amontons-Coulomb friction law of eq. (1.3.2), where the tread block of interest undergoes an imposed normal load and an imposed velocity. Experimentally, the normal force is implemented using a fully controlled hybrid (hydraulic/pneumatic) pressure loading system, attached to a sliding head, which moves horizontally. The tread block is fixed onto the head, compressed, and then slipped across the length of an opposite fixed surface. A schematic representation of those main components is shown in Figure 4.18.

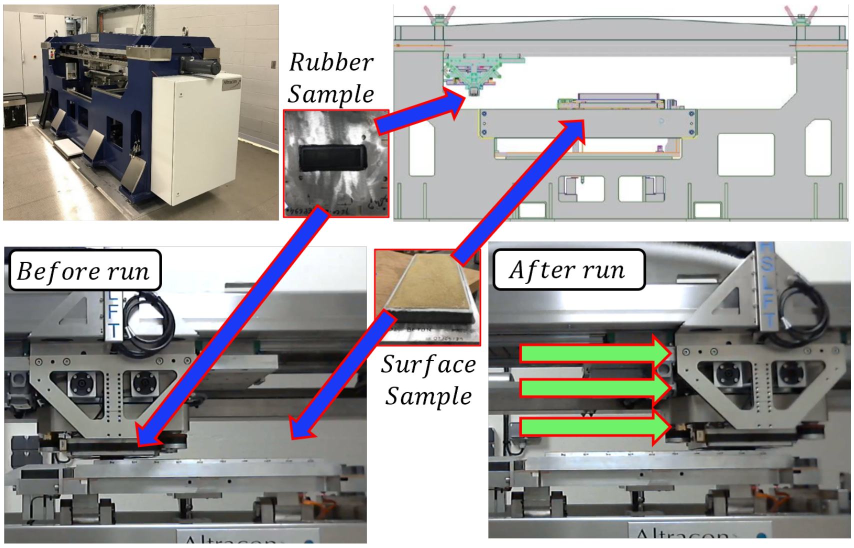

Figure 4.18: Surface profile decomposed into top and bottom profile (by [152] modified by Author).

Samples

There are two components to be evaluated in the experiment: the rubber tread block and the rough surface. Herein, surfaces Repro02 and Repro08 are going to be considered. Likewise, concerning the rubber tread block, the two defined Bulk and LE geometries/samples are used, with some specifications.

The interest of the procedure is to compare friction evolution with increasing pressure between Bulk and leading-edge geometries. In total, twelve sculptures are tested, which the first half consists of six Bulk geometries of the same geometry, while the other half contains six different lamelizations [10L, 12L, 14L, 16L, 18L, 19L] of the Leading edge geometry, as described in section 4.2.2.

The Bulk geometry contact is assumed to not vary strongly, therefore, the imposed pressure sweep $[0.5, 1, 2, 4, 5, 6]$ [Bar] is performed for six Bulk samples, where the pressure is applied on the upper portion of the sample. For LE geometries, the lamelizations are high enough to ensure contact in the front, for stabilized sliding conditions. The same pressure of 2.57 [Bar] is applied for all specimens. All the treads are shown in Figure 4.19.

Lastly, for the current discussion, a single type of rubber mix from Michelin is considered, here simply termed *Primacy*, whose main available characteristics are presented in Table 4.2.

	Primacy
Filler rate $[pce]$	120
Volume fraction [%]	23.43
Tg $[°C]$	-15

Table 4.2: Principal characteristics considered rubber mix (courtesy of Michelin).

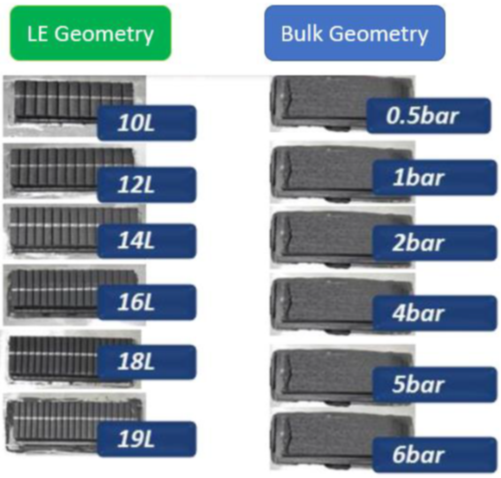

Figure 4.19: Tread samples used for the pressure sweep protocol (courtesy of Michelin).

Test conditions

The target speed for characterizing the different bases on MAPI has been defined at 1 [m/s]. The zone covered by a rough surface sample is quite large and potentially heterogeneous depending on its assembly to HSLFT and previous testing performed on it. To gather meaningful information over the whole texture range, the soil was separated into four horizontal zones (in the direction of the sliding), called *traces* and three perpendicular zones, termed *parallel*, as represented schematically in Figure 4.20.

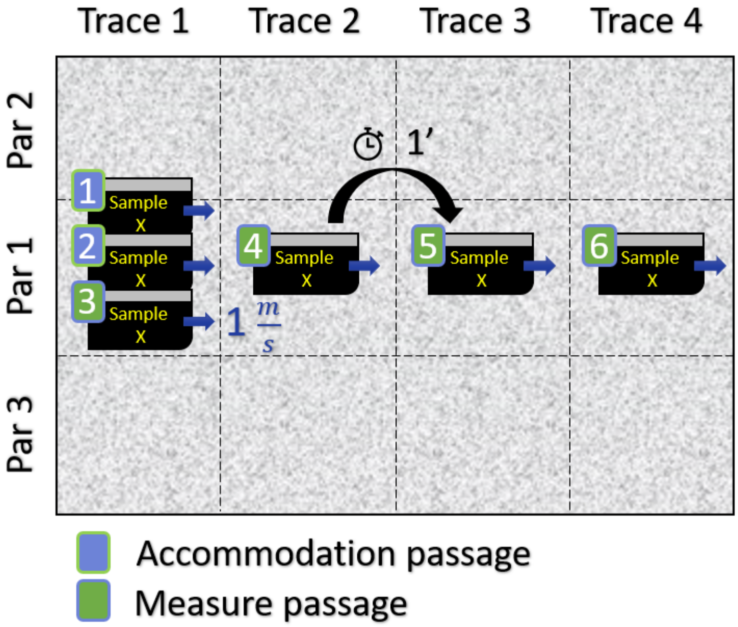

Figure 4.20: Surface repartition and passage description for a single specimen.

As shown in Figure 4.20, each sample, regardless of which, will perform six passages. To define a single passage, we recall one of the central quantities of interest to analyze: the dynamic friction coefficient, μ_{dyn}, found during stabilized sliding conditions between sculpture and rough surface (a concept already introduced in section 1.3). MAPI's load is vertically controlled and velocity horizontally controlled, meaning that a single passage consists of a quickly applied acceleration until a terminal velocity is achieved (normally close to breaking sliding conditions for the tire) and then decelerated. The connection between the stabilized zone of interest is schematically shown in Figure 4.21.

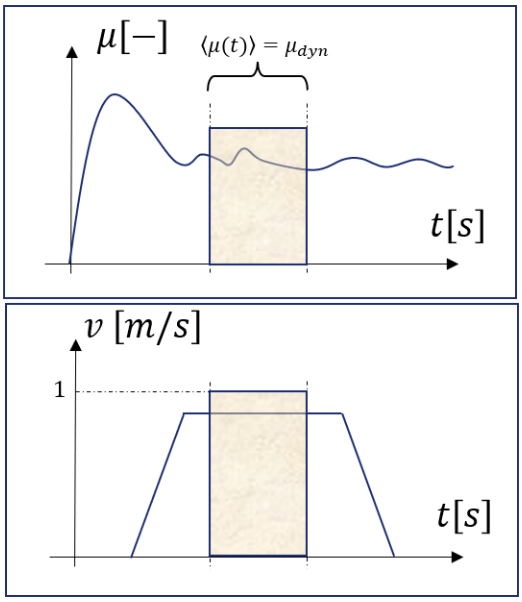

Figure 4.21: Stabilized friction recovered for a single passage over terminal velocity (made the by Author).

The first two passages (from Figure 4.20) are not considered in the statistical treatment of data, serving instead to: reduce the initial contribution of irreversible viscoelastic properties of the rubber (i.e. Mullins effect), remove possible surface particles that could interfere with the test (bubbles, dust and/or rubber particles) and readjust any gaps associated to the mounting of a new specimen into the movable head of HSLFT. Another very important characteristic is that all passages occur with the sample being immersed in temperature-regulated water to simulate wet conditions. A temperature of 15 °C was considered for Primacy, so that operating conditions are better controlled relative to its glass transition temperature as in Table 4.2. In addition, to minimize self-heating contributions (introduced in section 2.3.4), the specimens are immersed between passages in cold water for one minute (shown in Figure 4.20) before proceeding to the next passage, avoiding the cumulative thermal effects throughout the experiment.

The 24 samples from Figure 4.19 (12 × 2, since two grounds are considered) are then mounted to the test randomly to avoid any bias associated with surface polishing caused by a preferred sample geometry/configuration sliding first or last. This whole campaign is performed for a single parallel. Once finished, the other two parallels (with six passages per geometry-material) are evaluated for the same specimens, with of course, a new randomly generated passage ordering.

4.4.2 Experimental results

The principal results consist of two dynamic friction plots, as displayed in Figure 4.22. Figure 4.22a displays μ_{dyn} across the defined pressure range for the Bulk geometry sliding against Repro02 ground (marked blue line) and Repro08 ground (marked red line). Figure 4.22b displays μ_{dyn} for each Leading Edge lamelization siding against both available grounds. Reminding that each dynamic friction data is not only an average in time at stabilized velocity but also all 12 repeated measurements (across all 4 traces and 3 parallels), to which the colored highlighted area refers their respective dispersion.

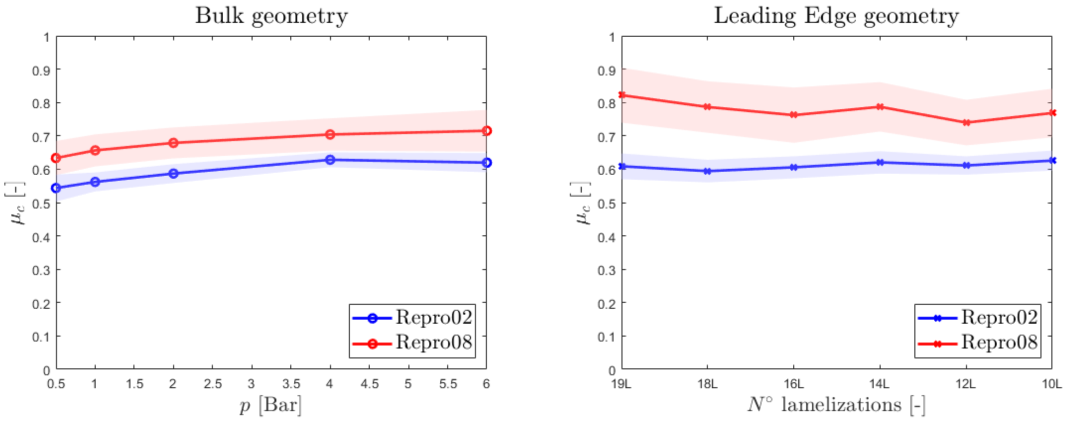

(a) Bulk - pressure sweep (b) Leading Edge - geometry sweep

Figure 4.22: (shear/slip @1m/s) of all tread element on wet Soil. Each plot represents both geometries for a certain Material/Temperature and soil type (courtesy of Michelin, modified by Author).

There is an impact on friction evolution for the Leading Edge geometry, where the decreasing trend number of *lamellae* is more pronounced for Repro08. Nonetheless, both geometries perceive an increase in absolute value. A first attempt to understand what takes place is made by considering the surfaces PSD (Figure 4.17, right plot). Repro08 contains a higher spectral content on lower and high frequencies, and since the hysteresis dissipation is strongly affected by the smaller scales, a higher overall dynamic friction value should be expected when exchanging to a more aggressive surface.

A more convoluted point concerns the specificity between Bulk and Leading Edge geometry, where the latter has stronger sensitivity to surface and a more complex friction evolution with pressure, especially to what concerns its decrease for more aggressive surfaces. As presented in Chapter 2, a lamelized sculpture presents a much more intricate interaction with the surfaces, because:

- **Complex geometry interaction**: Due to interlocking effects, the LE specimen could reach deeper portions of the surface, and therefore, interact with unpolished zones with different spectral information, especially in smaller scales.

- **Mixed multi-physical effects**: Usually, in lubricated wet conditions and breaking relative speeds, hysteresis friction is considered to be a first-order contributor to adherence (discussed in section 2.3.4). However, for LE geometry, the cyclic interlocking with larger asperities promotes a stick-and-slip behavior with periodic low relative speed, which could operate on the Boundary lubrication regimen with local dry contact, bringing back the relevance of direct adhesion contact of flash-heating effects.

- **non-linear viscoelastic behavior**: Although irreversible viscoelastic effects were diminished as per protocol, reversible contributors (i.e. Payne effect) can still act. This is especially the case for LE geometry, due to interlocking, which undergoes large deformations (as seen in Figure 2.17) and where the front end of the tread block remains pre-stretched most of the time.

4.4.3 Key features

Figure 4.22, displays many compelling trends to be evaluated, the most relevant being: (i) pressure/lamellae sweep; (ii) Repro02 compared Repro08 ground (iii) Bulk compared to Leading Edge geometry. If μ_{dyn} is treated as an independent event, since each value and their dispersions are recovered from an individual rubber sample, it becomes reasonable to implement a two-sample t-test [69].

By significance, a confidence level of 95% is considered sufficient. The interest is to verify if two averages μ_{dyn} can be considered distinct from one another, thus validating the trends themselves. The null hypothesis, H_0, and alternative hypothesis, H_a, are defined as

$$\begin{cases} H_0: \ \mu^1_{dyn} - \mu^2_{dyn} = 0 \\ H_a: \ \mu^1_{dyn} - \mu^2_{dyn} \neq 0 \end{cases} \tag{4.4.1}$$

Starting evaluating the trends observed in Figure 4.22b with pressure and lamellae number sweep. The test is performed by comparing all possible combinations of μ_{dyn} values for a given rubber geometry and ground profile. The results are displayed in Figure 4.23 where green squares represent that the H_0 can be rejected and the two friction values in questions are distinct with 95% of confidence, otherwise the square is red.

The original outputs from Figure 4.22 displayed an apparent increase of μ_{dyn} in pressure for the Bulk geometry and both grounds profile. This is consistent with the tests from Figures 4.23a and 8.2b where the increase in friction is significant as long as the increase in pressure is above 1 $[Bar]$ for Repro02 cases and 2 $[Bar]$ for Repro08. Concerning the Leading Edge, an interesting trend unfolds as an increase in μ_{dyn} with lamelization reduction when sliding against Repro02 and a decrease when sliding against Repro08. However, their large dispersions are reflected in Figures 4.23d and 4.23 where, although there is one significant case, there is no clear trend related to this sweep.

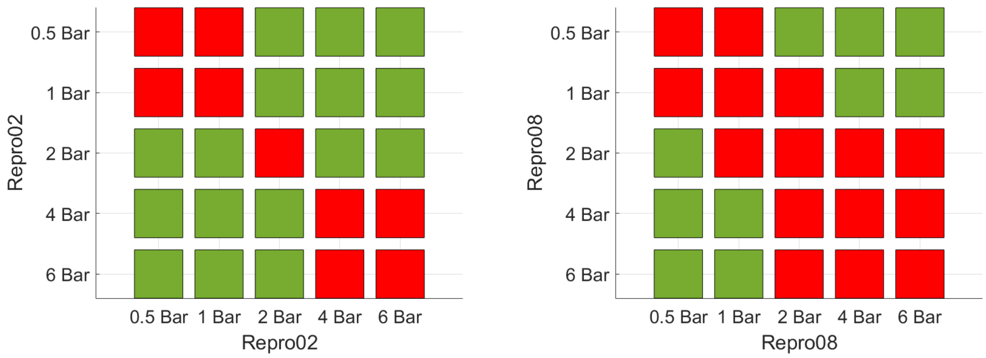

	0.5 Bar	1 Bar	2 Bar	4 Bar	6 Bar
0.5 Bar	🟥	🟥	🟩	🟩	🟩
1 Bar	🟥	🟥	🟩	🟩	🟩
2 Bar	🟩	🟩	🟥	🟩	🟩
4 Bar	🟩	🟩	🟩	🟥	🟥
6 Bar	🟩	🟩	🟩	🟥	🟥

	0.5 Bar	1 Bar	2 Bar	4 Bar	6 Bar
0.5 Bar	🟥	🟥	🟩	🟩	🟩
1 Bar	🟥	🟥	🟥	🟩	🟩
2 Bar	🟩	🟥	🟥	🟥	🟥
4 Bar	🟩	🟩	🟥	🟥	🟥
6 Bar	🟩	🟩	🟥	🟥	🟥

(a) Bulk-Repro02 versus Bulk-Repro02 (b) Bulk-Repro08 versus Bulk-Repro08

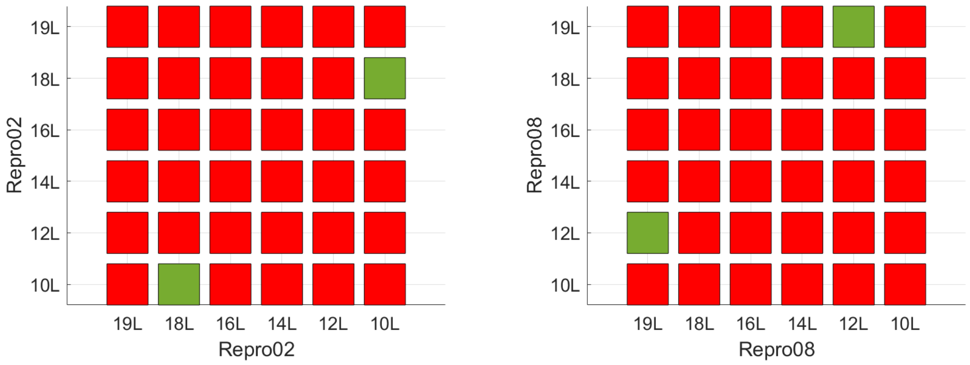

	19L	18L	16L	14L	12L	10L
19L	🟥	🟥	🟥	🟥	🟥	🟥
18L	🟥	🟥	🟥	🟥	🟥	🟩
16L	🟥	🟥	🟥	🟥	🟥	🟥
14L	🟥	🟥	🟥	🟥	🟥	🟥
12L	🟥	🟥	🟥	🟥	🟥	🟥
10L	🟥	🟩	🟥	🟥	🟥	🟥

	19L	18L	16L	14L	12L	10L
19L	🟥	🟥	🟥	🟥	🟩	🟥
18L	🟥	🟥	🟥	🟥	🟥	🟥
16L	🟥	🟥	🟥	🟥	🟥	🟥
14L	🟥	🟥	🟥	🟥	🟥	🟥
12L	🟩	🟥	🟥	🟥	🟥	🟥
10L	🟥	🟥	🟥	🟥	🟥	🟥

(c) LE-Repro02 versus LE-Repro02 (d) LE-Repro08 versus LE-Repro08

Figure 4.23: two-sample t-test combinatory - Pressure and lamelization sweep.

On the other hand, the distinctions between Bulk or Leading Edge geometries when the ground is swept are more pronounced, as demonstrated in Figure 4.24. All μ_{dyn} for Leading Edge are distinct from one another when the ground is changed, whilst for the Bulk that is mostly the case, except for low pressures using Repro08 and high pressures using Repro02, where their values approach.

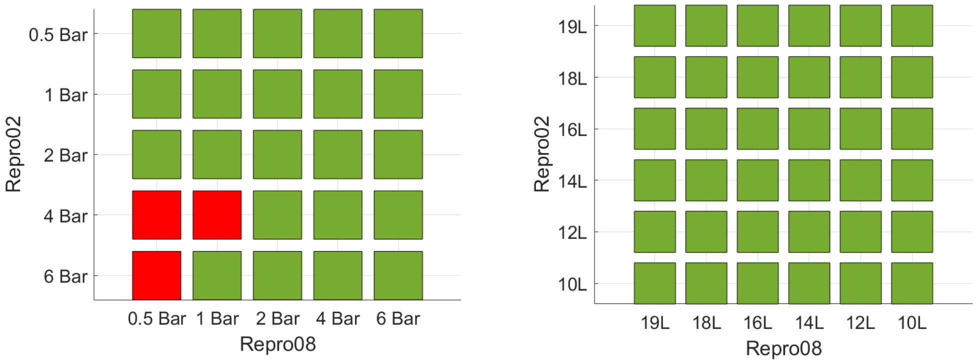

(a) Bulk-Repro02 versus Bulk-Repro08 (b) LE-Repro02 versus LE-Repro08

Figure 4.24: two-sample t-test combinatory - ground type effect.

Lastly, for the same ground, we present the act of using a Bulk geometry and a Leading Edge geometry in Figure 4.25. Interestingly, for Repro02 the Bulk cases compressed at high pressures approaches the Leading Edge result, nonetheless Bulk at low compression and Leading Edge with few lamelizations to contain a significant difference. For Repro02 the value of the Leading Edge is high enough to display an apparent distinction between the two geometries, showing an important interplay between rubber geometry when the proper ground is considered.

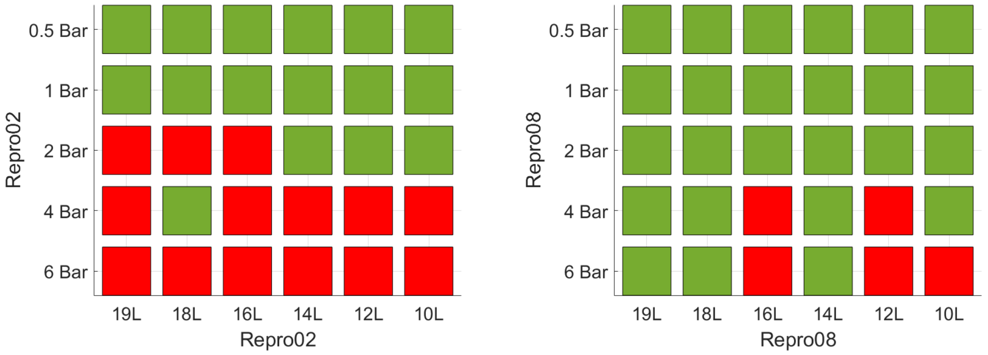

(a) Bulk-Repro02 versus LE-Repro02 (b) Bulk-Repro08 versus LE-Repro08

Figure 4.25: two-sample t-test combinatory - rubber geometry effect.

To summarize, the qualitative trends with pressure and lamelization are not to be judged without putting into question the dispersion of the measurement itself. Nonetheless, their absolute values with shifting ground or rubber geometry as a whole are representative enough to be further investigated.

4.5 Concluding remarks

We have introduced herein the specific configurations of the interest and started to analyze the road surfaces involved in such problems, including the roughness variation as function of depth. Different tools have been presented and implemented for analysis and reconstruction. It was observed that road surface contains a roughness gradient in depth. Moreover the limits of the power spectral density were outlined with respect to the objective at hand;

The results presented, when contextualized to the discussions found in the literature, indicate that even if the smallest scales pilot the local friction, macro-scale tread pattern geometry will also play a role on defining the local contacting area (shallow or deeper zones) and which mechanical effects are prevalent. In addition, the material viscoelastic characteristics contribute on how the sculpture will respond, being on equal footing with the geometry defined in the first place as observed in Figure 4.4.

To summarize the discussion presented on this chapter, from a practical standpoint, it follows that:

- The wear on asphalt surfaces could be correlated to the vertical depth of the soil;
- The Bulk/Leading Edge experimental protocol produced two statistically meaningful trends, they being:
  - Presence or absence of geometrical sculpture (Leading Edge or Bulk);
  - Type of rough ground (Repro02 or Repro08).
- Leading Edge Specificity presents a convoluted contribution from tread pattern and surface geometry, viscoelastic properties of the rubber mix and multi-physical aspects.

Those observations serve the following principal purposes:

- For the numerical simulations of the tribological tests to be done in the last two Chapters, the boundary conditions will be defined so that the operating conditions approximate as much as possible to the Bulk/LE protocol;
- The experimental investigations in Chapter 6 will attempt to isolate some of the convoluted physical mechanisms present simultaneously in Bulk/LE protocol, mainly lubrication and non-linear viscoelastic effects, while suppressing surface roughness effects.

Chapter 5

Proposed constitutive model

5.1 About the available data

Without considering tribological tests, there are five types of experiments available:

- Dynamic Mechanical Analysis (DMA): Amplitude and frequency sweep;
- Uniaxial Loading/Unloading: Constant stretch rate
- Uniaxial Loading/Unloading: Relaxation test
- MMAexpert: Extrapolated available data in shear conditions

Ideally, all tests attempted to consider three types of industrial filled rubber (A6, PCY4-RT and PS4) at two temperatures (7 °C and 15 °C). However, only a portion of those materials could undergo the chosen tests, and only a portion of the tests will be used to characterize the material law.

To organize all available data information, each test will be described with respect to its **Intended data**, **Experimental challenges** and **Surviving data**. Lastly, an important concept is the effort to *accommodate* the specimen. During the first solicitations of the specimen, the stress response is substantially higher due to irreversible filler-chain connections still present in the material (see Chapter 2). Since the model does not account for this effect, previous *accommodation* tests are performed and only afterwards the intended measurement is made, where the material response is reproducible, since reversible mechanisms would compose most of the response.

A schematic representation of the contents of each tests are shown in Figure 5.1.

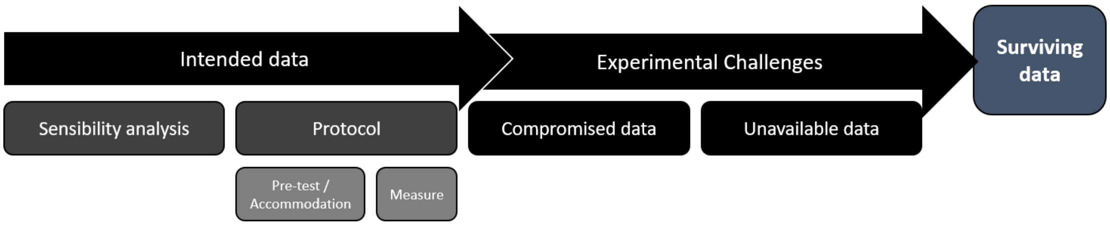

Figure 5.1: Schematic representation of topics discussed per experiment.

5.1.1 MMAexpert data

MMAexpert database is a model that partially considers experimental data post-treated with an internal industrial model. Different than previous experiments, only the post-treated outputs are available. In the next section, only the sensitivity analysis is presented.

Intended data

MMAexpert database contains the values of: the storage modulus, G^{MMA}_{Prime}, loss modulus, G^{MMA}_{Second}, and tangent delta, $\tan\left(\delta^{MMA}\right) = G^{MMA}_{Second}/G^{MMA}_{Prime}$, for a given deformation, ε_0, excitation frequency, $f_0 = \omega_0/(2\pi)$, and temperature, T_0. In particular, considering a simple shear solicitation whose shear component is γ_0 and the shear strain component is $\varepsilon_0 = \gamma_0/2$. The operational range of those inputs considering the three materials of interest are shown in Table 5.1.

Material	T_0 [°C]	ε_0 [−]	f_0 [Hz]
A6	-100 to 150	$3.15 \cdot 10^{-5}$ to 0.2	0.1 to 10^7
PCY4-RT	-100 to 130	$5 \cdot 10^{-6}$ to 1	0.1 to 10^7
PS4	-100 to 130	$5 \cdot 10^{-6}$ to 1	0.1 to 10^7

Table 5.1: Available values of dynamic parameters for a given range of temperature, deformation and frequency for chosen materials.

The temperature resolution is constant while the deformation and frequency resolution follow an exponential expression dependent on the data index, k and a constant C_Δ so that $\Delta\varepsilon = C_\Delta \exp(k)$, for example. Table 5.2 presents the characteristics concerning the data discretization (resolution and interval).

A6			
Input	T_0	ε_0	f_0
Index k	1 to 251	1 to 20	1 to 25
Δ	$1\ °C$	$2.32 \cdot 10^{-5} \cdot e^k$	$0.05 \cdot e^k$

PCY4-RT			
Input	T_0	ε_0	f_0
Index k	1 to 118	1 to 116	1 to 81
Δ	$2\ °C$	$10^{-6} \cdot e^k$	$0.02 \cdot e^k$

PS4			
Input	T_0	ε_0	f_0
Index k	1 to 118	1 to 116	1 to 81
Δ	$2\ °C$	$10^{-6} \cdot e^k$	$0.02 \cdot e^k$

Table 5.2: Discretization information for chosen materials.

To give a more intuitive visualization of the data, by fixing the temperature to a constant value, the dynamic parameters of a material can be presented as a surface plot, as in Figure 5.2. In the plot, it is possible to see the rise of G^{MMA}_{Prime} and G^{MMA}_{Second} for an increasing f_0, their respective decrease and sigmoidal evolution for an increasing ε_0, and their repercussions in $\tan\left(\delta^{MMA}\right)$.

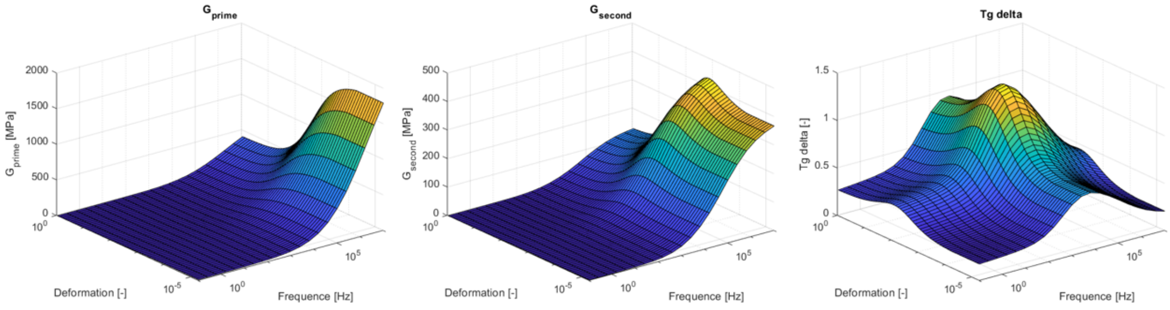

Figure 5.2: Visualization of dynamic parameters from PCY4-RT across available frequency and deformation for a given temperature, $T_0 = 15$ °C.

Lastly, the data is considered to be accommodated, so that the non-linearity would only be associated to reversible effects.

Experimental challenges

Some characteristics must be considered when using MMAexpert data:

- The proposed constitutive material model is not represented analytically by a formulation in the4 frequency domain with the dynamic parameters (G_{Prime}, G_{Second} and $\tan(\delta)$). Instead, the model is always identified with data in the time domain;
- The dynamic parameters from MMAexpert consists of corrective functions deformation-only dependent, $K(\varepsilon_0)$, multiplied to dynamic parameters, which were obtained with tests in small deformations and then extrapolated in frequency, so that

$$\begin{cases} G^{MMA}_{Prime}(\varepsilon_0, \omega_0) = K_{prime}(\varepsilon_0) G_{Prime}(\omega_0) \\ G^{MMA}_{Second}(\varepsilon_0, \omega_0) = K_{Second}(\varepsilon_0) G_{Second}(\omega_0) \\ \tan(\delta^{MMA})(\varepsilon_0, \omega_0) = K_{\tan(\delta)}(\varepsilon_0) \tan(\delta)(\omega_0) \end{cases} \tag{5.1.1}$$

  this notion becomes more apparent when slicing the three-dimensional surface plots in Figure 5.2 for multiple deformation values, resulting in a set of frequency dependent two-dimensional curves. We can recognize the multiplicative relationship by normalizing all curves, resulting in a single master curve, as in Figure 5.3.

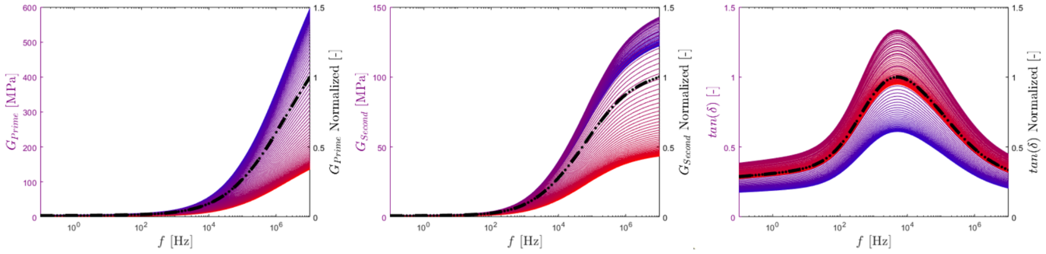

Figure 5.3: Set of dynamic parameters in frequency for single deformation (ε_0, f) (gradient red to blue) and their normalization (traced black).

- The MMAexpert data for the material A6 is, in fact, from an older formulation of the material (termed ”A5”), which contains slight differences in range (Table 5.1) and discretization (Table 5.2).

- In small deformations and large frequencies (up to 10^5 [Hz]), the dynamic parameters were validated indirectly via piezo-mechanical experiments. For lower frequencies (up to 300 [Hz]) the dynamic parameters were validated directly with temporal stress-strain response in time with compressive experiments.
- An elliptical stress-strain response require G^{MMA}_{Prime} and G^{MMA}_{Second} to be reconstructed. As the stress-strain response strays away from an elliptical behaviour, the dynamic parameters are not sufficient to uniquely represent the non-linear response.

Surviving data

To deal with the characteristics mentioned, the following actions are proposed:

- The dynamic parameters are converted into stress and strain time histories. If the response is linear, for a given G^{MMA}_{Prime} and G^{MMA}_{Second} in a certain frequency, ω_0, and deformation amplitude ε_0, the sinusoidal strain input and stress output can be recovered directly via

$$\varepsilon(t) = \varepsilon_0 \sin(\omega_0 t) \tag{5.1.2}$$

$$\begin{aligned} \sigma(t) &= \sigma_0 \sin(\omega_0 t + \delta) \\ &= \frac{\varepsilon_0}{\cos(\delta^{MMA})} G^{MMA}_{Prime}(\omega_0) \sin(\omega_0 t + \delta^{MMA}), \text{ or} \\ &= \frac{\varepsilon_0}{\sin(\delta^{MMA})} G^{MMA}_{Second}(\omega_0) \sin(\omega_0 t + \delta^{MMA}), \text{ or} \\ &= \varepsilon_0 G^{MMA}_{Prime}(\omega_0) \sin(\omega_0 t) + \varepsilon_0 G^{MMA}_{Second}(\omega_0) \cos(\omega_0 t) \end{aligned} \tag{5.1.3}$$

- The dynamic parameters considered must be known to have an elliptical time response beforehand. In previous DMA tests, it is observed that for deformations equal or smaller than 0.05, the stress-strain response approximates an elliptical path. Therefore, a single deformation range of 0.05 will be recovered from MMAexpert. For the frequency range, the interval $[0, 100]$ [Hz] is chosen;
- Since most of the tribological tests are operated in controlled temperatures of 7 °C and 15 °C, only those values shall be considered;
- Upon benchmark, it was informed that the mechanical properties differences between A5 and A6 are not substantial to rebuild another protocol and reconstruct its specific dynamic parameters.

To summarize, MMAexpert data will be considered in a single (and small) deformation amplitude covering three decades of frequency and two temperatures, as shown in Table 5.3. The dynamic parameters will be converted into four sets of sinusoidal strain and stress time history with frequencies $[0.1, 1, 10, 100]$ [Hz] as shown in Figure 5.4. Each cycles contains 1001 points and 10 cycle oscillations.

Material	T_0 [°C]	ε_0 [−]	f_0 [Hz]
A6	7 and 15	0.05	0.1 to 100
PCY4-RT	7 and 15	0.05	0.1 to 100
PS4	7 and 15	0.05	0.1 to 100

Table 5.3: Available values of dynamic parameters for a given range of temperature, deformation and frequency for chosen materials within acceptable range.

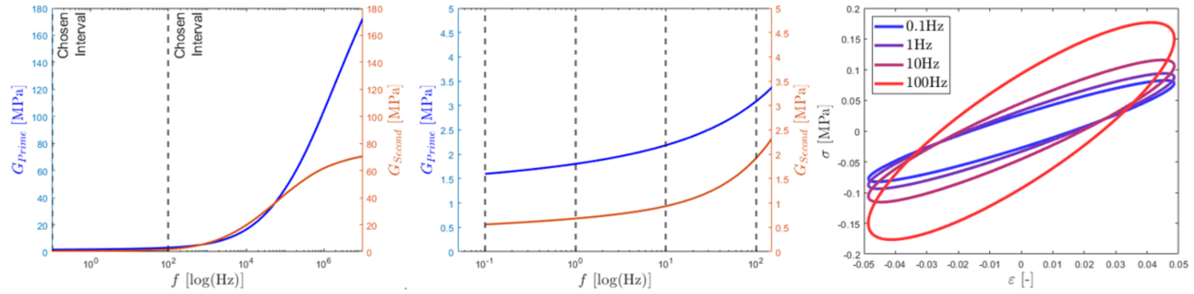

Figure 5.4: Stress-strain curves generated from pre-selected dynamic parameters. Exemplary MMAexpert data for PCY4-RT at 15 °C.

5.1.2 Uniaxial data

As mentioned in Section 5.1, the uniaxial experiment intended to evaluate three rubber mixes (A6, PCY4-RT and PS4). For each material, samples were fabricated with an internal flat dog-bone cutting die with similar (but not exact) dimensions as per ASTMD-638-IV. In this case, the effective length considered at Michelin is $l_{Eff} = 25$ [mm] and the rectangular area within this portion is $[2.5 \times 4]$ [mm] ($A_T = 10$ [mm^2]).

By uniaxial data, we refer to two types of experiments. Both categories undergo a particular stretch time history, given by

$$\lambda(t) = 1 + \frac{d_{Imp}(t)}{l_{Eff}} \tag{5.1.4}$$

differing only in their respective imposed displacements, $d_{Imp}(t)$, applied on a Universal traction/compression Machine. We shortly define each uniaxial test category, as:

- **Uniaxial Loading/Unloading**: Uniaxial tension loading at constant stretch rate $\dot{\lambda}_0$ up to a certain maximal set-point limit, λ_0, reached after a certain period T_1. Then, the specimen is compressed with a opposite stretch rate in the same magnitude until a period T_2 is reached, as in

$$\lambda(t) = \begin{cases} 1 + \dot{\lambda}_0 t & 0 \leq t \leq T_1 \\ 1 + \dot{\lambda}_0 t - \dot{\lambda}_0 (t - T_1) & T_1 < t \leq T_2 \end{cases} \tag{5.1.5}$$

  The evolution of the engineering stress, $F_{Exp}(t)/A_T$ (with $F_{Exp}(t)$ being the current reaction force response), is recorded at constant temperature;

- **Relaxation Test**: Loading in uniaxial tension with stretch held at $\lambda(t) = \lambda_0$. The specimen is deformed via a high stretch rate, $\dot{\lambda}_0$ (it should be done via an applied tension σ_0 at the beginning, but this functionality was not accessible), in a single-step and after a short period, the obtained stretch is fixed to λ_0, as in

$$\lambda(t) = \begin{cases} 1 + \dot{\lambda}_0 t & 0 \leq t \leq T_1 \\ \lambda_0 & T_1 < t \leq T_2 \end{cases} \tag{5.1.6}$$

The decrease in stress is recorded over prolonged period of exposure at constant temperature.

The stretch representation of a simple Loading/Unloading test and a single-step relaxation test are presented in Figure 5.5. These two elementary categories can become more elaborated as it will be shown in subsequent Section 5.1.2.

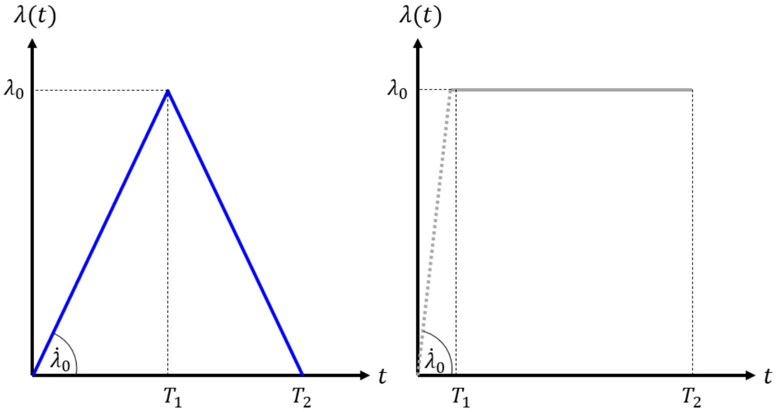

Figure 5.5: Stretch time history for simple uniaxial tests. Single Loading/Unloading cycle (left); Single-step relaxation (right).

Regardless of the class of uniaxial evaluation, similar principles were considered for both:

- Controlled temperature of 7 °C and 15 °C via a nitrogen-piloted chamber;
- Preconditioning (also kown as *accommodation*) of the samples were made by repeating the protocol twice per sample and considering only the second;
- Two (when possible three) samples per material, temperature and test category.

Intended data

A more complex form of the Loading/Unloading test was made using multiple triangular cycles with different stretch rates, $\dot{\lambda}_0$, and peak stretch magnitudes, λ_0, applied subsequently. For notation purposes, this protocol will be termed **CD** (*Chargement-Déchargement*). The coverage of those two quantities are presented in Table 5.4 and a global representation of each cycle is presented in Figure 5.6, where each point represents a single triangular cycle, as in Figure 5.5.

As mentioned in Section 5.1.2, a specific accommodation procedure was developed. This preconditioning was applied to a each sample before the CD protocol as per Figure 5.7, reaching higher solicitations to minimize the influence of irreversible processes.

Parameters	**Range**
$\dot{\lambda}_0\ [1/s]$	$[0.002; 0.01; 0.1; 0.5]$
$\lambda_0\ [-]$	$[1.18; 1.34; 1.63; 1.925; 2.21; 2.51]$

Table 5.4: Range of stretch magnitude and rate for loading/unloading test - CD protocol.

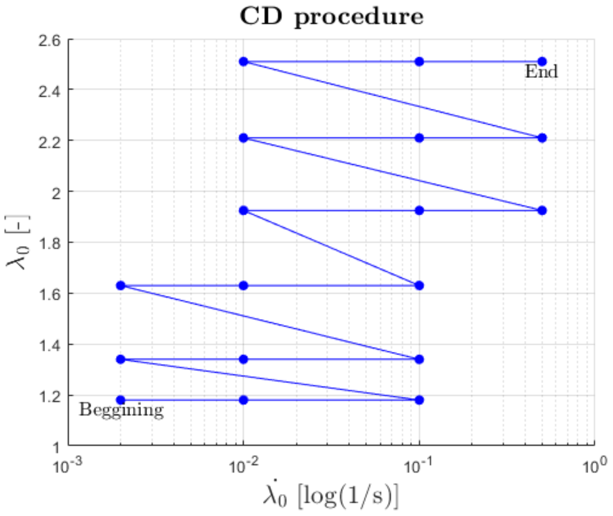

Figure 5.6: CD protocol (blue circle). Each filled circle represents an individual triangular cycle defined by a maximum stretch magnitude and constant stretch rate.

In essence, this step performs a stretch rate sweep and then this interval is re-applied for a higher stretch magnitude. For a better visualization, the imposed stretch time history and the recovered stress time history is shown in Figure 5.7 for one PCY4-RT sample deformed at 15 °C. In order to avoid buckling of the sample during the descent of the stretch, the machine setting begins the next triangular cycle when the stress goes to zero, which reflects on the history observed and minimizes out-of-plane errors.

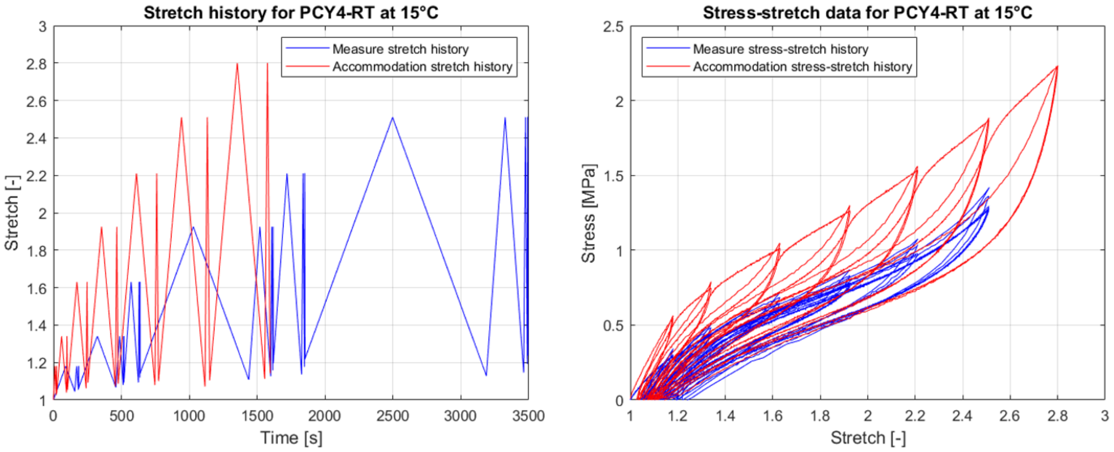

Figure 5.7: Measure (blue line) of stretch (left plot) and stress time history (right plot).

From a general perspective, the stress evolution in Figure 5.7 highlights the non-linearity of the material, presenting a softening effect for deformations up to 60%, and beyond this point a "stiffening" can be observed.

In addition to the CD procedure, a more complex form of the relaxation test (for reference, see right plot from Figure 5.5) was also proposed using subsequent steps with cumulative stretch magnitudes. For notation purposes, this protocol will be termed **MSR** (*Multi-Step Relaxation*). In this protocol, each new stretch magnitude, λ_0, is reached through a very high stretch rate $\dot{\lambda}_0$ and then kept fixed during 300 [s]. Table 5.5 presents the range of which this second protocol takes place.

Parameters	**Range**
$\dot{\lambda}_0$ $[1/s]$	$[0.7]$
λ_0 $[-]$	$[1.05; 1.34; 1.63; 1.925; 2.21]$

Table 5.5: Range of stretch magnitude and rate for multi-step relaxation procedure - MSR protocol.

A global representation of each cycle is presented in Figure 5.8, where each point represents a single step evolution, while the stress and stretch time histories are displayed in Figure 5.9.

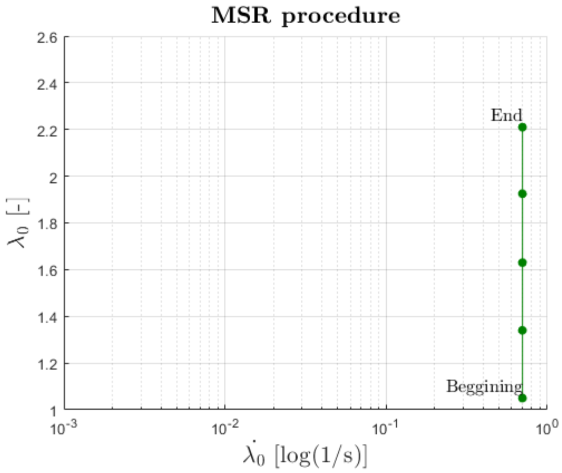

Figure 5.8: MSR protocol (green circle). Each circle represents an individual step defined by a maximum stretch magnitude and constant stretch rate.

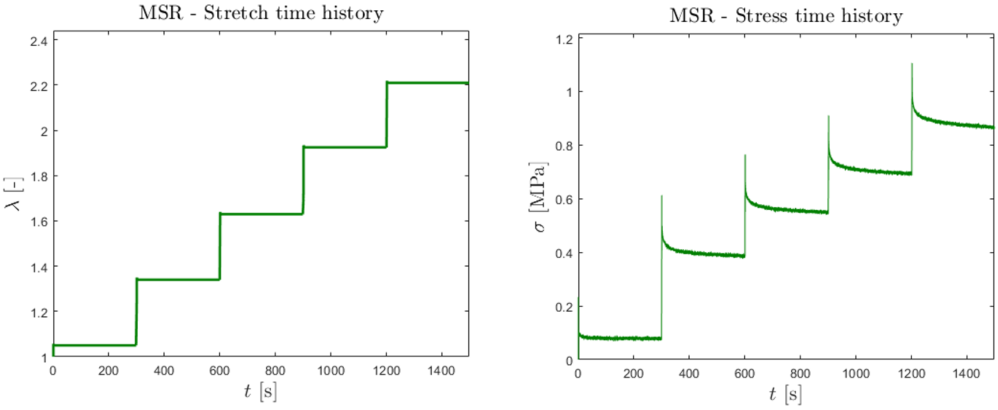

Figure 5.9: Measure (green line) of stretch (left plot) and stress time history (right plot).

The results from the MSR procedures presents two potentially important non-linearities of the material's relaxation time, τ: (i) a sensitivity with respect to strain rate; (ii) a sensitivity with respect to strain magnitude. To highlight this point, we consider the initial two steps of data individually displayed in Figure 5.10. In addition, we consider the significant range of the data accounting for measurement noise.

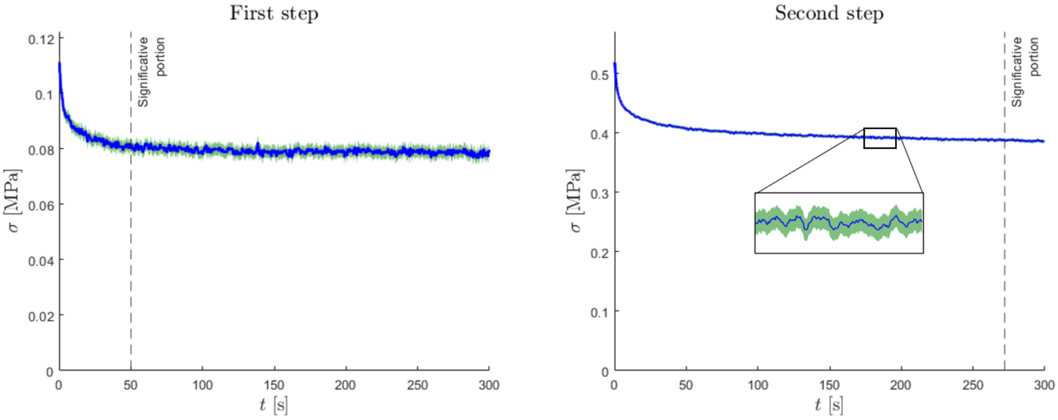

Figure 5.10: Smoothed stress (blue line) relaxation history and its dispersion (green area) via windowed averaging and standard deviation - First and Second MSR steps.

If we assume no such non-linearity in the relaxation time associated to the steps in Figure 5.10, the two stress responses could be justified via an exponential decay. If true, from linear viscoelasticity considerations, one could model a constant relaxation time, τ, derived via the experiment as

$$\log\left[\sigma(t) - \sigma_{Eq}\right] = -\frac{t}{\tau} + D \quad ; \quad \tau = -\frac{d}{dt}\log\left[\sigma(t) - \sigma_{Eq}\right], \tag{5.1.7}$$

where $\sigma(t)$ is the stress history and σ_{Eq} is and average of the the latest stress values of the step, being the closest to an equilibrium/elastic response and D is a constant. Individually running equation (5.1.7) for the first two MSR steps results in the evolution shown in Figure 5.11.

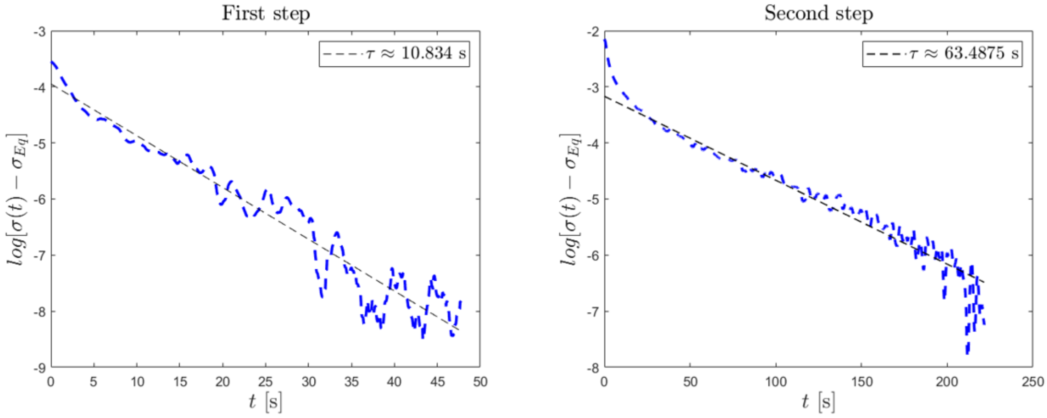

Figure 5.11: Evolution of experimental data by means of equation (5.1.7) - First and Second MSR steps.

The oscillations in Figure 5.11 at the end portions occurs due to noise and as $\sigma(t)$

approaches σ_{Eq}, leading to an magnified instability when computing the logarithm of their difference. Nonetheless, for the first step, a reasonable slope with its correspondent relaxation time, $\tau_{1st} = 10.8340$ [s], could be determined. This is coherent since the strain is considerably small, ($\lambda_0 = 1.05$, see Figure 5.8), being the most likely scenario to concur with linear viscoelastic considerations. For the second step in Figure 5.11, the function evolves non-linearly. Initially, the slope is very high (τ is small) then progressively decreases (τ increases) until its slope stabilizes to a relaxation time of approximately $\tau_{2nd} = 63.4875$ [s].

From this evaluation, we argue that non-linear viscoelastic considerations can be inferred from the first step at small strains and the second step at large strains, we observe: (i) a sensitivity in strain rate (mostly for the second step), since a non-linear evolution is verified during the initial portion of the test, which addresses most of the viscoelastic response for high velocity excitations; (ii) a sensitivity in strain magnitude verified by a clear difference in the relaxation times between the first and second step, even when the slope stabilizes for the later.

Lastly, as described by equation (5.1.4), the stretch time history, $\lambda(t)$, is derived from the displacement of the machine. This hypothesis assumes a direct correlation between sample strain and machine movement. To verify this hypothesis, a portion of the samples had their stretch recovered via optical measurements.

Experimental challenges

Some intrinsic limitations were identified during the experiments:

- Due to machine restrictions, not all samples, temperature and materials could be evaluated for the following reasons:
  - As it can be seen in Figure 5.7 and 5.9, a single sample takes around 35 minutes to be finished for CD test and close ot 27 minutes for MSR test. Due to their long duration, an adaptive campaign of test was made in order to ensure a compromise between variety in operational conditions (different procedure, material and temperature) and repetition. Table 5.6 presents the number of repetitions per temperature, material and experimental protocol.
  - The machine should not be left without an operator present;
  - A potential leakage of the nitrogen required a full stop of the machine for 3-4 hours;
  - The installation of the camera (and its equipment) by the end of the booked week to use the machine required in parallel 1-2 hours for it set-up.

15 °C	**A6**	**PCY4-RT**	**PS4**
CD	4	4	4
MSR	3	3	3
7 °C	**A6**	**PCY4-RT**	**PS4**
CD	3	3	3
MSR	2	2	2

Table 5.6: Sample repetition per operating point - temperature, protocol and material.

- From the left plot in Figure 5.7, the stretch does not return to $\lambda(t) = 1$. There are two reasons for it to be so:

  - During the ascend in stretch, the PID of the machine is displacement-controlled and it stops when a preset stretch value is reached.
  - During the descend in stretch, the PID of the machine is also displacement-controlled, however the cycle stops when the stress response becomes zero, and then for the next loading/unloading cycle the same logic is considered. This prevents the sample to buckle, where uniaxial strain assumption is no longer valid.

As a consequence, apart from the first loading/unloading, all subsequent cycles wont start at $\lambda_i = 1$, but they will all begin at $\sigma_i = 0$ [MPa], as in Figure 5.12.

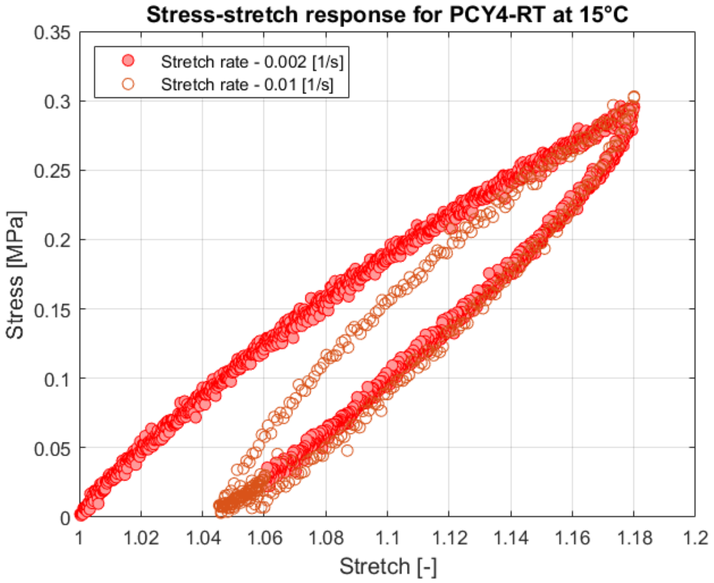

Figure 5.12: Accommodated stress-stretch response for two subsequent cycles of CD protocol.

This is a consequence of having all cycles connected in the same procedure. Splitting the tests would require a resting time not only per sample but per cycle.

- Figure 5.12 also shows that, since the cycles are connected, a same time sample was considered, which affects the resolution of high stretch rate and low stretch magnitude cycles.

- The generated MMAexpert experimental data used for calibration in small strains is available for all three materials of interest. However, since the solicited material in uniaxial and MMAexpert did not originated from the same batch, there could be a dispersion in their response, similar or more to the dispersion we would find per sample/specimen;

- As schematically displayed in Figure 5.13, the complementary optical measurement made with the camera to capture stretch history, revealed a non negligible difference between the output resulting directly from the machine.

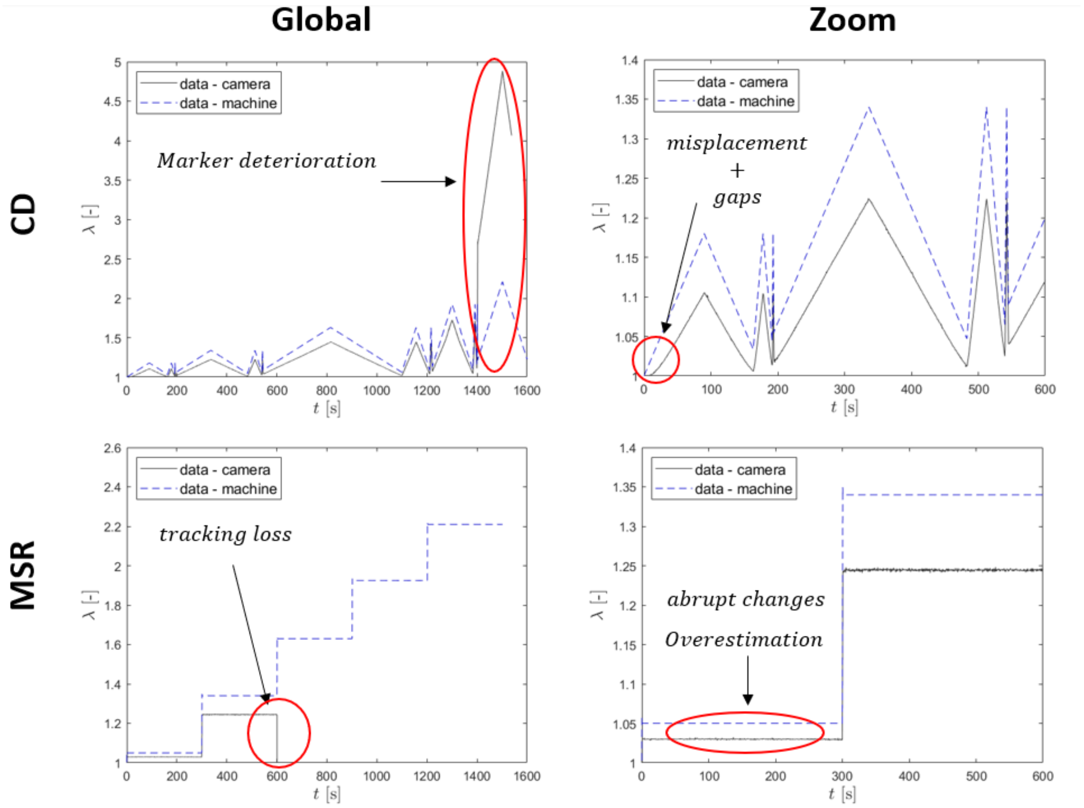

Figure 5.13: Stretch time history of Case 4 (upper plots) and Case 6 (under plots) - global data (left) initial portion of data (right) - representation of measurement challenges.

The disparity in stretch output between machine and camera have different causes. Even if it was possible to prepare the camera to do the measurement, the data recovery was still susceptible to two main technical challenges:

- The camera captured the image of the sample markers *behind* a two-layer glass window of the temperature chamber. This setup not only requires enough lighting but also precise illumination position to minimize reflection. In addition, in between the glass layers there was some dirt spots which could not be removed, so the focus needed to be properly set to balance a reasonable focused marker and the dirt spots reasonably blurred;
- The available camera had a limited resolution of 2.48 frames-per-second, which albeit our (and the usual operator) attempts, could not be increased;
- The method of image correlation requires two large circular spots marked within the effective length to which their centroid is found. However, as the deformation increases, non-inked grooves zones appears in the marked zone which degenerates the tracking capability of the software.

As a consequence:

- For very large displacements the tracked position of the markers can be lost and misplaced in a dirt spot;
- For very fast displacements the tracked position of the markers can also be lost and misplaced in a dirt spot.

These difficulties were identified before the official test, in preliminary control cases. In those procedures, it was found that a proper positioning of the light and the size of the spots marked on the sample reduce the risk of tracking loss, but cannot completely eradicate their occurrences. As a countermeasure, two trackers were set for a each marker, if it all trackers were lost mid-test, a new camera measurement was applied in the ongoing procedure. The trackers are re-calibrated, which sets the strain value to zero, but allow to recover a bit more information in a single test. For the reasons mentioned above, a portion of repetitions from table 5.6 were evaluated in a case-by-case basis, where each scenario will be post-treated individually in the following subsections.

Concerning the data recovered from the displacement of the machine clamps, the following challenges were identified:

- Any portion of the dog-bone sample that is not clamped and is also outside the effective length can result in an overestimated strain;
- Any misplacement of the sample, however small, during positioning in the machine can leave gaps. This degree of liberty can create micro-slidings until the sample is in a more stable position.

Surviving data

To deal with the characteristics mentioned, the following actions are proposed:

- Despite the occasional machine regulations, a reasonable number of sample repetitions were recovered for the 3 materials of interest, 2 protocols and one temperature. The data at 15 °C shall be used as the central point of evaluation, using 7 °C as a relative comparison;
- Concerning PID restriction during the descent of CD test (stretch does not return to 1), we shall consider/use the experimental test from the start (temporal beginning) expanding to later portions if the calibration allows it;
- To manage the incompatibility between machine and camera stretch data, an additional investigation was made to be presented in detail during the rest of the present section using a portion of the total samples, listed on Table 5.7.

Case	**Material**	**Protocol**	**Temperature**
1	A6	CD	7 °C
2	A6	CD	15 °C
3	A6	MSR	15 °C
4	PCY4-RT	CD	7 °C
5	PCY4-RT	CD	15 °C
6	PCY4-RT	MSR	15 °C
7	PS4	CD	7 °C
8	PS4	CD	15 °C
9	PS4	MSR	15 °C

Table 5.7: Measurements which considered optical measurement of strain.

In order to better understand the differences between camera/machine outcomes, we identify the central pros and cons of each measurement. For the machine data, its absolute stretch value quality is affected by sample positioning and clamping, nevertheless its data is available for all samples, including those beyond the 9 available cases with the camera. On the other hand, the two marked spots provide proper information of the absolute stretch value within the effective length, however the quality of the image correlation tracking is susceptible to be affected and/or completely lost.

To still benefit from the machine stretch history, $\lambda_{mac}(t)$, and the validity of the camera stretch measure, $\lambda_{cam}(t)$, a linear transfer function is proposed, written as

$$\lambda_{corr}(t) = 1 + k_{corr}\left[\lambda_{mac}(t) + g_{corr} - 1\right] = 1 + k_{corr}\left[\lambda_{mac,shift}(t) - 1\right], \tag{5.1.8}$$

where g_{corr} is a vertical shift that superposes the machine stretch with the stretch from image correlation during its first loading, when the evolution is no longer non-linear (the slope becomes constant), as shown in Figure 5.13 within the red circle on from the upper-right plot. This first correction assumes that the non-linearity is a micro-sliding caused by gaps during the initial portion of the test, but since this occurs when the procedure presents a small stretch rate and magnitude, the camera stretch value is still valid.

The second portion of the correction uses k_{corr}, obtained in an optimization problem (trust-region method, Matlab 2019b) with the stretch measured from the camera, $\lambda_{cam}(t)$, which minimizes

$$\mathcal{R}(k_{corr}) = \sum_{i \in \Omega_{cycle}} \frac{\left[\lambda_{corr} - \lambda_{cam}(t_i)\right]^2}{\left[\lambda_{cam}^{max}\right]^2 \left|\Omega_{cycle}\right|} \tag{5.1.9}$$

where $\lambda_{cam}^{max} = \max\left[\lambda_{cam}^{max}(t_i)\right]$, and $|\Omega_{cycle}|$ is the length of the dataset in question. This correction assumes the two clamps are separated by a distance bigger than the effective length, l_0, of the two marker spots. Therefore, since

$$\lambda_{mac,shift}(t) = 1 + \frac{d_{mac}(t)}{l_0}, \tag{5.1.10}$$

where $d_{mac}(t)$ is the history of displacement from the machine, we see that, by inserting (5.1.10) in (5.1.8), that k_{corr} is indeed a correction of the effective length with

$$\lambda_{corr}(t) = 1 + \frac{d_{mac}(t)}{\left(\frac{1}{k_{corr}}\right) l_0}. \tag{5.1.11}$$

This second correction also assumes that the contribution of any heterogeneous deformations from this larger effective length (beyond the two markers) is sufficiently small for its adjustment to be linear. Lastly, we consider that the sample size and the imposed stretch rates are sufficiently small to ignore dynamic and thermal effects.

All listed considerations attempt to rectify operational and machinery systematic errors. If the hypothesis are adequate and sufficient, one should expect not only to find a similar k_{corr} and g_{corr} across different materials and temperatures, but also a good superposition between $\lambda_{corr}(t)$ and $\lambda_{cam}(t)$.

The data collection of k_{corr} and g_{corr} considers a portion of the cases from Table 5.7 they being the procedures CD, with the exception of case 5, up to deformations of 100%. The rejection of the data from MSR procedures is due to a compromised quality of λ_{cam}, which contains, albeit expected, many discontinuities, as showcased in Figure 5.13. Moreover, the step increase from the protocol is too fast to properly identify a g_{corr}. The dismissal of case 5 is due to an exclusive assembly problem outside the expected systematic error, where the clamps presented a particular out-of-plane positioning. Thus, both camera and machine data of this particular sample repetition are discarded from future evaluations.

Although only a portion of the cases are considered, they: (i) contain a large (around 70% of the complete data) measured portion with preserved $\lambda_{mac}(t)$ and $\lambda_{cam}(t)$; (ii) operate under small strain rates and small/moderate strain magnitudes so to preserve the quality of λ_{cam}; (iii) present a diversity of 3 sample materials (A6, PCY4-RT and PS4) under two operating temperatures ($7°C$ and $15°C$), which consists of 5 manual sample placements and their operational dispersion. As an example from Table 5.7, the history of λ_{cam}, $\lambda_{mac,shift}$ and λ_{corr} for case 4 is presented in Figures,5.14 and the k_{corr} corrections values of each of the selected 5 cases are available in Table 5.8.

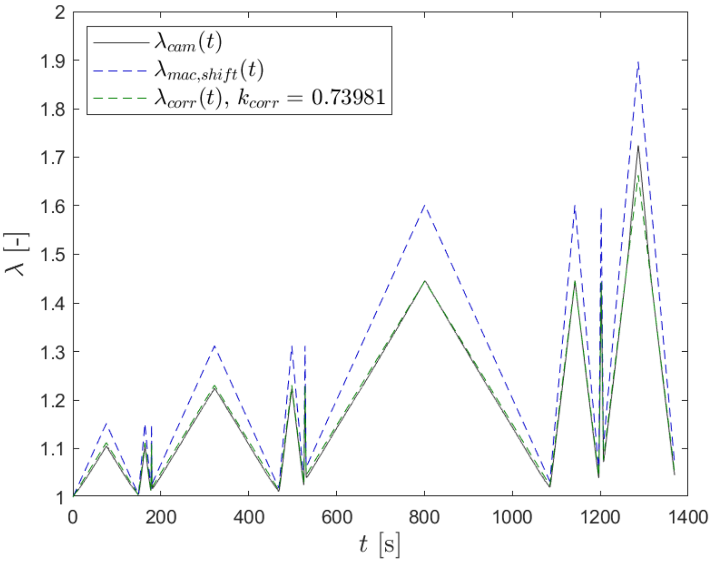

Figure 5.14: Stretch time history of $\lambda_{cam}(t)$, $\lambda_{mac,shift}(t)$ and $\lambda_{corr}(t)$ - Case 4.

Case	**Material**	**Protocol**	**Temperature**	g_{corr}	k_{corr}	$\mathcal{R}(k_{corr})$
1	A6	CD	7 °C	-0.0215	0.7477	$5.9038 \cdot 10^{-5}$
2	A6	CD	15 °C	-0.0120	0.9009	$7.7054 \cdot 10^{-5}$
4	PCY4-RT	CD	7 °C	-0.0284	0.7398	$5.4855 \cdot 10^{-5}$
7	PS4	CD	7 °C	-0.0275	0.7867	$7.2164 \cdot 10^{-5}$
8	PS4	CD	15 °C	-0.0251	0.7948	$3.1998 \cdot 10^{-5}$

Table 5.8: Correction term, correction factor and residual - Selected cases.

The correction resulted in a reasonable superposition with the linearly corrected data. In addition, all correction factors presented values lower than 1, which is coherent, since only a portion of the total strain is felt by the sample at its center, and an over-deformation occurs when close to the holdings (machine data) as confirmed by the camera data. The average residual before optimization (thus when $k_{corr} = 1$) is $\tilde{\mathcal{R}}_{before} = 2.51 \cdot 10^{-3}$ while the average residual after optimization is $\tilde{\mathcal{R}}_{after} = 5.46 \cdot 10^{-5}$, representing 1% of the original residual.

We can recover a representative correction factor and correction term with their associated deviations resulted from the most reliable part of the experiments. The means, $\tilde{k}_{corr}$ and $\tilde{g}_{corr}$, and their standard deviations, σ_k and σ_g, are

$$\tilde{k}_{corr} = 0.794 \quad ; \quad \sigma_k = 0.0644 \quad ; \quad \tilde{g}_{corr} = -0.0229 \quad ; \quad \sigma_g = 0.0067. \tag{5.1.12}$$

The highest k_{corr} in case 2 is accompanied by the smallest g_{corr}, indicating similar effective lengths between the clamping distance and the marker's distance during sample mounting, resulting in a more reactive and correlated response. Albeit it contains different value from the rest, it is coherent with the assumptions considered and it falls within operator precision, thus its computation is kept.

5.2 About the model

5.2.1 Original formulation

Tensorial representation

The law is described in tensorial form via the stress equation

$$\mathbf{P} = \left[\sum_{r=1}^{2} \mu_r \left(\frac{I_1}{3}\right)^{\alpha_r - 1}\right] \mathbf{F} + \left[\sum_{r=1}^{2} m_r \left(\frac{I_1^e}{3}\right)^{a_r - 1}\right] \mathbf{F}\mathbf{D}^v + \left[\Lambda J(J-1) - \sum_{r=1}^{2} (\mu_r + m_r)\right] \mathbf{F}^{-T} \tag{5.2.1}$$

and an evolution equation

$$\dot{\mathbf{D}}^v = \frac{\sum_{r=1}^{2} m_r \left(\frac{I_1^e}{3}\right)^{a_r - 1}}{\eta_k(I_1^e, I_2^e, I_1^v)} \left[\frac{I_1^e}{3}\mathbf{D}^v - \mathbf{D}^v\mathbf{C}\mathbf{D}^v\right] \tag{5.2.2}$$

where

$$\eta_k(I_1^e, I_2^e, I_1^v) = \eta_\infty + \frac{\eta_0 - \eta_\infty + k_1[I_1^{v\beta_1} - 3^{\beta_1}]}{1 + (k_2 J_2^{NEq})^{\beta_2}} \tag{5.2.3}$$

where $\mathbf{D}^v$ is the internal variable and $\mathbf{F}$ is the gradient deformation tensor, which composes the right Cauchy-Green deformation tensor $\mathbf{C} = \mathbf{F}^T\mathbf{F}$. The invariants presents are $I_1 = tr(\mathbf{C})$, $I_1^e = tr(\mathbf{C}\mathbf{D}^v)$, $I_1^v = tr(\mathbf{D}^{v-1})$, $I_2^e = \frac{1}{2}\left\{[tr(\mathbf{C}\mathbf{D}^v)]^2 - tr(\mathbf{C}\mathbf{D}^v\mathbf{C}\mathbf{D}^v)\right\}$ and $J = det(\mathbf{F})$. In these expressions, μ_r, α_r, m_r and a_r (for $r = 1, 2$) are real-valued material parameters associated with the non-Gaussian statistical distribution of the underlying polymer chains. On the other hand, $\eta_0 \geq \eta_\infty$, $\beta_r \geq 0$, $K_r \geq 0$ (for $r = 1, 2$) are real-valued material parameters associated with reptation dynamics. The constitutive law is composed of 14 material parameters. J_2^{NEq} is the non-equilibrium stress-based second invariant, where for incompressible materials is written as

$$J_2^{Neq} = \frac{1}{2}\boldsymbol{\sigma}_{Dev}^{NEq} : \boldsymbol{\sigma}_{Dev}^{NEq} = \left(\frac{I_1^{e2}}{3} - I_2^e\right)\left[\sum_{r=1}^{2} m_r \left(\frac{I_1^e}{3}\right)^{a_r - 1}\right]^2 \tag{5.2.4}$$

where the Cauchy stress tensor $\boldsymbol{\sigma}_{Dev}^{NEq}$ is the deviatoric part of the non-equilibrium part of the stress, relating to the second term from (5.2.1) via (3.1.22). By taking the Frobenius norm of $\boldsymbol{\sigma}_{Dev}^{NEq}$, given by $\|(\cdot)\| = \sqrt{(\cdot) : (\cdot)}$, and manipulating equation (5.2.2), we obtain

$$\|\boldsymbol{\sigma}_{Dev}^{NEq}\| = \eta_k \|\dot{\mathbf{D}}^v \mathbf{D}^{v-1}\| \tag{5.2.5}$$

where we verify the role of $J_2^{NEq} = \|\boldsymbol{\sigma}_{Dev}^{NEq}\|^2/2$ in η_k to make the viscosity a non-linear function of the non-equilibrium state rate.

Scalar representation - Simple shear

If simple shear tests are used for identification of the coefficients of the constitutive law, the model may be rewritten in scalar form. The gradient deformation tensor for simple shear is given by

$$[\mathbf{F}] = \begin{bmatrix} 1 & \gamma & 0 \\ 0 & 1 & 0 \\ 0 & 0 & 1 \end{bmatrix} \tag{5.2.6}$$

In the previous tensorial formulation, $\mathbf{D}^v$ is in fact a clever composition of a more intrinsic internal variable, $\mathbf{F}^v$, whose field is assumed to follow the same functional form of the gradient deformation tensor, therefore

$$[\mathbf{F}^v] = \begin{bmatrix} 1 & \gamma_v & 0 \\ 0 & 1 & 0 \\ 0 & 0 & 1 \end{bmatrix} \quad \text{therefore} \quad [\mathbf{D}^v] = \left[\left(\mathbf{F}^{vT} \mathbf{F}^v \right)^{-1} \right] = \begin{bmatrix} 1+\gamma_v^2 & -\gamma_v & 0 \\ -\gamma_v & 1 & 0 \\ 0 & 0 & 1 \end{bmatrix}. \tag{5.2.7}$$

Since the interest is the shear component (first line, second column), the stress and evolution equation can now be expressed solely in the component interest regarding a simple shear deformation. The expression are as follows

$$P_\gamma = \left[\sum_{r=1}^{2} \mu_r \left(\frac{3+\gamma^2}{3} \right)^{\alpha_r - 1} \right] \gamma + \left\{ \sum_{r=1}^{2} m_r \left[\frac{3+(\gamma-\gamma_v)^2}{3} \right]^{a_r-1} \right\} (\gamma - \gamma_v) \tag{5.2.8}$$

for the stress component, and

$$\dot{\gamma}_v = \frac{\left\{ \sum_{r=1}^{2} m_r \left[\frac{3+(\gamma-\gamma_v)^2}{3} \right]^{a_r-1} \right\}}{\eta_k(\gamma,\gamma_v)} \left\{ \gamma - \left[\frac{3+(\gamma-\gamma_v)^2}{3} \right] \gamma_v \right\} \tag{5.2.9}$$

for the evolution equation, with

$$\eta_k(\gamma,\gamma_v) = \eta_\infty + \frac{\eta_0 - \eta_\infty + k_1[(3+\gamma_v^2)^{\beta_1} - 3^{\beta_1}]}{1+(k_2 J_2^{NEq})^{\beta_2}} = \frac{\eta_\infty (k_2 J_2^{NEq})^{\beta_2}}{1+(k_2 J_2^{NEq})^{\beta_2}} + \frac{\eta_0 + k_1[(3+\gamma_v^2)^{\beta_1} - 3^{\beta_1}]}{1+(k_2 J_2^{NEq})^{\beta_2}} \tag{5.2.10}$$

with J_2^{Neq} being the second invariant of the non-equilibrium stress tensor, given as

$$J_2^{NEq} = (\gamma-\gamma_v)^2 \left[\frac{3+(\gamma-\gamma_v)^2}{3} + \frac{(\gamma\gamma_v)^2}{2} \right] \left\{ \sum_{r=1}^{2} m_r \left[\frac{3+(\gamma-\gamma_v)^2}{3} \right]^{a_r-1} \right\}^2 \tag{5.2.11}$$

In the case of small deformations, where $|\gamma - \gamma_v| \ll 1$, we observe that indeed $\sqrt{J_2^{NEq}}/\eta_k \approx \dot{\gamma}_v$, thus respecting the proportionality from (5.2.5).

Scalar representation - Uniaxial

If uniaxial tests are used for identification of the coefficients of the constitutive law, the model may be rewritten in scalar form. Beforehand, the consideration or not of incompressibility did not affect the result, here it will be assumed that the model is *incompressible*. Therefore the Tensorial form of (5.2.1) becomes

$$\mathbf{P} = \left[\sum_{r=1}^{2} \mu_r \left(\frac{I_1}{3}\right)^{\alpha_r - 1}\right]\mathbf{F} + \left[\sum_{r=1}^{2} m_r \left(\frac{I_1^e}{3}\right)^{a_r - 1}\right]\mathbf{F}\mathbf{D}^v - p\mathbf{F}^{-T} \tag{5.2.12}$$

where p is called the Lagrange multiplier. The gradient deformation tensor for uniaxial case is given by

$$[\mathbf{F}] = \begin{bmatrix} \lambda & 0 & 0 \\ 0 & \lambda^{-1/2} & 0 \\ 0 & 0 & \lambda^{-1/2} \end{bmatrix} \tag{5.2.13}$$

In the previous tensorial formulation, $\mathbf{D}^v$ is in fact a composition of a more intrinsic internal variable, $\mathbf{F}^v$, whose field is assumed to follow the same functional form of the gradient deformation tensor, therefore

$$[\mathbf{F}^v] = \begin{bmatrix} \lambda_v & 0 & 0 \\ 0 & \lambda_v^{-1/2} & 0 \\ 0 & 0 & \lambda_v^{-1/2} \end{bmatrix} \quad \text{therefore} \quad [\mathbf{D}^v] = \left[\left(\mathbf{F}^{vT}\mathbf{F}^v\right)^{-1}\right] = \begin{bmatrix} \frac{1}{\lambda_v^2} & 0 & 0 \\ 0 & \lambda_v & 0 \\ 0 & 0 & \lambda_v \end{bmatrix}. \tag{5.2.14}$$

Since the interest is the axial stress component (first line, first column). From the boundary conditions and symmetric considerations, the tensorial stress must have the form

$$\mathbf{P} = P_{11}\mathbf{e}_1 \otimes \mathbf{e}_1 + P_{22}\mathbf{e}_2 \otimes \mathbf{e}_2 + P_{33}\mathbf{e}_3 \otimes \mathbf{e}_3 \tag{5.2.15}$$

The stress and evolution equation can now be expressed solely in the component interest regarding a simple shear deformation. However, the Lagrange multiplier can be obtained from the boundary conditions, where $P_{22} = P_{33} = 0$, therefore $\mathbf{P} = P_\lambda \mathbf{e}_1 \otimes \mathbf{e}_1$. The pivotal expressions are as follows

$$P_\lambda = \left[\sum_{r=1}^{2} \mu_r \left(\frac{2+\lambda^3}{3\lambda}\right)^{\alpha_r - 1}\right]\left(\frac{\lambda^3 - 1}{\lambda^2}\right) + \left[\sum_{r=1}^{2} m_r \left(\frac{2\lambda_v^3 + \lambda^3}{3\lambda\lambda_v^2}\right)^{a_r - 1}\right]\left(\frac{\lambda^3 - \lambda_v^3}{\lambda^2\lambda_v^2}\right) \tag{5.2.16}$$

for the stress component, and

$$\dot{\lambda}_v = \frac{\left[\sum_{r=1}^{2} m_r \left(\frac{2\lambda_v^3 + \lambda^3}{3\lambda\lambda_v^2}\right)^{a_r - 1}\right]}{\eta_k(\lambda, \lambda_v)} \left[\frac{\lambda^3 - \lambda_v^3}{3\lambda\lambda_v}\right] \tag{5.2.17}$$

for the evolution equation, with

$$\eta_k(\gamma, \gamma_v) = \eta_\infty + \frac{\eta_0 - \eta_\infty + k_1\left[\left(\frac{2+\lambda_v^3}{\lambda_v}\right)^{\beta_1} - 3^{\beta_1}\right]}{1 + (k_2 J_2^{NEq})^{\beta_2}} = \frac{\eta_\infty (k_2 J_2^{NEq})^{\beta_2}}{1 + (k_2 J_2^{NEq})^{\beta_2}} + \frac{\eta_0 + k_1\left[\left(\frac{2+\lambda_v^3}{\lambda_v}\right)^{\beta_1} - 3^{\beta_1}\right]}{1 + (k_2 J_2^{NEq})^{\beta_2}} \tag{5.2.18}$$

with J_2^{Neq} being the second invariant of the non-equilibrium stress tensor, given as

$$J_2^{NEq} = \frac{1}{3}\left[\frac{\lambda^3 - \lambda_v^3}{\lambda\lambda_v^2}\right]^2 \left[\sum_{r=1}^{2} m_r \left(\frac{2\lambda_v^3 + \lambda^3}{3\lambda\lambda_v^2}\right)^{a_r - 1}\right]^2 \tag{5.2.19}$$

Once again, in the case of small deformations, where $|\lambda_v - 1| \ll 1$, we observe that indeed $\sqrt{J_2^{NEq}}/(\sqrt{3}\eta_k) \approx \dot{\lambda}_v$, also respecting the proportionality from (5.2.5).

5.2.2 Modified formulation

Reduction of terms

Let us consider the stress-strain and evolution equations presented in (5.2.1) and (5.2.2) at section 5.2.1. The second term in the equilibrium and non-equilibrium stress contributions (when $r = 2$) describes the “stiffening” behaviour in stress after its initial softening as it was shown in Figure 5.7 after the stretch surpasses a value of around 2.2. This aspect is usually present in *non-Gaussian* hyperelastic models like Yeoh and Gent and the present model from Kumar and Pamies.

It is known, from our simulations, that even in extreme deformations like the curling effect at a sliding lamelized sample, if the effective geometric strain (a strain-based invariant) is collected, the uniaxial stretch required to match it is around 1.3 to 1.6, which is far bellow the “stiffening” evolution portion of the data. This indicates that a non-Gaussian mechanism is not required. To simplify our problem, we shall simply remove one term of the equilibrium and non-equilibrium so that the stress-strain relation is now

$$\mathbf{P} = \left[\mu_{Eq}\left(\frac{I_1}{3}\right)^{\alpha_{Eq}-1}\right]\mathbf{F} + \left[m_{NEq}\left(\frac{I_1^e}{3}\right)^{a_{NEq}-1}\right]\mathbf{F}\mathbf{D}^v - p\mathbf{F}^{-T} \tag{5.2.20}$$

also treated as incompressible (during calibration only) and the evolution equation is

$$\dot{\mathbf{D}}^v = \frac{m_{NEq}\left(\frac{I_1^e}{3}\right)^{a_{NEq}-1}}{\eta_k(I_1^e, I_2^e, I_1^v)}\left[\frac{I_1^e}{3}\mathbf{D}^v - \mathbf{D}^v\mathbf{C}\mathbf{D}^v\right]. \tag{5.2.21}$$

Notice that those relations do not affect the viscosity equation (5.2.3), but it will simplify the stress-based invariant form equation (5.2.4) reducing to

$$J_2^{NEq} = \left(\frac{I_1^{e2}}{3} - I_2^e\right)\left[m_{NEq}\left(\frac{I_1^e}{3}\right)^{a_{NEq}-1}\right]^2. \tag{5.2.22}$$

All the previous modifications, can be considered analogously into the shear and uniaxial component formulations without loss of generality.

Alternative viscosity

Consider once more the original viscosity function, η_k, proposed by Kumar and Pamies

$$\eta_k(I_1^e, I_2^e, I_1^v) = \eta_\infty + \frac{\eta_0 - \eta_\infty + k_1[I_1^{v\beta_1} - 3^{\beta_1}]}{1 + (k_2 J_2^{NEq})^{\beta_2}} = \frac{\eta_0 + k_1[I_1^{v\beta_1} - 3^{\beta_1}] + \eta_\infty(k_2 J_2^{NEq})^{\beta_2}}{1 + (k_2 J_2^{NEq})^{\beta_2}}. \tag{5.2.23}$$

As depicted in (5.1.1) dynamic parameters available dataset contain a multiplicative coupling. This flexibility is limited for the viscosity function at (5.2.23) as it does not allow for a sensitivity to deformation at large strain rates ($k_2 J_2^{NEq} \gg 1$)). To overcome this limitation, we propose a viscosity function that also has a multiplicative coupling, thus

$$\eta_k = \eta^\times \eta^\omega \eta_0 = \eta^\times\left[\frac{1 + q_2(k_2 J_2^{NEq})^{\beta_2}}{1 + (k_2 J_2^{NEq})^{\beta_2}}\right]\eta_0. \tag{5.2.24}$$

where $q_2 = \eta_\infty/\eta_0$. In this scenario, the sensitivity to deformation is now contained in $\eta^\times$ and the goal is to define an appropriated $\eta^\times = \eta^\times(I_1^v)$. To give further insight into this potential function, we want that $\eta^\times$ should:

- Be near 1 when strain is small;
- Be around a controllable value when strain is at the level found in uniaxial tests;
- The *increase* of $\eta^\times$ should start slow and then rises at a controlled slope when the viscous strain invariant reaches a certain limit.

Bringing those notions together with, some subtle assumptions must be addressed:

- Since $\eta^\times = \eta^\times(I_1^v)$ and our small strain reference for linear behaviour is our shear test, we shall define its invariant value as $I_1^v = I_{1,shear}^v$, where $3 \le I_{1,shear}^v \le 3 + \epsilon_1$ (with ϵ_1 being hopefully, but not necessarily, small);
- For uniaxial, we certainly have $I_1^v \ge 3$. It is for the most part, bigger than $I_{1,shear}^v$, but not *always*.

For the sake of simplicity we consider the first invariant expression for the shear case and we reiterate

$$I_1^v = 3 + \gamma_v^2 \quad \text{we take} \quad I_{1,ref}^v = \max(I_{1,shear}^v). \tag{5.2.25}$$

We choose the shear level of deformation to serve as baseline for small viscosity. Better yet, in the interval where $3 \le I_1^v \le I_{1,ref}^v$, we impose $\eta^\times$ to be small. A proposed formulation that meet those requirements is

$$f(I_1^v) = \frac{I_1^v - 3}{I_{1,ref}^v}, \tag{5.2.26}$$

in addition a proposition of the multiplicative factor is defined as

$$\eta^\times(I_1^v) = \frac{1 + q_1\left[k_1 f(I_1^v)\right]^{\beta_1}}{1 + \left[k_1 f(I_1^v)\right]^{\beta_1}}. \tag{5.2.27}$$

This framework provides a degree of liberty on *how fast* $\eta^\times$ increases when $I_1^v \approx I_{1,shear}^v$. Moreover, the inequality

$$\eta_0^\times \ge \frac{1 + q_2\left[k_1 f(I_{1,ref}^v)\right]^{\beta_1}}{1 + \left[k_1 f(I_{1,ref}^v)\right]^{\beta_1}}, \tag{5.2.28}$$

could be used as a constraint during optimization where $\eta_0^\times$ is an arbitrary value close to 1, limiting the interference of large strains in small strains.

Lastly, recalling the proportionality between $\mathbf{P}_{dev}^{Neq}$ and $\dot{\mathbf{D}}^v$ from (5.2.5), we may get a non-dimensional value of $\dot{\mathbf{D}}^v$ at an observed frequency, f_0, we may use $J^* = \sqrt{J_2^{NEq}(\eta_0 f_0)s^{-1}}$ so that we substitute $(k_2 J_2^{NEq})^{\beta_2} = (k^* J^*)^{2\beta_2}$ in (5.2.24) at η^ω, controlling the transition rate between η_0 and $\eta_\infty = \eta_0 q_2$. In summary, the viscosity function is now given by

$$\eta_k = \eta^\times \eta^\omega \eta_0 = \left[\frac{1 + q_1\left[k_1 f(I_1^v)\right]^{\beta_1}}{1 + \left[k_1 f(I_1^v)\right]^{\beta_1}}\right]\left[\frac{1 + q_2 (k^* J^*)^{2\beta_2}}{1 + (k^* J^*)^{2\beta_2}}\right]\eta_0. \tag{5.2.29}$$

A visualization of each contribution to modifying η_0 is shown in Figure 5.15.

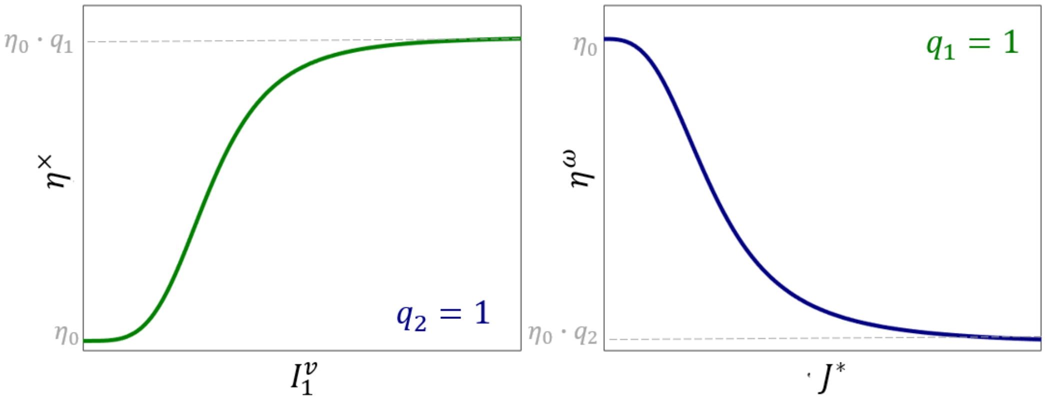

Figure 5.15: Evolution of η_k via $\eta^\times$ and η^ω.

Optional branch

In the present development, the viscoelastic dissipation is dealt by the non-linear viscosity function across the frequency range of $[0.1, 100]$ [Hz]. To increase its coverage and numerical stability, we shall consider an additional, thermodynamically stable, rheological branch. With this inclusion, the tensorial representation of the total stress becomes

$$\mathbf{P} = \left[\mu_{Eq} \left(\frac{I_1}{3}\right)^{\alpha_{Eq}-1}\right] \mathbf{F} + \left[m_{NEq} \left(\frac{{}^{(1)}I_1^e}{3}\right)^{a_{NEq}-1}\right] \mathbf{F} \ {}^{(1)}\mathbf{D}^v + m_+ \mathbf{F} \ {}^{(2)}\mathbf{D}^v - p\mathbf{F}^{-T}. \tag{5.2.30}$$

where the extra branch is represented as an additional non-equilibrium stress contribution with stiffness m_+ and internal variable ${}^{(2)}\mathbf{D}^v$. The the previously defined internal variable (and all its invariants) is now represented with the superscript ${}^{(1)}(\cdot)$.

For each internal variable, their respective evolution equation are now written as

$${}^{(1)}\dot{\mathbf{D}}^v = \frac{\left[m_{NEq} \left(\frac{{}^{(1)}I_1^e}{3}\right)^{a_{NEq}-1}\right]}{\eta_k} \left(\frac{{}^{(1)}I_1^e}{3} \, {}^{(1)}\mathbf{D}^v - {}^{(1)}\mathbf{D}^v \mathbf{C} \ {}^{(1)}\mathbf{D}^v\right) \tag{5.2.31}$$

with η_k defined by equation (5.2.29) from Section 5.2.2n, while the new evolution equation is

$${}^{(2)}\dot{\mathbf{D}}^v = \frac{1}{\tau_+} \left(\frac{{}^{(2)}I_1^e}{3} \, {}^{(2)}\mathbf{D}^v - {}^{(2)}\mathbf{D}^v \mathbf{C} \ {}^{(2)}\mathbf{D}^v\right). \tag{5.2.32}$$

where the relaxation time $\tau_+ = \eta_+/m_+$, for η_+ being a constant viscosity.

This singular branch will identify the viscoelastic response for excitations at $1000Hz$. Since its contribution is superposed to the previous non-linear formulation, one expects a weaker interference at lower frequencies, allowing for a reasonably simple identification together with an increased frequency coverage.

5.2.3 Specific formulations

Specific cases are derived from the constitutive model and/or from linear viscoelastic considerations. Those manipulations serve to aid the calibration procedure, to be presented in section 5.4.

Quasi-linearized formulation - shear

In a simple shear test, when considering the equations (5.2.8), (5.2.9) and (5.2.11), in small strains such that

$$\frac{3+\gamma^2}{3} \approx 1 \quad ; \quad \frac{3+(\gamma-\gamma_v)^2}{3} \approx 1 \tag{5.2.33}$$

we have simply

$$P_\gamma = \sigma_\gamma = \mu_{Eq}\gamma + m_{NEq}(\gamma - \gamma_v). \tag{5.2.34}$$

$$\dot{\gamma}_v = \frac{m_{NEq}}{\eta_k}(\gamma - \gamma_v) \tag{5.2.35}$$

to which J_2^{NEq} is written only with the leading order terms, giving

$$J_2^{NEq} = \left[m_{NEq}(\gamma - \gamma_v)\right]^2. \tag{5.2.36}$$

We will, nevertheless, keep the non-linear viscosity from (5.2.29), in a version of small strains ($\eta^\times \approx 1$), but potentially large strain rates, J^*, so that $\eta_k \approx \eta^\omega \eta_0$.

Analytical formulation - uniaxial

For reference, we remind the full formulation of the non-linear model

$$\mathbf{P} = \left[\mu_{Eq}\left(\frac{I_1}{3}\right)^{\alpha_{Eq}-1}\right]\mathbf{F} + \left[m_{NEq}\left(\frac{I_1^e}{3}\right)^{a_{NEq}-1}\right]\mathbf{F}\mathbf{D}^v - p\mathbf{F}^{-T} \tag{5.2.37}$$

$$\dot{\mathbf{D}}^v = \frac{m_{NEq}\left(\frac{I_1^e}{3}\right)^{a_{NEq}-1}}{\eta_k(I_1^e, I_2^e, I_1^v)}\left[\frac{I_1^e}{3}\mathbf{D}^v - \mathbf{D}^v\mathbf{C}\mathbf{D}^v\right]. \tag{5.2.38}$$

In uniaxial conditions, the components of the gradient deformation tensor and the internal variable are given by the matrices defined previously in (5.2.13) and (5.2.14), from Section 5.2.1.

$$\mathbf{P} = \boldsymbol{\sigma} = 2\mu_{Eq}\boldsymbol{\varepsilon} + 2m_{NEq}(\boldsymbol{\varepsilon} - \boldsymbol{\varepsilon}_v) - p\mathbf{I} \tag{5.2.39}$$

with

$$\dot{\boldsymbol{\varepsilon}}_v = \frac{m_{NEq}}{\eta_0}(\boldsymbol{\varepsilon} - \boldsymbol{\varepsilon}_v). \tag{5.2.40}$$

For uniaxial, the components of the linearized strain tensor, $\boldsymbol{\varepsilon}$, and the linearized internal variable, $\boldsymbol{\varepsilon}_v$, are

$$[\boldsymbol{\varepsilon}] = \begin{bmatrix} \lambda-1 & 0 & 0 \\ 0 & \frac{1-\lambda}{2} & 0 \\ 0 & 0 & \frac{1-\lambda}{2} \end{bmatrix} \quad ; \quad [\boldsymbol{\varepsilon}_v] = \begin{bmatrix} \lambda_v-1 & 0 & 0 \\ 0 & \frac{1-\lambda_v}{2} & 0 \\ 0 & 0 & \frac{1-\lambda_v}{2} \end{bmatrix}. \tag{5.2.41}$$

Therefore, the linearized incompressible formulation, written in component form is

$$\sigma_\lambda = 2\mu_{Eq}(\lambda - 1) + 2m_{NEq}(\lambda - \lambda_v) - p, \tag{5.2.42}$$

where we solve for p by recognizing that $\sigma_{22} = \sigma_{33} = 0$, thus

$$p = 2\mu_{Eq}\left(\frac{1-\lambda}{2}\right) + 2m_{NEq}\left[\left(\frac{1-\lambda}{2}\right) - \left(\frac{1-\lambda_v}{2}\right)\right],$$

so that the stress becomes

$$\sigma_\lambda = 3\mu_{Eq}\left(\lambda - 1\right) + 3m_{NEq}\left(\lambda - \lambda_v\right), \tag{5.2.43}$$

and the evolution equation results in

$$\dot{\lambda_v} = \frac{m_{NEq}}{\eta_0}\left(\lambda - \lambda_v\right). \tag{5.2.44}$$

With the formulation derived above, it is possible to obtain μ_{Eq}, m_{Neq} and $\tau = \eta_0/m_{NEq}$ analytically using a relaxation test, as long it is well conditioned and its stretch magnitude is small enough to operate well within the framework of small strains. In Section 5.1.2, we demonstrated using equation (5.1.7) that the first step from the MSR procedure is adequate for such considerations (see Figure 5.11). However, oscillations observed in the peak stress caused by the PID hinder a proper recovery of m_{Neq}, which is then not identified.

To identify the relaxation time, τ, analytically we use equation (5.1.7), previously defined on Section 5.1.2, reiterated here as

$$\log\left[\sigma(t) - \sigma_{Eq}^{exp}\right] = -\frac{t}{\tau} + D, \tag{5.2.45}$$

so that identifying τ is now a simple problem of linear regression.

By the end of the decay the stress response is treated as purely elastic, therefore the the amount of stress remaining is mainly provided by the equilibrium portion of equation (5.2.43), so

$$\sigma_{Eq}^{exp} \approx 3\mu_{Eq}(\lambda - 1). \tag{5.2.46}$$

Analytical formulation - shear

The complete linearization of the non-linear model components in shear collapses to a simple Zener model, where its components for simple shear in small strains, are

$$\sigma_\gamma = 2\mu_{Eq}\varepsilon + 2m_{NEq}(\varepsilon - \varepsilon_v) \tag{5.2.47}$$

and

$$\dot{\varepsilon_v} = \frac{m_{NEq}}{\eta}(\varepsilon - \varepsilon_v) = \frac{1}{\tau}(\varepsilon - \varepsilon_v), \tag{5.2.48}$$

with $\varepsilon = \gamma/2$, $\varepsilon_v = \gamma_v/2$ and $\tau = \eta/m_{NEq}$.

Considering that the strain history is given by a sinusoidal signal

$$\varepsilon(t) = \varepsilon_0 \sin(\omega_0 t), \quad \forall t \in [0, \infty], \tag{5.2.49}$$

with $\varepsilon_v(t = 0) = 0$, one can solve the non-homogeneous linear first order ODE from (5.2.48) and obtain

$$\varepsilon_v(t) = \frac{\varepsilon_0}{1 + \left(\omega_0\tau\right)^2}\left\{\sin\left(\omega_0 t\right) + \omega_0\tau\left[e^{-\frac{t}{\tau}} - \cos\left(\omega_0 t\right)\right]\right\}, \tag{5.2.50}$$

which simplifies, in steady-state conditions, to

$$\varepsilon_v(t) = \varepsilon_0\frac{1}{1 + \left(\tau\omega_0\right)^2}\sin\left(\omega_0 t\right) - \varepsilon_0\frac{\tau\omega_0}{1 + \left(\tau\omega_0\right)^2}\cos\left(\omega_0 t\right). \tag{5.2.51}$$

Inserting equation (5.2.51) within equation (5.2.47), results in

$$\sigma_\gamma(t) = \varepsilon_0 \left[2\mu_{Eq} + 2m_{NEq} \frac{(\omega_0\tau)^2}{1+(\omega_0\tau)^2} \right] \sin(\omega_0 t) + \varepsilon_0 \left[2m_{NEq} \frac{\omega_0\tau}{1+(\omega_0\tau)^2} \right] \cos(\omega_0 t). \tag{5.2.52}$$

The first and second term in brackets are, respectively, the in-phase and out of phase stiffness contributions to the stress. From linear viscoelasticity, those parameters are called storage modulus and loss modulus, represented as

$$\sigma_\gamma(t) = \varepsilon_0 G^{Model}_{Prime} \sin(\omega_0 t) + \varepsilon_0 G^{Model}_{Second} \cos(\omega_0 t). \tag{5.2.53}$$

and so, one may represent the dynamic parameters as a function of the material parameters from the Zener model, with

$$G^{Model}_{Prime}(\omega_0) = 2\mu_{Eq} + 2m_{NEq} \frac{(\omega_0\tau)^2}{1+(\omega_0\tau)^2} \quad ; \quad G^{Model}_{Second}(\omega_0) = 2m_{NEq} \frac{\omega_0\tau}{1+(\omega_0\tau)^2}. \tag{5.2.54}$$

Likewise, the parameters can also be described by the dynamic function with the introduction of an additional relation, in this case, the derivatives of the storage and loss modulus with respect to ω. From (5.2.54), we recognize

$$G^{Model}_{Prime}(\omega_0) = 2\mu_{Eq} + 2m_{NEq} \frac{(\omega_0\tau)^2}{1+(\omega_0\tau)^2} = 2\mu_{Eq} + \omega_0\tau G^{Model}_{Second}(\omega_0)$$

whose derivative with respect to frequency, ω, results in

$$\frac{dG^{Model}_{Prime}}{d\omega}(\omega_0) = \tau \left(G^{Model}_{Second}(\omega_0) + \omega_0 \frac{dG^{Model}_{Second}}{d\omega}(\omega_0) \right) \tag{5.2.55}$$

For a constant viscosity, one now has three parameters and three equations, allowing for an analytical solution of μ_{Eq}, m_{NEq} and $\tau = \eta/m_{NEq}$ for a *single frequency.* Rearranging (5.2.54) and (5.2.55) we find that, for $\omega = \omega_0$, that

$$\tau = \frac{\frac{dG^{Model}_{Prime}}{d\omega}(\omega_0)}{\left(G^{Model}_{Second}(\omega_0) + \omega_0 \frac{dG^{Model}_{Second}}{d\omega}(\omega_0) \right)} \tag{5.2.56}$$

and

$$\mu_{Eq} = \frac{1}{2} \left[G^{Model}_{Prime} - \omega_0\tau G^{Model}_{Second} \right] \quad ; \quad m_{NEq} = \frac{1}{2} \left[G^{Model}_{Second} \left(\frac{1}{\omega_0\tau} + \omega_0\tau \right) \right]. \tag{5.2.57}$$

Considering that equation (5.2.53) is equivalent to equation (5.1.3) from Section 5.1.1, renders an interesting connection as the storage modulus, loss modulus and their derivatives are provided by MMAexpert data, as shown in Figure 5.16, by imposing

$$G^{Model}_{Prime}(\omega_0) = G^{Model}_{MMA}(\omega_0) \quad ; \quad G^{Model}_{Second}(\omega_0) = G^{MMA}_{Second}(\omega_0). \tag{5.2.58}$$

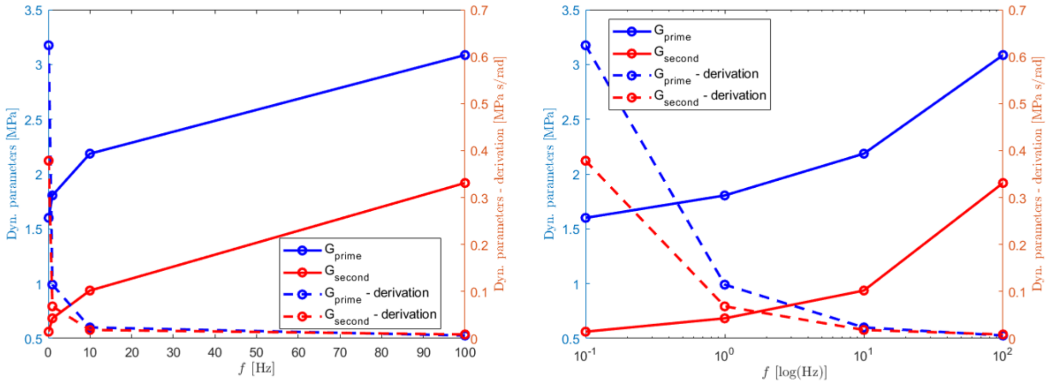

Figure 5.16: Dynamic parameters (lines) and their derivatives (intermittent line) recovered numerically from MMAexpert data. Linear abscissa plot (left) logarithmic abscissa plot (right).

During calibration, there are instances where the analytical formulations are required, but the equilibrium stiffness, is already provided by a previous step, $\mu_{Eq} = \mu^*$. In that case, the equations simplify to

$$\mu_{Eq} = \mu^* \quad ; \quad m_{NEq} = \frac{1}{2}\left[G^{MMA}_{Second}\left(\frac{1}{\omega_0\tau} + \omega_0\tau\right)\right] \quad ; \quad \tau = \frac{G^{MMA}_{Prime} - 2\mu^*}{\omega_0 G^{MMA}_{Second}}. \tag{5.2.59}$$

5.3 Optimization method

5.3.1 General definitions

In order to characterize the constitutive model to operating conditions of interest, an identification strategy must be developed.

The Finite non-linear Visco-elastic law requires 14 parameters to be identified. In addition, the parameters can become heavily coupled rendering a manual search via sensitivity analysis impractical. For this reason, two non-linear optimization approaches from the Newton-step family were considered: Levenberg-Marquardt and Trust Region algorithm.

As an optimization problem, the objective function was initially chosen to be the sum of the square of the differences between the model solution with fixed parameters and the best solution. The advantage of this approach is that multiple experiments can be added in the numerical-experimental residual, since all experiments use the same constitutive law, and consequently, parameters to be calibrated.

The problem in question requires to solve non-linear least squares problems by minimizing a sum of squared function values. The difference array (residual), r_i, for a single experiment dataset is given by

$$r_i(\mathcal{P}) = P_i^{Experimental} - P_i^{numerical}(\mathcal{P}), \tag{5.3.1}$$

where $\mathcal{P} = \mathcal{J} \cup \mathcal{U}$ is the set of material parameters chosen to be identified, where the set $\mathcal{J} = \{\mu_{Eq}, m_{NEq}, \eta_0\}$ contains the fundamental values of equilibrium and non-equilibrium stiffness and viscosity and the dimensionless set $\mathcal{U} = \{\alpha_{Eq}, a_{NEq}, q_1, k_1, \beta_1, q_2, k_2, \beta_1\}$ contains the non-linear corrector. The term $P_i^{numerical}(\mathcal{P})$ is the stress data of interest to fit with the true data $P_i^{Experimental}$. The residual will be the sum of all the elements of r_i

$$R(\mathcal{P}) = \sum_{i=1}^{m} (r_i(\mathcal{P}))^2 \tag{5.3.2}$$

with m being the size of the numerical and true outputs. However, the objective function of this problem can consider multiple experiments, as exemplified for the a, b and c exemplary cases.

$$R^{total}(\mathcal{P}) = \sum_{i=1}^{m} (r_i^a(\mathcal{P}))^2 + \sum_{j=1}^{n} (r_j^b(\mathcal{P}))^2 + \sum_{k=1}^{p} (r_k^c(\mathcal{P}))^2. \tag{5.3.3}$$

In other words, the optimization problem can be stated in generic form as

$$\hat{\mathcal{P}} \in argmin_{\mathcal{P}} \left[R^{total}(\mathcal{P}) \right] = argmin_{\mathcal{P}} \left[\sum_{i=1}^{m} (r_i^a(\mathcal{P}))^2 + \sum_{j=1}^{n} (r_j^b(\mathcal{P}))^2 + \sum_{k=1}^{p} (r_k^c(\mathcal{P}))^2 \right]. \tag{5.3.4}$$

A simple Gauss-Newton method starts with an initial guess $\mathcal{P}_0$, which is iterated as

$$\mathcal{P}_{s+1} = \mathcal{P}_s - (\mathbf{J}_r^T \mathbf{J}_r)^{-1} \mathbf{J}_r^T \mathbf{r}(\mathcal{P}_s) \tag{5.3.5}$$

or

$$\mathbf{J}_r^T \mathbf{J}_r \Delta\mathcal{P} = -\mathbf{J}_r^T \mathbf{r}(\mathcal{P}_s) \text{ for } \mathcal{P}_{s+1} = \mathcal{P}_s + \Delta\mathcal{P} \tag{5.3.6}$$

with $(\mathbf{J}_r^T \mathbf{J}_r)$ the approximation of the Hessian of the total residual sum function formulated via the gradient $\mathbf{J}_r$

$$(\mathbf{J}_r)_{ij} = \frac{\partial \mathbf{r}_i(\mathcal{P})}{\partial \mathcal{P}_j}. \tag{5.3.7}$$

The Newton method has quadratic convergence when the current guess is close to the minimal value of the objective function. However, a solution is only ensured if the Hessian (or its approximation) is positive definite. For very complex functions, when the guess is far from the minima, the residual solution space can present locations of negative Hessian. To circumvent this, Levenberg-Marquardt and Trust Region algorithm utilises an additional term to the Hessian term

$$\left(\mathbf{J}_r^T + \lambda \mathbf{I} \right) \mathbf{J}_r \Delta\mathcal{P} = -\mathbf{J}_r^T \mathbf{r}(\mathcal{P}_s). \tag{5.3.8}$$

Using a default library from MATLAB 2019b's version, the Trust-Region method was chosen as the main non-linear optimization method after being tested against other methods like Sequential quadratic programming (sqp), Interior-point, Expected Improvement-based Bayesian and Levenberg-Marquardt itself. The Trust-Region algorithm is based on the fact that there is a certain step size $||\Delta\mathcal{P}|| \leq \delta_k$ where global convergence still is maintained, performing then a long step $||\Delta\mathcal{P}|| = \delta_k$ to "move" quickly to a more interesting area. In general, Trust Region algorithm will exhibit a better performance each time a negative curvature is encountered, compared to the Levenberg-Marquardt methods.

As previously mentioned, the experimental results chosen to be inserted on this optimization are the homogeneous deformation cases under uniaxial and shear deformation. This choice removes the need to specify the geometry of the body, greatly simplifying the equations and so that those implementations are made not in a FEM environment, but directly in a routine written in MATLAB/Python.

5.3.2 Chosen objective function

If multiple M stress-strain data are considered simultaneously, where each k-data contains a dataset Ω_k, we will use as a general objective function of $R(\mathcal{P})$ to be

$$R(\mathcal{P}) = \sum_{k=1}^{M} \sum_{i \in \Omega_k} \frac{\left[\sigma^k_{model}(t_i) - \sigma^k_{data}(t_i)\right]^2}{\left[\sigma_{ref}(k)\right]^2 |\Omega_k|}. \tag{5.3.9}$$

where $\sigma_{ref}(k) = \max(\sigma^k_{data}(t))$.

For uniaxial data, the information is recovered directly from experiments. For shear stress-strain cycles, the information is recovered from MMAexpert data. In addition, to quickly identify the numerical storage modulus and loss modulus, their values can be obtained from linear viscoelastic considerations, as schematically represented in Figure 5.17.

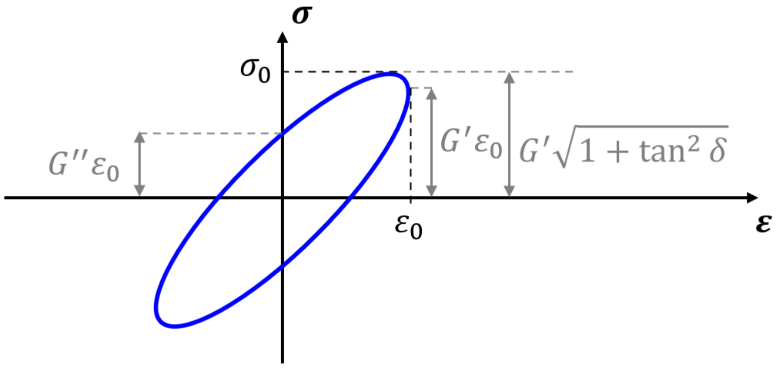

Figure 5.17: Stress-strain curve for linear viscoelastic materials and their correspondence to their dynamic parameters.

5.4 Hierarchical calibration procedure

The extended constitutive model contains important non-linearities of interest and ideally, one would want to characterize those effects using as much experimental data as possible. However, the extended model from Section 5.2.2 has a parametrical set, $\mathcal{P}$, of

$$\mathcal{P} = \{\mu_{Eq}, \alpha_{Eq}, m_{\tilde{N}Eq}, a_{NEq}, \eta_0, q_1, k_1, \beta_1, q_2, k^*, \beta_2, I^v_{v1,ref}, m_+, \tau_+\}, \tag{5.4.1}$$

which contain 14 strongly coupled parameters. A Global procedure using the present optimization method does not produce adequate, nor unique, outcomes. For this reason, an hierarchical optimization is developed using 7 procedural steps which are summarized bellow and then further explored subsequently.

- Step 1
    - Recovered dataset: Uses the equilibrium stress response by the end of each magnitude stage from MSR test (see Figure 5.9 from Section 5.1.2);
    - Considered model: Uses only the equilibrium stress contribution from equation 5.2.20 (see Section 5.2.2);
    - Identified parameters: A range of equilibrium stiffness based on the data correction (see Section 5.1.2) and its respective equilibrium exponent

$$\mathcal{P}_1 = \{[\mu_{Eq}^{Min}, \tilde{\mu_{Eq}}, \mu_{Eq}^{Max}], \alpha_{Eq}\};$$

  - Optimization procedure: Matlab's built-in Trust-region algorithm using equation (5.3.9) as objective function (see Section 5.3).

- Step 2
  - Recovered dataset: Uses only the first stage of MSR test (see Figure 5.9 from Section 5.1.2);
  - Considered model: Uses the uniaxial components from a linearized Zener model defined by equations (5.2.43) and (5.2.44) (see Section 5.2.3);
  - Identified parameters: A single additional equilibrium stiffness based on the data correction (see Section 5.1.2, it does not considers the dispersion) and a relaxation time associated to very slow excitations frequencies, here denominated as VLF

$$\mathcal{P}_2 = \{\tilde{\mu_{Eq}^{VLF}}, \tau^{VLF}\};$$

  - Optimization procedure: Analytical identification using equations (5.2.45) and (5.2.46) (see Section 5.2.3).

- Step 3
  - Recovered dataset: Recovered dataset: Uses the stress-strain excitations from the lowest frequencies available in MMAexpert, here termed LF, and the highest frequency of interest, here termed HF (see Figure 5.4 from Section 5.1.1). In addition, we recover the average equilibrium stiffness coefficient recovered in Step 1, $\tilde{\mu_{Eq}}$;
  - Considered model: Uses the shear components from the linearized Zener model defined by equations (5.2.34) and (5.2.35) (see Section 5.2.3);
  - Identified parameters: two parameter sets containing different non-equilibrium stiffness and viscosities but identical equilibrium stiffness are recovered. Each set identifies a single Zener model at low frequencies (LF) and high frequences (HF)

$$\mathcal{P}_3 = \{\tilde{\mu_{Eq}}, m_{NEq}^{LF}, \eta_0^{LF}, m_{NEq}^{HF}, \eta_0^{HF}\};$$

  - Optimization procedure: Analytical identification using equation (5.2.59) with provided $\tilde{\mu_{Eq}}$ (see Section 5.2.3).

- Step 4
  - Recovered dataset: Uses the stress-strain excitations data from Step 3 and the average equilibrium stiffness coefficient recovered in Step 1, $\tilde{\mu_{Eq}}$;
  - Considered model: Uses the shear components from the linearized Zener model defined by equations (5.2.34) and (5.2.35) (see Section 5.2.3);
  - Identified parameters: two parameter sets containing different viscosities but identical equilibrium and non-equilibrium stiffness are recovered. Each set identifies a single Zener model at low frequencies (LF) and high frequencies (HF)

$$\mathcal{P}_4 = \{\tilde{\mu_{Eq}}, \tilde{m_{NEq}}, \eta_0^{HF}, \eta_0^{HF}\};$$

  - Optimization procedure: Matlab's built-in Trust-region algorithm using equation (5.3.9) as objective function (see Section 5.3).

- Step 5

  - Recovered dataset: Uses all available stress-strain excitations within (and including) LF and HF and all intermediary frequencies within them, spaced from each other by a decade (see Figure 5.4 from Section 5.1.1). In addition, we recover the relaxation time coefficient, τ^{VLF}, recovered in Step 2, the non-equilibrium stiffness, $m_{\tilde{N}Eq}$, from Step 5 and the maximum/minimum available values of equilibrium stiffness, $[\mu_{Eq}^{lower}, \mu_{Eq}^{upper}]$, from both Step 1 and 2;
  - Considered model: Uses the shear components from the quasi-linearized model derived in equations (5.2.34) and (5.2.35) (see Section 5.2.3);
  - Identified parameters: All parameters necessary to completely describe the quasi-linearized model are found

    $$\mathcal{P}_5 = \{\mu_{Eq}, m_{\tilde{N}Eq}, \eta_0, q_2, k^*, \beta_2, I_{1,ref}^{v}\};$$

  - Optimization procedure: Matlab's built-in Trust-region algorithm using equation (5.3.9) as objective function (see Section 5.3) using $[\mu_{Eq}^{lower}, \mu_{Eq}^{upper}]$ as upper and lower limits of the equilibrium stiffness during optimization. In addition the nominal viscosity, η_0, is obtained analytically (and kept fixed during optimization) via

    $$\eta_0 = \tau^{VLF} m_{\tilde{N}Eq},$$

    together with $I_{v,ref}^{v}$ defined from the model response after being identified as

    $$I_{v,ref}^{v} = \max\left(I_{1,shear}^{v}\right).$$

- Step 6

  - Recovered dataset: Uses the LF and HF stress-strain shear excitations data from Step 3 in shear (see Figure 5.4 from Section 5.1.1) plus a portion of the uniaxial CD and MSR data (see Figures 5.7 and 5.9 from Section 5.1.2). In addition, we recover all coefficients, $\mathcal{P}_6$ and the interval $[\mu_{Eq}^{lower}, \mu_{Eq}^{upper}]$ from Step 6 together with the equilibrium exponent, α_{Eq}, from Step 1;
  - Considered model: Uses the finite non-linear formulation derived in equations (5.2.20) and (5.2.21) with the proposed alternative viscosity (see Section 5.2.2);
  - Identified parameters: All parameters necessary to completely describe the finite non-linear model are found.

    $$\mathcal{P}_6 = \{\mu_{Eq}, \alpha_{Eq}, m_{\tilde{N}Eq}, a_{NEq}, \eta_0, q_1, k_1, \beta_1, q_2, k^*, \beta_2, I_{v,ref}^{v}\};$$

  - Optimization procedure: Matlab's built-in Trust-region algorithm using equation (5.3.9) as objective function (see Section 5.3) using $[\mu_{Eq}^{lower}, \mu_{Eq}^{upper}]$ as upper and lower limits of the equilibrium stiffness during optimization.

- Step 7

  - Recovered dataset: Uses the HF stress-strain shear excitations data and an additional high frequency data, here termed VHF recovered via equations 5.1.2 and (5.1.3) (see Section 5.1.1). In addition, we recover all coefficients, $\mathcal{P}_7$ obtained during Step 7;

- Considered model: Uses the finite non-linear formulation with an additional non-equilibrium branch defined by equations 5.2.30, (5.2.31) and (5.2.32) (see Section 5.2.2);
- Identified parameters: All parameters necessary to completely describe the finite non-linear model are found.

$$\mathcal{P}_7 = \{\mu_{Eq}, \alpha_{Eq}, m_{\tilde{N}Eq}, a_{NEq}, \eta_0, q_1, k_1, \beta_1, q_2, k^*, \beta_2, I^v_{v1,ref}, m_+, \tau_+\};$$

- Optimization procedure: Matlab's built-in Trust-region algorithm using equation (5.3.9) as objective function (see Section 5.3).

In the following subsections, the data considered are schematically shown together with the parameter set configuration used during optimization concluding with the final superposed result and respective identified parametric values. Lastly, in this document, the calibration process will focus on identifying the model with regards to a single material, PCY4-RT, at 15°C.

5.4.1 Step 1: Equilibrium terms

In this step, we use the asymptotic solutions from the multi-step relaxation data as presented in Figure 5.9, we are interested in the end-points of the stress history in each individual stretch stage, as highlighted on Figure 5.18.

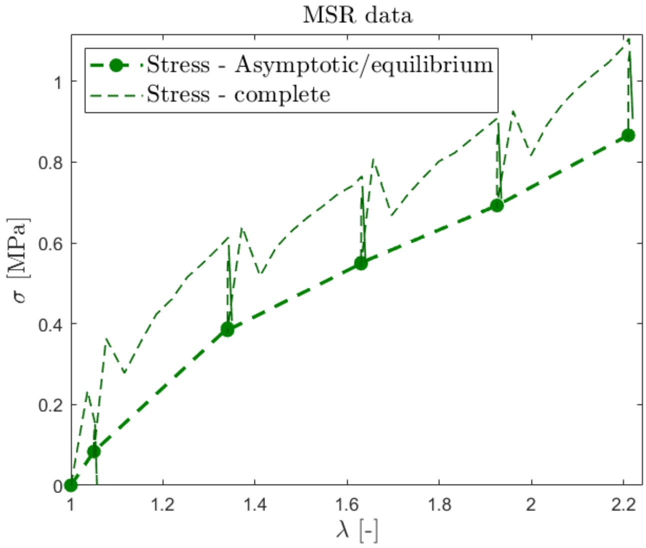

Figure 5.18: Uniaxial equilibrium characterization.

Those asymptotic value of stress are assumed to be the equilibrium contribution of the stress, thus the model consists solely of the equilibrium portion of the formulation in 5.2.20 from Section 5.2.2, resulting simply in

$$\mathbf{P} = \left[\mu_{Eq}\left(\frac{I_1}{3}\right)^{\alpha_r - 1}\right]\mathbf{F} - p\mathbf{F}^{-T} \tag{5.4.2}$$

In an uniaxial case with a incompressible material, the component/scalar form is

$$P_\lambda = \left[\mu_{Eq}\left(\frac{2+\lambda^3}{3\lambda}\right)^{\alpha_r - 1}\right]\left(\frac{\lambda^3 - 1}{\lambda^2}\right). \tag{5.4.3}$$

For the present model, the validity of its hyperelastic formulation is best kept when only the first five data points are considered, thus the calibration will be constrained to a stretch range $0 \leq \lambda_0 \leq 2$, covering the “softening” observed in the stress-stretch curve in Figure 5.18, whilst the “stiffening” at higher deformations, $\lambda_0 > 2$, would require another formulation.

As previously discussed in Section 5.1.2, the CD and MSR procedure stretch history from the machine should be corrected using equation 5.1.8, whose corrective parameters $k_{corr} = \tilde{k}_{corr} \pm \sigma_k = 0.794 \pm 0.0644$ and $g_{corr} = \tilde{g}_{corr} \mp \sigma_g = -0.0229 \mp 0.0067$ were obtained via valid measurements made using image correlation. However, as previously discussed, only k_{corr} shall be considered un the correction of MSR data. The resulting calibration of the model when the data is corrected using (5.1.8) when $k_{corr} = \tilde{k}_{corr} = 0.794$ and $g_{corr} = 0$ is displayed in Figure 5.19 with their respective identified parameters presented in Table 5.9.

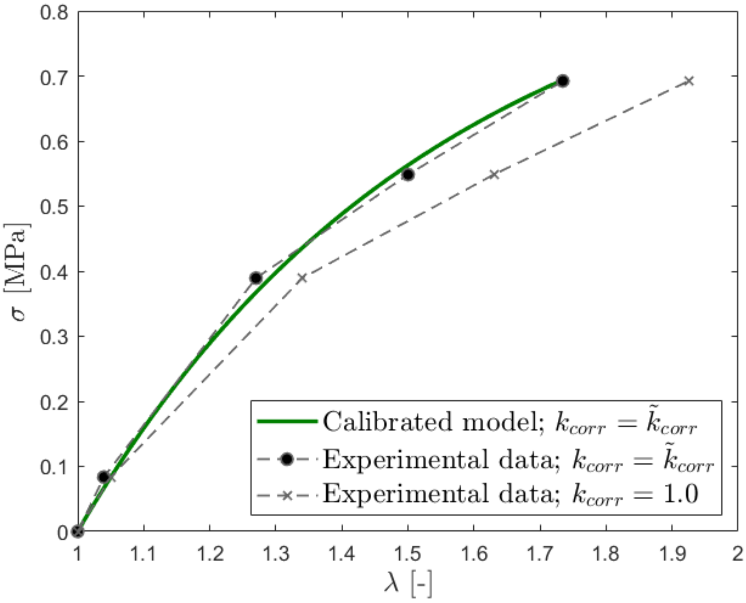

Figure 5.19: MST Asymptotic calibration with corrected data - additional uncorrected data for reference.

Table 5.9 also contains the resulting μ_{Eq} and α_{Eq} if the dispersion σ_k was also accounted for in the correction of the data.

Param.	$\tilde{k}_{corr}$	$\tilde{k}_{corr} + \sigma_k$	$\tilde{k}_{corr} - \sigma_k$
μ_{Eq} [MPa]	0.5826	0.5581	0.6177
α_{Eq} $[-]$	0.5010	0.5010	0.5010

Table 5.9: Resulting material equilibrium parameters values for new version of MSR test - k_{corr} correction only.

As explained in the beginning of this chapter, this steps ends with the identification of a defined value of $\alpha_{Eq} = 0.501$ and an interval of $\mu_{Eq} = [0.5581, 0.6177]$ [MPa], associated to the dispersion in the correction factor, k_{corr}.

5.4.2 Step 2: Low amplitude relaxation time

In this Step we use the first relaxation stage from the MSR data, which contains a small stretch magnitude of $\lambda_{max} = 1.05$, which, when corrected using $\tilde{k}_{corr} = 0.794$ becomes $\lambda_{max}^{corr} = 1.0397$. The stress and stretch time history are presented in the left plot from Figure 5.20.

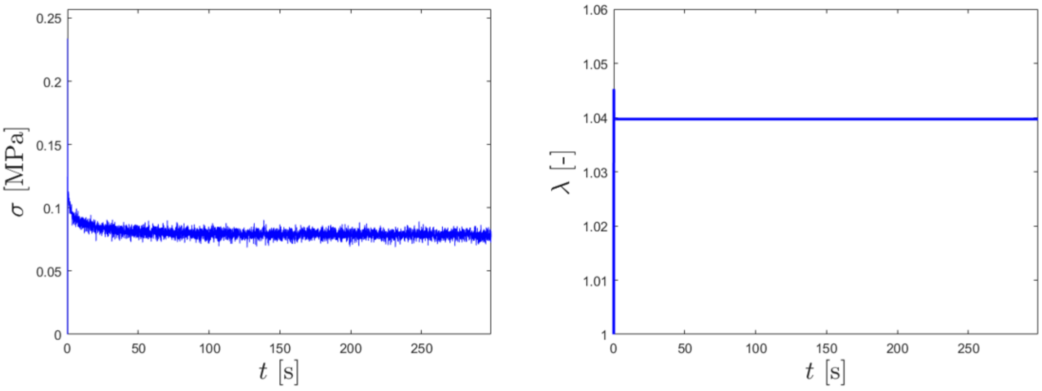

Figure 5.20: Original first stage of relaxation test from MSR protocol - Stress time history (left plot) and Stretch time history (right plot).

However, there are some ill-conditioning occurrences in the data. During the initial 0.1% portion (0.3 [s]) from the totality of the experiment (300 [s]), the PID from the machine oscillates and overshoots around the intended stretch, as shown in the right plot from Figure 5.21. In addition, the value of the stress decay is considered to be significant until $t \approx 23$ [s], after the stress value falls within the noise of the measurement, as shown in the left plot from Figure 5.21.

The adequate portion of the data, when only Considering only the stable and significant portions of the experiment, are presented in Figure 5.22.

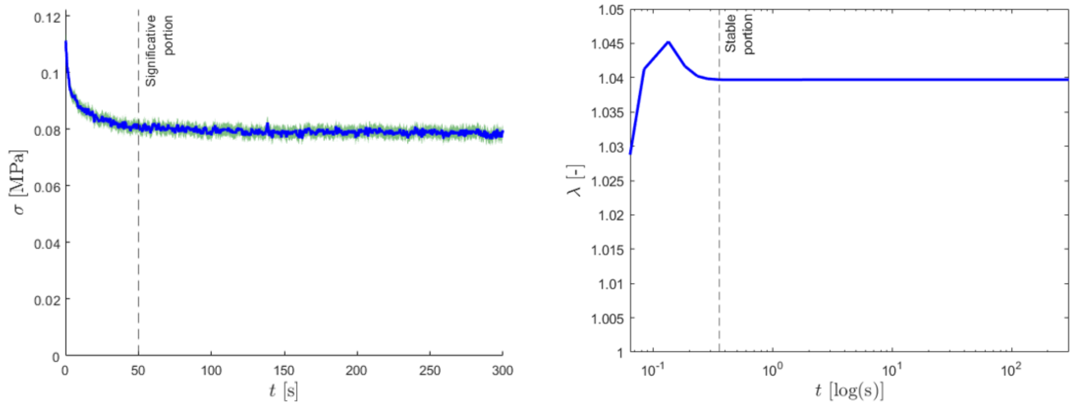

Figure 5.21: Ill-conditioning challenges identified during experimental data recovery - Stress smoothed via sliding mean and standard deviation window (left plot) and Stretch logarithmic time history (right plot).

Using this version of the test, an analytical recovery of the material parameters of the model is proposed. However, due to the partitions made, the incertitude of the peak

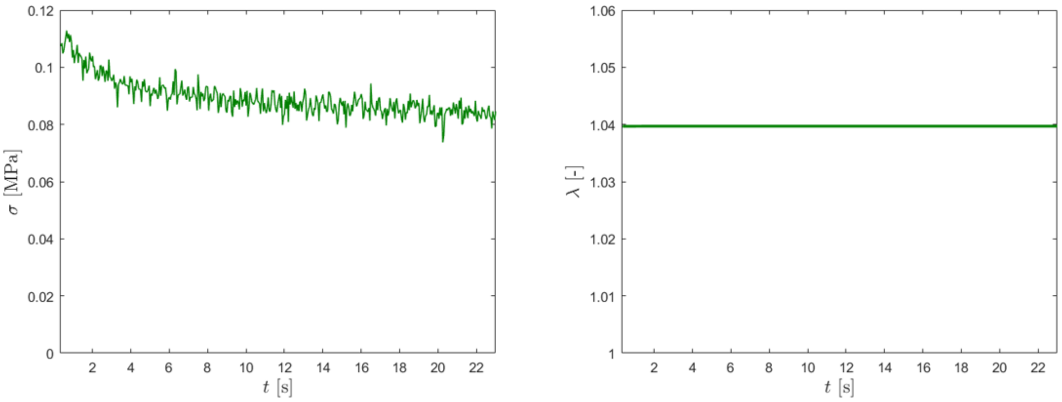

Figure 5.22: Sectioned first stage of relaxation test from MSR protocol - Stress time history (left plot) and Stretch time history (right plot).

stress due to the PID could hinder the response of m_{Neq}, thus, the identification limits itself on finding a valid relaxation time, $\tau = \eta_0/m_{Neq}$ and μ_{Eq}. To do so, we consider, equations (5.2.45) and (5.2.46) from Section 5.2.3, where μ_{Eq} is directly proportional to the asymptotic/equilibrium stress by the end of the signal and τ is obtained via least-square fit to recover the slope. The resulting superposition of equation (5.2.45) is displayed in Figure 5.23 and their respective parameters are also shown in Table 5.10.

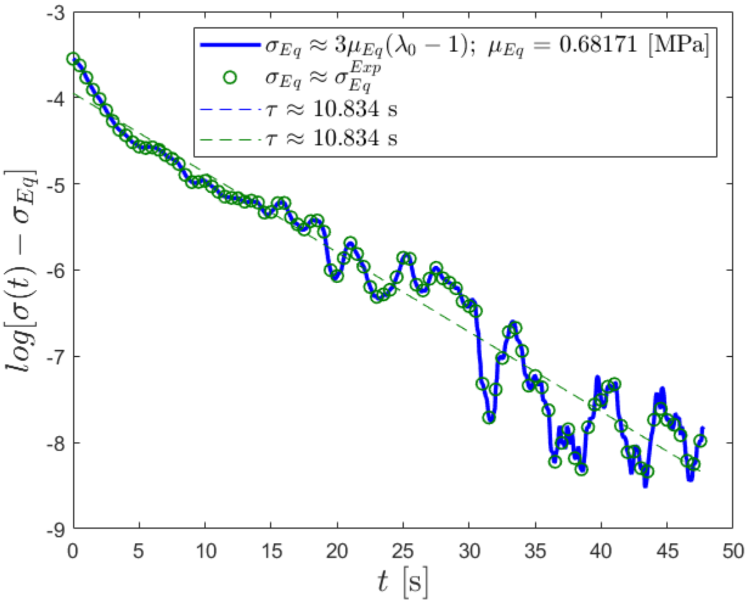

Figure 5.23: Identification of τ and μ_{Eq} by means of the preconditioned relaxation test data.

As explained in the beginning of this Chapter, this steps ends with the identification of another defined value of $\mu_{Eq} = 0.6817$ [MPa] and an relaxation time of $\tau^{VLF} = 10.834$ [s], associated to the average correction factor, $k_{corr} = \tilde{k_{corr}} = 0.794$.

We notice that the value found for the equilibrium stiffness,$\mu_{Eq} = 0.6817$ [MPa] during this step is beyond the interval $\mu_{Eq} = [0.5581, 0.6177]$ [MPa], shown in Table 5.9, from Section 5.4.1, although they belong to the same data. The justification can be observed

Parameters	1st MSR
μ_{Eq} [MPa]	0.6817
τ [s]	10.834

Table 5.10: Resulting material equilibrium parameters - First stage of MSR data.

qualitatively in Figure 5.19 from Step 1 where, in order to find a compromise of equilibrium stress response for a large stretch range, the present model formulation must slightly underestimate the stiffness in the first MSR stage. Nonetheless, the stiffness found in the present step shall be used in later iterations.

5.4.3 Step 3: Unique equilibrium stiffness

During this step, by means of the formulation derived in Section 5.2.3, one can derive the material parameters of a Zener model using solely the dynamic parameters provided by the MMAexpert database.

Using equation (5.2.59), two Zener models are identified using two sets of dynamic parameters values for a maximum shear strain of $\varepsilon_0 = 0.05$, two frequencies: 0.1 [Hz] and 100 [Hz] and a fixed equilibrium stiffness, $\mu_{\tilde{Eq}} = 0.5826$ [MPa], obtained in Step 1 (see Table 5.9 from Section 5.4.1) when the average correction factor $k_{corr} = \tilde{k}_{corr} = 0.794$ was considered for the uniaxial data.

The resulting superposition of stress-strain shear data for $0.1Hz$ and 100 [Hz] are displayed in Figure 5.24 and their respective parameters are also shown in Table 5.11.

Parameters	0.1 [Hz] constrained	100 [Hz] constrained
μ_{Eq} $[MPa]$	0.5826	0.5826
m_{NEq} $[MPa]$	0.5802	1.9184
η $[MPa \cdot s]$	0.7152	0.0031

Table 5.11: Resulting material parameters values for 0.1 [Hz] and 100 [Hz] with fixed μ_{Eq}.

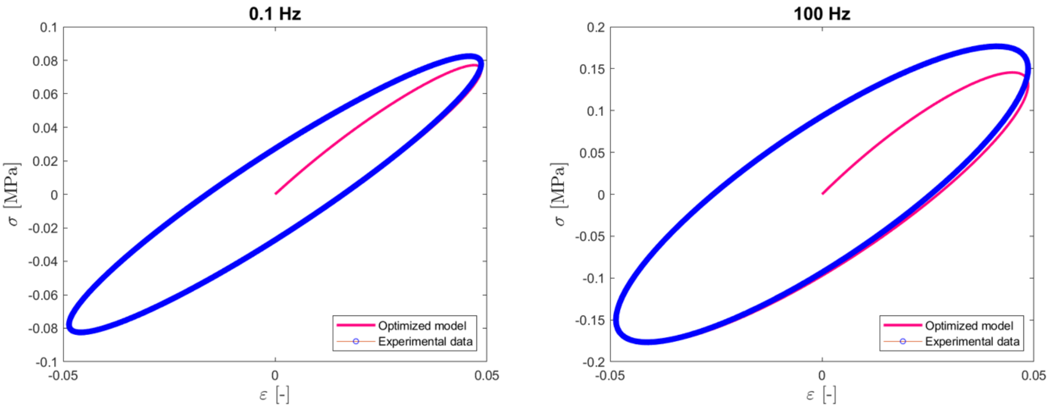

Figure 5.24: Validation via stress-strain superposition for 0.1 [Hz] and 100 [Hz].

This steps ends with the analytical identification of two Zener models that superposes elliptical stress-strain generated data from MMAexpert at 0.1 [Hz] and 100 [Hz].

5.4.4 Step 4: Unique non-equilibrium stiffness

Similarly the previous step, the present part of the hierarchical calibration also attempts to identify two Zener formulations that superposes stress-strain shear cycles at 0.1 [Hz] and 100 [Hz], with some differences.

This time, both models must have identical equilibrium and non-equilibrium stiffness (μ_{Eq} and m_{NEq}, respectively), while using the two different viscosities. This is made via a numerical optimization where m_{NEq} is allowed to vary within the maximum and minimum values found in Table 5.11 (see Section 5.4.3, Step 3), while attempting to minimize the objective function consisting of two terms

$$R^{total}(m_{NEq}) = r^{Low\ Hz}(\mu^*, m_{NEq}, \eta_{LF}) + r^{High\ Hz}(\mu^*, m_{NEq}, \eta_{HF}), \tag{5.4.4}$$

with fixed η_{LF} and η_{HF} values obtained in the previous Section 5.4.3. The residuals $r^{Low\ Hz}$ and $r^{High\ Hz}$ are built using the objective function 5.3.9 (see Section 5.3.2) using solely the experimental data from the lowest and highest considered frequency ($[0.1, 100]$ [Hz]).

The value of μ_{Eq} is relaxed to vary within an interval which encompasses the distribution, $[0.5581, 0.6177]$ [MPa], found in Table 5.9 from Section 5.4.1 (Step 1), but also the stiffness value of 0.6817 [MPa], identified in Section 5.4.2 (Step 2) shown in Table 5.10. In other words, the equilibrium stiffness, μ_{Eq}, is allowed to vary within the bounds of $[0.5581, 0.6817]$ [MPa]. The validation of this procedure is showcased in Figure 5.25 and the final parameters are presented in Table 5.12.

Parameters	0.1 [Hz] relaxed	100 [Hz] relaxed
μ_{Eq} [MPa]	0.6798	0.6798
m_{NEq} [MPa]	1.8463	1.8463
η [MPa $\cdot$ s]	0.7152	0.0031

Table 5.12: Resulting material parameters values for 0.1 [Hz] and 100 [Hz] with relaxed μ_{Eq}.

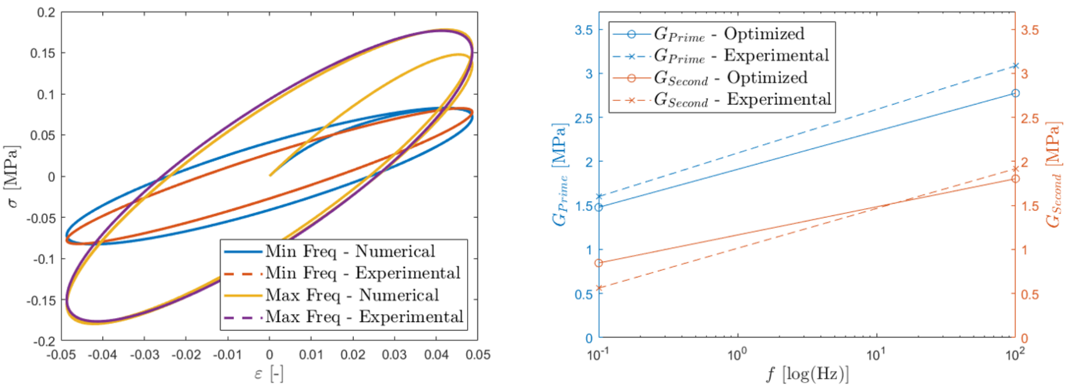

Figure 5.25: Compromised stress-strain superposition for 0.1 [Hz] and 100 [Hz] (left) and corresponding dynamic parameters (right) with relaxed μ_{Eq}.

This steps also ends with the identification of two Zener models that superposes elliptical stress-strain generated data from MMAexpert at 0.1 [Hz] and 100 [Hz] with identical equilibrium and now with non-equilibrium stiffness as well, while still keeping two distinct viscosities.

5.4.5 Step 5: Non-linearity in rate

In this step, the calibration will consider simultaneously the stress-strain data of $[0.1, 1, 10, 100]$ [Hz] obtained via the procedure from Section 5.1.1, shown in Figure 5.4. The model to be identified is the quasi-linearized formulation from Section 5.2.3.

During this optimization, the equilibrium stiffness and the non-equilibrium stiffness from Table 5.12 (see Section 5.4.4) are kept fixed. In addition, the viscosity, η_0, is composed using the relaxation time, τ^{VLF}, found in Section 5.4.2 (Step2) and the present non-equilibrium stiffness, so that $\eta_0 = 20.0032$ [s], which is also kept fixed. Table 5.13 presents the value of the fixed parameters and the range of the relaxed parameters before identification.

Parameters	**Fixed Coef.**	**Param. Range**
μ_{Eq} [MPa]	0.6798	–
m_{NEq} [MPa]	1.8463	–
η_0 [MPa · s]	20.0032	–
q_2 [–]	–	$[10^{-5}\ -\ 0.99999]$
k^* [–]	–	$[0\ -\ 2\cdot10^5]$
β_2 [–]	–	$[0.1\ -\ 10]$

Table 5.13: Parameter set configuration before optimization - Step 5.

After the optimization procedure, resulting parameters are displayed on Table 5.14, the superposition of stress-strain curves for each cycle is shown in Figure 5.27 and the superposition of the dynamic parameters in Figure 5.27. Its rhomboid stress-strain shape is a direct consequence of the varying viscosity to the varying strain rate from the sinusoidal strain history.

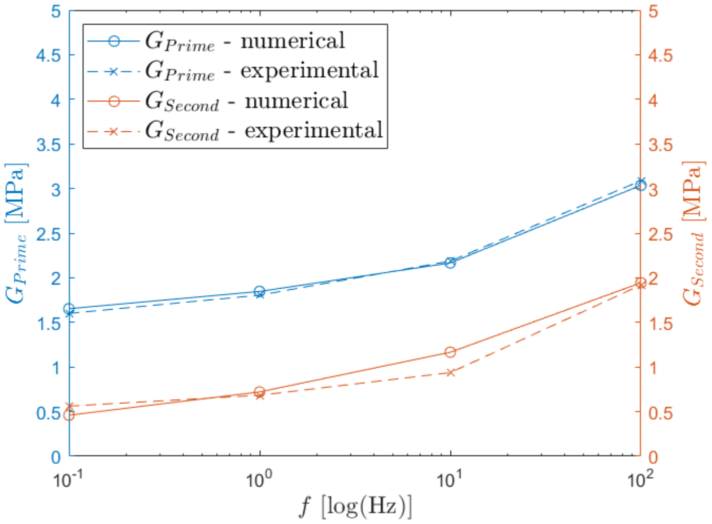

Figure 5.26: Storage modulus and Loss modulus superposition for $[0.1, 1, 10, 100]$ [Hz] based on parametric set from Table 5.13.

Parameters	$[0.1, 1, 10, 100]$ [Hz]
μ_{Eq} [MPa]	0.6798
m_{NEq} [MPa]	1.8463
η_0 [MPa $\cdot$ s]	20.0032
q_2 $[-]$	$7.7020 \cdot 10^{-5}$
k^* $[-]$	3602.0429
β_2 $[-]$	1.6627
$I^v_{1,ref}$ $[-]$	3.0085

Table 5.14: Resulting material parameters for $[0.1, 1, 10, 100]$ [Hz] based on parametric set Table 5.13.

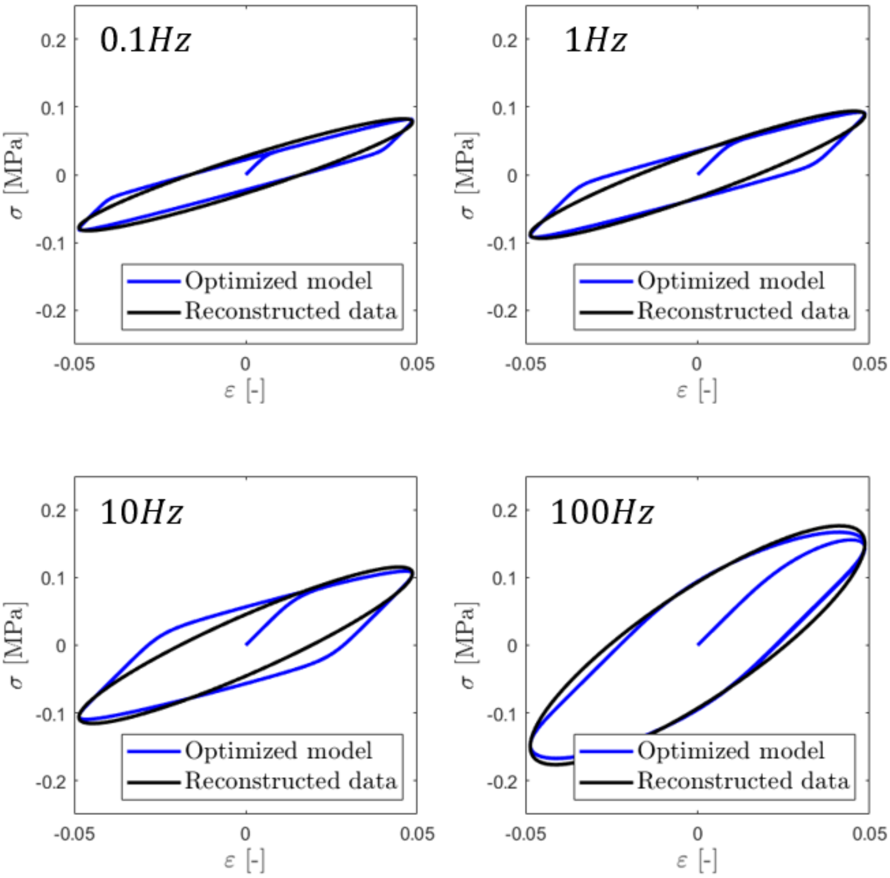

Figure 5.27: stress-strain superposition for $[0.1, 1, 10, 100]$ [Hz] based on parametric set from Table 5.13.

After the analysis, we found that optimization procedure was able to display a coherent superposition with stress-strain and dynamic parameter data, for both viscosity scenarios. Furthermore, both models presented as output $(q_2\eta_0)_{Scenario\ 1} = 2.64 \cdot 10^{-3}$ [MPa $\cdot$ s] and $(q_2\eta_0)_{Scenario\ 2} = 1.54 \cdot 10^{-3}$ [MPa $\cdot$ s], which represents the smallest viscosity possible. Their results not only are similar between themselves, but they have the same order as $\eta_0^{HF} = 3 \cdot 10^{-3}$ [MPa $\cdot$ s], found for the Zener identified uniquely at 100 [Hz] as shown in Table 5.12 in the previous Section 5.4.4 (Step 4).

Lastly, with this identified model, one can also find *a posteriori* the parameter $I^v_{1,ref}$ which is the maximum value of the first invariant of the internal variable, $I^v_1(\gamma_v) = 0.0085$.

This steps ends with the identification of the single quasi-linearized model that superposes elliptical stress-strain generated data from MMAexpert for $[0.1, 1, 10, 100]$ [Hz].

5.4.6 Step 6: Non-linearity in magnitude

In this step, the data which will be used during optimization consists on the two high-end shear cycles at $[0.1, 100]$ [Hz] from MMAexpert (see Figures 5.24 or 5.4) and a portion of the MSR and CD protocols (see Figures 5.7 and 5.9) from uniaxial experiments, their chosen partitions being displayed on Figure 5.28.

The CD protocol will consider mainly the deformations to which the camera is considered to be reliable (bellow 100% in deformation), so that its procedure can be double checked if needed in the future. The chosen portion of the MSR protocol covers the second stage of the lower-left plot from Figure 5.9. The reason for this cut is because, as already discussed on Section 5.4.2 (Step 2), the first stage of the MSR protocol is not adequate due to ill-conditioning problems (which is why m_{NEq} was not identified during this step). Due to this initial cut, to properly define the mechanical problem for MSR in the second stage, we consider as initial condition $\lambda_v^{Stage\ 2}(t_0) \approx \lambda_0^{Stage\ 1}(t_{end})$, assuming the equilibrium stress is reached by the end first MSR stage (qualitatively observed in Figures 5.20 and 5.9).

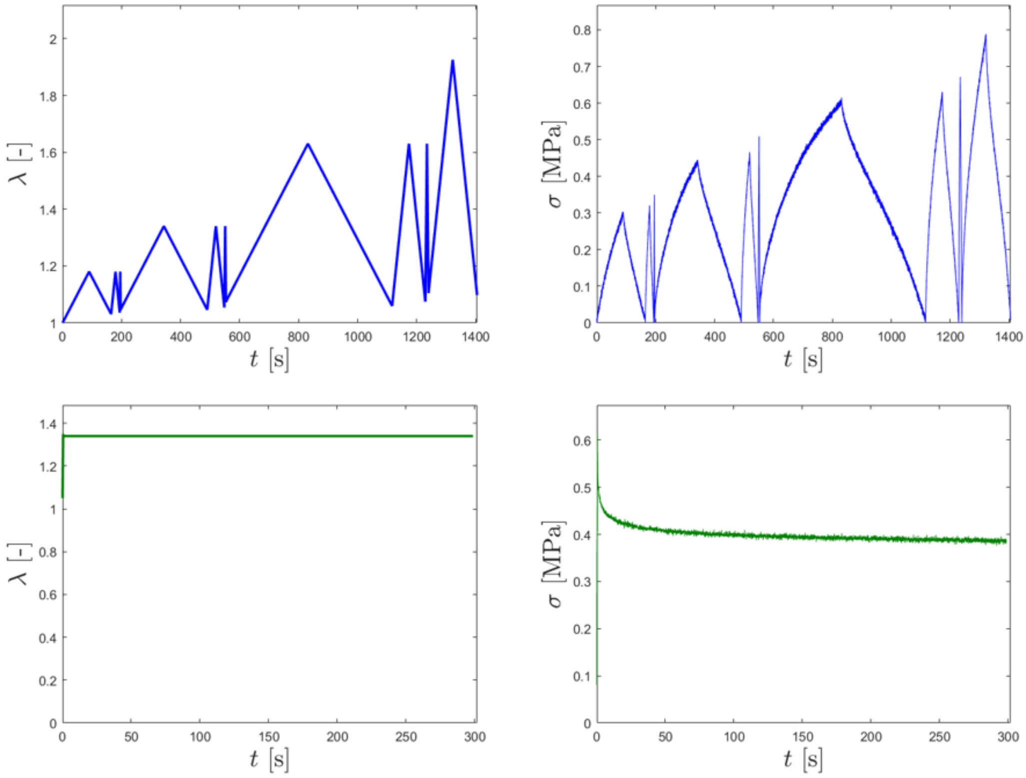

Figure 5.28: Partial experimental uniaxial data considered during calibration - CD (first row) ; MSR (second row) ; Stretch time history (first column) ; Stress time history (second column).

In this step, the full non-linear formulation proposed in Section 3.2 from Section 5.2.2 (with the exception of the considerations from the subsection is used.

The optimization procedure, considers all the parameters obtained in Table 5.14, from Section 5.4.5, being defined and presented in Table 5.15.

Parameters	**Fixed Coef.**	**Param. Range**
μ_{Eq} [MPa]	–	$[0.5581 \; - \; 0.6817]$
α_{Eq} $[-]$	0.501	–
m_{NEq} [MPa]	1.8463	–
a_{NEq} $[-]$	–	$[0.501 \; - \; 2.000]$
η_0 $[\mathrm{MPa} \cdot \mathrm{s}]$	20.0032	–
q_1 $[-]$	–	$\left[\frac{\tau_{2nd}}{\tau_{1st}} \; - \; 10^3\right]$
k_1 $[-]$	–	$[0 \; - \; 2 \cdot 10^4]$
β_1 $[-]$	–	$[1 \; - \; 2.5]$
q_2 $[-]$	$7.7020 \cdot 10^{-5}$	–
k^* [s]	3602.0429	–
β_2 $[-]$	1.6627	–
$I_{1,ref}^v$ $[-]$	3.0085	–

Table 5.15: Parameter set configuration before optimization - Step 6

As in 5.4.4, μ_{Eq} is once again relaxed within the interval $[0.5581, 0.6817]$ [MPa]. For the newly introduce parameter q_1, we emphasize the conclusions made in Section 5.1.2, where Figure 5.11 presented how the relaxation time of the second MSR stage is almost *one order of magnitude* higher than the relaxation time from the first smaller stage, with $\tau_{1st} = 10.8340$ [s] and $\tau_{2nd} = 63.4875$ [s]. As q_1 factor defines the maximum value of viscosity sensitivity upon deformation, we define the ratio τ_{2nd}/τ_{1st} as reference to build bounds of this parameter. The resulting parameters are presented on Table 5.16 and its results are displayed in Figure 5.29.

Parameters	**After optim.**
μ_{Eq} [MPa]	0.6064
α_{Eq} $[-]$	0.501
m_{NEq} [MPa]	1.8463
a_{NEq} $[-]$	0.501
η_0 $[\mathrm{MPa} \cdot \mathrm{s}]$	20.0032
q_1 $[-]$	999.9970
k_1 $[-]$	16.9446
β_1 $[-]$	2.4779
q_2 $[-]$	$7.7020 \cdot 10^{-5}$
k^* [s]	3602.0429
β_2 $[-]$	1.6627
$I_{1,ref}^v$ $[-]$	3.0085

Table 5.16: Resulting material parameters after optimization - Step 6.

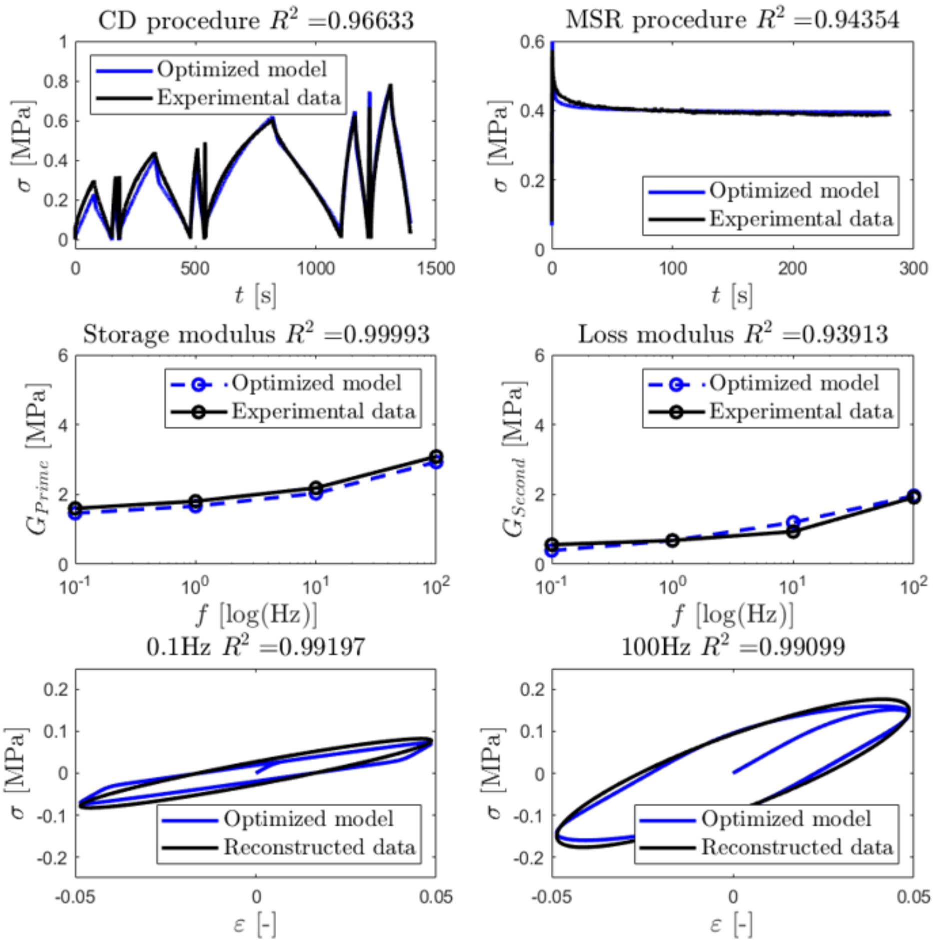

Figure 5.29: Resulting data superposition after optimization - Step 7, procedure from Table 5.15.

This steps ends with the identification of the non-linear model formulation that superposes elliptical stress-strain generated data from MMAexpert for $[0.1, 1, 10, 100]$ [Hz] and the valid chosen portions of CD and MSR uniaxial data. We precise that although MMAexpert dynamic data is an extrapolated approach from experiments and not an experimental data itself, it is labelled as such as it is used altogether with experimental data, for simpler differentiation with the numerical results.

5.4.7 Step 7: Additional linear branch

In the present development, the viscoelastic dissipation is dealt by the non-linear viscosity function across the frequency range of $[0.1, 1, 10, 100]$ [Hz]. To increase its coverage and numerical stability, we shall consider the full non-linear formulation used in the previous step together with an additional, thermodynamically stable branch defined in Section 5.2.2, which now include two parameters to be determined: m_+ and τ_+.

The experimental data comes from the MMAexpert dynamic parameters dataset. The optimization during this step shall consider, as reference data, only the stress-strain exitations of 100 [Hz] and 1000 [Hz] as shown in Figure 5.30.

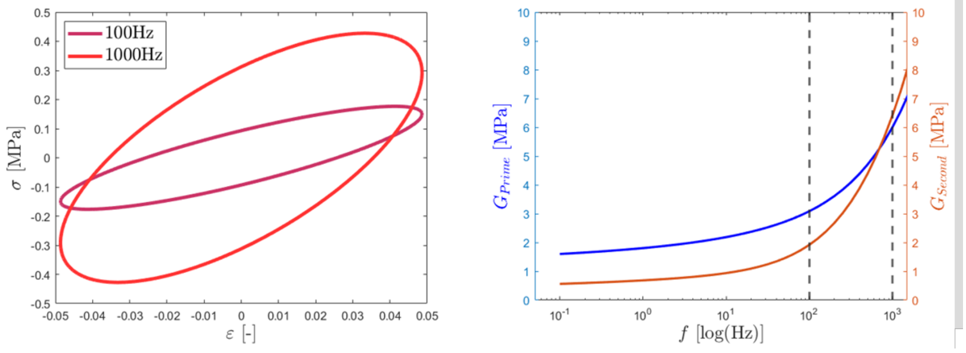

Figure 5.30: Stress-strain curve per selected frequencies (left plot) and correspondent dynamic parameters (right plot).

All previously obtained parameters parameters from Table 5.16 during Section 5.4.6 are kept fixed. For the optimization procedure, the two new coefficients are relaxed around a the range defined in Table 5.17. The resulting parameters after the optimization are provided in Table 5.18 and the resulting superposition is displayed in Figure 5.31.

Parameters	**Fixed Coef.**	**Param. Range**
μ_{Eq} [MPa]	0.6064	$-$
α_{Eq} $[-]$	0.501	$-$
m_{NEq} [MPa]	1.8463	$-$
a_{NEq} $[-]$	0.501	$-$
η_0 $[\mathrm{MPa}\cdot\mathrm{s}]$	20.0032	$-$
q_1 $[-]$	999.9970	$-$
k_1 $[-]$	16.9446	$-$
β_1 $[-]$	2.4779	$-$
q_2 $[-]$	$7.7020\cdot10^{-5}$	$-$
k^* [s]	3602.0429	$-$
β_2 $[-]$	1.6627	$-$
$I^v_{1,ref}$ $[-]$	3.0085	$-$
m_+ [MPa]	$-$	$[m_+^{Analytical,1000Hz}\cdot3^{-1}-m_+^{Analytical,1000Hz}\cdot3]$
τ_+ [s]	$-$	$[\tau_+^{Analytical,1000Hz}\cdot8^{-1}-\tau_+^{Analytical,1000Hz}\cdot8]$

Table 5.17: Parameter set configuration before optimization - Step 7

Parameters	**After optim.**
μ_{Eq} [MPa]	0.6064
α_{Eq} $[-]$	0.501
m_{NEq} [MPa]	1.8463
a_{NEq} $[-]$	0.501
η_0 $[\mathrm{MPa}\cdot\mathrm{s}]$	20.0032
q_1 $[-]$	999.9970
k_1 $[-]$	16.9446
β_1 $[-]$	2.4779
q_2 $[-]$	$7.7020\cdot10^{-5}$
k^* [s]	3602.0429
β_2 $[-]$	1.6627
$I^v_{1,ref}$ $[-]$	3.0085
m_+ [MPa]	16.9431
τ_+ [s]	$1.9894\cdot10^{-5}$

Table 5.18: Resulting material parameters after optimization - Step 7.

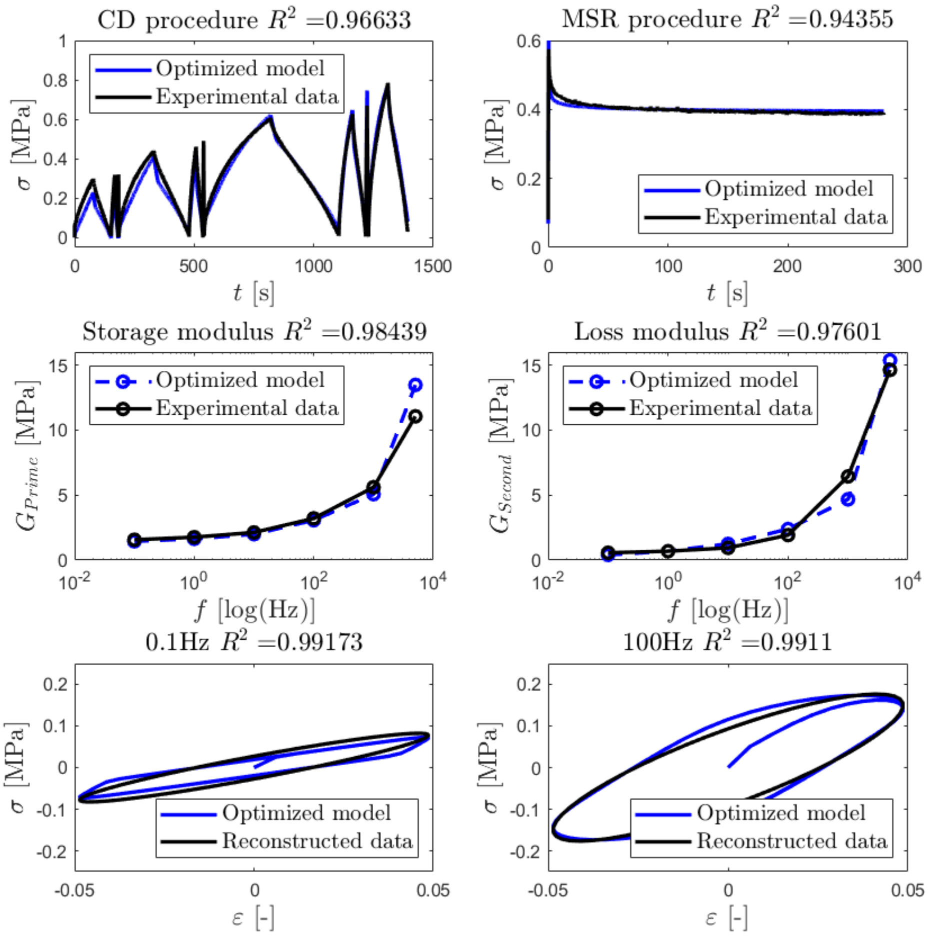

Figure 5.31: Resulting data superposition after optimization - Step 7.

5.4.8 Calibration of finite linear model

The sensitivity to strain rate by the linear viscoelastic model is accounted by means of four Maxwell branches and their respective stiffness and viscosity values. However, as constants, the branches are not sensitive to deformation magnitude. Given those limitations, only DMA tests were used for its identification. The dynamic parameters used cover a frequency range of $[0.1, 1, 10, 100, 1000, 10000]$ $[Hz]$. The final optimized parameters are displayed in Table 5.19.

For the identification, the strain magnitude in the DMA data is 8%. This value is such that, if a numerical reconstruction of the sphere contact problem (to be implemented on Chapter 6) is made with an imposed vertical displacement, the vertical load response would best match experimental output.

Parameters	**After optim.**
μ_{Eq} [MPa]	0.6975
$m_{NEq,1}$ [MPa]	0.5911
η_1 [MPa $\cdot$ s]	0.3630
$m_{NEq,2}$ [MPa]	0.7051
η_2 [MPa $\cdot$ s]	0.0324
$m_{NEq,3}$ [MPa]	1.1113
η_3 [MPa $\cdot$ s]	0.0041
$m_{NEq,4}$ [MPa]	3.5022
η_4 [MPa $\cdot$ s]	0.0008

Table 5.19: Resulting material parameters after full calibration of the non-linear model.

5.5 Numerical verification

So far, the calibration of the constitutive model is run in MATLAB assuming homogeneity and no inertia. To transfer the model to the IMPETUS environment, it must be written in tensorial form in Fortran 77 within IMPETUS to compute the stress update, as per Section 3.4.4. Thus, before attempting to reconstruct tribological contact cases, patch cases for homogeneous mechanical problems are verified.

The verification is made considering the formulation without the additional linear branch from Section 5.4.6. In a first instance, the para-metrical set is arbitrary and not based on a specific calibration.

Using the notation from section 3.1, Figure 5.32 defines a rectangular cuboid structure, that occupies the reference configuration Ω_0 with boundary $\partial\Omega_0$, such that

$$\partial\Omega_0 = \partial\Omega_0^{+XY} \cup \partial\Omega_0^{-XY} \cup \partial\Omega_0^{+XZ} \cup \partial\Omega_0^{-XZ} \cup \partial\Omega_0^{+YZ} \cup \partial\Omega_0^{-YZ} \tag{5.5.1}$$

The body is made of a quasi-incompressible isothermal viscoelastic material, with constant mass density $\rho_0 = 1182$ [kg/m^3]. The body is not subjected to body forces so that $\mathbf{B}(\mathbf{X}, t) = \mathbf{0}$ in its volume, but inertial contributions are still present. The problem is summarized as: (i) a zero shear force, $\mathbf{e}_i \cdot \mathbf{P}\mathbf{e}_j$, applied in all boundaries $\partial\Omega_0$; (ii) an elongation is applied via an imposed velocity $v(t)$ in $\partial\Omega_0^{+XZ}$; (iii) a zero normal displacement applied on $\partial\Omega_0^{-XY}$, $\partial\Omega_0^{-YZ}$, $\partial\Omega_0^{-XZ}$.

Under those consideratiosn, a stretch in the y axis still preserves an homogeneous field in $\mathbf{F}$. The velocity $v(t)$ is such that stretch rate is $\dot{\lambda} = 0.01$ [1/s], and the simulation is carried out until a maximum stretch, $\lambda_{max} = 300\%$, is reached at T. The numerical

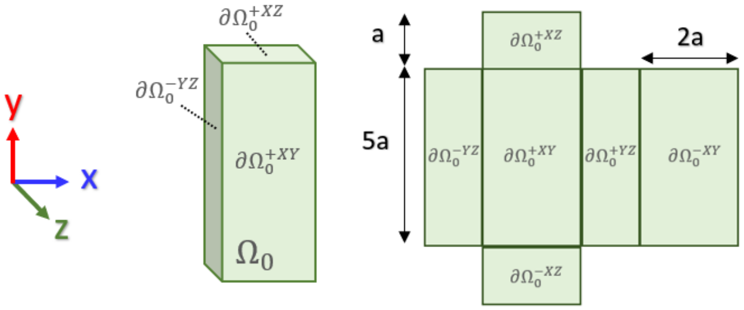

Figure 5.32: Representation of the body considered for the uniaxial case.

discretization, consists of a mesh with 128 quadratic hexahedron elements. The homogeneous behaviour is verified in Figure 5.33, for the Cauchy Stress field σ_{yy}, with good superposition for the 289 nodal stress histories belonging to a transversal section with respect to the stretch direction.

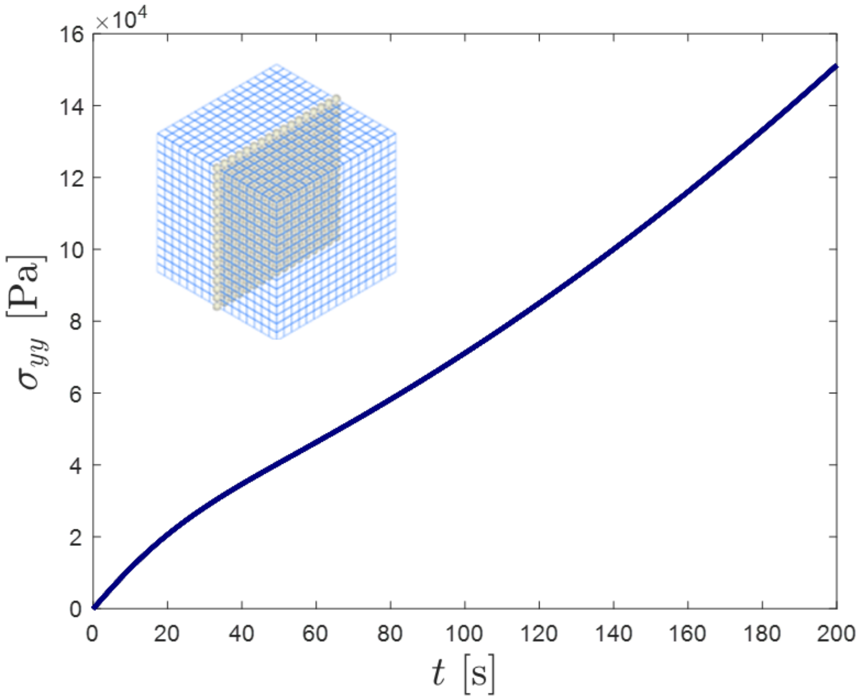

Figure 5.33: Uniaxial homogeneous deformation case. Current logarithmic strain component field in the direction of the stretch. Use of the non-linear law.

As homogeneous deformation is verified (Figure 5.34), incompressibility can also be checked for a single node via the third invariant from $(3.2.15)_3$ and (3.2.18) (the Jacobians J and J^v), verifying from J a robust quasi-incompressible numerical implementation and from J^v a proper formulation of the two-potential method, to which the evolution equation should ensure its incompressibility.

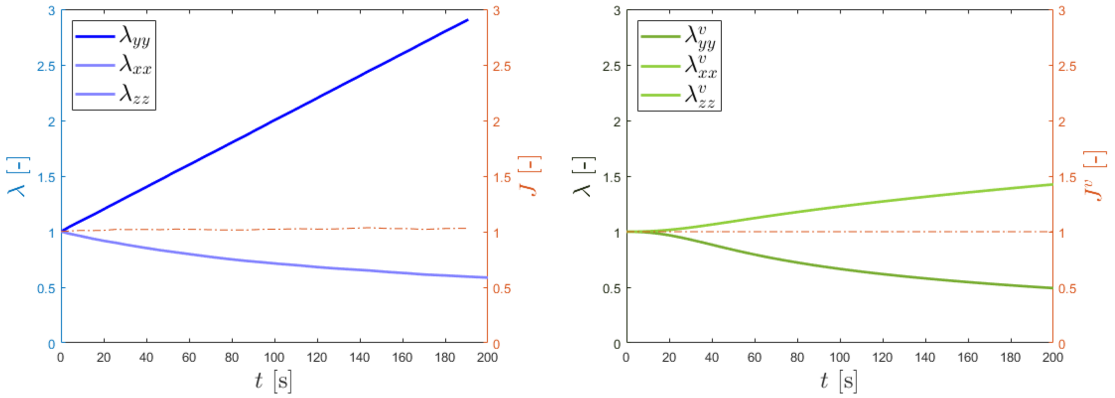

(a) Stretch - λ (b) Internal variable - λ^v

Figure 5.34: $\bar{p}$ and $\bar{V}_g$ occurrences - Geometry effect for Repro08, *ad hoc* μ and *Model A*.

As described in Chapter 3, IMPETUS Afea operates in the current configuration. To ensure that the stress update remains objective, a modification is made to the uniaxial problem, the top, $\partial\Omega^{+XZ}$, and bottom, $\partial\Omega^{-XZ}$, boundaries are now piloted via a multi-point constraint. Therefore, although the problem is not homogeneous anymore, the simulation remains pertinent to evaluate objectivity and robustness of the software.

The description defines an elongation caused by opposite displacements top-bottom boundaries (while keeping their planes parallel) until half of the simulation time, $T_{1/2}$, is reached. From this point forward, the system now operates under cylindrical coordinates with origin n the center of mass of the body. A constant angular velocity, $\omega(t)$ is applied on the top and bottom boundaries, completing a 90° revolution at T. The verification is made by comparing the problem to another case when, instead of rotating, the stretched sample is simply held in place until T is reached. A simplified schematic of both cases is shown in Figure 5.35.

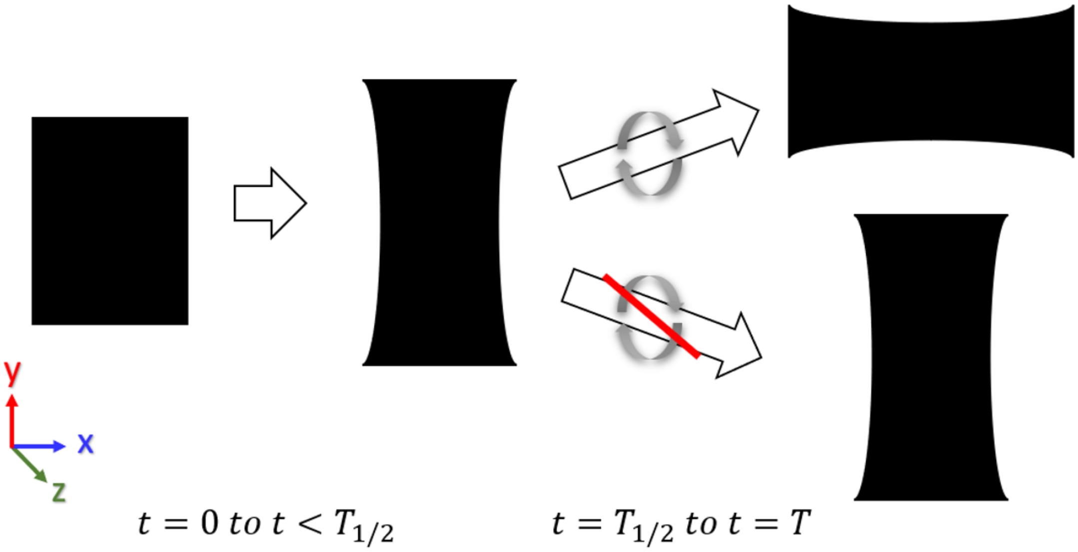

Figure 5.35: Schematic representation of objectivity test with and without rotation.

To truly confirm that the computations are just, the analytical form of the rotated Cauchy Stress tensor, $\boldsymbol{\sigma}'$, is related to its non-rotated counterpart, $\boldsymbol{\sigma}$, via

$$\boldsymbol{\sigma}' = \mathbf{R}\boldsymbol{\sigma}\mathbf{R}^T. \tag{5.5.2}$$

In this particular test case, the uniaxial tension loading has maximal stretch of $\lambda_{max} = 115\%$ and stretch rate of $\dot{\lambda} = 0.05$ [1/s]. The resulting components are shown in Figure 5.36, where a satisfactory result confirms a correct stress update procedure that preserve its objectivity.

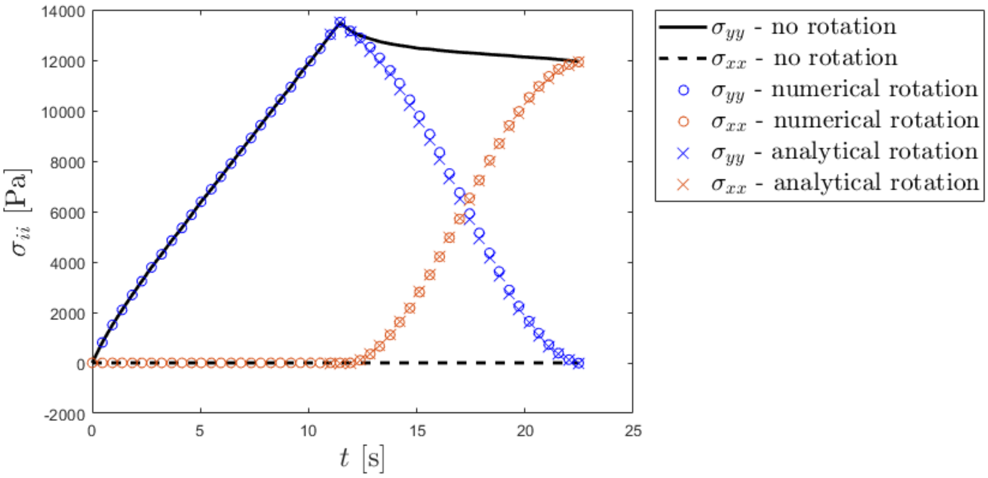

Figure 5.36: Numerical and analytical verification of objectivity condition for IMPETUS. Use of the non-linear law.

From this point on a quantitative comparison between MATLAB output and FEM output is made. This time, the parametrical set is recovered from Table 5.16 and we direct the attention to a simple shear mechanical problem, since the experimental dynamic moduli is available for high strain rates, allowing not only to validate the numerical implementation but also verify the impact of inertial effects altogether.

Take a cylindrical structure, represented in Figure 5.37, that occupies the reference configuration Ω_0 with boundary $\partial\Omega_0$, such that

$$\partial\Omega_0 = \partial\Omega_0^{+Y} \cup \partial\Omega_0^{-Y} \cup \partial\Omega_0^{L} \tag{5.5.3}$$

.

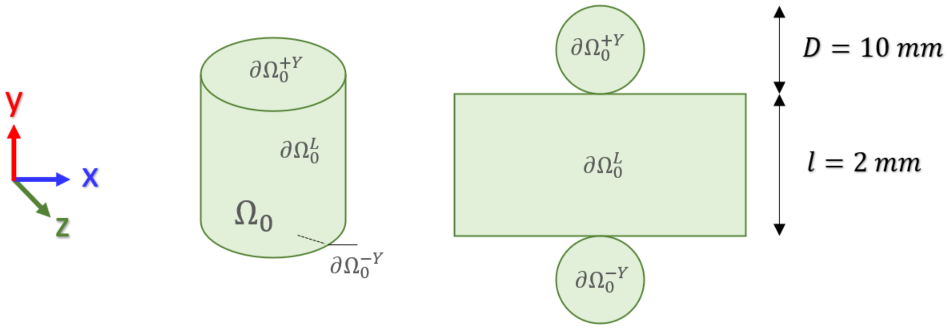

Figure 5.37: Representation of the body considered for the uniaxial case (made by author).

Apart from geometry and the boundary conditions all material considerations for the domain (incompressibility, absence of body forces, isothermal, etc) are the same as defined for the uniaxial case. The simple shear is induced by an imposed sinusoidal translation parallel to the plane Ω_0^{+Y}, whilst Ω_0^{-Y} is kept fixed and the boundary $\partial\Omega_0^{L}$ is free.

To display a clearer depictions of the central trends across a large spectral range, we choose to display the Dynamic parameters for both numerical environments, they are computed from stress-strain cycles as schematically shown in Figure 5.17 and their final results are given in Figure 5.38.

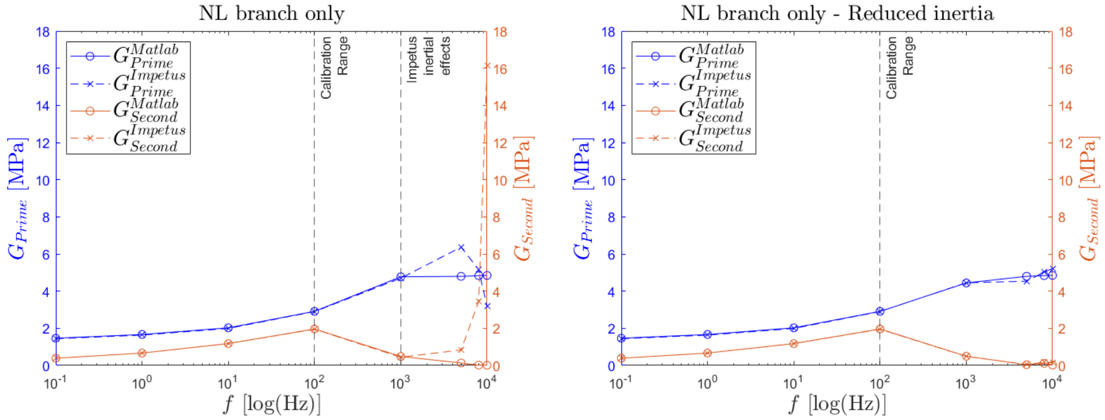
NL branch only

NL branch only - Reduced inertia

(a) $\rho = 1182$ [kg/m^3]

(b) $\rho = 118.2$ [kg/m^3]

Figure 5.38: Dynamic moduli calibrated output - MATLAB and IMPETUS.

The dynamic parameters from Figure 5.38a presents an adequate superposition between MATLAB and IMPETUS environments within the calibrated range $[0.1, 100]$ [Hz]. As expected, above the calibration range the loss modulus decreases and the storage modulus stabilizes. However, above 1000 [Hz], Figure 5.38b displays a divergence. Figure 5.38b refers to a secondary campaign which the difference that the density was $10\times$ smaller than the original comparison. As the superposition strongly improves for IMPETUS beyond 1000 [Hz], we attribute the previous discrepancy to inertial effects.

5.6 Concluding remarks

This chapter addressed four essential mechanical evaluations without contact considerations: (i) experimental homogeneous experimentation; (ii) viscoelastic modelling and (iii) calibration procedure (iv) Finite Element numerical reconstruction.

The first axis considered existent and new protocols, developing appropriated corrections when necessary. Two important non-linear effects were identified, they being related to softening effects and the increase in the relaxation time with deformation. The second axis extended a thermodynamically stable model based on considerations from the available data. Lastly, the third axis coupled the first two via a procedural approach, obtaining reasonable results with a large coverage in strain magnitude and strain rate. Lastly, we validate numerical implementation in FEM environment, whose results can now be traced back with enough confidence to their correspondent experimental results from Figure 5.29.

Those efforts ensure the foundation to implement a non-linear viscoelastic model in non-homogeneous tribological simulations with different degrees of complexity on the following Chapters.

Chapter 6

Study of a Multi Sphere sliding contact problem

6.1 Context

A major challenge in the rolling contact of a rubber material is the prediction of tangential forces generated by the relative sliding of a rubber mix material with a complex geometry (tread pattern) on a road surface with multi-scale roughness. Apart from the underlying geometric complexity, answering this challenge requires handling the complex hysteretic behavior of the rubber and taking into account the large deformation that locally occurs in such problems. Therefore, two types of non-linear responses must be combined: the non-linear viscoelastic response of the rubber material with its sensitivity to both strains and strain rates, and the large change of geometries observed by the material when sliding under compression above macroscopic obstacles.

The use of non-linear Finite Elements to handle the real interface geometry up to a certain scale is a promising option for numerical reconstruction while considering more complex constitutive models in finite strains, at the cost of a much larger computational complexity. Its validation faces two challenges. On one hand, due to computer limitations, the size of the finite elements rarely goes below the millimeter scale, which filters the soil asperities occurring at a lower scale, although the latter significantly contribute to the friction forces. On the other hand, the constitutive laws that are used in such simulations are either quite simplified and ignore important non-linear effects that are present in the viscoelastic response of the rubber, or they are used in a regime far from the experimental conditions under which they were validated. In practice, many software utilizes hyper-viscoelastic models, based on a division of the stress tensor between an equilibrium hyperelastic contribution and a non-equilibrium viscoelastic contribution (N parallel Maxwell rheological models fitted by DMA analysis), while more sophisticated laws such as the one proposed in [6] have mainly been tested in simple configurations at low speed. To progress in the understanding of the behavior of rubber mix materials in sliding or rolling contact, it is thus important to devise and experiment with a test configuration that isolates the hysteretic contribution of the rubber to the friction force from the other mechanisms occurring at the interface.

For this purpose, in the present work, we have developed and analyzed a new experimental setup to highlight the contributions of the viscoelastic dissipation induced by the large deformations in the bulk of the rubber material due to the cyclic loading caused by the presence of surface indenters. The rubber specimen has the geometry of a circular annulus (Figure 6.2) which slides over a cylindrical base inside a hydraulic angular tribometer (Figure 6.1). The base contains a ring of detachable spherical indenters, which will enter into contact with the elastomer. The spheres were coated in Teflon, to minimize the contribution of microscopic scales. In addition, the contact test always occurs underwater, at a controlled temperature, to minimize flash-temperature effects. This water is mixed with small doses of an emulsion to reduce its surface tension, hence its risk of dewetting. This setup allows to cover a large range of compressive loads and sliding velocities on different filler-reinforced rubber specimens provided by Michelin.

The experimental results are to be compared with the output of a numerical simulation using a commercial Finite Element software (namely Impetus Afea) with a second-order explicit solver and a penalized treatment of the contact constraint. This numerical reconstruction will use and compare two different non-linear constitutive models, which are first calibrated with Dynamic Mechanical Analysis procedures complemented with adequate uniaxial tests in large deformations: a typical hyper-viscoelastic formulation combining a Mooney-Rivlin free-energy and 4 linear Maxwell branches and another, thermodynamically stable, non-linear constitutive law [5] based on the work of [6].

6.2 Experimental framework

This test was devised to better understand the non-linear effects under large deformations of a filled-rubber material. To do so, a sample is compressed and then slid against a soil/substrate containing a series of smooth spheres. The relative speed between the sample and substrate and the compression load is independently controlled.

Materials

The apparatus used to compress and move the sample along the substrate is an MTS angular tribometer. As shown in Figure 6.1, it imposes a controlled compression load via hydraulic circuitry together with an electronically piloted angular displacement around its vertical axis Z.

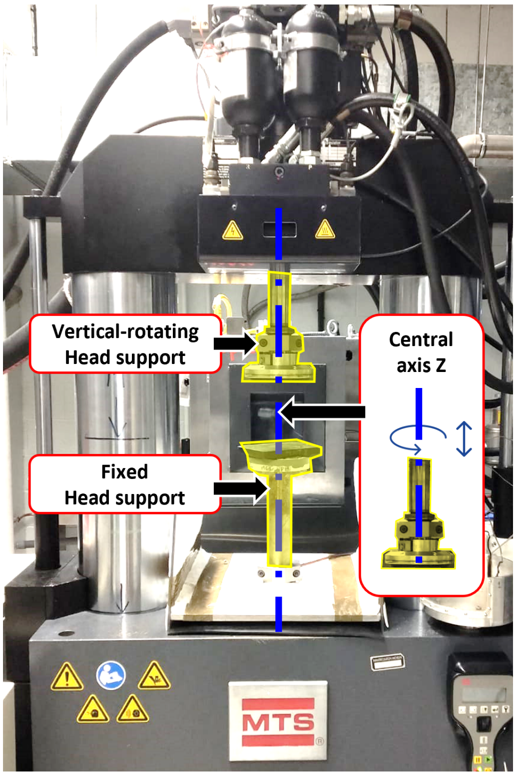

Figure 6.1: Angular tribological machine - central components.

A load cell of $500 - 2000$ [N] (resolution of 1.5 [N]) was used to measure the vertical compression load. In addition, four additional piezoelectric force sensors are placed in precise locations in the vertical-rotating head support to retrieve the measured torque. The displacement sensor tracks the angular position/velocity of the movable head, which is one of the controlled quantities. To summarize, the tribological tests are performed by imposing a PID-controlled vertical load history and a PID-controlled angular displacement/velocity history, giving access to the measured time history of:

- the vertical load as imposed by the PID controller;
- the angular position as imposed by the PID controller;
- the torque resulting from these imposed controls.

The rubber samples are made from an industrial-filled rubber Primacy4-RT (PCY4-RT) produced by Michelin. The geometry of each specimen is a torus with a rectangular cross-section, as shown in Figure 6.2. The internal and external radius of the torus is $R_i = 52$ [mm] and $R_e = 62$ [mm], respectively with a height of $h = 8$ [mm]. This sample is glued against an aluminum disk which is attached to the movable head of the tribometer (Figure 6.1).

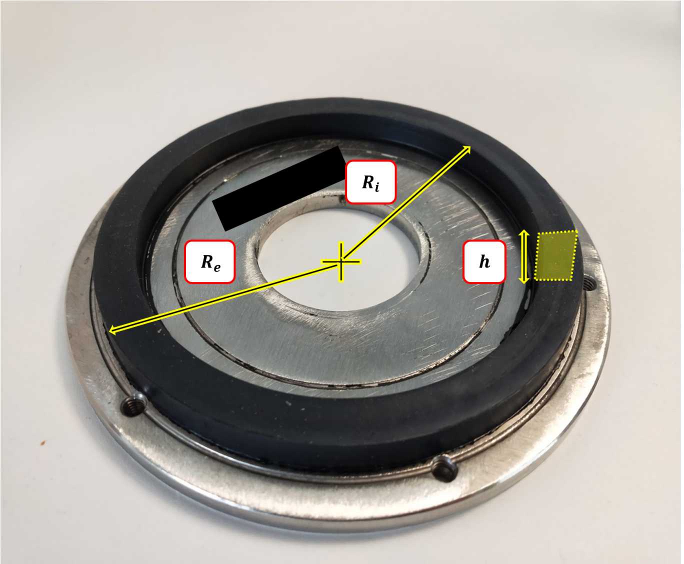
[redacted]

Figure 6.2: Rubber sample - geometrical parameters.

The substrate contains two main parts, a cylindrical base, and spherical heads, which are screwed on this base, as shown in Figure 6.3. The base was machined and pierced to accommodate 18 screws equally distributed around its perimeter at a radial distance of $R_m = (R_i + R_e)/2 = 57$ [mm] from the center, which faces the middle line of the rubber specimen. Each screw may hold a spherical head made of steel of radius $R_s = 4$ [mm].

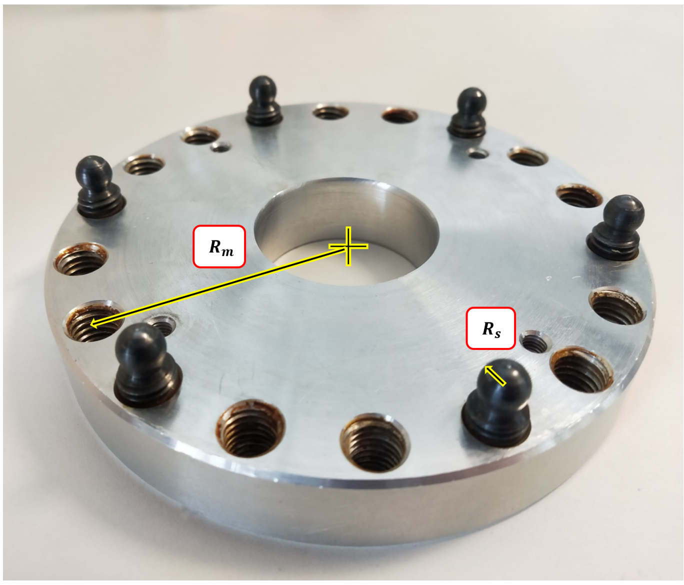

Figure 6.3: Substrate presented in a configuration containing six spherical indenters.

The 18 spheres' threads were screwed and then glued to the base's hole with a thread-locking fluid which can be unscrewed after a slight heating. This assembled substrate is attached to the Fixed Head Support (6.1) and is placed within a water tank (Figure 6.4).

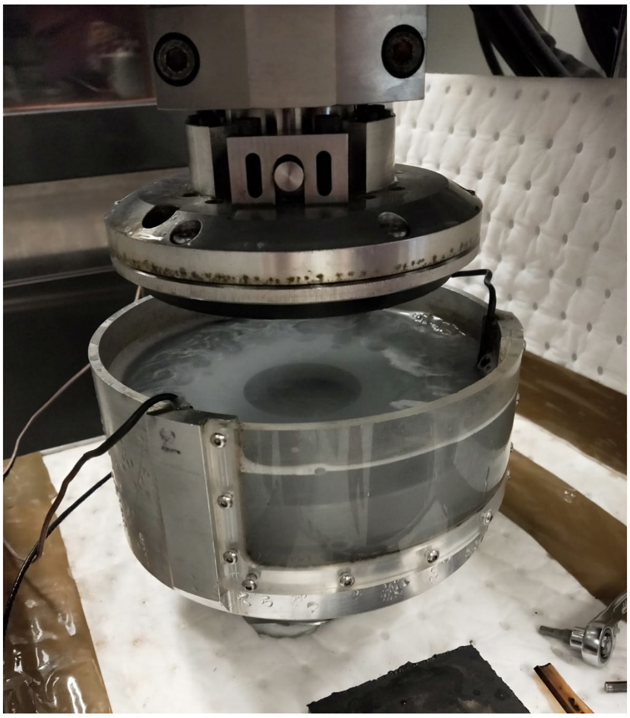

Figure 6.4: Substrate submerged inside a water tank attached to the Fixed Head support.

Last, to minimize local adhesion effects on the interface, a thin Teflon coating, a hydrophilic dry lubricant, was added to the spheres' surfaces. Moreover, Sinnozon (Sodium Dodecylbenzene Sulphonate) was added into the water tank to lower its surface tension to avoid local dewetting of the indenters.

Experimental procedure

Hereafter

- *a passage* denotes a sliding occurrence with a given target load history, target displacement/velocity history, and sample material;
- *a run* corresponds to a sequence of *passages* with varying load and displacement histories, performed on a single sample material;

In a given *passage*, the angular motion chains a clockwise rotation followed by a reverse anti-clockwise rotation. The velocity history during the clockwise phase is an angular acceleration of approximately 5000 [rad/s^2] up to a predefined terminal angular velocity, which is then kept until 1/6 (60°) of a full rotation is reached. Next, a deceleration is made until the angular velocity reaches zero. The angular position is reset and the same (but reversed) velocity history is applied. The quality of this trajectory depends on the sample-substrate contact and the feedback loop calibration of the P.I.D controller. For all *passages* described below, the temperature of the tank is kept at 15 °C, and the sphere-soil configuration involves 18 teflonated spheres screws. A single *run* is a protocol of 15 *passages* as listed in Table 6.1, split into two main steps:

- Accommodation: This preconditioning step corresponds to the first 6 *passages* and aims to remove/minimize irreversible non-linear effects by performing passages at large vertical loads $P_{run} = 1200$ [N] together with passages performed at a lower load $P_{run} = 40$ [N] but at different velocities $V_{run} = \omega R_m = [0.5; 1.0; 1.5]$ [m/s];
- Measure: this step regroups 9 *passages* combining three target loads $P_{run} = [100; 290; 580]$ [N] and three target velocities $V_{run} = \omega R_m = [0.5; 1.0; 1.5]$ [m/s].

Passage order	**Run type**	**Loading** [N]	**Velocity** [m/s]
1	Accommodation	40	1.0
2	Accommodation	1200	0.5
3	Accommodation	1200	1.5
4	Accommodation	40	0.5
5	Accommodation	40	1.0
6	Accommodation	40	1.5
7	Measure	100	0.5
8	Measure	100	1.0
9	Measure	100	1.5
10	Measure	290	0.5
11	Measure	290	1.0
12	Measure	290	1.5
13	Measure	580	0.5
14	Measure	580	1.0
15	Measure	580	1.5

Table 6.1: Defined protocol - single *run*. The vertical loads and sliding velocities indicated here correspond to the target values to be attained in the stabilized regime.

To summarize, a substrate containing 18 teflonated spheres is submerged in a water tank at 15 °C containing diluted Sinnozon. Within a *run*, a series of *passages* are made to first accommodate the material and then to observe the friction torque for different values of vertical loads and of sliding velocity.

6.3 Experimental results

Analysis of an individual passage

For illustration purposes, we first restrict ourselves to a specific *passage*, in this case, a *measure* of a PCY4-RT sample at 15 °C sliding over 18 teflonated spheres at 100 [N] and 0.5 [m/s], as described in the seventh line of Table 6.1. The measured quantities available in this single passage are time-sampled values of:

- Linear velocity $v(t)$ [m/s] (recovered from the time history of the angular position [rad]);
- Vertical force, $F_N(t)$ [N]
- Tangential force $F_T(t)$ [N] (recovered by dividing the torque [$\mathrm{N} \cdot \mathrm{m}$] by the radius R_m);

The time histories of $F_N(t)$ [N] and $\omega_z(t) = v(t)/R_m$ [rad/s] are the values resulting from their given PID control strategy. Due to the imperfections of this control strategy, these time histories are not constant as displayed in Figure 6.5. By contrast, the observed tangential force $F_T(t)$ [N] is entirely due to the applied mechanical loading induced by the controlled vertical load and sliding velocity. The vertical lines displayed in the output separate three main steps occurring during a passage:

1. Positioning stage: The vertical-rotating head (see Figure 6.1) is lowered down until a first normal reaction is detected within the range $[-1.5, +1.5]$ [N];
2. Pre-indentation stage: The vertical-rotating head is further lowered down at zero angular velocity and a slower pace until a prescribed normal force close to 40 [N] is detected;
3. Sliding/indentation stage: The vertical-rotating head begins its rotation at a given angular acceleration of around 5000 [rad/s^2] and the vertical load is increased to reach the expected target value. Once the rotation of the head reaches 60° the angular velocity is reversed so that it returns to the original position with the same target velocity and vertical load.

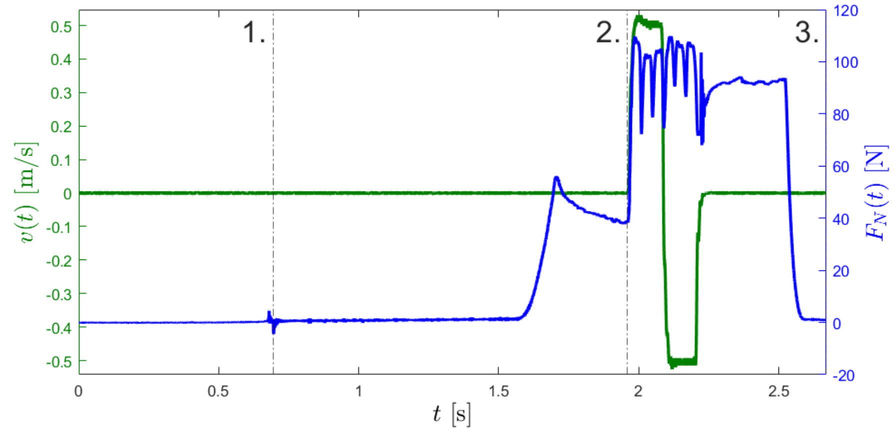

Figure 6.5: Inputs - $F_N(t)$ and $v(t)$ as resulting from the imposed PID strategy - test of a PCY4-RT specimen sliding over 18 spheres at 15 °C under a target load 100 [N] and a target angular velocity of 0.5 [m/s].

The time history of the resulting tangential force is displayed in Figure 6.6.

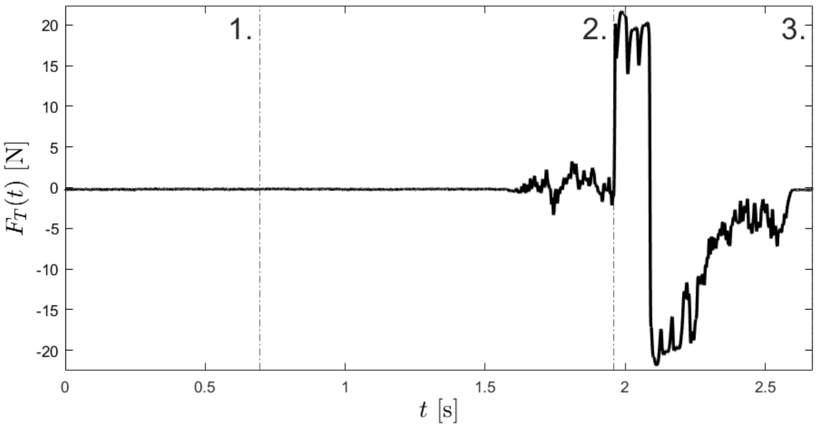

Figure 6.6: Output - Time history of the tangential force $F_T(t)$ in Newton - test of a PCY4-RT specimen sliding over 18 spheres at 15 °C under a target load 100 [N] and at a target angular velocity of 0.5 [m/s].

We can see in Figures 6.5 and 6.6, oscillations occurring at times corresponding to space intervals of 20°. This indicates that the pre-indentation phase has left indentations on the rubber specimen in front of each of the 18 spheres, resulting in a decrease of the vertical load when the indenters come to match these preexisting indentations.

The normal force in Figure 6.5 and the tangential force in Figure 6.6 also reveals that, for the most part, the consigned normal load of 100 [N] was attained during both the clockwise and anti-clockwise direction. However, for a larger loading of 290 [N], the load only stabilizes in the second (anti-clockwise) portion of the sliding, as shown in Figure 6.7.

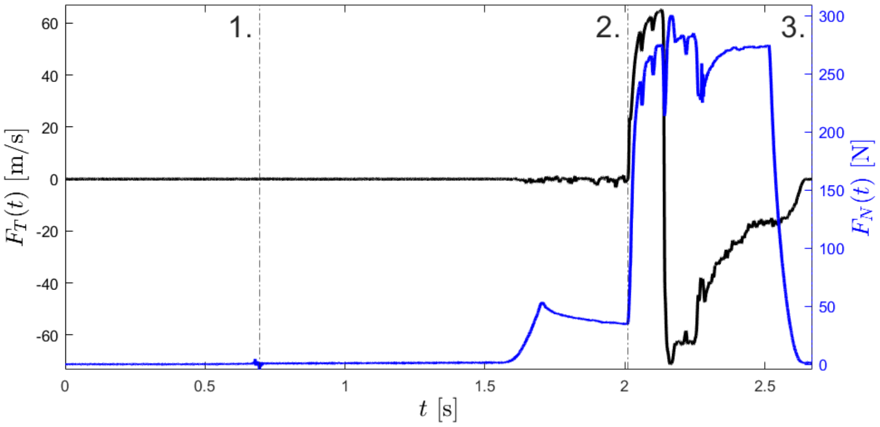

Figure 6.7: time history of $F_T(t)$ and $F_N(t)$ - PCY4-RT specimen at 15 °C sliding over a substrate of 18 spheres under a target vertical load of 290 [N] at a speed of 0.5 [m/s].

Comparative Measure Analysis

To objectively compare study cases with different working points, the temporal data of tribological variables $F_T(t)$ and $F_N(t)$ are plugged into a single curve plotting one variable as a function of the other. Figure 6.8 displays the interval of the data from which the mean of those tribological variables are recovered. The data are recovered from time regions where the linear/angular velocity and the normal load are mostly stabilized. Moreover, only the anti-clockwise sliding portion is considered, as the normal load value is closest to the imposed target.

The normal load and velocity range of interest to be compared numerically is illustrated in Figure 6.9 the curve obtained in the case of a (PCY4-RT) specimen at a temperature of 15 °C sliding over a substrate of 18 spheres.

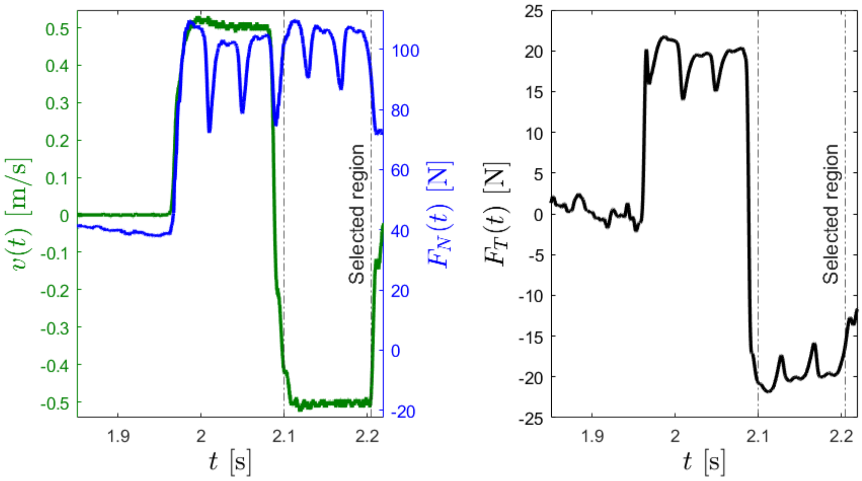

Figure 6.8: Selected region of input/output - $F_T(t)$ - PCY4-RT; 15 °C; 100 [N]; 0.5 [m/s]; 18 spheres.

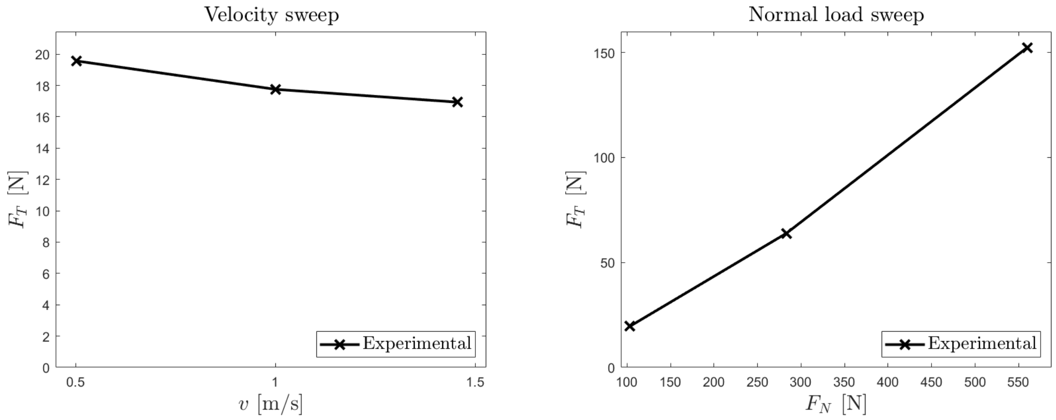

(a) Velocity sweep

(b) Normal load sweep

Figure 6.9: Time averaged values of $\tilde{F}_T$ vs time average values $\tilde{F}_N$ at different loads and different sliding velocities. The values are averaged during the stabilized part of the experiments run here for PCY4-RT at 15 °C sliding over 18 spheres.

6.4 Numerical results

In this state, the experimental conditions were reconstructed as an Initial-Boundary-Value-Problem (IBVP), assuming that the interface between the rubber and the beads was perfectly smooth.

Initial-boundary value problem

Figure 6.10 describes the domain of study.

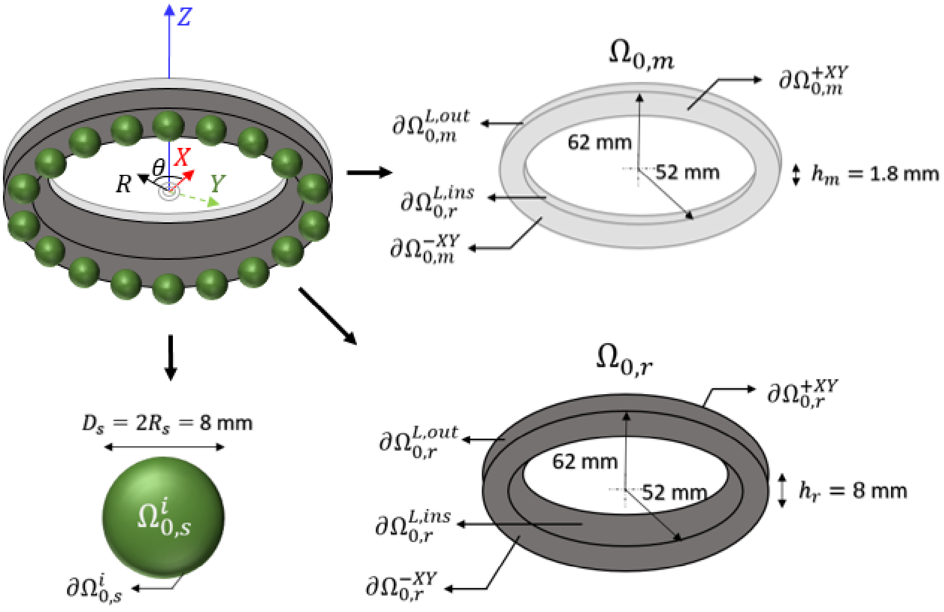

Figure 6.10: System components - principal geometrical bodies.

It involves a torus of rectangular cross-section, $\Omega_{0,r}$, containing the rubber mix and 18 rigid spheres $\Omega^i_{0,s}$. The rubber is quasi-incompressible, isotherm, and viscoelastic, governed by one of the viscoelastic laws introduced in Chapter 5. It has a constant mass density ρ_0 and inertial contributions are taken into account. As indicated in Section 6.3, the rubber sample is attached to a rigid plate, $\Omega_{0,m}$, also toroidal with a rectangular cross-section that is glued on the top of $\Omega_{0,r}$. In more detail, we have obvious notations

$$\Omega_{0,r} = \{\mathbf{x} \in \mathbb{E}^3 \mid 0 < \mathbf{x}\cdot\mathbf{e}_Z < h_r \;\&\; R_i < \mathbf{x}\cdot\mathbf{e}_r < R_e\}$$

$$\Omega_{0,m} = \{\mathbf{x} \in \mathbb{E}^3 \mid h_r < \mathbf{x}\cdot\mathbf{e}_Z < h_r + h_m \;\&\; R_i < \mathbf{x}\cdot\mathbf{e}_r < R_e\} \tag{6.4.1}$$

$$\Omega^i_{0,s} = \{\mathbf{x} \in \mathbb{E}^3 \mid |\mathbf{x} - \mathbf{x}_i| < R_s\}, \quad i = 1, ..., 18. \tag{6.4.2}$$

with boundaries

$$\begin{aligned}
\partial\Omega_{0,r} &= \partial\Omega^{+XY}_{0,r} \cup \partial\Omega^{-XY}_{0,r} \cup \partial\Omega^{L,out}_{0,r} \cup \partial\Omega^{L,ins}_{0,r} \\
\partial\Omega_{0,m} &= \partial\Omega^{+XY}_{0,m} \cup \partial\Omega^{-XY}_{0,m} \cup \partial\Omega^{L,out}_{0,m} \cup \partial\Omega^{L,ins}_{0,m} \\
\partial\Omega^i_{0,s} &= \partial\Omega^i_{0,s} \quad \text{for} \quad i = 1, ..., 18.
\end{aligned} \tag{6.4.3}$$

Initial and boundary conditions are then specified as

$$\left\{\begin{array}{ll} \textit{Initial conditions} & \\ \mathbf{x}(\mathbf{X},0)=\mathbf{X} & \forall\mathbf{X}\in\Omega_{0,r},\Omega_{0,m},\Omega_{0,s} \\ \dot{\mathbf{x}}(\mathbf{X},0)=\mathbf{0} & \forall\mathbf{X}\in\Omega_{0,r},\Omega_{0,m},\Omega_{0,s} \\ \textit{Boundary conditions} & \\ \dot{\mathbf{x}}(\mathbf{X},t)=(\mathbf{x}_s\cdot\mathbf{e}_r)\bar{\omega}(t)\mathbf{e}_\theta & \forall(\mathbf{X},t)\in\partial\Omega^{i}_{0,s}\times(0,T] \\ \mathbf{x}_r(\mathbf{X},t)=\mathbf{x}_m(\mathbf{X},t) & \forall(\mathbf{X},t)\in\partial\Omega^{+XY}_{0,r},\partial\Omega^{-XY}_{0,m}\times(0,T] \\ \int_{\partial\Omega_0}\mathbf{e}_Z\cdot\mathbf{P}\mathbf{e}_Z\,d\Omega=\bar{F}(t) & \forall t\in(0,T] \\ \mathbf{x}(\mathbf{X},t)=u_z(t)\mathbf{e}_Z+\mathbf{X} & \forall(\mathbf{X},t)\in\partial\Omega^{+XY}_{0,m}\times(0,T], u_z(t)\text{ unknown} \end{array}\right. \tag{6.4.4}$$

The first line on *Boundary conditions* specifies the relative angular velocity between the sphere and the sample (see Figure 6.10), $\bar{\omega}(t)$. The second line states that the lower surface of the metallic plate is glued on the top of the rubber specimen. The third line imposes a given resulting load, $\bar{F}(t)$, across the upper boundary of the metallic plate, which consequently leads to a pure vertical displacement of unknown intensity ($\mathbf{u}(\mathbf{X},t) = u_z(t)\mathbf{e}_z$), according to the last boundary condition, where the unknown vertical velocity is the Lagrange multiplier of the imposed vertical load.

The imposed time history for angular velocity, $\bar{\omega}(t)$, and vertical load, $\bar{F}(t)$, are recovered from measurements. Figure 6.5 displays the seventh *passage* temporal data from the protocol (see Table 6.1).

Due to time constraints and computational power, some simplifications were necessary:

- The viscoelastic models used are identified using preconditioned mechanical data, thus *passages* 1-6 are not modeled numerically since they serve to precondition the sample (see Section 6.3);
- The time duration of a single passage is 2.5 seconds. This interval is relatively large for the explicit solver considered, requiring 40 hours of CPU to be simulated. Thus, although a single experimental sample undergoes all *passages* 7-15 serially, the simulation will limit itself to an individual *passage*.

Simulations are restricted to *passages* 7, 8, 9, 10, and 14 (see Table 6.1). Those passages provide the minimal set necessary for sensitivity analysis in velocity (at low loads) and loading (at low velocities).

The finite element model to be used is displayed in Figure 6.11. Each sphere contains 384 rigid 3D linear hexahedral elements. The rubber domain contains 12288 deformable 3D hexahedral elements, the top 6144 located in the upper half using first-order elements, and the bottom 6144 ones which undergo larger deformation using quadratic elements. The metallic plate contains a grid of 1536 rigid 3D hexahedral elements matching the finite element grid used for the rubber on the interface. Two constitutive models will be considered: *Model A* (respectively *Model B*) is the linear (respectively non-linear) viscoelastic model of Section 4, as calibrated in Section 5.

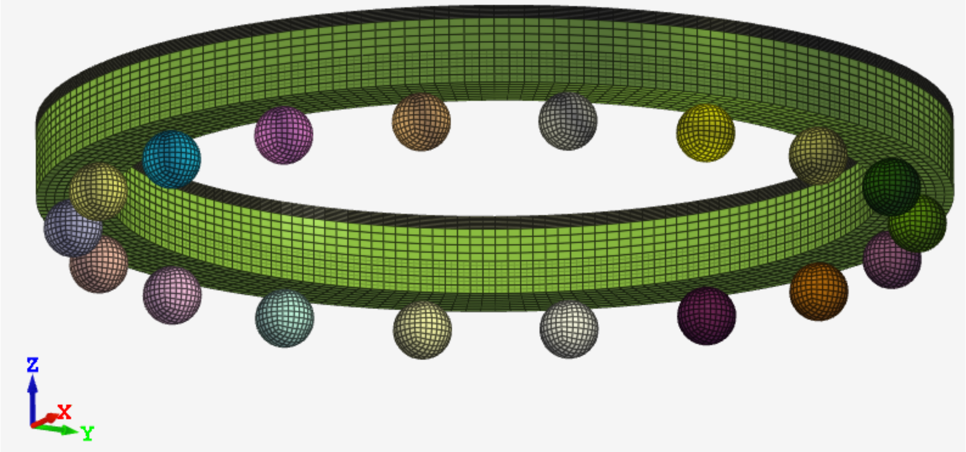

Figure 6.11: Finite Element Model used for the simulation of the multi-sphere contact problem within the Impetus Afea environment.

The accuracy of this finite element model was checked by running a test case with a coarser, intermediary, and finer mesh. In the contact interface, the diagonal length of the element face was kept fixed as $l_d^s \approx 0.97$ [mm], whilst the rubber element diagonal length varies with $l_d^r \approx [2.96, 2.26, 0.98]$ [mm]. The average tangential force defined in Section 6.3 is used as the reference output to evaluate each mesh size, with results displayed in Table 6.2.

l_d^r [mm]	$\tilde{F}_T$ [N]	ϵ_{rel}^{finer} [%]
2.96	16.67	20.51
2.26	21.25	4.91
0.98	22.34	0.0

Table 6.2: Convergence evaluation for average tangential force and rubber element diagonal length at the contact interface.

The results from Table 6.2 ratifies a convergence for this simple contact, however, for each study case, the finer mesh requires 100 hours of computational time for its completion. Thus, the present study limits itself to the intermediary mesh size (2.26 [mm]), implying a relative error of 4.9%, if the finer mesh (0.98 [mm]) is used as a reference.

Two constitutive models will be considered: *Model A* is the linear viscoelastic model of Section 3.2.4, and *Model B* corresponds to the general non-linear viscoelastic model using the enriched viscosity of Section 5.2.2.

Result of the reference case at low velocity and load

For *passage* 7 (Table 6.1), the specimen undergoes the smallest solicitation (vertical load of 100 [N] and angular velocity of 0.5 [m/s]). At the contact between the rubber and the spheres, the local friction coefficient is first set to zero, $\mu_{loc} = 0$. This choice will be reviewed later on. Lastly, the material parameters are defined in Table 5.18.

For this particular *passage*, we verify that the boundary conditions are properly imposed by comparing in Figure 6.12 the reaction vertical force and angular velocity given by the numerical model to the experimental values.

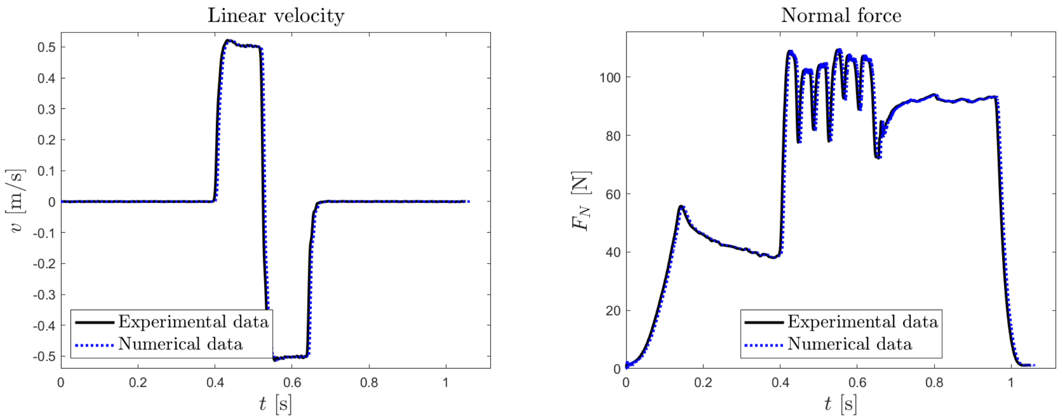

(a) Angular velocity (b) Vertical load

Figure 6.12: $F_N(t)$ and $\omega_z(t)$ comparison - Numerical values (blue) induced by the boundary conditions and their experimental counterpart (black).

We now compare the experimental tangential force (as displayed in Figure 6.6) with the numerical responses for Model A and B, displayed in Figure 6.13.

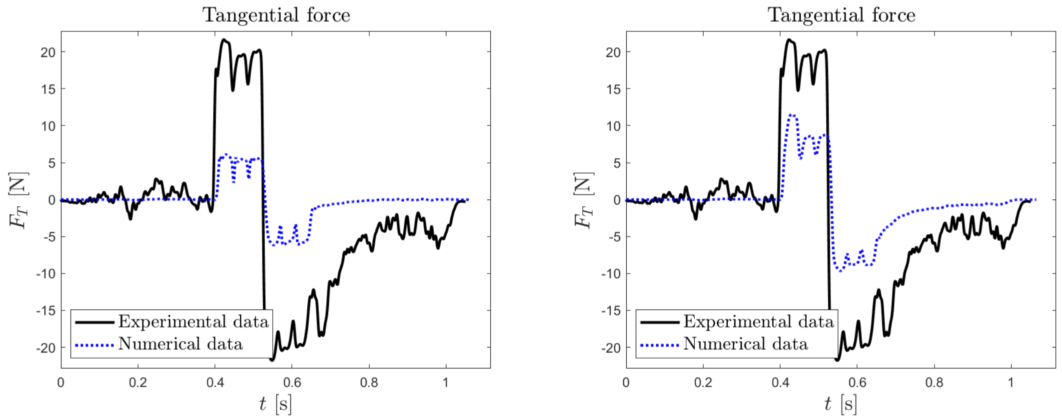

(a) Model A (b) Model B

Figure 6.13: $F_T(t)$ comparison - Numerical (blue) and experimental (black) values. The above numerical values were obtained assuming that there was no local friction between the spheres and the rubber interface.

Figure 6.13 draws three main observations. The first one is the presence of the 3 oscillations in each rotating direction which appear in both numerical and experimental results. This is clearly due to the apparition of 18 hollows on the rubber lower face, which are formed by the indenting spheres during the pre-indentation phase (see Section 6.3) and are not fully relaxed afterward. These oscillations do indeed occur in a 20° span, which corresponds to the spacing between the 18 spheres. These hollows are seen in Figure 6.14 which displays the vertical displacement at the rubber's lower face as predicted by the linear model. During experiments, this effect is then retroactively magnified by the normal load, as the test is PID-controlled (see Section 6.3).

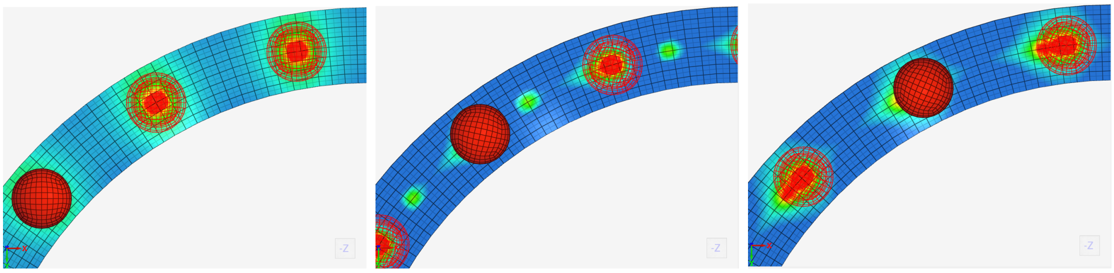

(a) $\theta(t) = 0°$ (b) $\theta(t) = 10°$ (c) $\theta(t) = 23°$

Figure 6.14: Color view of the Z displacement field (Worm's-eye view) at the rubber lower face-angular position $\theta(t)$ time frame - Visualization using Model A.

When comparing both numerical responses, Model B tends to have a higher initial peak in tangential force which is then drastically reduced. This effect is likely attributed to its non-linear viscosity, formulated in (5.2.29) and represented in Figure 5.15 (see Section 5.2.2). The viscosity for Model B increases with deformation, a sensitivity not present for Model A. Any deformed portion of the rubber with Model B takes longer to recover, creating a "tunnel-like" indentation on top of the performing, as displayed in 6.15. As the rubber takes longer to relax, the sphere receives progressively less resistance from the rubber material, resulting in less tangential resistance.

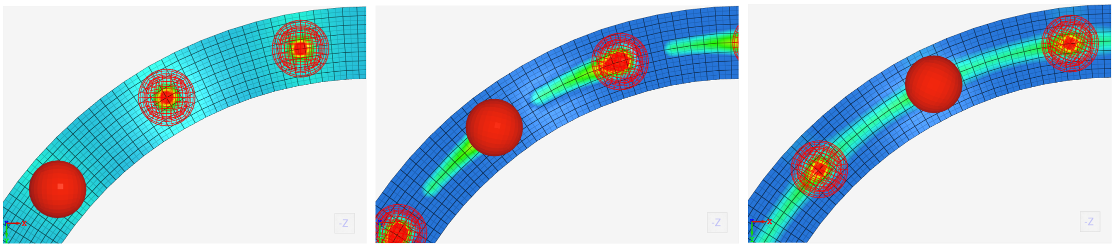

(a) $\theta(t) = 0°$ (b) $\theta(t) = 10°$ (c) $\theta(t) = 23°$

Figure 6.15: Color view of the Z displacement field (Worm's-eye view) at the rubber lower face-angular position $\theta(t)$ time frame - Visualization using Model B.

The second observation is the difference between Model A and Model B's tangential force in absolute values. Locally, the tangential force originates from an asymmetric contact pressure distribution on the sphere due to the material hysteresis (see Section 2.13). Figure 6.16 presents the pressure distribution on a single sphere when $\theta = 10°$ for both models. Figure 6.16b highlights a larger lack of symmetry for Model B in the sliding direction, which, when integrated across the contact area results in an overall higher tangential force for Model B.

The last observation is the fact that the experimental value of the tangential force is approximately two times larger than the numerical reconstructions. The latter assumed that there was no local friction between the rubber and the teflonated beads. It seems that this assumption is not true. There might be two reasons for the persistence of local friction: viscous dissipation in the inter-facial film or local dewetting inducing potential flash heating and local mechanical friction between the rubber and the teflonated beads.

Due to the large-scale nature of the test, local flash-heating effects should have a low impact on the total volumetric dissipation, especially with water-immersed samples. On the other hand, due to the limited range of sliding velocities, the potential viscous contribution of the interfacial film could be supposed to be rather uniform in the experiment. Similarly, even if dewetting occurs, the friction of the Teflon coating has a very low sensitivity to sliding velocity and pressure. Thus, as a first-order approximation, viscous

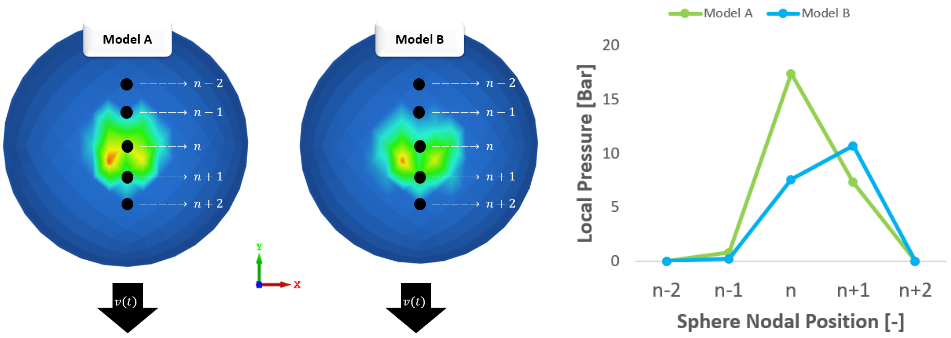

(a) Field

(b) Sliding cross-section

Figure 6.16: Contact pressure - field and cross-section display - range of $[0, 25]$ [Bar].

dissipation in the inter-facial film and local friction after dewetting can be modeled by a constant but low non-zero friction coefficient. To verify the relevance of the presence of such a local friction coefficient, we have tested different values of the local friction coefficients μ_{loc} in our numerical simulations. Figure 6.17 displays the results obtained with the optimal choices of this coefficient and presents a much better match with the experimental result for the reference test case.

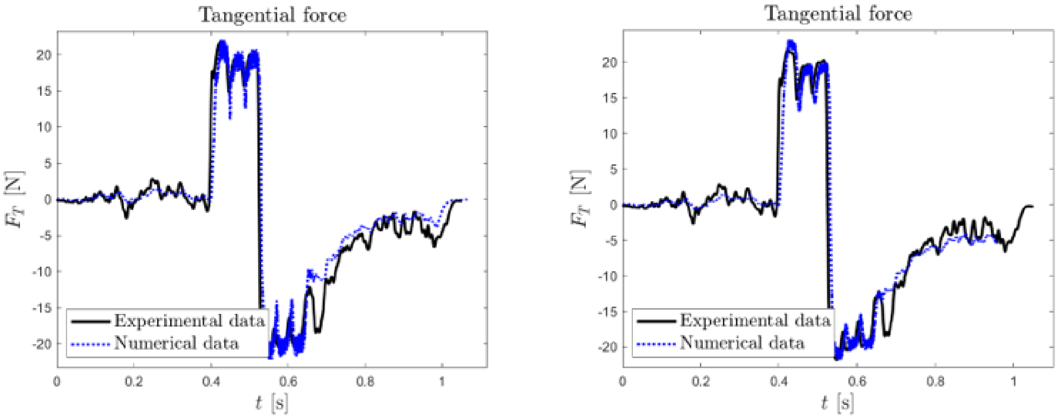

(a) Model A - $\mu_{loc} = 0.15$

(b) Model B - $\mu_{loc} = 0.1$

Figure 6.17: $F_T(t)$ comparison - Numerical (blue) and experimental (black) values - *Passage* 7, $v = 0.5$ [m/s], nominal $F_N = 100$ [N]. The above numerical values were obtained using a best-fitted value of the local friction coefficient between the spheres and the rubber interface.

Velocity sweep at low loads

The velocity sweep consists of adding *passages* 8 and 9 (Table 6.1) with nominal velocities respectively equal to $[1.0, 1.5]$ [m/s] while keeping the nominal load as 100 N. This analysis considers a non-zero and constant *local* friction coefficient for Model A and Model B as $\mu_{loc}^A = 0.15$ and $\mu_{loc}^B = 0.1$, respectively. The resulting tangential force for Model A and Model B are shown in Figure 6.18 and Figure 6.19, respectively.

Figure 6.20 takes the average of the second rotation during stabilized angular velocity. From Figures 6.18 and 6.19, we observe a better average response for Model B, decreasing with velocity. For Model A, the average tangential force *increases* with the velocity, which is expected since an increase in velocity brings the model closer to its $\tan(\delta)$ peak inducing a larger dissipation.

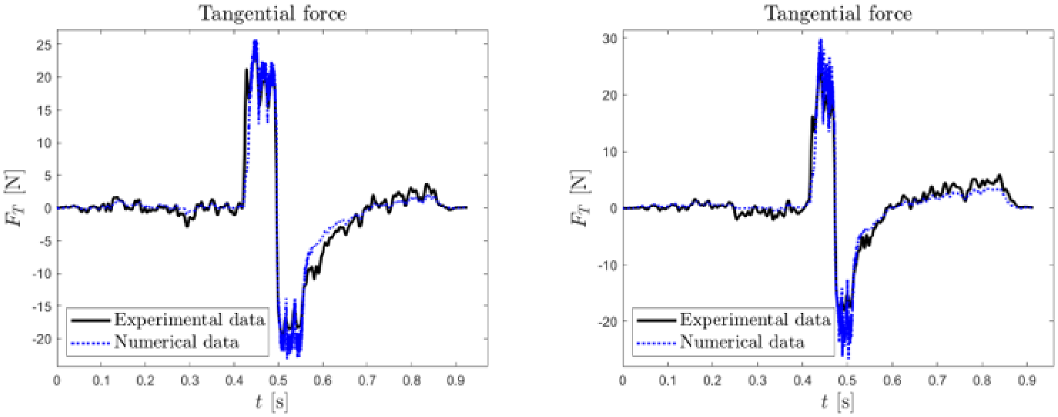

(a) $v = 1.0\ m/s$ (b) $v = 1.5\ m/s$

Figure 6.18: Tangential force $F_T(t)$ - Velocity sweep - Model A. Observe the excess of friction force predicted at larger velocities.

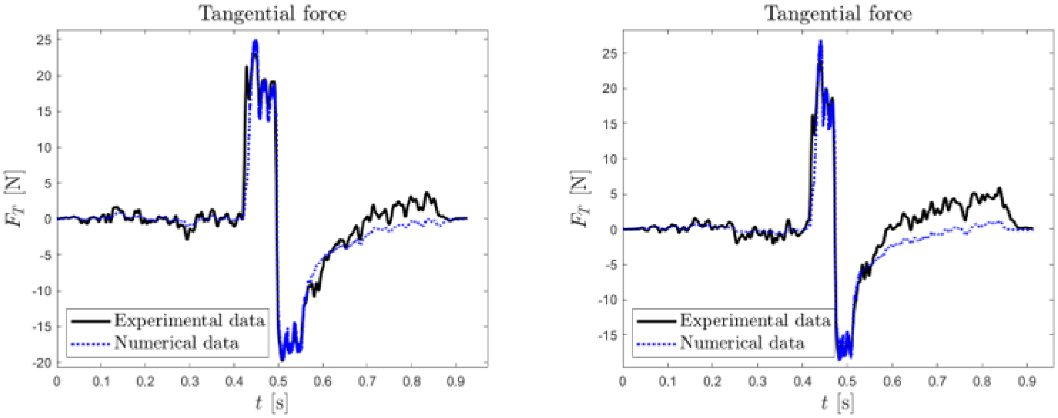

(a) $v = 1.0\ m/s$ (b) $v = 1.5\ m/s$

Figure 6.19: Tangential force $F_T(t)$ - Velocity sweep - Model B. The prediction force remains consistent at larger sliding velocities.

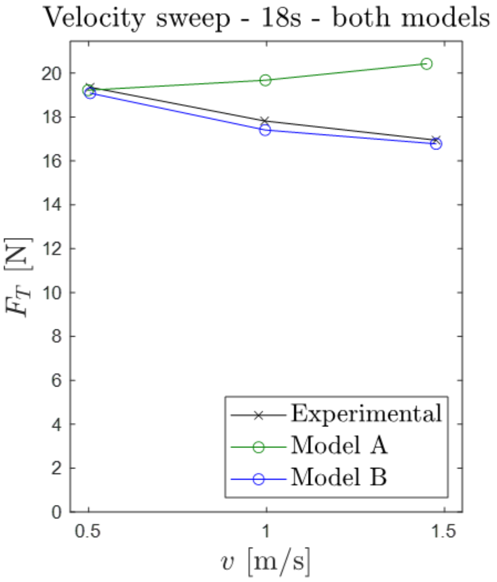

Figure 6.20: $\tilde{F}_T$ - sweep of $\tilde{v}$ - PCY4-RT; 15 °C; 18 spheres.

Load sweep at low velocities

The load sweep consists of adding *passages* 10 and 13 (Table 6.1) where the nominal vertical loads are respectively $[290, 580]$ [N] while keeping the nominal sliding velocity as 0.5 [m/s]. This sensitivity analysis also considers a non-zero and constant *local* friction coefficient for Model A and Model B as $\mu_{loc}^{A} = 0.15$ and $\mu_{loc}^{B} = 0.1$, respectively (see Section 6.4). The resulting tangential force for Model A and Model B are shown in Figure 6.21 and 6.22, respectively.

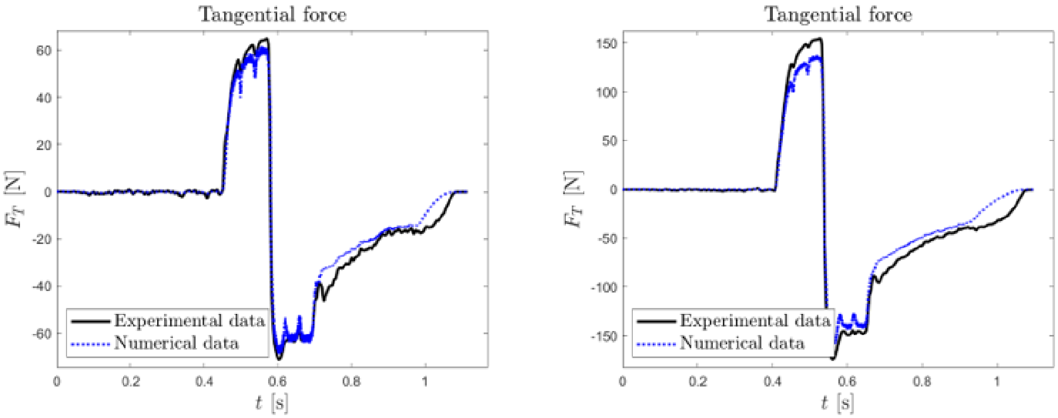

(a) $F_N = 290\ N$, $v = 0.5\ m/s$ (b) $F_N = 580\ N$, $v = 0.5\ m/s$

Figure 6.21: Tangential force $F_T(t)$ - Load sweep - Model A.

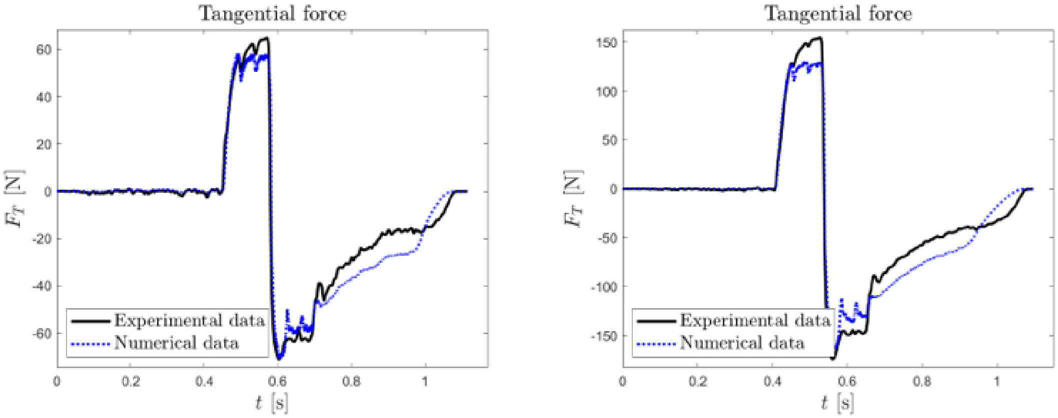

(a) $F_N = 290\ N$, $v = 0.5\ m/s$ (b) $F_N = 580\ N$, $v = 0.5\ m/s$

Figure 6.22: Tangential force $F_T(t)$ - Load sweep - Model B.

Figure 6.23 takes the average of the second rotation when the angular velocity is stabilized to better evaluate the trend of this sweep in nominal load. In Figures 6.21 and 6.22, we observe this time a slightly better result obtained by Model A. For Model B, as the sliding progresses, the tangential force peaks progressive decline. This effect seems to be related to an excessive "tunnel-like" geometrical mechanism, associated with an over-prediction of the viscosity at large loads, which lowers the tangential force as the sliding continues.

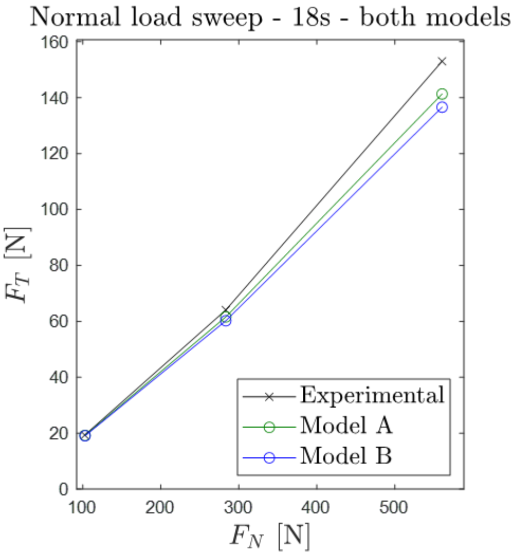

Figure 6.23: $\tilde{F}_T$ - sweep of $\tilde{F}_N$ - PCY4-RT; 15 °C; 18 spheres.

In conclusion, the presence of the non-linear viscosity in Model B is promising and can capture the sensitivity of the friction force to the sliding velocity (with a constant local friction coefficient). However, from the load sweep, we conclude that its evolution at large loads and moderate velocity is exaggerated. This indicates that we should try to develop a better-coupled influence of the deformation intensity and velocity on the local viscosity.

Chapter 7

Multiscale strategy

7.1 Mechanical problem for rough contact

The main objective of this chapter is to be able to reconstruct a numerical solution that matches and explains the experimental results presented in Chapter 4.

7.1.1 Geometrical description

The situation of interest is a contact problem between a deformable body, $\Omega_{0,r}$, of the rubber mix containing the *slave* surface and a rigid body, $\Omega_{0,s}$, containing the measured *slave* surface, which is textured via the procedure described in 4.3. In addition, as explained in Chapter 4, the Linear Tribometer HSLFT applies controlled pressure to a system attached to the movable sliding head, containing an attached aluminum plate where the rubber mix sculpture is glued. For this reason, a rigid body, $\Omega_{0,m}$, representing the metallic plate is also considered and attached to the top of the rubber mix. All bodies are described according to Figure 7.1 for the bulk specimen or to 7.2 for the leading edge specimen. The boundaries are respectively

$$\partial\Omega_{0,m} = \partial\Omega_{0,m}^{+XY} \cup \partial\Omega_{0,m}^{-XY} \cup \partial\Omega_{0,m}^{+XZ} \cup \partial\Omega_{0,m}^{-XZ} \cup \partial\Omega_{0,m}^{+YZ} \cup \partial\Omega_{0,m}^{-YZ} \tag{7.1.1}$$

$$\partial\Omega_{0,s} = \partial\Omega_{0,s}^{+XY} \cup \partial\Omega_{0,s}^{-XY} \cup \partial\Omega_{0,s}^{+XZ} \cup \partial\Omega_{0,s}^{-XZ} \cup \partial\Omega_{0,s}^{+YZ} \cup \partial\Omega_{0,s}^{-YZ} \tag{7.1.2}$$

$$\partial\Omega_{0,r} = \partial\Omega_{0,r}^{+XY} \cup \partial\Omega_{0,r}^{-XY} \cup \partial\Omega_{0,r}^{+XZ} \cup \partial\Omega_{0,r}^{-XZ} \cup \partial\Omega_{0,r}^{-YZ} \tag{7.1.3}$$

.

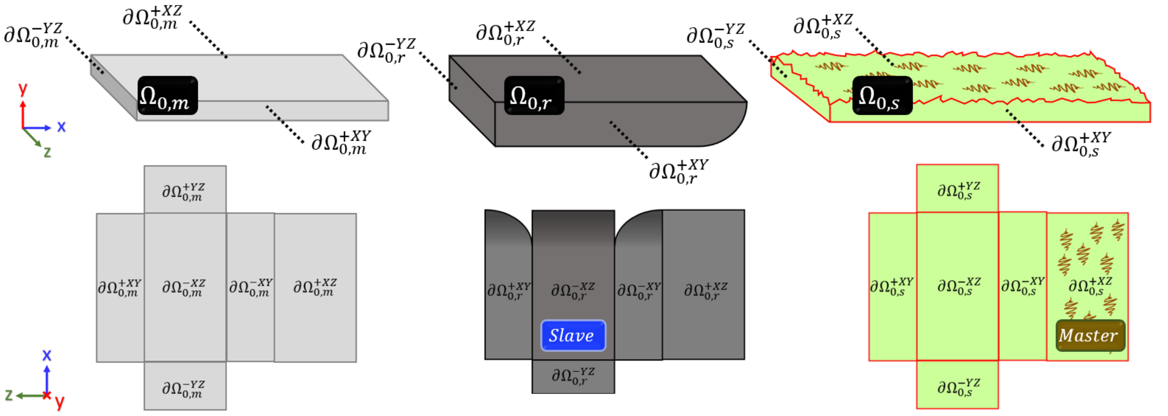

Figure 7.1: Representation of the three bodies considered for the contact case.

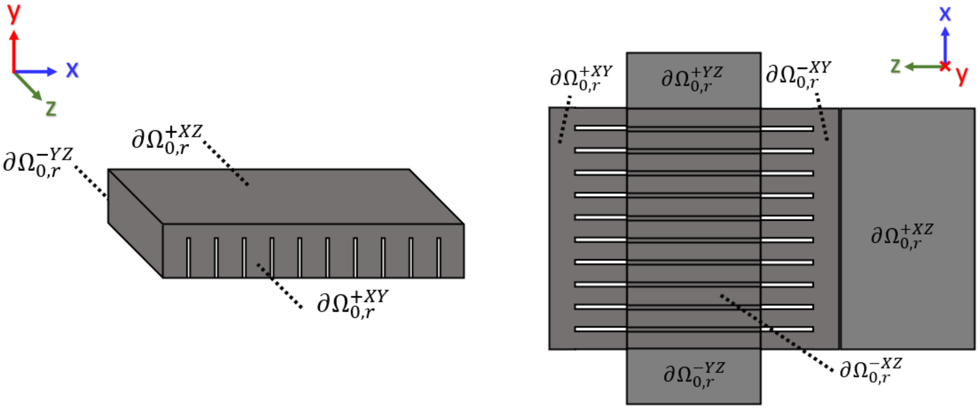

Figure 7.2: Representation of the deformable rubber mix body considered lamelized sculpture.

More precisely, for a sculpture with N_l^o lamellae (and $N_l^o + 1$ individual tread blocs), each tread block (i) contains its own Leading Edge, $\partial\Omega_{0,r,LE(i)}^{-XZ}$, its opposite *Trailing Edge*, $\partial\Omega_{0,r,TE(i)}^{-XZ}$, a base $\partial\Omega_{0,r,B(i)}^{-XZ}$ and (exempting the first and last) two lamellae attached, as shown schematically in Figure 7.3.

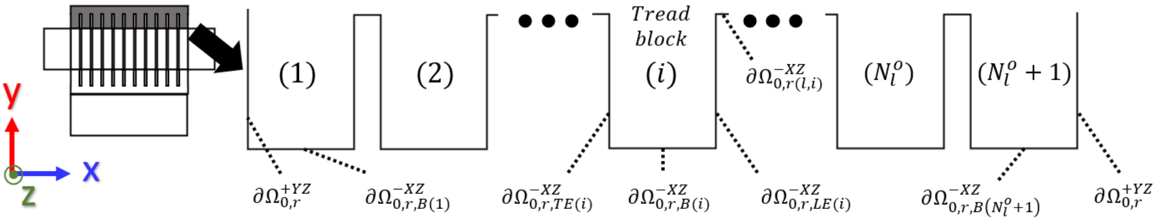

Figure 7.3: Detailed description of Leading Edge boundaries.

Therefore, an additional relation for a portion of the boundaries with respect to the tread block is also considered

$$\begin{aligned}\partial\Omega_{0,r}^{-XZ} = \bigcup_{i=1}^{N_l^o} &\left(\partial\Omega_{0,r,TE(i)}^{-XZ} \cup \partial\Omega_{0,r,B(i)}^{-XZ} \cup \partial\Omega_{0,r,TE(i)}^{-XZ}\right) \\ &\cup \Omega_{0,r,TE(N_l^o+1)}^{-XZ} \cup \partial\Omega_{0,r,B(N_l^o+1)}^{-XZ}\end{aligned} \tag{7.1.4}$$

.

Observe that for the LE configuration, as *self-contact* between rubber blocks can occur (see Figure 2.17 and 4.4). The Leading and Trailing edge of a single block (i) $(\partial\Omega_{0,r,LE(i)})$ can potentially interact with their respective neighbors, also, its base $(\partial\Omega_{0,r,B(i)})$ can interact with itself due to curling effects.

7.1.2 Construction of the Initial Boundary Value Problem

Regardless of the choice between Bulk or Leading Edge sculpture, and apart from contact, the specific boundary and initial value conditions for this case are defined as

$$\begin{cases} \textit{Initial conditions} & \\ \mathbf{x}(\mathbf{X},0) = \mathbf{X} & \forall \mathbf{X}^{(i)} \in \Omega_{0,r}, \Omega_{0,s}, \Omega_{0,m} \\ \dot{\mathbf{x}}(\mathbf{X},0) = \mathbf{0} & \forall \mathbf{X}^{(i)} \in \Omega_{0,s} \\ \textit{Boundary conditions} & \\ \mathbf{x}_r(\mathbf{X},t) = \mathbf{x}_m(\mathbf{X},t) & \forall (\mathbf{X},t) \in \partial\Omega_{0,r}^{+XZ}, \partial\Omega_{0,m}^{-XZ} \times (0,T] \\ \dot{\mathbf{x}}(\mathbf{X},t) = -\bar{v}(t)\mathbf{e}_X & \forall (\mathbf{X},t) \in \partial\Omega_{0,s}^{-YZ} \times (0,T] \\ \mathbf{x}(\mathbf{X},t) = u_y(t)\mathbf{e}_Y + \mathbf{X} & \forall (\mathbf{X},t) \in \partial\Omega_{0,m}^{+XZ} \times (0,T], u_y(t) \text{ unknown} \end{cases} \tag{7.1.5}$$

.

where the unknown vertical displacement, $u_y(t)$ results from an given homogeneous distributed pressure $\bar{p}(t)$ applied on the upper boundary of the metallic place with

$$\mathbf{PN} = -\bar{p}(t)\mathbf{e}_Y \quad \forall (\mathbf{X},t) \in \partial\Omega_{0,m}^{+XZ} \times (0,T] \tag{7.1.6}$$

The initial position of all bodies eq.$(7.1.5)_{1,2}$ is represented in Figure 7.4, where the rubber mix base is already in contact with the rough surface, and the base of the metallic plate is "glued" to the top of the rubber body, as also imposed by eq. $(7.1.5)_3$ until the end of the simulation. We describe the motion in the frame of reference defined by the moving head.

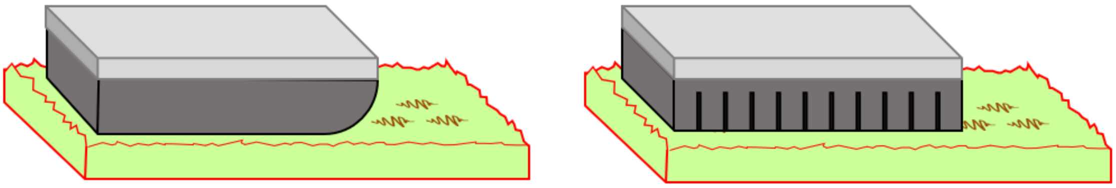

Figure 7.4: Assembled bodies and representation of their initial position.

The time histories of the imposed pressure, $\bar{p}(t)$, and velocity, $\bar{v}(t)$, are taken from the experimental procedure. Although their absolute values change depending on the test and sample evaluated, their evolution follow a similar procedure, represented in Figure 7.5.

First a compression phase occurs, where the pressure gradually increases to a set maximum, $\bar{p}_{max}$ at time t_{comp}. Right after, an accommodation time period, Δt_{accom},

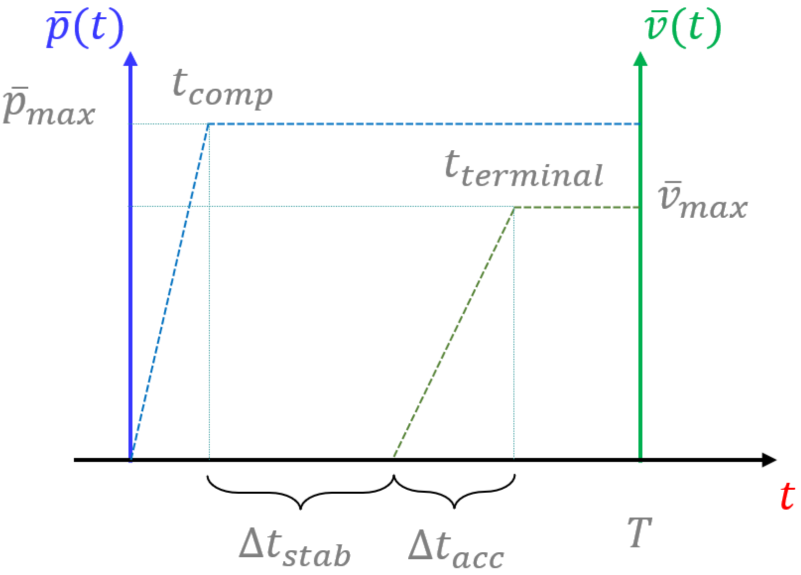

Figure 7.5: History of pressure and evolution for numerical tribological study cases.

takes place with constant maximum pressure. Once finished, an acceleration of the rough surface occurs during Δt_{acc} up to a set maximum velocity, $\bar{v}_{max}$, reached at time $t_{terminal}$. From this point forward, until the end of the run at T, enough time is given so that the friction coefficient reaches a stabilized sliding condition.

As previously discussed in section 3.5, three important characteristics are recalled for contact problems: (1) penetrability constraints are defined in all positions $\mathbf{X}$, belonging to slave surface in the reference configuration for a given pair of motions in the *current* configuration parameterized by it (i.e. $\hat{\mathbf{n}}^s = \hat{\mathbf{n}}^s(\mathbf{X}, t)$); (2) The frictional traction vector is defined by resolving the Piola traction $\bar{\mathbf{T}}(\mathbf{X}, t)$ in terms of the spatial basis to obtain the (spatial) frictional traction $\mathbf{t}_N$; (3) the formulation of Hertz-Signori-Moreau and Kuhn-Karush-Tucker inequalities follows the enforcement of constraints via the penalty method (with the use of ϵ_N and ϵ_T) defined in section 3.5.6. More information can be found in the works of Laursen [47] or Wriggers [66].

Herein, when the Bulk geometry is considered, only surface-rubber contact is expected (no self-contact). Since the rough surface is rigid, its contacting surface is readily chosen as the master surface. For the Leading Edge geometry the problem must account for self-contact conditions originated from curling effects and inter-tread block interactions. To solve this problem, a symmetric treatment is used, where both master-slave states are considered simultaneously for both surfaces.

The contact conditions will include a friction force associated to an *ad hoc* friction coefficients for rubber-rubber contact, $\mu_{r,r} = 1$, and rubber-surface contact, $\mu_{s,r}$, which shall be defined later on. Rubber-rubber contact friction is based on previous internal documentation considerations, due to the same nature of the interfaces and their relative slow sliding velocity.

7.2 Direct strategy

The *Direct strategy* solves the mechanical problem from Section 7.1, when:

- The rubber bodies are discretized with second order tetrahedral elements with element size of $l_d = 2.1$ [mm];

- The ground body is discretized with first order hexahedral elements with regular horizontal resolution of $\Delta x_{soil} = 0.3$ [mm] and after filtering length scales below 0.3 [mm];
- A regularized frictional contact with a constant friction value of $\mu_{s,r} = 0.6$;
- Built-in finite linear viscoelastic models, from Impetus Afea material library.

This framework was developed prior to this thesis work. The friction value accounting for the road surface smaller scales is identified by a sensitivity analysis using Bulk geometry for the lower imposed homogeneous pressure on the metallic plate, 0.5 [Bar], until the resultant global coulomb friction matches the output from its experimental counterpart (see Figure 4.22, in Chapter 4).

Convergence evaluation

In such a direct approach, the ground (master) surface discretization is finer than the rubber (slave) surface which creates sharp rigid indentors that potentially promote undetected penetrations, as discussed in Section 3.5.6 (see Figure 3.11),which may generate mesh dependent results. Therefore, to evaluate the relevance of the numerical ground and rubber discretization, a preliminary mesh sensitivity analysis is performed changing the mesh refinement of the rubber body while keeping a single discretization configuration for the rigid ground. The candidates are displayed in Figure 7.6 and their characteristics are summarized as follows:

- Rough ground: as described in Chapter 4, the body used in FEM simulations consists of a 40×150 [mm^2] slab containing hexahedral first order elements. The profile is treated with a discretization of 300×300 [μm^2];
- Rubber sample: a Leading Edge containing 16 lamellae geometry will be used, due to its high rich behaviour in contact (rubber-ground and rubber-rubber). This geometry is meshed with second order tetrahedral elements. Four different grids are tested with element size respectively of , $l_d = \{2.1, 1.5, 0.7\}$ [mm].

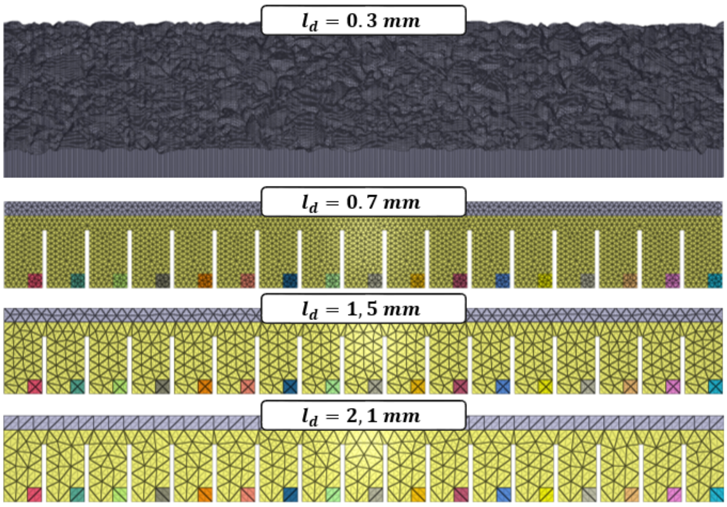

Figure 7.6: Rubber-ground mesh configurations.

The tests use the linear viscoelastic constitutive law given by *Model A* as evaluated in Chapter 6. For each case, we extract two global outputs, Θ:

- Stabilized global Coulomb friction, $\Theta = \mu_c$ $[-]$, obtained by dividing the total horizontal reaction by the applied external load. As per equation (1.3.2), it is a central indicator of adherence;

- Stabilized energy dissipation rate $\Theta = \dot{E}_{diss}$ [J/s]: being an important global indicator of the hysteretic content of the response.

Those outputs are obtained by averaging their time history during stabilized sliding conditions (see Figure 1.3 from Section 1.3). The results are displayed in Figure 7.7.

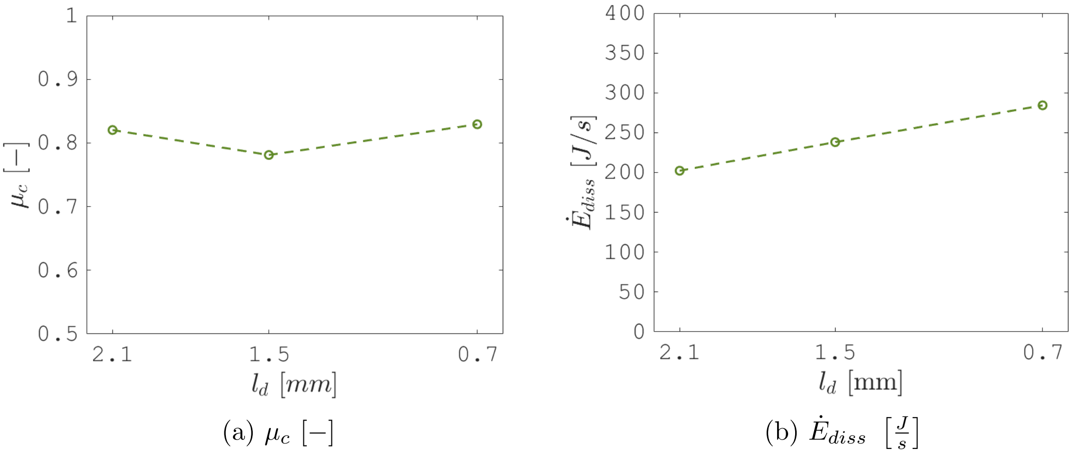

(a) μ_c $[-]$ (b) $\dot{E}_{diss}$ $\left[\frac{J}{s}\right]$

Figure 7.7: Mesh convergence analysis for the unfiltered ground discretization and *Model A* - central outputs.

We define the relative error, δ_Θ, for each parameter by

$$\delta_{\mu_c} = 100 \left| \frac{\mu_c^{0.7mm} - \mu_c^{1.5mm}}{\mu_c^{0.7mm}} \right| = 5.81\% \quad ; \quad \delta_{\dot{E}_{diss}} = 16.25\%. \tag{7.2.1}$$

Figure 7.7 shows the absence of convergence for the selected mesh sizes, indicating that an even more refined mesh would be necessary. However, any finer meshes have an excessive computational time due to an increase number of elements and a reduction of the time step due to CFL conditions, as the solver is explicit.

7.3 Filtered strategy

To overcome this lack of convergence limitation without introducing additional refinement nor considering coarser ground meshing, previous convergence analysis [105], [130] argued that rough surfaces should be discretized by element sizes 6× to 10× smaller than the shortest roughness length scale λ_s. Thus, as shown in Figure 7.8, a new ground discretization is introduced, which uses a 2D low pass filtering length scale below $\lambda_s/2 = 1800$ [mm], whilst keeping the original element size for the ground discretization.

In this case, we define the configuration of the *Filtered strategy* similarly to the *Direct strategy*, but this time:

- The rubber bodies are discretized with second order tetrahedral elements with element size of $l_d = 0.7$ [mm];

- The ground body is discretized with first order hexahedral elements with regular horizontal resolution of $\Delta x_{soil} = 0.3$ [mm] and after filtering length scales below 1.8 [mm];

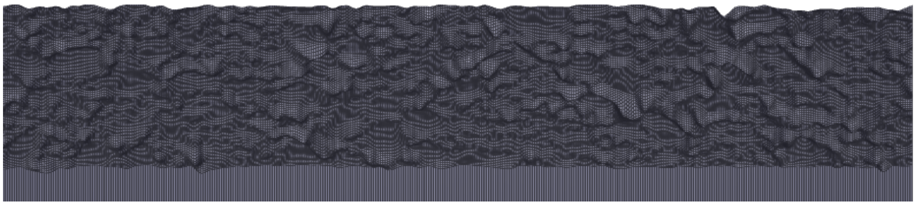

Figure 7.8: Ground proposed mesh configuration.

- A regularized frictional contact is used with a constant friction value, $\mu_{s,r}$ based on a sensitivity analysis that best superposes one experimental study case (to be discussed in Chapter 8);
- The simulations will use the viscoelastic law defined by model B, taken as an user defined finite non-linear viscoelastic model, added into Impetus Afea directly during the stress update process.

Again, the friction coefficient is identified by matching low compression Bulk numerical response to experiments. The non-linear viscoelastic model is considered due to its more challenging computation and higher solicitations. To ensure the relevance of the approach, the convergence analysis is re-run considering the new ground discretization proposal.

Convergence evaluation

The results for the two central parameters, Θ, are presented in Figure 7.9 which also displays the results of the convergence analysis run on the direct approach. In this case, if the outputs from the mesh size of 0.7 [mm] are defined as reference, using the previous coarser mesh size of $l_d = 1.5$ [mm] results in a relative error of

$$\delta_{\mu_c} = 100 \left| \frac{\mu_c^{0.7mm} - \mu_c^{1.5mm}}{\mu_c^{0.7mm}} \right| = 1.09\% \quad ; \quad \delta_{\dot{E}_{diss}} = 7.85\%. \tag{7.3.1}$$

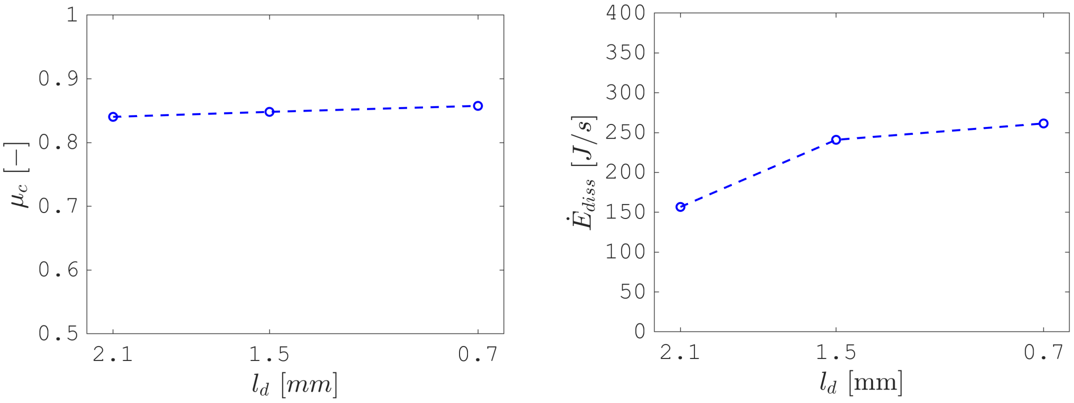

(a) μ_c [−] (b) $\dot{E}_{diss}$ [J/s]

Figure 7.9: Mesh convergence with proposed ground discretization and *Model B* - central outputs.

Based on these improved results, from this point on a mesh configuration with $l_d = 0.7$ [mm] for rubber bodies are defined as a standard configuration along a rigid ground with a grid size of $\Delta x_{soil} = 0.3$ [mm] constructed after low-pass filtering for length scales smaller than $\lambda_s/2 = 1.8$ [mm].

7.4 Coupling strategy

The problem in the filtered strategy is that it erases all available information on the smaller scales of the road geometry. This was replaced by an experimental fit of an *ad hoc* low scale friction coefficient. A multi-scale approach is thus needed to include in a more intrinsic way the road geometry at fine scale. As reported in [40], [66], [89], most multi-scale algorithms for contact simulations are based on a decomposition of the original structure into several overlapping subdomains which may have different models, geometries and discretization strategies. The global three dimensional structure is first discretized with a mesh that does not resolve the details along the contact boundary, whereas at the contact area, an overlapping patch with a different approximation is introduced.

In our case, we will couple our global finite element solver as described in the previous section to a series of half-space models as introduced in Chapter 2. There will be one half-space model per each boundary integration point of the finite element grid which is in contact with the soil. As described in Chapter 2, the half-space model will use a detailed geometry of the soil surface. In line of the assumptions done by the physical models of friction reviewed in Chapter 2, we also assume that at the scale involved in the half-space model, the rubber interface can be considered as flat, and vertically loaded by a pressure distribution exerted by the soil in order to impose the soil rubber contact condition at finer scales. We also assume that at those scales, non-linear effects could be neglected inside the rubber, meaning that we can use a linear viscoelastic model to describe its constitutive behavior. The last assumption is that the solution is spatially periodic along the sliding direction as observed from the soil in local coordinates $\bar{\mathbf{x}} = (x - V_t t, y, z)$. The length of the period along x is given from the finer scale resolved in the finite element grid.

Each model (finite element or local half-space) will independently satisfy its contact conditions at the soil surface. The coupling conditions between the finite element model and the local half-space model are inspired from the physical friction models, and are then given by

- The nominal sliding velocity used in the local half-space domain is equal to the local value of sliding velocity of the global finite element model;
- The average soil pressure in the local half-space domain is equal to the local value of the normal pressure, T_N, of the global finite element model;
- The local power $\dot{W} = T_t V_t da$ developed per unit surface by the contact forces of the global model is equal to the power $\dot{W}_{loc}$ developed per unit surface by the contact forces of the half-space model, which thus specifies an apparent friction coefficient to be locally used in the global model as $\mu = \dot{W}_{loc}(T_N, V_T)/(T_N V_t)$

For this strategy, a wet road is used via two considerations: isothermal FEM, a semi-analytical half-space approach, material models and a detailed consideration of ground geometry resolution up to 1 [μm] where any smaller information are assumed to be sealed off by water pockets and dust particles [45]. This simplified implementation is feasible by combining the available resources currently present on IMPETUS Afea solver and could still produce meaningful results for lubricated contact cases as discussed in Section 2.3.4 for high sliding velocities.

7.5 Continuous Convolution FFT solver

Each local problem is now to be solved by a semi-analytical FFT-based half-space approach called Continuous Convolution Fast Fourier Transform (CC-FFT). In 1996, Ju and Farris first used the FFT to greatly reduce the computation cost of evaluating the linear convolutions for contact problems [29]. Later on, their work was further developed for rough surfaces and viscoelastic domains [135], [140], [148].

The CC-FFT approach is commonly used for periodic (or infinite) contact problems [140] which aligns with our proposed assumption in smaller scales (see Section, 7.4). Thus, in the present Section, a simple mechanical problem is defined for a purely elastic domain. Subsequently, the framework is progressively expanded to a steady-state sliding contact between a viscoelastic half-space and a periodic indenter.

7.5.1 Distributed periodic pressure in half-space

The problem of equilibrium state of an isotropic elastic half-space with given Neumann or Dirichlet boundary conditions in its planar boundary has been known historically as the *Boussinesq contact problem* [1] posed in the nineteenth century, firstly for a concentrated load in an elastic half-space. In this section, the problem is extended to distributed and period pressure for an elastic media and then adapted to a viscoelastic case.

Elastic media

As illustrated in Figure 7.10, consider an hemispheric domain, Ω, containing both planar, $\partial\Omega_p$, and hemispherical, $\partial\Omega_h$, boundaries so that

$$\Omega = \{\mathbf{x} \in \mathbb{E}^3 \mid \mathbf{x} \cdot \mathbf{e}_z > 0 \ \ \& \ \ ||\mathbf{x}|| < R\}, \tag{7.5.1}$$

where $\mathbf{x} = x\mathbf{e}_x + y\mathbf{e}_y + z\mathbf{e}_z$.

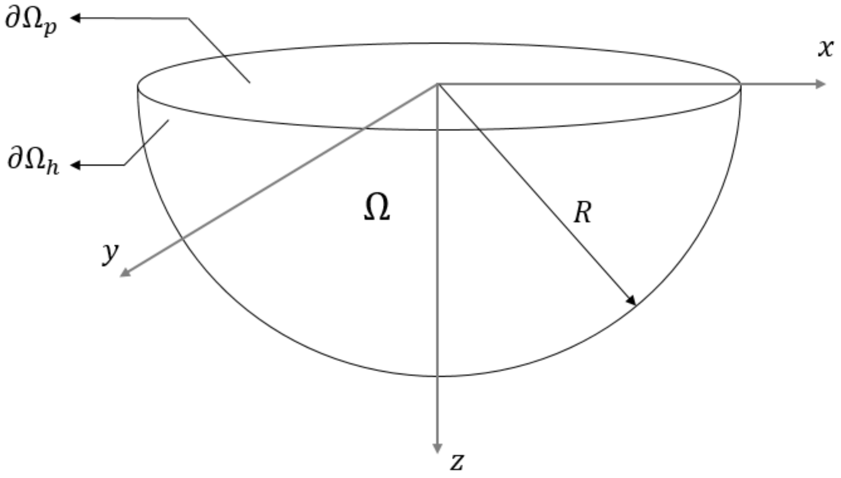

Figure 7.10: Hemispherical domain, Ω, with large R.

The domain is isothermal, homogeneous, elastic and isotropic and within the framework of small deformations [15], therefore

$$\Big\{ \boldsymbol{\sigma} = 2\mu\boldsymbol{\varepsilon} + \lambda tr(\boldsymbol{\varepsilon})\mathbf{I} \quad ; \quad \boldsymbol{\varepsilon} = \tfrac{1}{2}\left(\nabla\mathbf{u} + \nabla\mathbf{u}^T\right). \qquad \forall \mathbf{x} \in \Omega. \tag{7.5.2}$$

In Figure 7.11, we represent a close-up portion of Ω, where the curvature of the hemisphere is no longer within the frame. We introduce a periodic distributed pressure, $p^{per}(x,y) = p^{per}(x+mL_x, y+nL_y)$ where $m,n \in \mathbb{Z}$. The elementary distribution is applied on an elementary period, $\partial\Omega_p^{per}$, and repeatedly copied (and within) the planar boundary $\partial\Omega_p$. There are no tangential tractions (friction-less 'contact') at any point on both boundaries.

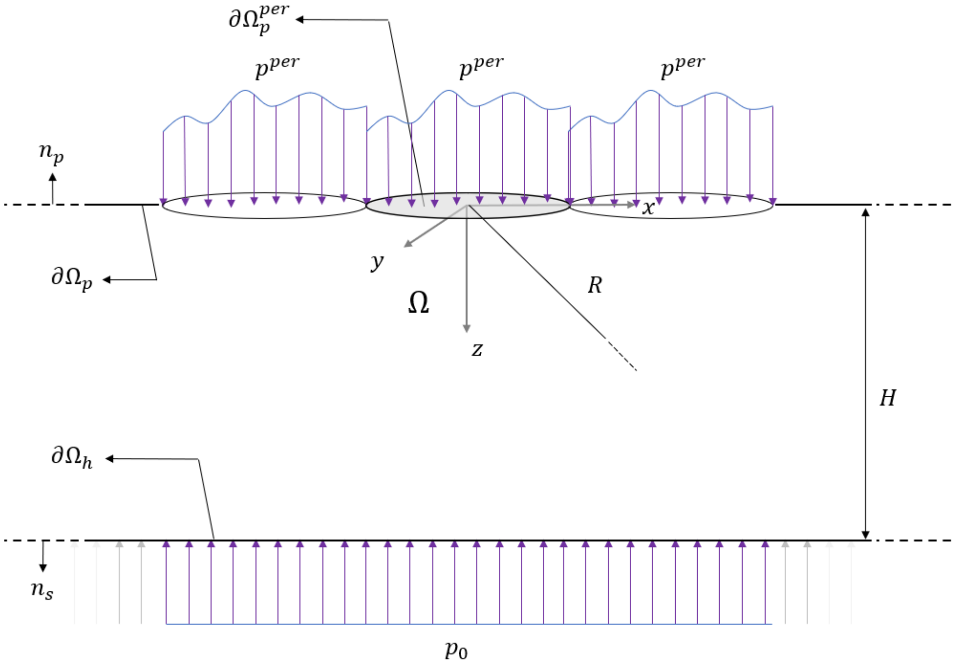

Figure 7.11: Portion of the hemispherical domain, Ω, with large R.

Assuming that the distance H between the planar portion $\partial\Omega_p$ and $\partial\Omega_h$ at infinity is large with respect to L_x and L_y, the boundary conditions for this problem are defined as

$$\begin{cases} \boldsymbol{\sigma}\cdot\mathbf{n}_p = p^{per}(x,y)\mathbf{e}_z & \forall\mathbf{x}\in\partial\Omega_p; \quad i\neq j \\ \boldsymbol{\sigma}\cdot\mathbf{n}_s = -p_0\mathbf{e}_z & \forall\mathbf{x}\in\partial\Omega_h; \quad \{H, z=H\} \end{cases} \tag{7.5.3}$$

where, differently from (7.5.3), the distribution pressure, albeit periodic, also covers $\partial\Omega_p$.

To illustrate that the problem is bounded, as the radii of the hemisphere becomes increasingly large, so does the number M of elementary regions, $\partial\Omega_p^{per}$, subjected to p^{per}. Correspondingly, in deeper (high z component values) regions of the domain, the stress also becomes uniform as shown in Figure 7.11. Moreover, by taking advantage from the periodicity of the pressure function and for the equilibrium (7.5.7) to be verified, we find that

$$-\sigma_{zz} \approx p_0 = \frac{1}{|\partial\Omega_p|}\int_{\partial\Omega_p} p^{per}(\zeta,\eta)d\Omega = \frac{M}{M\,|\partial\Omega_p^{per}|}\int_{\partial\Omega_p^{per}} p^{per}(\zeta,\eta)d\Omega = \frac{1}{|\partial\Omega_p^{per}|}\int_{\partial\Omega_p^{per}} p^{per}(\zeta,\eta)d\Omega \tag{7.5.4}$$

where $|\cdot|$ represents the area covered by a certain domain. Now, the domain, Ω, can be represented as a semi-infinite material, also termed *half-space*, body with a boundary, $\partial\Omega$, at $z=0$, described as

$$\Omega = \{\mathbf{x}\in\mathbb{E}^3 \mid \mathbf{x}\cdot\mathbf{e}_z > 0\} \tag{7.5.5}$$

and in this case, the compact representation of the boundary conditions become

$$\begin{cases} \boldsymbol{\sigma} \cdot \mathbf{e}_z = p^{per}(x,y)\mathbf{e}_z & \forall \mathbf{x} \in \partial\Omega_p \\ \boldsymbol{\sigma} \cdot \mathbf{e}_z = -p_0\mathbf{e}_z & \forall \mathbf{x} \text{ at infinity} \end{cases} \tag{7.5.6}$$

Under those conditions, the system is considered to be in equilibrium, the tractions applied at the surface are taken as being much larger than any body forces and the condition is assumed to be steady-state. Hence, the stress equilibrium can be stated as

$$\begin{cases} div(\boldsymbol{\sigma}) = \mathbf{0} \qquad \forall \mathbf{x} \in \Omega. \end{cases} \tag{7.5.7}$$

If the superposition principle is considered for the Boussinesq's solution, then for a half-space, through the potential theory one finds the vertical displacement as

$$\begin{aligned} u_z^{per}(x,y,z) \mid_{z=0} &= \frac{(1-\nu)}{2\pi\mu} \iint_{\partial\Omega_p} \frac{p^{per}(\zeta,\eta)}{\sqrt{(x-\zeta)^2+(y-\eta)^2}}\, d\Omega \\ &= \frac{(1-\nu)}{2\pi\mu} \iint_{-\infty}^{+\infty} \frac{p^{per}(\zeta,\eta)}{\sqrt{(x-\zeta)^2+(y-\eta)^2}}\, d\zeta\, d\eta \end{aligned} \tag{7.5.8}$$

which is the convolution between a periodic pressure function and a Green function, $G_f = (1-\nu)/(2\pi\mu\sqrt{x^2+y^2})$.

This particular solution benefits from the *convolution theorem* [69], where the Fourier transform in space of the convolution between the periodic pressure, p^{per}, and the Green function, G_f, is their product of their Fourier space, thus

$$u_z^{per}(x,y,z) \mid_{z=0} = (G_f * p^{per})(x,y) \quad \underset{\longleftrightarrow}{\mathcal{FT}_{x,y}} \quad \hat{u}_z^{per}(q_x,q_y) \mid_{z=0} = \hat{G}_f(q_x,q_y)\hat{p}^{per}(q_x,q_y) \tag{7.5.9}$$

where *wave numbers* q_x and q_y are analogous to frequency components, however in space. The superscript $\hat{(\cdot)}$ shall be used when describing a transformed term in Fourier space

Visco-elastic media

Built on the principles obtained, consider a deformable half-space body, Ω, through a right-handed set of Cartesian coordinates (x,y,z) as defined in (7.5.5). The half-space is considered to be isothermal, homogeneous, isotropic, viscoelastic and incompressible. A non-zero periodic pressure, $p^{per}(x,y) = p^{per}(x+mL_x, y+nL_y)$ where $m,n \in \mathbb{Z}^+$, is applied and defined through the whole planar boundary $\partial\Omega$ across all time, $t \in [-\infty,\infty] = \mathcal{T}$. As the problem is posed for all time, by applying the Fourier transform in time, the mechanical problem becomes

$$\begin{cases} \text{Balance of linear momentum} & \\ div\left[\hat{\sigma}(\mathbf{x},\omega)\right] = \mathbf{0} & \forall(\mathbf{x},\omega) \in \Omega \times \mathcal{F}_t\{\mathcal{T}\} \\ \text{Constitutive relation} & \\ \hat{\sigma}(\mathbf{x},\omega) = 2\hat{\mu}(\omega)\hat{\varepsilon}(\mathbf{x},\omega) + \hat{\lambda}(\omega)\hat{\varepsilon}(\mathbf{x},\omega)\mathbf{I} & \forall(\mathbf{x},t) \in \Omega \times \mathcal{F}_t\{\mathcal{T}\} \\ \text{Boundary conditions} & \\ \hat{\sigma}(\mathbf{x},\omega)\cdot\mathbf{n} = \hat{p}^{per}(\mathbf{x},\omega)\mathbf{e}_z & \forall(\mathbf{x},\omega) \in \partial\Omega \times \mathcal{F}_t\{\mathcal{T}\} \\ \hat{\sigma}(\mathbf{x},\omega)\cdot\mathbf{n} = -\hat{p_0}(\mathbf{x},\omega)\mathbf{e}_z & \forall\mathbf{x} \text{ at infinity, } \forall\omega \in \mathcal{F}_t\{\mathcal{T}\} \end{cases} \tag{7.5.10}$$

where the value of $\hat{\mu}(\omega)$, for incompressible viscoelasticity, can be obtained for a rheological model and provided DMA, and $\hat{\lambda}(\omega)$ follows from incompressibility.

From (7.5.10), it is observed that the problem is equivalent to the elastic problem. This equivalence is known as the *Correspondence Principle* [23] and, as long it is operated in Fourier space, the vertical displacement from Boussinesq's solution located at $z = 0$ should verify the problem as well, with

$$\hat{u}_z(x, y, \omega) \mid_{z=0} = \frac{(1-\nu)}{2\pi\hat{\mu}(\omega)} G_f(x, y) * \hat{p}^{per}(x, y, \omega) \tag{7.5.11}$$

with G_f being the Green function. If the spatial Fourier transform, $\mathcal{F}_{x,y}$, is applied, then

$$\hat{\hat{u}}_z(q_x, q_y, \omega) = \frac{(1-\nu)}{2\pi\hat{\mu}(\omega)} \hat{G}_f(q_x, q_y) \hat{\hat{p}}^{per}(q_x, q_y, \omega), \tag{7.5.12}$$

where the superscript $\hat{\hat{(\cdot)}}$ describes a Fourier transformation in both time and space.

With a general description and solution of interest, we introduce the notion that, with progressing time, the previously defined distributed pressure shifts its position in space on the x-axis direction with a constant velocity of V_x. By using a shifting Cartesian coordinate system, $\bar{x}O\bar{y}$, that moves horizontally with the same velocity, the connection with the original coordinate system, xOy is made

$$\begin{cases} \bar{x} = x - V_x t \\ \bar{y} = y \end{cases}, \tag{7.5.13}$$

moreover, restricting this analysis to steady-state conditions, we conclude that the pressure function observed through $\bar{x}O\bar{y}$ approximates to

$$p^{per}(x, y, t) \approx p^{per}(x - V_x t, y) = p^{per}(\bar{x}, \bar{y}). \tag{7.5.14}$$

The spatial and time Fourier transform of (7.5.14) is

$$\begin{aligned} \hat{\hat{p}}^{per}(q_x, q_y, \omega) &= \mathcal{F}_{x,y}\left\{\mathcal{F}_t\left\{p^{per}(x - V_x t, y)\right\}(x, y, \omega)\right\}(q_x, q_y, \omega) \\ &= \mathcal{F}_{x,y}\left\{\frac{1}{|V_x|}\hat{p}^{per}\left(-\frac{\omega}{V_x}, y\right) e^{i\left(-\frac{\omega}{V_x}\right)x}\right\}(q_x, q_y, \omega) \\ &= \frac{1}{|V_x|}\hat{p}\left(-\frac{\omega}{V_x}, q_y\right) 2\pi\delta(q_x + \omega/V_x) \end{aligned} \tag{7.5.15}$$

Inserting (7.5.15) in (7.5.12) renders

$$\hat{\hat{u}}_z(q_x, q_y, \omega) = \frac{(1-\nu)}{2\pi\hat{\mu}(\omega)} \hat{G}_f(q_x, q_y) \frac{1}{|V_x|} \hat{p}^{per}\left(-\frac{\omega}{V_x}, q_y\right) 2\pi\delta(q_x + \omega/V_x). \tag{7.5.16}$$

The resulting viscoelastic displacement in time and space can be recovered by computing the triple Inverse Fourier Transform (in time and space), $\mathcal{F}^{-1}_{\bar{x},\bar{y},t}$, of (7.5.18). The development, together with Dirac's distribution property, renders

$$\begin{aligned} u_z(x, y, t) &= \mathcal{F}^{-1}_{x,y,t}\left\{\hat{\hat{u}}_z(q_x, q_y, \omega)\right\} \\ &= \frac{1}{(2\pi)^3}\iiint_{-\infty}^{\infty} \hat{\hat{u}}_z(q_x, q_y, \omega) e^{i(\omega t + q_x x + q_y y)} d\omega dq_x dq_y \\ &= \frac{1}{(2\pi)^2}\iint_{-\infty}^{\infty} \frac{(1-\nu)}{2\pi\hat{\mu}(-V_x q_x)} \hat{G}_f(q_x, q_y) \hat{p}\left(q_x, q_y\right) e^{i[q_x(x - V_x t) + q_y y]} dq_x dq_y. \end{aligned} \tag{7.5.17}$$

Then, provided that the system operates in the coordinate space $\bar{x}O\bar{y}$, (7.5.17) becomes

$$
\begin{aligned}
u_z(\bar{x}, \bar{y}) &= \frac{1}{(2\pi)^2} \iint_{-\infty}^{\infty} \frac{(1-\nu)}{2\pi\hat{\mu}(-V_x q_x)} \hat{G}_f(q_x, q_y) \hat{p}\,(q_x, q_y)\, e^{i(q_x\bar{x}+q_y\bar{y})} dq_x dq_y. \\
&= \mathcal{F}^{-1}_{\bar{x},\bar{y}} \left\{ \frac{(1-\nu)}{2\pi\hat{\mu}(-V_x q_x)} \hat{G}_f(q_x, q_y) \hat{p}^{per}\,(q_x, q_y) \right\}.
\end{aligned} \tag{7.5.18}
$$

In steady-state conditions, the resulting displacement from (7.5.18) becomes independent of time. Lastly, since the applied pressure is assumed to be periodic in space, we expand p^{per} as a Fourier series

$$
p^{per}(\bar{x}, \bar{y}) = \sum_{m,n\in\mathbb{Z}} p_{m,n} e^{i\left(\frac{2m\pi\bar{x}}{L_x} + \frac{2n\pi\bar{y}}{L_y}\right)} \tag{7.5.19}
$$

and calculate the last inverse Fourier transform from (7.5.18), returning

$$
u_z(\bar{x}, \bar{y}) = \sum_{m,n\in\mathbb{Z}} \left\{ \frac{(1-\nu)}{2\pi\hat{\mu}_m\left(-V_x \frac{2m\pi}{L_x}\right)} \hat{G}_{f,m,n}\left(\frac{2m\pi}{L_x}, \frac{2n\pi}{L_y}\right) p_{m,n} \right\} e^{i\left(\frac{2m\pi\bar{x}}{L_x} + \frac{2n\pi\bar{y}}{L_y}\right)} \tag{7.5.20}
$$

The transform of the radially symmetric Green function is given by expression (8.4.21) (see Appendix 8.4). When plugged into (7.5.20), we recover

$$
u_z(\bar{x}, \bar{y}) = \sum_{m,n\in\mathbb{Z}} \left\{ \frac{(1-\nu)}{2\pi\hat{\mu}_m\left(-V_x \frac{2m\pi}{L_x}\right)} \frac{p_{m,n}}{\sqrt{\left(\frac{m}{L_x}\right)^2 + \left(\frac{n}{L_y}\right)^2}} \right\} e^{i\left(\frac{2m\pi\bar{x}}{L_x} + \frac{2n\pi\bar{y}}{L_y}\right)}. \tag{7.5.21}
$$

Using the notation $\hat{\mu}_m = \hat{\mu}_m\left(-2V_x m\pi/L_x\right)$, we also define $K_{m,n}$

$$
K_{m,n} = \frac{1-\nu}{2\pi\hat{\mu}_m\sqrt{\left(\frac{m}{L_x}\right)^2 + \left(\frac{n}{L_y}\right)^2}} = \frac{1-\nu^2}{\pi\hat{E}_m\sqrt{\left(\frac{m}{L_x}\right)^2 + \left(\frac{n}{L_y}\right)^2}}, \tag{7.5.22}
$$

usually known in the literature as the *influence coefficient.* This leads to a more explicit representation

$$
u_z(\bar{x}, \bar{y}) = \sum_{m,n\in\mathbb{Z}-(0,0)} K_{m,n} p_{m,n} e^{i\left(\frac{2m\pi\bar{x}}{L_x} + \frac{2n\pi\bar{y}}{L_y}\right)}. \tag{7.5.23}
$$

Observe that in this formula, the pressure and the vertical displacement have zero average. They do represent the real pressure and displacement within a constant, which correspond to the unspecified vertical translation h_0 of the body and to the possibility for an incompressible body to resist to an uniform pressure $\bar{p}$ without deformation.

7.5.2 Indentation of a periodic rigid punch in half-space

To bring the problem closer to a sliding contact, we attribute the resulting pressure field from the indentation of a rigid, and periodic, profile against a half-space. However, most contact cases are not saturated, therefore the contact boundary where the pressure is applied, $\partial\Omega_p^{per}$, is not necessarily known.

When dealing with both unknown contact area and pressure distribution, a common and general description of this problem is known as the *Hertz-Signori-Moreau* contact case

[36], [149]. It is described by two equations and two complementary conditions. The first equation used to define it is called *gap height*.

$$h(\bar{x}, \bar{y}) = h_0 + s^{per}(\bar{x}, \bar{y}) + u_z(\bar{x}, \bar{y}), \tag{7.5.24}$$

containing the superposition of the periodic height profile of the indentor, $s^{per}(\bar{x}, \bar{y})$, the rigid body displacement h_0, and the viscoelastic zero averaged half-space displacement, $u(\bar{x}, \bar{y}) = u_z(\bar{x}, \bar{y}) \mid_{z=0}$, obtained previously in (7.5.23). We split the boundary into two domains, $\partial\Omega_p^{per} = \partial\Omega_{p,o}^{per} \cup \partial\Omega_{p,i}^{per}$, where in $\Omega_{p,i}$ traction should always be compressive in the contact zone, and in $\Omega_{p,o}$ the gap between the half-space and the indentor should always be positive without any traction. Those requirements are enforced by the *complementary* conditions, defined as

$$\begin{cases} h(x, y) = 0 \quad \& \quad \bar{p} + p^{per}(\bar{x}, \bar{y}) > 0 \qquad \forall \mathbf{x} \in \partial\Omega_{p,i}^{per} \\ h(x, y) > 0 \quad \& \quad \bar{p} + p^{per}(\bar{x}, \bar{y}) = 0 \qquad \forall \mathbf{x} \in \partial\Omega_{p,o}^{per}. \end{cases} \tag{7.5.25}$$

The vertical equilibrium is verified through the use in an imposed average pressure, $\bar{p}$, which will control the amount of rigid displacement h_0.

Each local problem thus reduces to the system (7.5.25) (7.5.24) (7.5.23). Its solution requires an iterative approach such as the Conjugate Gradient Method (CGM) with projection described in [36], [112], [130], [134] and employed by the local solver used in this study. The geometric information on the soil surface is encoded in the map $s^{per}(\bar{x}, \bar{y})$ describing the local road profile.

7.5.3 Reconstruction of missing scales

As discussed in Section 7.3, to improve convergence without introducing more elements to the ground for the *Filtered strategy* in FEM, a 2D filtering attempts to provide to the smallest indentor at least 6 nodes, with a length scale of 1800 [μm].

In order to best preserve the geometrical integrity of the ground profile, the periodic indentor, $\partial\Omega_p^{per}$, used in the CC-FFT approach will also contain dimensions of 1800 × 1800 [μm^2]. Its smallest discretization is bounded by the ground's measurement resolution (see Section 4.3.1, which is 25×25 [μm^2]. This spectral coverage of $1800 - 25$ [μm] for an arbitrary local selection of Repro02 ground is showcased in Figure 7.12.

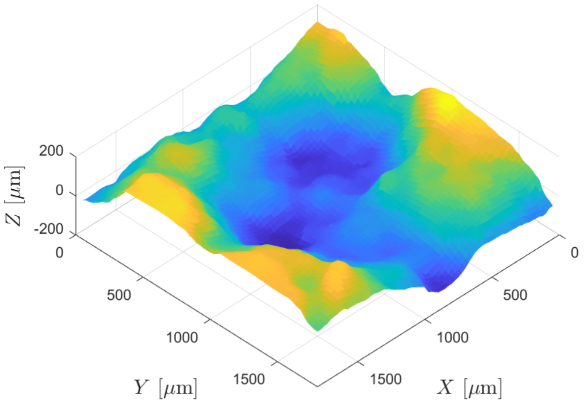

Figure 7.12: Repro02 - Arbitrary local selection.

The scale interval of $25 - 1$ [μm] is not available although simplified lubricated contact should involve scales which are at least in $1800 - 1$ [μm] (see Section 7.4). Therefore, a simple approximation generates the ground profile from the missing scales by extending the power spectral density (PSD) of the whole ground by *re-scaling* it. This approach requires self-affinity and benefits from a large sizing of measured ground (see Figure 4.7). Fortunately, the available measured profiles cover a total length of 138 × 202 [mm^2]. For a more detailed description of the PSD, see Section 2.3.2.

From this point on, we shall develop the procedure using the experimental soil Repro02 as an example, but the approach is analogous for Repro08. As shown in Figure 7.13, we verify that self-affinity is present in the ground from its Radial PSD computation. This descriptor is recovered from the largest squared selection $N \times N$, for $N = 5521$.

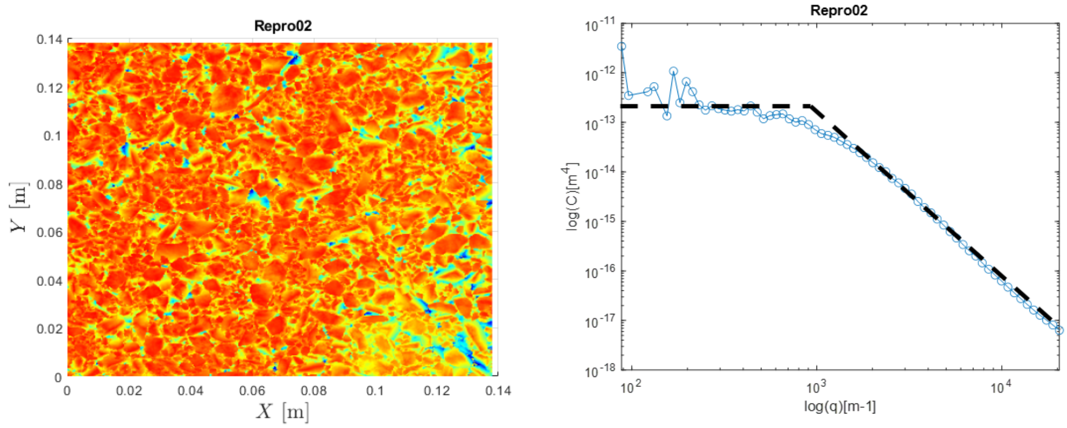

(a) Height profile (b) Radial PSD

Figure 7.13: Repro02 - largest squared grid selection.

The preeminent spectral content sought is the part *after* roll-off frequency, $q \geq q_0$ (see Section 2.3.2). One possibility is to select smaller portions of the ground, at the risk of loosing meaningful statistical characteristics. The PSD of smaller subsets $n \times n$ with $n = N/K$ (rounded) and $K = \{2, 4, 8, 10, 16, 32\}$ are presented in Figure 7.14. Each partition n contains K selections.

From the selections, $K = 10$ was chosen as a reference, with sufficiently narrow spectral coverage and low dispersion, when compared to even smaller partitions.

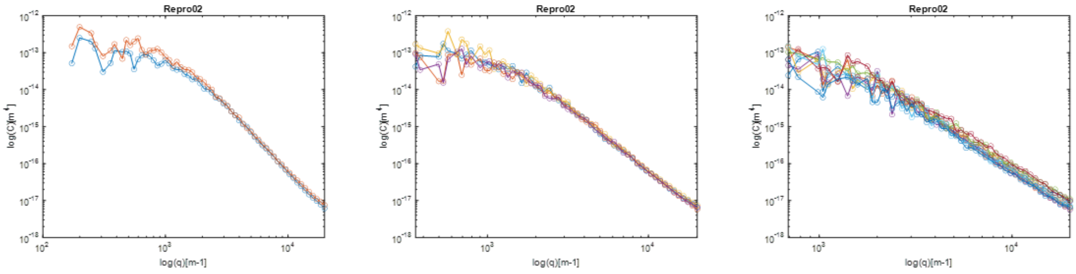

(a) $K = 2$ (b) $K = 4$ (c) $K = 8$

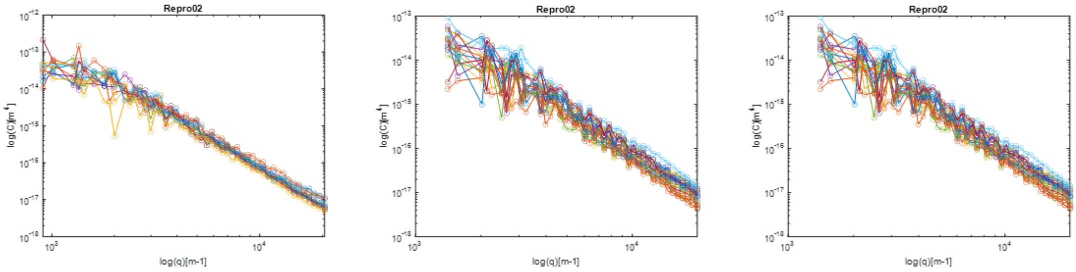

(d) $K = 10$ (e) $K = 16$ (f) $K = 32$

Figure 7.14: Repro02 Radial PSD - $n \times n$ partitions.

This approach assumes that the PSD is sufficient to characterize the most essential aspects of the ground at finer scale, thus, based on the works of Putignano *et al* [90], we create from this new selection an artificial generated profile, as shown in Figure 7.15.

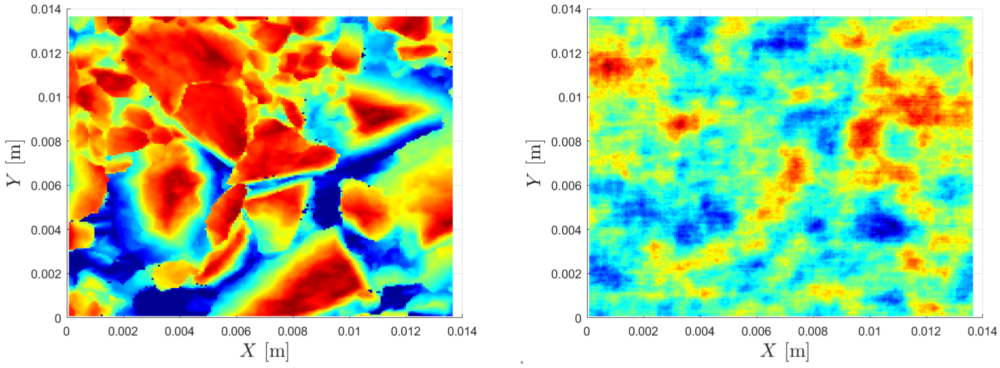

(a) Repro02 (b) Repro02Gen

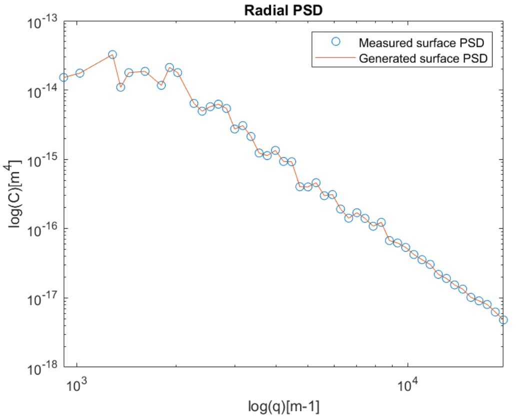

(c) Radial PSD

Figure 7.15: Repro02 - Measured and generated profiles.

Noticing that the reconstruction matches the Radial PSD from the measured data and contains a Gaussian random distribution for its phase. From this point on, we shall refer to this artificially generated profile as *Repro02Gen*. This profile is now re-scaled, based on highest/lowest ratios for q [m^{-1}] and C [m^4], serving re-scaling factors to be applied on width/length and amplitude, they being

$$\epsilon_{x,y} = \frac{q_{max}}{q_{min}} \quad ; \quad \epsilon_z = \left(\frac{C_{max}}{C_{min}}\right)^{\frac{1}{4}} . \tag{7.5.26}$$

We shall refer to this artificial ground as *Repro02GenResize* from now on. Figure 7.16 displays the Radial PSD of the re-scaled Repro02Gen and the measured Repro02, highlighting how self-affinity is essential to preserve asperity proportionality as a power law and continuity between original and re-scaled profile. Therefore, Repro02GenResize shall be used to enrich ground selections, like the one from Figure 7.12 via direct addition.

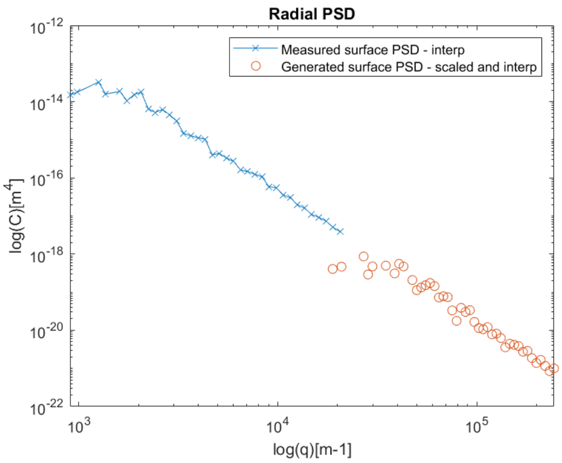

Figure 7.16: Radial PSD - Repro02 and re-scaled Repro02Gen.

To verify the approach, Repro02GenResize is added to the large measured portion of Repro02. To do so: (a) The larger ground is interpolated to match Repro02GenResize resolution; (b) Repro02GenResize is trimmed and "stitched" with itself, as per Figure 7.17, via rotation and reflection to match the total width/length of Repro02; (c) direct addition.

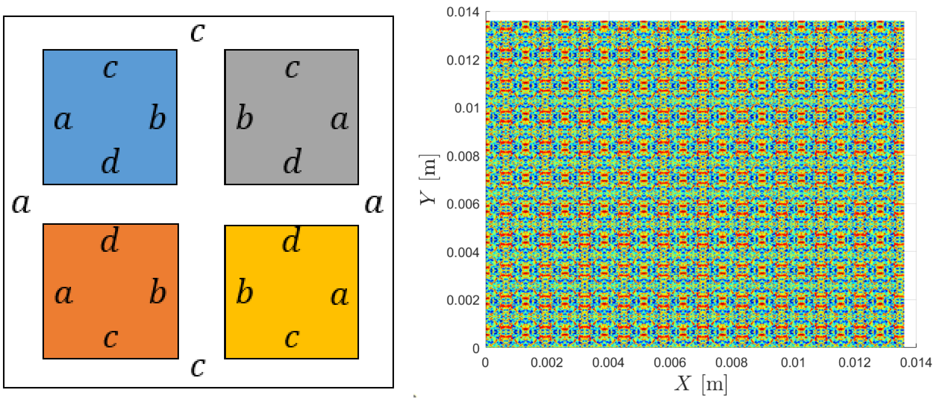

(a) Assembly strategy (b) Assembled generated profile

Figure 7.17: Repro02GenResize - Assembling approach.

Figure 7.18 displays the measured Repro02 and assembled Repro02GenResize individually and added together. Although the assembly from Figure 7.17a avoids abrupt discontinuities during juxtaposition, it does introduces periodic content at lower frequencies (see Figure 7.18a). Nonetheless, one should expect a low impact within $1800-25$ [μm], as the spurious signals are orders of magnitude smaller. The PSD of the original Repro02 before and after addition is shown in Figure 7.18.

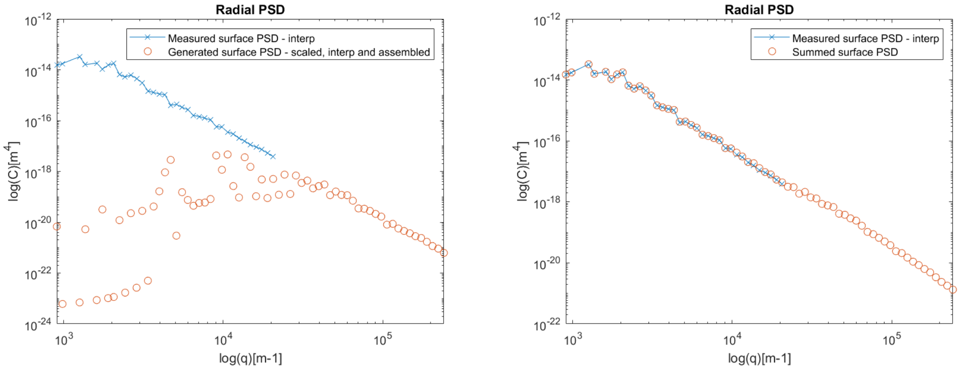

(a) Decoupled (b) Added

Figure 7.18: Radial PSD - measured Repro02 and assembled Repro02GenResized.

As an example, the exemplary ground selection from Figure 7.12 is displayed before and after the approach, in Figure 7.19.

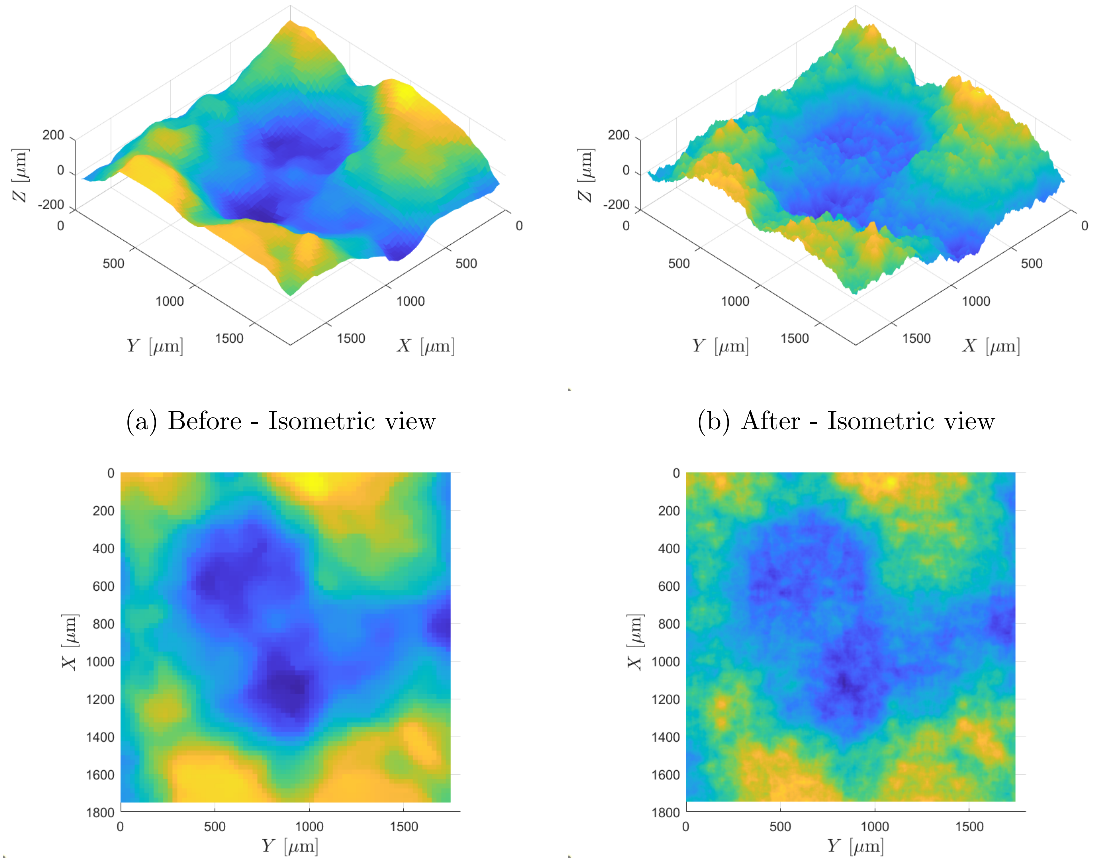

(a) Before - Isometric view (b) After - Isometric view

(c) Before - Top view (d) After - Top view

Figure 7.19: Repro02 - portion PSD extrapolation approach.

7.6 Generation of $\mu(P,V)$

In Section 7.4, the *Coupling strategy* proposes that the friction value evaluated during regularization in FEM (see Section 3.5.6) is recovered from the resulting apparent friction solution of CC-FFT when itself considers, as homogeneous boundary conditions, the local velocity and pressure from FEM. In other words, the evaluated friction during slip is a function

$$\mu_{s,r} = \mu(\dot{\mathbf{g}}_{T,i}, T_{N,i}) \tag{7.6.1}$$

recovered from an interpolated friction grid data already added *beforehand* into Impetus. To provide this data, CC-FFT model is independently launched prior to the FEM method 108 times using as boundary conditions a combination of different nominal homogeneous pressures, $\bar{p}$ [Bar], and nominal velocities, $\bar{V}_g$ [m/s]. These nominal values are chosen in order to cover the range of values which are expected during the global simulations. Here, we have chosen

$$\begin{cases} \bar{p} = \{0.1, 0.25, 0.5, 1, 2.5, 5, 10, 20, 40, 60, 80, 100\} \\ \bar{V}_g = \{0.025, 0.1, 0.25, 0.5, 1, 3, 7, 10\} \end{cases}, \tag{7.6.2}$$

Those boundary conditions are applied to a single 1800×1800 [μm^2] local selection of the ground using the reconstructed approach from Section 7.5.3. However, although the scales $25-1$ [μm] from those selections are representative, the same thing cannot be said from $1800-25$ [μm]. Thus, as shown in Figure 7.20, 20 additional local portions are simulated using the same campaign configurations, totaling 2160 runs using viscoelastic CC-FFT. This generates 20 friction grid data, in total.

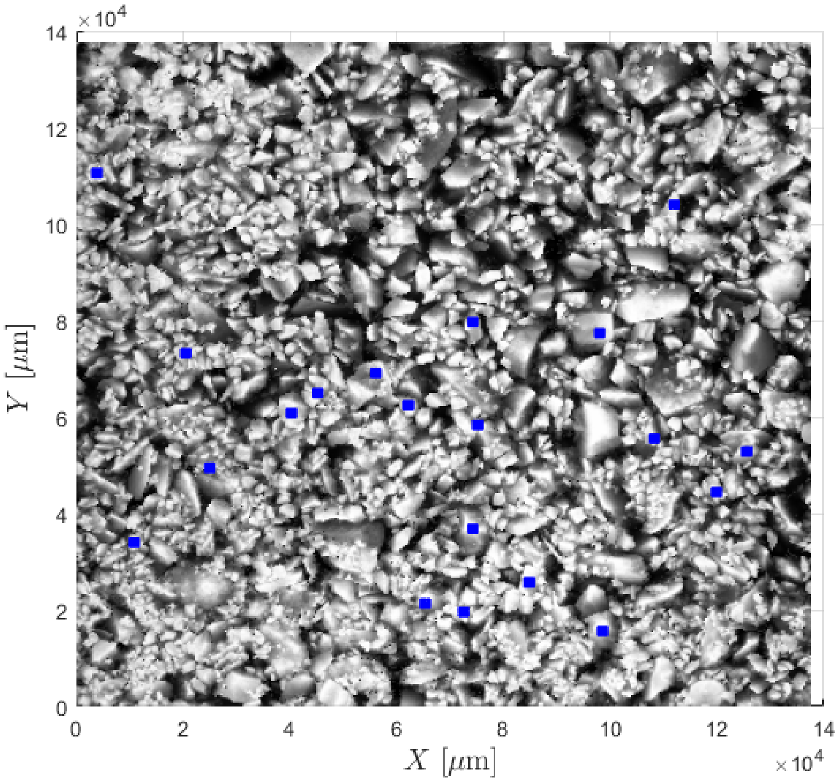

Figure 7.20: Repro08 ground - 20 1800×1800 [μm^2] selections.

The functional friction from all selections are then averaged to obtain a single surface, which is re-interpolated to a logarithmic scale, completing the necessary steps to generate the frictional dataset added on IMPETUS. This approach is made for two grounds (Repro02 and Repro08), and their obtained grids are displayed in Figure 7.21. The interpolation approach is Built-in on Impetus solver and it linearly extrapolates any "end/corner" data by default. For this reason, the corners of the curves are extrapolated as constant values to avoid extrapolation towards negative values.

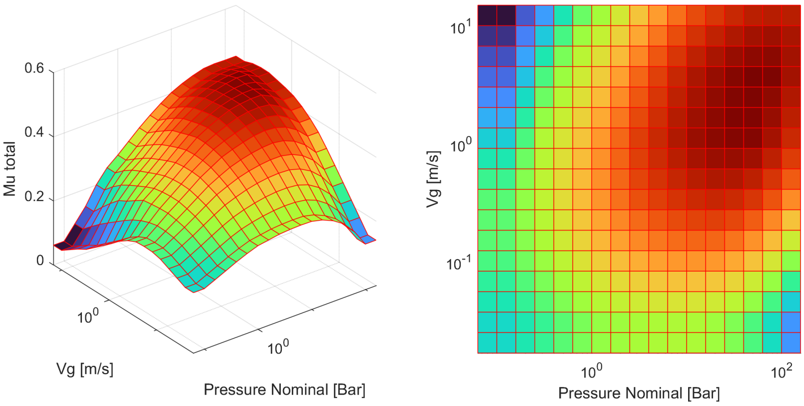

(a) For Repro02 profile

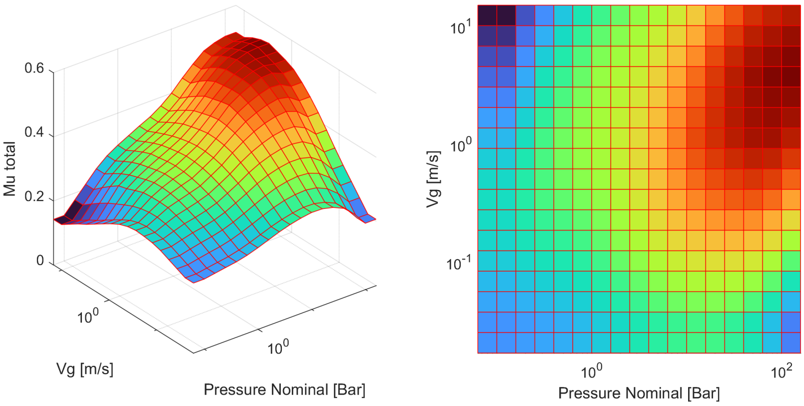

(b) For Repro08 profile

Figure 7.21: Average functional friction - Repro02 and Repro08 cases.

To estimate the pertinence of the the chosen interval from 7.6.2, we recover the working points from a Leading Edge simulation (with 16 lamellae) using *Model A* as its material sliding against Repro08 ground with a calibrated constant local friction coefficient. Figure 7.22 displays an occurrence distribution with respect to the local pressure, $\bar{p}$, and the local sliding velocity component, $\bar{V}_g$, with respect to the nominal sliding direction of the rubber. Sub-figure 7.22a displays said distribution while Sub-figure 7.22b highlights in green the portion within the coverage of the functional friction from Figure 7.21b.

The study-case displays a large working range, reflecting on its complex rubber-ground interactions due to the tread pattern geometry and aggressive roughness profile. Nonetheless, the coverage of the functional friction is still significant, covering 84.45% of the total spectrum of local pressures and velocities, including the epicenter of most occurrences. Figure 7.22 also shows that out-of-bounds working points are mostly located in less frequent low pressure values, where the functional friction will behave as a constant due to the flattening treatment on the corners of its general curve (see Figure 7.21).

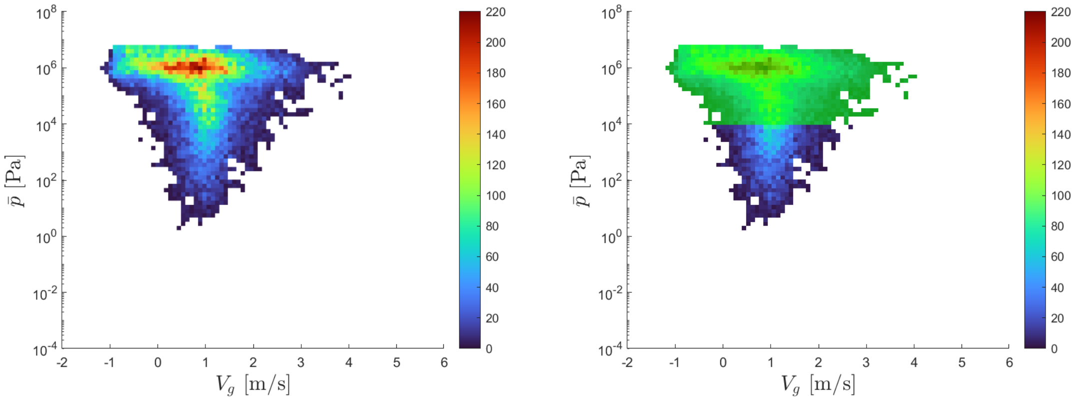

(a) Working points - LE 16L (b) Coverage - LE 16L

Figure 7.22: Working points and local friction coverage - Estimation using *Model A* and constant local friction estimated for Repro08 ground profile.

An schematic representation of the coupling strategy between FEM and the half-space CC-FFT approach is presented in Figure 7.23. The CC-FFT produces the frictional master-curves which are then implemented within the FE environment to cover the viscoelastic response from the centimeter to the micrometer.

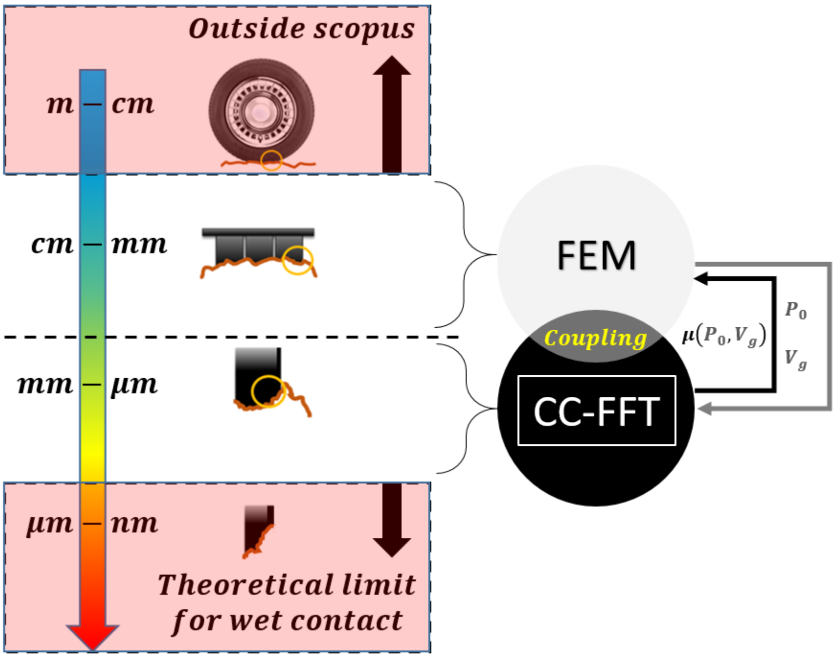

Figure 7.23: Schematic representation of the coupling strategy for the scales of interest.

A multi-scale model with master-curve-like friction is efficient in contrast to other FE-based approaches (see Chapter 2) whilst still introducing meaningful considerations from smaller scales in contrast to a constant friction coefficient. In addition, Figure 7.21 also indicates that the chosen range appears to be appropriate. Both maximums in velocity (tightly related to the effective $\tan(\delta)$) and in pressure (saturation conditions based on the provided rough profile) were captured within the covered bounds of friction master-curve.

Chapter 8

Multiscale Simulations of sliding contact on rough surfaces

8.1 Bulk/LE protocol reconstruction

In this chapter, we consider the mechanical problem defined in Chapter 7 to simulate the experimental protocol from Chapter 4. This test finds a sliding contact between new and worn-out ground and viscoelastic rubber material with or without geometrical sculptures.

The situations under consideration combine

- Sculpture: Six Leading Edge geometries (with 10, 12, 14, 16, 18, and 19 lamellae respectively) and one Bulk geometry to be loaded at 3 different pressures;
- Ground: Two ground surfaces (Repro02 and Repro08);
- Local friction: Two local friction approaches (constant, μ_{cte}, and coupled, $\mu(P, V)$);
- Material model: Two constitutive laws (viscoelastic with linear viscosity, *Model A* and viscoelastic with non-linear viscosity, *Model B*).

A selection of 24 configurations has been made, as described in Table 8.1. Both material models were considered. Moreover, certain tests come with a detailed output of local fields, and are identified in Table 8.1 as "*Global+Local*".

Repro02	10L	16L	19L	Bulk 0.5 [Bar]	Bulk 2 [Bar]	Bulk 6 [Bar]
μ_{cte}	Global	Global	Global	Global	Global	Global
$\mu(P, V)$	Global	Global	Global	Global	Global+Local	Global
Repro08	10L	16L	19L	Bulk 0.5 [Bar]	Bulk 2 [Bar]	Bulk 6 [Bar]
μ_{cte}	Global	Global+Local	Global	Global	Global+Local	Global
$\mu(P, V)$	Global	Global+Local	Global	Global	Global+Local	Global

Table 8.1: Available numerical data - simplified reconstruction of Bulk/LE protocol.

In this iteration, "*Global*" numerical cases are to be compared directly with experimental results from Figure 4.22 in Section 4.4.2. The "*Global+Local*" numerical cases produce statistics of the values of pressures and sliding velocities to be imposed on the local model as introduced in Section 7.6 (see Chapter 7).

8.2 Numerical predictions with ad-hoc μ

In this campaign, we apply the *Filtered strategy* from Section 7.3 (see Chapter 7) to reconstruct the protocol. A constant local friction was identified via a sensitivity analysis. To do so, we compare a Bulk loaded with the lowest available compression (0.5 [Bar]), the local friction value is swept in order to match experimental global stabilized Coulomb friction", μ_{dyn} (see equation (1.3.2)), corresponding to the ratio between the total horizontal force to the total vertical force applied to the rubber.

All μ_{dyn} experimental values from Figure 4.22b (see Section 4.4.2, in Chapter 4) are superposed with their numerical counterparts in Figure 8.1 for both Model A and B. From the image, we can observe a close proximity between numerical and experimental for both models. The distinction between Repro02 and Repro08 are overall well captured for both geometries even though the local friction was calibrated for a single μ_{dyn} data-point.

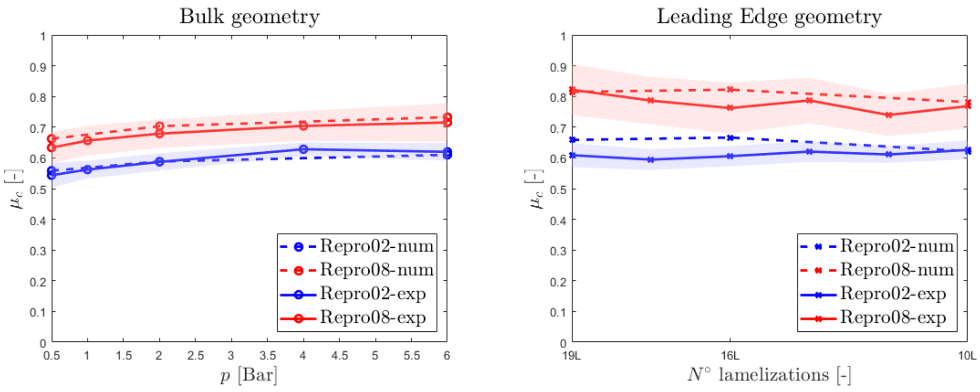

(a) Bulk - *Model A* (b) LE - *Model A*

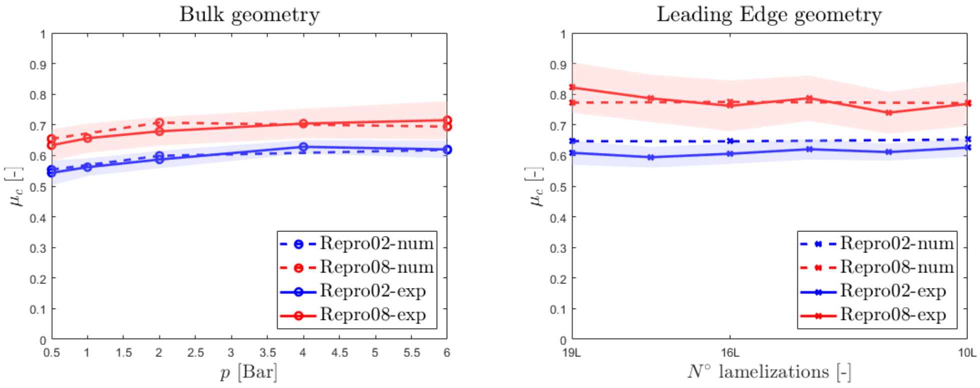

(c) Bulk - *Model B* (d) LE - *Model B*

Figure 8.1: Bulk/LE protocol: reconstruction of the global friction coefficient - a local *ad hoc* friction coefficient μ is used herein for both material models.

The *qualitative* evolution from simulations with pressure and lamellization number do not perfectly match experimental results. However, most of them are in the interval of confidence of the experimental results as presented in Figure 4.23 in Section 4.4.3. Both models predict an adequate overall absolute value of the friction coefficient as compared to experiments. In addition, the models can reasonably differentiate between Bulk/LE geometry or Repro02/08 with adequate statistical significance (when using the experimental dispersion), as observed in Figure 8.2, which was also the case for experimental results from Figures 4.24 and 4.25. The few exceptions correspond to high pressure simulations where the Model A does not discriminate well the 10 lamellae geometry and where the Model B is not discriminating the case with many lamellae.

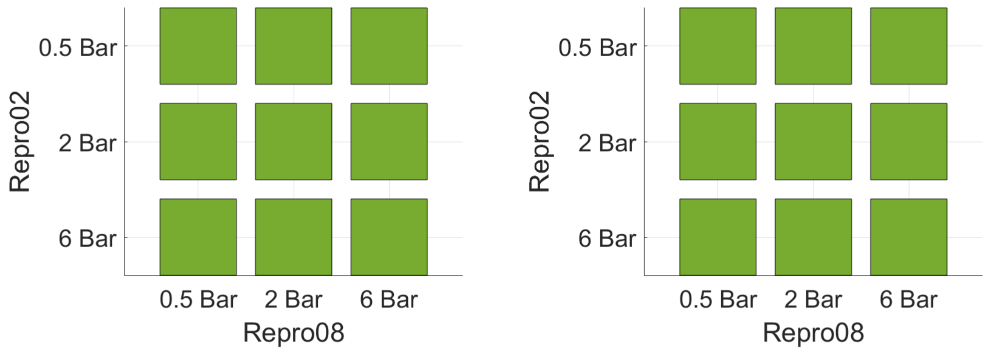

(a) Model A - Bulk-Repro02 vs Bulk-Repro08 (b) Model B - Bulk-Repro02 vs Bulk-Repro08

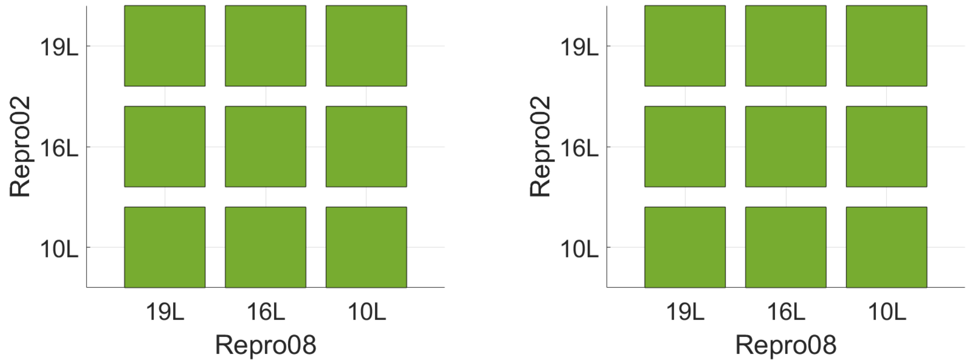

(c) Model A - LE-Repro02 vs LE-Repro08 (d) Model B - LE-Repro02 vs LE-Repro08

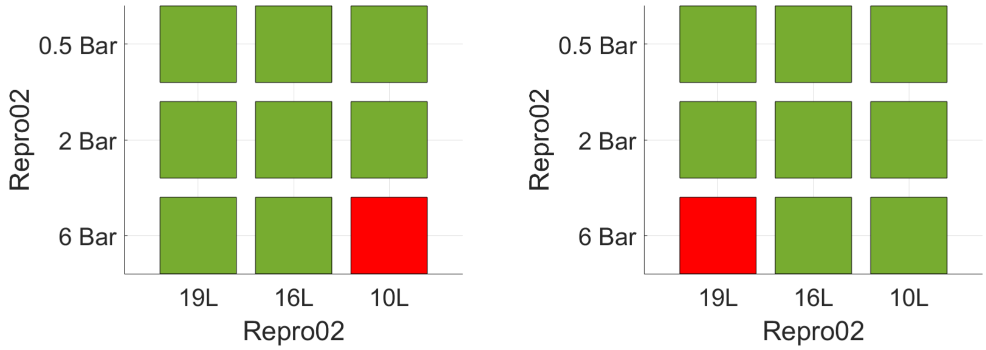

(e) Model A - Bulk-Repro02 vs LE-Repro02 (f) Model B - Bulk-Repro02 vs LE-Repro02

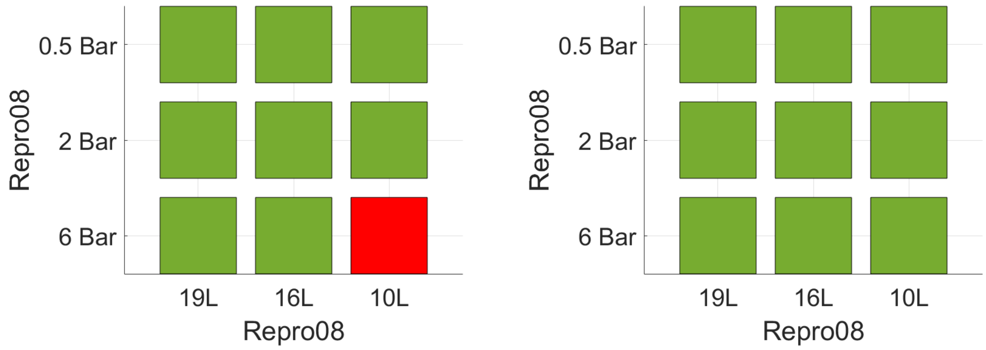

(g) Model A - Bulk-Repro08 vs LE-Repro08 (h) Model B - Bulk-Repro08 vs LE-Repro08

Figure 8.2: Two-sample t-test combinatory as obtained from the numerical results- Geometry and ground sweep for both material models - *ad hoc* μ.

In summary, an ad hoc fixed local friction coefficient used at the finer scale level already reproduces qualitatively this complex tribological test, at the cost of a proper description of the surface and rubber geometry.

8.3 Numerical predictions with $\mu(P, V)$

This campaign displays the same available data from Table 8.1, this time, implementing the *Coupling strategy* from Section 7.4. *This coupling strategy does not need any a posteriori experimental fitting of the local friction coefficient.* Apart from the considerations from Section 7.6, no additional adjustment were made to estimate $\mu(p_0, V_g)$, which are direct outputs from the CC-FFT method (see Section 7.5) and the FEM local working points.

From Figure 8.3, albeit the superposition quality is modified, the trend of interest is preserved. Changing from a *Filtered* to a *Coupling* strategy does not affect the *qualitative* response of the simulations, but their absolute values are shifted, with a bias which does depend on the viscoelastic model which is considered. The non-linear model B performs better on the bulk geometry for both soils and the leading edge geometry for the aggressive soil Repro08. On the other hand, the linear model seems to be of better quality for the smoother surface Repro02. Both models are slightly off for the low pressure simulation on the Repro08 soil. These qualitative observations need to be detailed by carefully revisiting the corresponding experimental results.

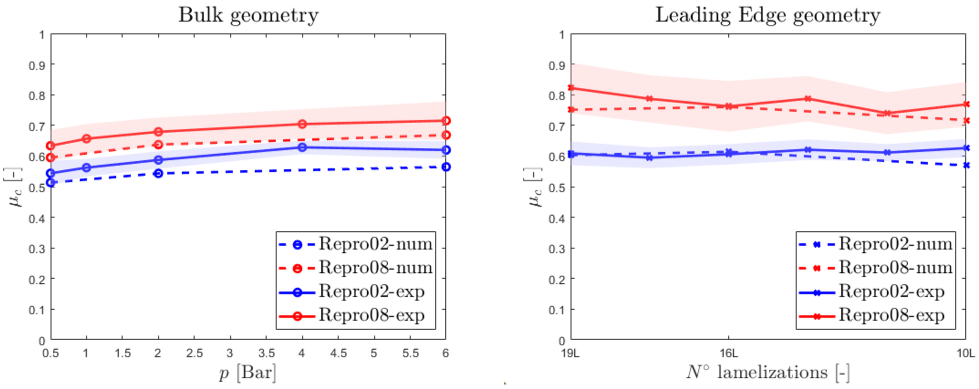

(a) Bulk - *Model A* (b) Leading Edge - *Model A*

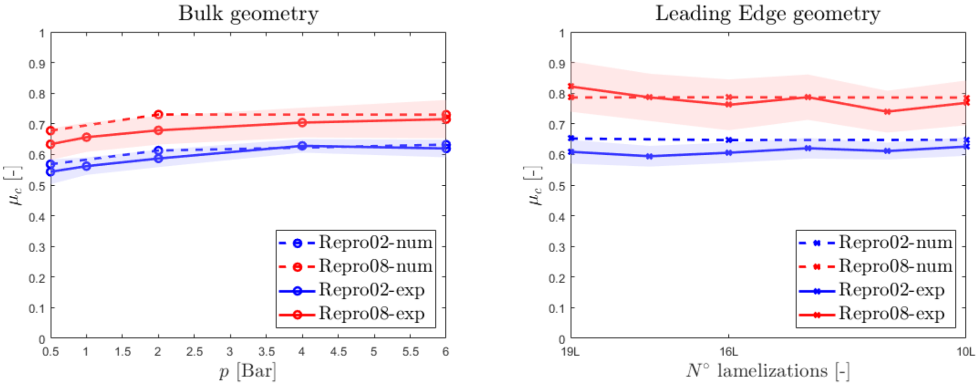

(c) Bulk - *Model B* (d) Leading Edge - *Model B*

Figure 8.3: Bulk/LE protocol : reconstruction of the global friction coefficient - the *half-space* friction coefficient $\mu(P, V)$ is used herein for both material models.

Lastly, the *Coupling strategy* displays a computational time 30% larger than the *Filtered strategy*, which is a very small penalty when compared to other usual multi-scale approaches [128], [129].

8.4 Key features

In order to gain further insight, we profit from the accessibility of internal and local information that the numerical environment provides to better understand the effect of sculpture and material model.

Sculpture effect

A pivotal trend that differentiates the Leading Edge from Bulk was discussed in Section 2.3.4 in Chapter 2, which is the presence of *interlocking*, namely a conformal contact also previously called as mechanical gearing [129]. Experimentally, its effects can be qualitatively observed (see Figure 2.17). This behaviour was also captured numerically, as shown in Figure 8.4 depicting the tread block (in yellow) and highlighting in vivid color the regions subjected to interlocking and snailing/curling effects.

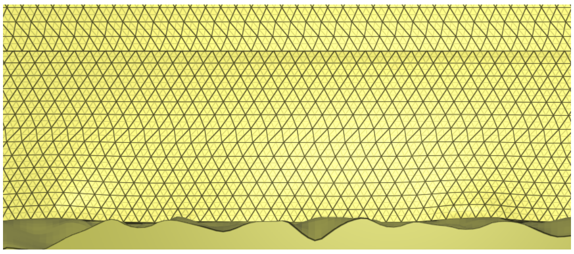

(a) Bulk 2 *Bar*

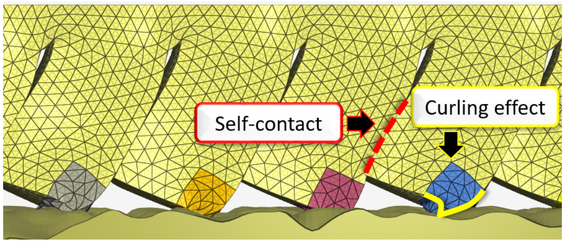

(b) LE - 16L

Figure 8.4: Lateral view of discretized bodies at stabilized sliding conditions - *Filtered Approach* using *Model A*.

Although still qualitative, the difference in operating conditions between Bulk and Leading Edge is already noticeable at the centimeter scale. Two general behaviours are highlighted for the Leading Edge: near the ground the front of each individual tread block presents strong “snailing” effect, while far from the ground a self-contact of neighboring tread blocks is also in agreement with experiments (see Figure 4.4).

To better understand the specificity’s of the Leading Edge, a schematic colored representation of the total accumulated contact area across a single sliding simulation is displayed in Figure 8.5. For the same ground, viscoelastic model and contact strategy, the Leading Edge sculpture maps a region of the ground 6.5× larger than the Bulk sample. In addition, the quality of contact is more intricate, interacting with the lateral side of the pebbles skewed from the sliding plane and also reaching deeper portions of the ground, where for a sculpture of 16L, almost 29% of the load is ported in depths whose regions Bulk samples are not able to interact.

Those distinctions may also impact the working points for both types of rubber geometry. To get an estimation, Figure 8.6 displays the occurrence distribution for Bulk and

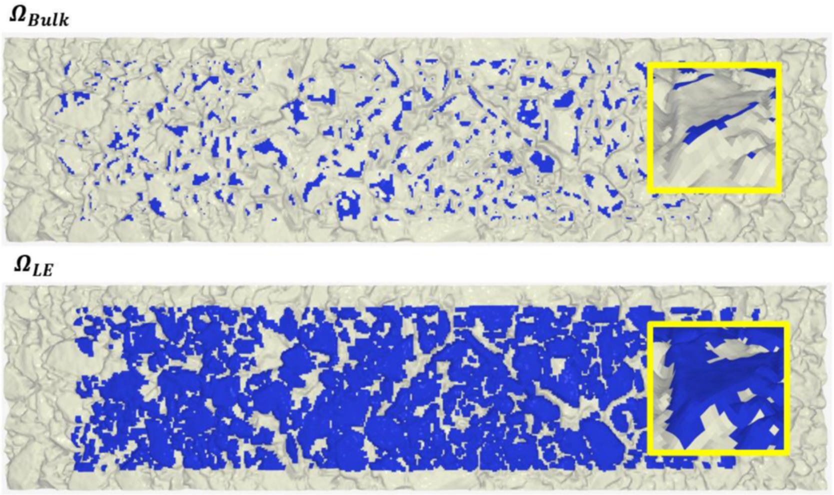

Figure 8.5: Visualization of the true contact points covered by each tread geometry – (yellow frame) Zoom into the same asperity.

Leading edge (16 lamellae) geometries with respect to the local pressure, $\bar{p}$, and the local sliding velocity component, $\bar{V}_g$, with respect to the nominal sliding direction of the rubber. For both case studies the rubber slides with a nominal velocity of 1 [m/s] against Repro08 ground profile with a calibrated constant friction. In addition, both rubber samples consider *Model A* as their constitutive model. Lastly, this 2D histogram is weighted in space and across the same time interval where the stabilized dynamic friction from Figures 8.1 and 8.3 were recovered.

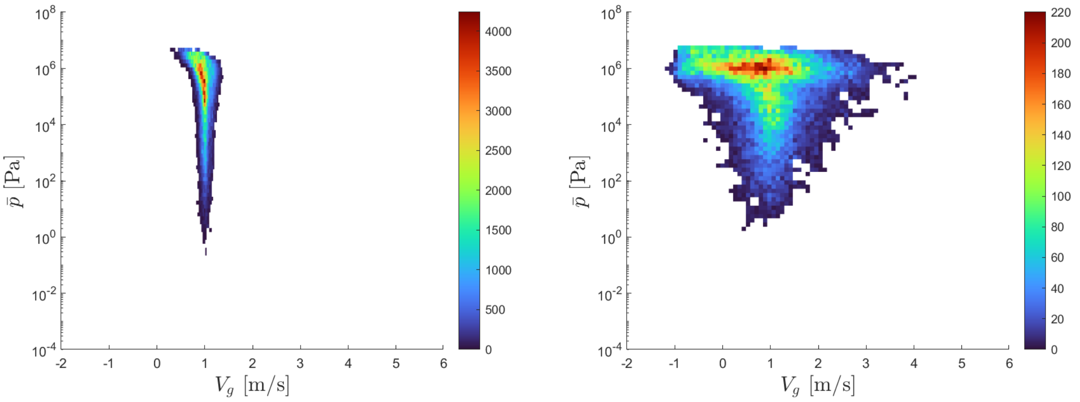

(a) Bulk 2 *Bar* - *Model A*

(b) Leading Edge - *Model A*

Figure 8.6: $\bar{p}$ and $\bar{V}_g$ occurrences - Geometry effect for Repro08, *ad hoc* μ and *Model A*.

For both case studies, the occurrences are scattered around the nominal velocity, which is expected for simulations with imposed longitudinal displacement. However, there are some important distinctions in their distributions. For instance, the dispersion of Leading Edge case is more pronounced than the Bulk case in the sliding velocity axis. This is attributed to a higher degree of freedom enabled by the tread-pattern geometry, which also leads to the disparity in load distribution across ground depth and the total accumulated contact area (see Figure 8.5). These trends emphasize that even if the same *half-space* functional friction is considered with the *Coupling strategy*, the friction curve would not be solicited in the same manner for a Bulk and a LE sample, justifying the importance of a proper computation of sculptures from the cm-mm scale in FEM.

In Figure 8.6b, we also remark a slight imbalance where most concentrated occurrences (yellow-red zones) are skewed bellow the 1 [m/s] mark, while also being balanced by short-lived responses at very high velocities. This unevenness hints on the stick-slip interaction for LE samples, where the rubber spends a large period in a near-stick mechanical gearing followed by a short-lived “whipping” behavior during slip-off to catch up with the moving upper metallic plate. This simple measurement is consistent with the interlocking trend seen experimentally in Figure 2.17 (see Section 2.3.4). A similar asymmetry is also found for the Bulk geometry with smaller breadth in sliding velocity due to its confined geometry (see Figure 8.4a) .

Lastly, the absolute number of occurrences for both geometries is an indirect sign of their contact area. Although a very large region is mapped with tread-pattern samples (see Figure 8.5), only a small fraction of the rubber is in contact with the ground at all times, as seen in Figure 8.4. This also depicts why most concentrated occurrences (red zones from Figure 8.6) are located at higher pressures for the Leading Edge and and lower (and more spread out) results are found for Bulk’s geometry.

The deformation field of both geometries are evaluated. Figure 8.7 displays the Von-Mises of Strain, ε^{VM}, an invariant available within IMPETUS environment, for the interval $[0, 2]$. For the Bulk geometry, the largest magnitudes for this invariant are found in the rubber-ground interface, with values around $\tilde{\varepsilon}^{VM}_{Bulk,Base} \approx 25\%$. For the sculpture sample, we distinct two regions: tread bloc region far from rubber-ground contact and the Leading Edge *per se*. The first zone displays an average strain invariant of $\tilde{\varepsilon}^{VM}_{TB} \approx 10\%$, whilst this value can be up to 7 times larger near the rubber-contact zone due to the curling deformation.

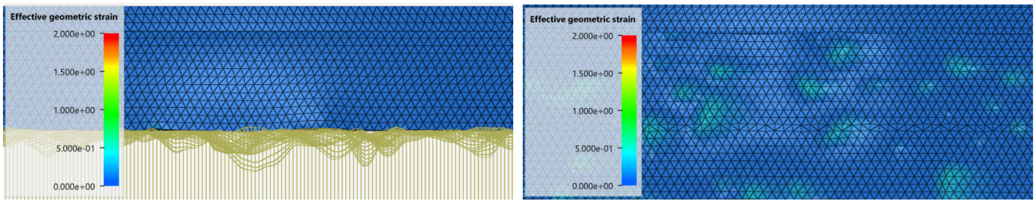

(a) Lateral view - Bulk 2 *Bar* (b) Bottom view - Bulk 2 *Bar*

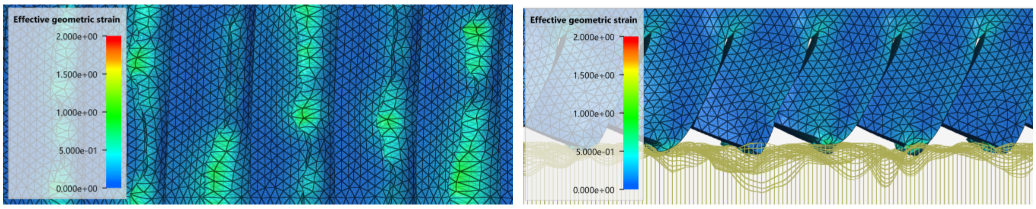

(c) Bottom view - LE 16L (d) Lateral view - LE 16L

Figure 8.7: Von-Mises Strain field - *Filtered Approach* using *Model A*.

The strong disparity in deformation field for the Leading Edge justifies the importance of considering a proper sensitivity to strain deformation for the viscoelastic model. For a simple Generalized Maxwell rheological model, its parameters would be identified for a given single strain magnitude from DMA data and inevitably underestimate/overestimate the response for one or both regions in the geometry. Prioritizing the Leading Edge is not preferable too, since although a big portion of the dissipation occurs at the Leading Edge (around 70% of the total dissipation), the tread blocks pivots the rubber-ground interaction, strongly affecting the trends from Figures 8.6 and 8.5.

Effect of the material model

So far, *Model A* and *Model B* were compared with experiments individually, but not against each other. We direct our attention to the results obtained with the *Coupling strategy*. Figure 8.8 displays a bottom view of Bulk compressed at 2 [Bar] at stabilized sliding velocities for each viscoelastic model. The average values of this Von Mises strain ε^{VM} as calculated in the true contact surface is of of 25% for *Model A* and 40% for *Model B*. This larger indentation for *Model B* also reflects on a contact area which is 20 percent larger for *Model B*.

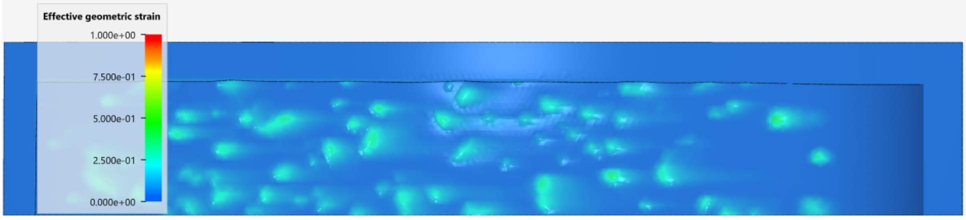

(a) Bottom view - Bulk - *Model A*

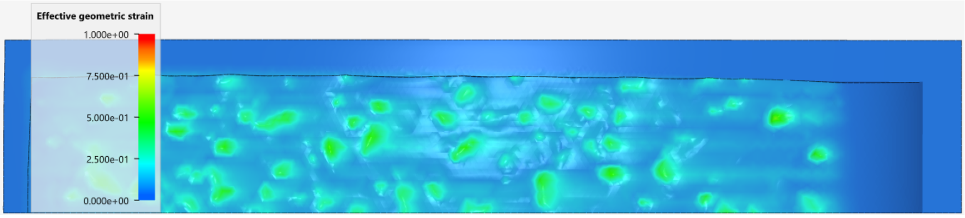

(b) Bottom view - Bulk - *Model B*

Figure 8.8: Von-Mises Strain field on the bottom surface within the range $\varepsilon^{VM} = [0, 1]$ - Results obtained on the bulk geometry with the *Coupling strategy* using *Model A/B* for Repro08.

The same disparity was found for the Leading Edge but with larger observed values, as shown in Figure 8.9 within the the range $\varepsilon^{VM} = [0, 2]$.

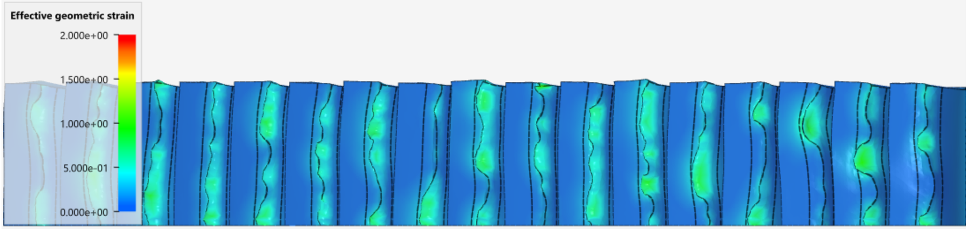

(a) Bottom view - LE - *Model A*

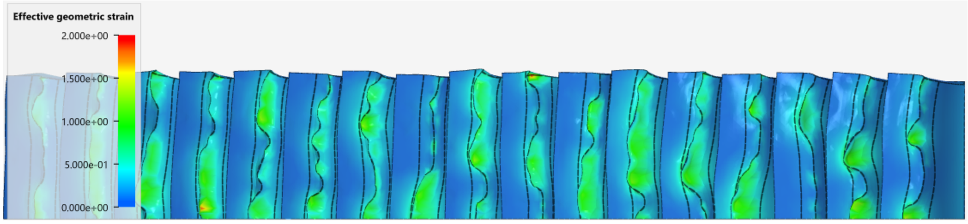

(b) Bottom view - LE - *Model B*

Figure 8.9: Von-Mises Strain field on the bottom surface within the range $\varepsilon^{VM} = [0, 2]$ - Results obtained on the leading edge geometry with the *Coupling strategy* using *Model A/B* for Repro08.

For the leading edge geometry, the average values of the Von Mises strain field on the true contact surface are of 70% for *Model A* and of 85% for *Model B*. Similarly the contact area for *Model B* is 40% larger than the contact area using *Model A*. Consequently, the same geometrical trends from Figure 8.10a displaying *self-contact* and *curling* are present on Model B albeit more pronounced, as shown in Figure 8.10

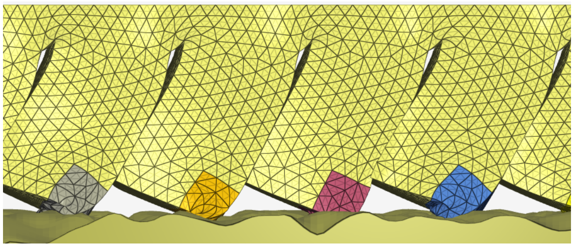

(a) LE *Model A*

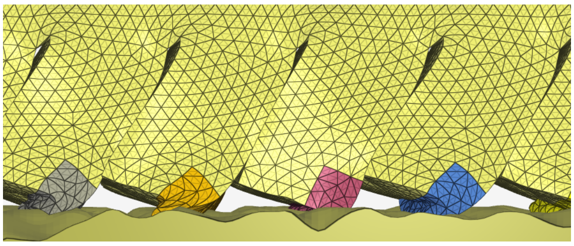

(b) LE - *Model B*

Figure 8.10: Lateral view of discretized sculptures at stabilized sliding conditions - *Filtered Approach* using both viscoelastic models and a Leading Edge geometry.

The occurrence distribution from previous sections is also made for *Coupling strategy* using *Model A/B* for Repro08 in Figure 8.11.

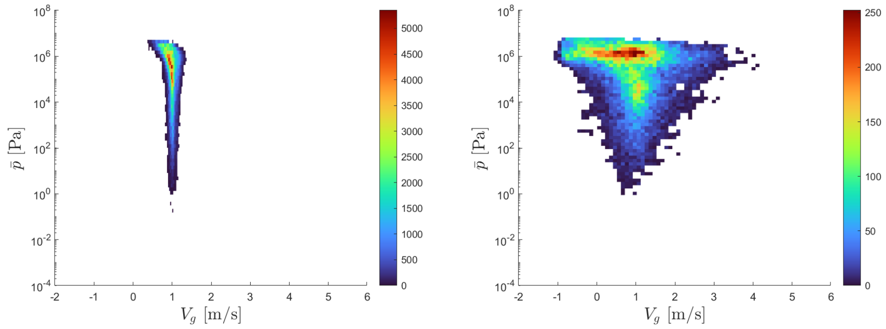

(a) Bulk 2 *Bar* - *Model A* (b) Leading Edge - *Model A*

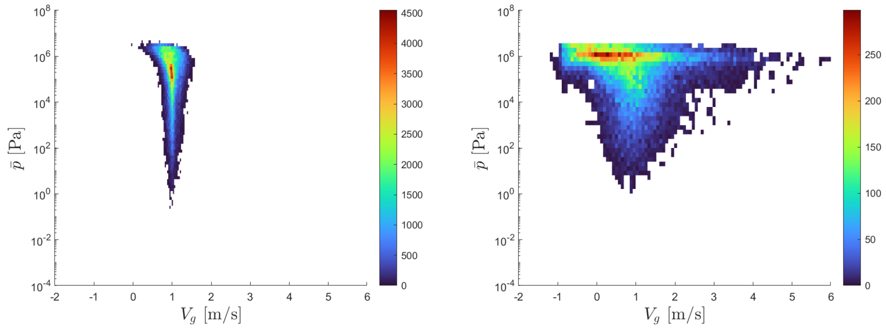

(c) Bulk 2 *Bar* - *Model B* (d) Leading Edge - *Model B*

Figure 8.11: $\bar{p}$ and $\bar{V}_g$ occurrences - Geometry/material effect for Repro08 and *half-space* μ.

When comparing both material models, we notice an even more distinct skewness in the sliding velocity axis with *Model B* which could indicate a longer near-stick mechanical gearing with the ground profile and thus a more aggressive “whipping” slip-off (especially for the Leading Edge).

The discrepancies when implementing *Model B* could originate from two non-linear effects presents in its formulation. The first is the pronounced softening in stiffness (see Chapter 5), which would allow a larger indentation in Bulk geometries (see Figure 8.8) and a larger flexion of the tread blocs for the Leading Edge sculptures (see Figure 8.9). The second, as also observed for tribological sphere-rubber cases from Chapter 6, is a stronger asymmetry in the pressure distribution when interacting with an indentor.

Those distinctions between constitutive models are still present even if an *ad-hoc* local friction is considered, as shown in Figure 8.12. In addition, the working points from this scenario is similar to Figure 8.11, when a *half-space* friction is used, which is consistent with the similarities found in Figures 8.1 and 8.3.

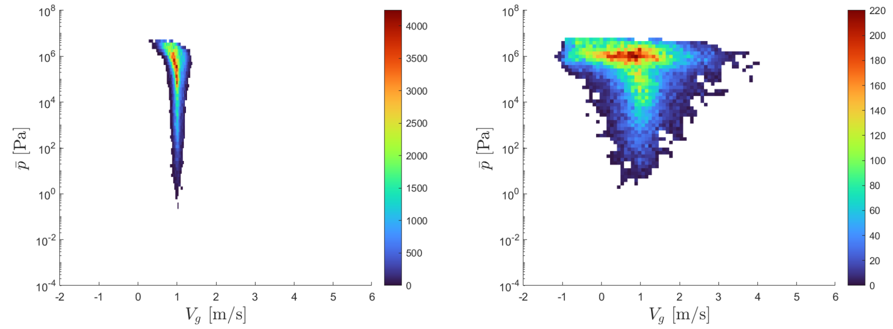

(a) Bulk 2 *Bar* - *Model B* (b) Leading Edge - *Model B*

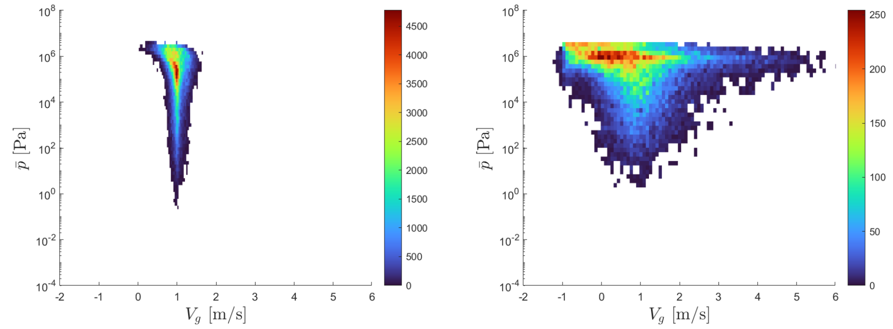

(c) Bulk 2 *Bar* - *Model B* (d) Leading Edge - *Model B*

Figure 8.12: $\bar{p}$ and $\bar{V}_g$ occurrences - Geometry/material effect for Repro08 and *ad-hoc* μ.

Conclusion

The work presented here dealt with the prediction of tangential forces generated by the relative sliding of a rubber mix material with a complex geometry (tread pattern) on a wet rough road surface. First-order effects such as *material* characteristics, *contact* interactions, and *geometrical* contributions were identified and accounted for via a comprehensive multi-scale contact model taking into account all these effects. The construction of this model used a series of experiments of increasing complexity. The final result displays qualitative and quantitative correlation with tribological experiments for sample geometries of moderate complexity and a range of working points in normal compression.

Due to the large scope of the study, the topics of the research can be viewed as two parallel investigations: (a) the development of the mechanical problem in the order of scales from centimeter to millimeter, introduced in Chapter 5 and validated in Chapter 6; (b) the implementation of an effective local model from the literature covering the millimeter to micrometer scale, introduced in Chapter 4 and developed on Chapter 7. Those two parts are then assembled into a final multi-scale model, also introduced in Chapter 7 and validated in Chapter 8. Along the way, four experiments were performed, to assess each component of the model with a corresponding experimental basis of comparable complexity.

The first experimental campaign concerns the development of the constitutive model considering mainly *material* characteristics. This is done via specific homogeneous mechanical tests to assess the properties of the industrial-filled rubber. Dynamic Mechanical Analysis in simple shear and uniaxial Loading/Unloading tests were performed experimentally or recovered from previous internal datasets, providing viscoelastic properties across a large range strain rate from 10^{-1} [s^{-1}] to 10^{-4} [s^{-1}] and magnitude that reach 150%. In addition, the data highlighted non-linear viscoelastic effects, the central ones being sensitivity to strain rate, stiffness softening, and a non-linear change in relaxation time with deformation. Based on those characteristics, a proposed finite non-linear viscoelastic material has been selected, extended, and calibrated in Chapter 5. The constitutive law is thermodynamically consistent and was able to account for a portion of the non-linear effects, while its experimental calibration imports a large range in strain magnitude and strain rate. Nonetheless, it's important to acknowledge that the model identification does not cover the full available data and recovers non-linearity indirectly as experiments stem from simple mechanical tests that are not specially designed to precisely identify a particular non-linear effect.

The second experiment mixes *material* contributions with *contact* interactions on smooth lubricated surfaces. This evaluation is made by a simplified landing-sliding contact procedure between a flat specimen of chosen industrial-filled rubber and a substrate featuring simple spheres coated with dry lubricant and immersed in a temperature-controlled water tank with diluted surfactant. The experimental layout tried to minimize adhesive contributions and temperature effects to highlight hysteresis dissipation induced by the finite indenters. The numerical modeling of this experiment was performed within a Finite Elements framework to handle non-homogeneous deformations like indentation, using either the proposed non-linear viscoelastic constitutive model or a simpler classical finite linear viscoelastic model, to be used for comparison. The model recovered the non-linear geometric effects observed in the experiments and was able to explain the specific time history of the observed forces. The results also proved that local non-hysteretic friction forces were present, and had to be experimentally fitted. Its exact physical cause is yet to be understood, although they are expected for rubber Teflon interfaces. Numerical results did nevertheless introduce a slight overshoot and were not completely able to finely reproduce the results of the tests performed at high compression, probably indicating a lack of maturity in the non-linear model used for viscosity.

The third set of experimental data dealt in Chapter 4 with the identification of the *geometrical* characteristics from the millimeter to micrometer scale needed for the development of a local model. Confocal microscopy recovered the typical profile encountered in real roads. In addition, a novel qualitative multi-depth descriptor was proposed for its characterization to provide further insights into the texture aggressiveness, revealing polished zones on the summit of larger pebbles across different length scales. The approach also highlights the repercussions of phase-related information loss when using reconstructed Gaussian grounds. Based on these observations in Chapter 4, it was decided to keep the full soil signal in our simulations. The CC-FFT method was then chosen in Chapter 7 as the local model as it imports the full information of the ground via its FFT, preserving phase contents of available data. Smaller scales outside measurement resolution were reconstructed based on the profile measured at larger scales. This approach produced a master curve for the local friction coefficient as a function of the local pressure and velocity observed at the macroscopic scale. This frictional function covers a large range of local pressure and velocity and is capable of discerning between different types of rough soil surfaces. Regrettably, the experimental resolution was limited to 25 [μm], thus impacting the quality of the ground reconstruction at the lowest scales (from 25 [μm] to $1-2$ [μm]), based on an extrapolation technique using a random phase which may alter the fidelity of the soil reconstruction.

The fourth and final experimental tests took into account all relevant first-order effects: *material*, *contact*, and *geometry*, on the whole scale range from centimeter to micrometer. This procedure involved the use of rubber mix samples with or without simplified tread patterns sliding against two known rough ground slabs in wet conditions. The sculptured specimens differed by the number and the width its rubber blocks. The samples with no sculpture were tested for a range of compression loads relevant to what is observed in real tires. For its numerical reconstruction in Chapter 8, FEM simulation was used to directly simulate the scales ranging from the centimeter to the millimeter. To account for the scales from the millimeter to the micrometer, two frictional contact approaches were considered: (i) a constant ad hoc friction calibrated with global experimental data; (ii) the multi-scale approach of Chapter 7 producing a local friction master curve of the local contact pressure and tangential velocity to be taken into account in global finite element simulation. The combination of the two proposed frictional approaches and constitutive models was compared with their experimental counterparts. The results displayed a good correlation with the experimental results and confirmed important qualitative deformation trends like Leading Edge “curling” and tread bloc self-contact, highlighting the need for an explicit consideration of the tread pattern. In addition, they demonstrated that the consideration of the ground geometry is necessary for a correct prediction of the local grip. The multi-scale approach was able to produce global predictions of similar quality as for the constant ad hoc friction, avoiding the need for lengthy ad hoc calibration. It would be nevertheless interesting to have more local information on the pressure distribution to better identify the different contributions of the material model, of the geometric effects such as gearing and self-contact, or of the local micro-mechanical model that was used in the simulation.

Important insights were gained from each of the above approaches.

- A broad range in strain magnitude and strain rate was successively covered during the identification process of the non-linear Viscous Model using simple optimization procedures and adequate cost functions;
- A strong coupling between geometrical effects and long-term relaxation properties were observed experimentally in the proposed smooth contact experiment and explained numerically using the non-linear Viscous Model;
- At smaller scales, the local friction model was able to differentiate between a worn soil surface Repro02 and a more aggressive surface Repro08, a difference which usually observed indirectly from tribological experiments;
- Considering the non-linear Viscous Model and the local friction models did eliminate the need of fitting (not known *a priori*) variables as used in the classical approach, namely: (i) the value of the local friction coefficient and (ii) a reference maximum strain magnitude to be used when selecting the relevant Dynamic Mechanical Analysis data in the calibration process of the linear model;
- An adequate correlation between rough contact experiments and their numerical counterparts was achieved, highlighting ground/rubber geometry, scale range and viscoelastic properties as first-order mechanisms to be considered.

In terms of perspectives, some mechanisms identified in Chapter 2 were not explicitly considered, such as adhesion, thermal effects and lubrication. Moreover, our experiments mainly produced global outputs, and some would require further validation. Thus, there are still many paths to be explored, that we can classify in three categories: (a) global experimentation; (b) material modelling and (c) micro-modelling of contact.

Concerning the overall experimental aspect, three extensions are recommended The first one would be to apply the already designed experimental campaigns and protocols to a larger class of industrial rubber-mixes, instead of concentrating as we did on the Michelin Primacy 4 rubber mix. It would be interesting to confirm the relevance of the proposed non-linear stiffness and non-linear relaxation time for such materials. This would indicate if the proposed model is sufficient or if additional effects are needed. Next, for the second extension, arrangements should be made to recover the local deformation fields using, for instance, Digital Image Correlation (DIC) with a speckle pattern. As shown in Chapter 5, even a simplified two-point DIC proved to be essential for a correct estimation of the material's stiffness. Moreover, optical measurements could provide more detailed data, help to verify the assumption of an homogeneous field and of quasi incompressibility in uniaxial tests even for very large strains. Lastly, for tribological tests, contact pressure fields could also be partially recovered via Contact Pressure Sensitive Paper (CPSP), at least for dry contact during the static compression phase. If such technique is paired up with DIC measurements, local information could be checked with their numerical counterparts in addition to the original global outputs.

The third aspect would deal with the experimental identification of the local friction coefficient between teflonated metal spheres and rubber. Indeed, the sphere-soil campaign described in Chapter 6 has proven the presence of a local friction between those materials. The current protocol cannot quantify the relative contribution of hysteretic effects and of local friction to the resulting total tangential force. Therefore, instead of attempting to fit a posteriori the local contribution, an estimation of a single experimental local friction should be sought instead. This could be attempted in different manners. One proposition is to minimize the hysteretic contributions by lowering the imposed nominal normal load to better identify local contributions. One could also apply a sweep in nominal velocity at such low compression values or test other substrate configurations, such as different number and distribution of spheres with or without Teflon coating.

The subsequent aspect considers the material model as implemented at the centimeter to millimeter scale for FEM simulations. The foundation of this model was based on the comprehensive Two-Potential approach proposed by O. Lopez-Pamies and A. Kumar, where their work also identified other finite formulations from the literature to be equivalent or a subset from the same framework [107]. Yet, even similar formulations of stress and evolution equations can present large discrepancies due to different expression for the viscosity coefficients. The present research does not sufficiently discriminate the choice of viscosity function from other existing strategies accounting for strain rate and/or magnitude sensitivity. For instance, one could use models that also implements viscous invariants, but with different viscosity formulations [150], or models that adds an additional internal variable in the viscosity function to account for transient effects [85], or even a combination of the above with a classical implementation of a multiple branch model. Those options are still an open topic of debate. For this reason, we suggest to first look for discriminating data. To the authors knowledge, there is no definite experiment that can properly isolate the viscosity trends for elastomers. Nevertheless, we identify temporal data as an irreplaceable asset for such identifications. For instance, simple shear tests with transitory excitations beyond simple sinusoidal history signals, like Haversine or double sine (two sinusoidal of different amplitudes and frequencies superposed), could be promising candidates. The interest of temporal data was emphasized in the sphere soil test. There, although the non-linear model displayed important trends in velocity sweep in contrast to its linear counterpart, its underestimation in load sweep could indicate an overshoot in viscosity, and be a ground for upgrading the model. This has to be confirmed by looking at local values (in space and time) of the proposed viscosity. A more subtle viscosity formulation could then be derived from this analysis. Naturally, all previous stated propositions such as the estimation of an experimental local friction and a richer temporal transient data could complement this evaluation as well. Another aspect of material modeling would be to take into account thermomechanical effects as in LION, especially for samples with tread patterns. Indeed, for real tires in wet conditions, the isothermic conditions used here because of short sliding distances and temperature-controlled wet contact may not fully apply.

Regarding the micro-modeling aspect, all suggested investigations for the future still assume periodicity and a half-space domain. The first and most straightforward proposition solely modifies the geometrical reconstruction on the smaller scales. For context, if experimental characterizations of the full ground for a resolution of 1 [μm] were available, this would remove the need of reconstructing strategies entirely, using only measured data instead. However, such measurements are not often accessible. We then need to develop a more robust extrapolation strategy only using the Power Spectrum Density at close to these small scales, to be acquired with improved precision.

The next set of propositions for the micro-modeling aspect deals concerns the extension of the viscoelastic half-space approach. First, the analytical displacement solution from Chapter 7 could be extended to account for a local Amontons-Coulomb friction at the scale of 1 [μm], emulating simplified adhesion contributions [130]. Alternatively, the same analytical displacement solution could be extended to consider material anisotropy by means of multiple half-space vertical layers with distinct material properties [139]. Furthermore, it would be interesting to investigate the impact of material and geometrical non-linearities at local scales. For example, by matching the constitutive choice made for FEM and considering the true normal to the surface. However, doing so, would require a non-linear FFT technique, which is much more complex to implement.

To conclude, a final set of propositions for the micro-modeling aspect accounts for the inclusion of specific physical mechanisms referenced in Chapter 2. The first concerns Elastohydrodynamics (EHL) effects for the local contact problem. In the present version, lubrication is considered as a conceptual sealing effect that masks the profile of the ground for scales below 1 [μm]. However, in real cases, such masking can dynamically change, [108], [151]. Lastly, local flash-heating effects can occur at local scales, especially when sliding against very aggressive ground profiles [63]. Its exact contribution for wet contact is still an open topic [134]. Nonetheless, experimental comparisons with models using thermomechanical coupling should aid in quantifying its participation.

The recommendations are not exhaustive, but each topic should have enough proximity to the present study for the future researcher to benefit from its laid foundation.

Bibliography

[1] M. J. Boussinesq, "Application des potentiels a l'étude de l'équilibre et du mouvements des solides élastique," *Gauthier-Villars*, 1885.

[2] L. Mullins, "Effect of stretching on the properties of rubber," *Journal of Rubber Chemistry and Technology*, vol. 21, pp. 281–300, 1948. DOI: 10.5254/1.3546914. [Online]. Available: https://doi.org/10.5254/1.3546914.

[3] A. Schallamach, "The load dependence of rubber friction," *Proceedings of the Physical Society. Section B*, vol. 65, p. 657, 1952. DOI: 10.1088/0370-1301/65/9/301. [Online]. Available: https://doi.org/10.1088/0370-1301/65/9/301.

[4] J. Dyson and W. Hirst, "The true contact area between solids," *Proceedings of the Physical Society. Section B*, vol. 67, pp. 309–312, 1954. DOI: 10.1088/0370-1301/67/4/305. [Online]. Available: https://doi.org/10.1088/0370-1301/67/4/305.

[5] M. Williams, R. Landel, and J. Ferry, "The temperature dependence of relaxation mechanisms in amorphous polymers and other glass-forming liquids," *Journal of the American Chemical Society*, vol. 77, pp. 3701–3707, 1955. DOI: 10.1021/ja01619a008. [Online]. Available: https://doi.org/10.1089/big.2014.0018.

[6] J. F. Archard, "Elastic deformation and the laws of friction," *Proceedings of the Royal Society of London. Series A, Mathematical and Physical Sciences*, vol. 243, pp. 190–205, 1957. DOI: 10.1098/rspa.1957.0214. [Online]. Available: https://doi.org/10.1098/rspa.1957.0214.

[7] F. Bueche, "Molecular basis for the mullins effect," *Journal of Applied Polymer Science*, vol. 4, pp. 107–114, 1960. DOI: 10.1002/app.1960.07004101. [Online]. Available: https://doi.org/10.1002/app.1960.070041017.

[8] F. Bueche and L. Mullins, "Mullins effect and rubber-filler interaction," *Journal of Applied Polymer Science*, vol. 5, pp. 271–281, 1961. DOI: 10.1002/app.1961.070051504. [Online]. Available: https://doi.org/10.1002/app.1961.070051504.

[9] A. R. Payne, "The dynamic properties of carbon black-loaded natural rubber vulcanizates. part i," *Journal of applied polymer science*, vol. 6, pp. 57–63, 1962. DOI: 10.1002/app.1962.070061906. [Online]. Available: http://doi.org/10.1002/app.1962.070061906.

[10] A. R. Payne, "The dynamic properties of carbon black-loaded natural rubber vulcanizates. part ii," *Journal of applied polymer science*, vol. 6, pp. 368–372, 1962. DOI: 10.1002/app.1962.070062115. [Online]. Available: http://doi.org/10.1002/app.1962.070062115.

[11] K. Grosch, "The relation between the friction and visco-elastic properties of rubber," *Proceedings of the Royal Society mathematical, physical and engineering sciences*, vol. 274, pp. 21–39, 1963. DOI: 10.1098/rspa.1963.0112. [Online]. Available: https://doi.org/10.1098/rspa.1963.0112.

[12] J. Harwood, L. Mullins, and A. Payne, "Stress softening in natural rubber vulcanizates. part ii. stress softening effects in pure gum and filler loaded rubbers," *International Journal of Solids and Structures*, vol. 9, pp. 3011–3021, 1965. DOI: 10.1002/app.1965.070090907. [Online]. Available: https://doi.org/10.1002/app.1965.070090907.

[13] J. A. Greenwood and J. B. P. Williamson, "Contact of nominally flat surfaces," *Lubricants*, vol. 295, p. 1442, 1966. DOI: 10.1098/rspa.1966.0242. [Online]. Available: https://doi.org/10.1098/rspa.1966.0242.

[14] J. Harwood, L., and A. Payne, "Stress softening in natural rubber vulcanizates. part ii. carbon black-filled vulcanizates," *International Journal of Solids and Structures*, vol. 910, pp. 315–324, 1966. DOI: 10.1002/app.1966.070100212. [Online]. Available: https://doi.org/10.1002/app.1966.070100212.

[15] L. Landau and E. Lifshitz, *Theory of Elasticity*, 2nd ed., P. press, Ed. Pergamon press, 1970.

[16] P. R. Nayak, "Random process model of rough surfaces," *Journal of Lubrication Technology*, vol. 93, pp. 398–407, 1971. DOI: 10.1115/1.3451608. [Online]. Available: https://doi.org/10.1115/1.3451608.

[17] D. F. Moore, "On the decrease in contact area for spheres and cylinders rolling on a viscoelastic plane," *Wear*, vol. 21, no. 1, pp. 179–194, 1972, ISSN: 0043-1648. DOI: https://doi.org/10.1016/0043-1648(72)90256-6. [Online]. Available: https://www.sciencedirect.com/science/article/pii/0043164872902566.

[18] A. Payne and R. Whittaker, "Effect of vulcanization on the low-strain dynamic properties of filled rubbers," *Journal of Applied Polymer Science*, vol. 16, pp. 1191–1212, 1972. DOI: 10.1002/app.1972.070160513. [Online]. Available: https://doi.org/10.1002/app.1972.070160513.

[19] A. Bush, R. Gibson, and T. Thomas, "The elastic contact of a rough surface," *Wear*, vol. 35, pp. 87–111, 1975. DOI: 10.1016/0043-1648(75)90145-3. [Online]. Available: https://doi.org/10.1016/0043-1648(75)90145-3.

[20] D. Fuller K. N. G. andTabor, "The effect of surface roughness on the adhesion of elastic solids," *Proceedings of the Royal Society*, vol. 345, p. 1642, 1975. DOI: 10.1098/rspa.1975.0138. [Online]. Available: https://doi.org/10.1098/rspa.1975.0138.

[21] E. Rowe, "The friction and lubrication of elastomers," *The Aeronautical Journal*, vol. 79, pp. 45–45, 1975. DOI: 10.1017/S0001924000034795. [Online]. Available: https://doi.org/10.1017/S0001924000034795.

[22] T. T. Sayles R.S, "Surface topography as a nonstationary random process," *Nature*, vol. 271, 271:43, 1978. DOI: 10.1038/271431a0. [Online]. Available: https://doi.org/10.1038/271431a0.

[23] R. M. Christensen, *Theory of Viscoelasticity: An Introduction*, 2nd ed., A. Press, Ed. Academic press, 1982.

[24] S. W. Zhang, "Mechanisms of rubber abrasion in unsteady state," *Rubber Chemistry and Technology*, vol. 57, pp. 755–768, 1984. DOI: 10.5254/1.3536031. [Online]. Available: https://doi.org/10.5254/1.3536031.

[25] J. Hallquist, G. Goudreau, and D. Benson, "Sliding interfaces with contact-impact in large-scale lagrangian computations," *Computer Methods in Applied Mechanics and Engineering*, vol. 51, no. 1, pp. 107–137, 1985, ISSN: 0045-7825. DOI: https://doi.org/10.1016/0045-7825(85)90030-1. [Online]. Available: https://www.sciencedirect.com/science/article/pii/0045782585900301.

[26] A. Savkoor, “Dry adhesive friction of elastomers: A study of the fundamental mechanical aspects,” Ph.D. dissertation, Mechanical Maritime and Materials Engineering, 1987.

[27] P. Le Tallec, C. Rahier, and K. Ahmed., “Three-dimensional incompressible viscoelasticity in large strains: Formulation and numerical approximation,” *Computer Methods in Applied Mechanics and Engineering*, vol. 109, no. 3, pp. 233–258, 1993, ISSN: 0045-7825. DOI: https://doi.org/10.1016/0045-7825(93)90080-H. [Online]. Available: https://www.sciencedirect.com/science/article/pii/004578259390080H.

[28] Z. Zhong, *Finite Element Procedures for Contact-Impact Problems*, O. U. Press, Ed. Linköping, Sweden: Oxford University Press, 1993.

[29] Y. Ju and T. N. Farris, “Spectral analysis of two-dimensional contact problems,” *Journal of Tribology*, vol. 118, no. 2, pp. 320–328, 1996, ISSN: 0742-4787. DOI: 10.1115/1.2831303.

[30] Z. Radó, “A study of road surface texture and its relationship to friction,” Ph.D. dissertation, Pennsylvania State University, 1996.

[31] H. M. Stanley and T. Kato, “An FFT-Based Method for Rough Surface Contact,” *Journal of Tribology*, vol. 119, no. 3, pp. 481–485, 1997. DOI: 10.1115/1.2833523.

[32] J. Bergström and M. Boyce, “Constitutive modeling of the large strain time-dependent behavior of elastomers,” *Journal of the Mechanics and Physics of Solids*, vol. 46, no. 5, pp. 931–954, 1998, ISSN: 0022-5096. DOI: https://doi.org/10.1016/S0022-5096(97)00075-6. [Online]. Available: https://www.sciencedirect.com/science/article/pii/S0022509697000756.

[33] M. Pascal and F. Brochard Wyard, “Dewetting at soft interfaces,” *Physical Review Letters*, vol. 80, p. 15, 1998. DOI: 10.1103/PhysRevLett.80.3296. [Online]. Available: https://doi.org/10.1103/PhysRevLett.80.3296.

[34] S. Reese and S. Govindjee, “A theory of finite viscoelasticity and numerical aspects,” *International Journal of Solids and Structures*, vol. 35, no. 26, pp. 3455–3482, 1998, ISSN: 0020-7683. DOI: https://doi.org/10.1016/S0020-7683(97)00217-5. [Online]. Available: https://www.sciencedirect.com/science/article/pii/S0020768397002175.

[35] G. Zavarise and P. Wriggers, “A segment-to-segment contact strategy,” *Mathematical and Computer Modelling*, vol. 28, no. 4, pp. 497–515, 1998, Recent Advances in Contact Mechanics, ISSN: 0895-7177. DOI: https://doi.org/10.1016/S0895-7177(98)00138-1. [Online]. Available: https://www.sciencedirect.com/science/article/pii/S0895717798001381.

[36] A. Lubrecht and C. Venner, “Elastohydrodynamic lubrication of rough surfaces.,” *Journal of Engineering Tribology*, vol. 213, pp. 397–404, 1999. DOI: 10.1243/1350650991542767. [Online]. Available: https://doi.org/10.1243/1350650991542767.

[37] I. Polonsky and L. Keer, “A numerical method for solving rough contact problems based on the multi-level multi-summation and conjugate gradient techniques,” *Wear*, vol. 231, no. 2, pp. 206–219, 1999, ISSN: 0043-1648. DOI: https://doi.org/10.1016/S0043-1648(99)00113-1.

[38] H. G.A., *Nonlinear Solid Mechanics: A Continuum Approach for Engineering*, Wiley, Ed. Chichester and New York, EUA: Wiley, 2000.

[39] A. N. Gent and J. Walter, *Chapter 2 - Mechanical Properties of Rubber*, N. H. T. S. Administration, Ed. New York, United States: National Highway Traffic Safety Administration, 2000.

[40] A. Haraldsson and P. Wriggers, “A strategy for numerical testing of frictional laws with application to contact between soil and concrete,” *Computer Methods in Applied Mechanics and Engineering*, vol. 190, no. 8, pp. 963–977, 2000, ISSN: 0045-7825. DOI: https://doi.org/10.1016/S0045-7825(99)00456-9.

[41] M. Klüppel and G. Heinrich, “Rubber friction on self-affine road tracks,” *Rubber Chemistry and Technology*, vol. 73, pp. 578–606, 2000. DOI: 10.5254/1.3547607. [Online]. Available: http://dx.doi.org/10.5254/1.3547607.

[42] B. Persson, *Sliding Friction*, Springer, Ed. Jülich, Germany: Springer, 2000.

[43] C. H. Venner and A. A. Lubrecht, *Multilevel Methods in Lubrication*, D. Downson, Ed. Amsterdan, The Netherlands: Elsevier, 2000.

[44] P. Chabrand, O. Chertier, and F. Dubois, “Complementarity methods for multibody friction contact problems in finite deformations,” *International jJournal for Numerical Methods in Engineering*, vol. 51, pp. 553–578, 2001. DOI: 10.1002/nme.170. [Online]. Available: https://doi.org/10.1002/nme.170.

[45] B. Persson, “Contact mechanics for randomly rough surfaces,” *Journal of Chemical Physics*, vol. 15, 2001. DOI: 10.1063/1.1388626. [Online]. Available: https://doi.org/10.1063/1.1388626.

[46] B. Persson, “Elastoplastic contact between randomly rough surfaces,” *Surface Science Reports*, vol. 87, 2001. DOI: 10.1103/PhysRevLett.87.116101. [Online]. Available: https://doi.org/10.1103/PhysRevLett.87.116101.

[47] T. Laursen, *Computational Impact and Contact Mechanics*, Springer, Ed. Berlin, Germany: Springer, 2002.

[48] B. N. J. Persson, F. Bucher, and B. Chiaia, “Elastic contact between randomly rough surfaces: Comparison of theory with numerical results,” *Physical Review B*, vol. 65, p. 19, 2002. DOI: 10.1103/PhysRevB.65.184106. [Online]. Available: https://doi.org/10.1103/PhysRevB.65.184106.

[49] C. Truesdell and W. Noll, *The Non-Linear Field Theories of Mechanics*, S. S. A., Ed. Berlin, Germany: Springer, 2003.

[50] J. D. Ferry, *Viscoelastic Properties of Polymers*, J. Wiley and Sons, Eds. New York, United States of America: Wiley, 2004.

[51] S. Hyun, L. Pei, J.-F. Molinari, and M. O. Robbins, “Finite-element analysis of contact between elastic self-affine surfaces,” *Physical review. E Statistical, nonlinear, and soft matter physics*, vol. 70, p. 13, 2004. DOI: 10.1103/PhysRevE.70.026117. [Online]. Available: https://doi.org/10.1103/PhysRevE.70.026117.

[52] B. Persson, O. Albohr, U. Tartagline, A. Volokitin, and E. Tosatti, “On the nature of surface roughness with application to contact mechanics, sealing, rubber friction and adhesion,” *Journal of Physics: Condensed Matter*, vol. 17, 2004. DOI: 10.1088/0953-8984/17/1/R01. [Online]. Available: https://doi.org/10.1088/0953-8984/17/1/R01.

[53] I. M. Ward and J. Sweeney, *An Introduction to the Mechanical Properties of Solid Polymers*, J. Wiley and Sons, Eds. West Sussex, England: Wiley, 2004.

[54] I. M. Ward and J. Sweeney, *Chapter 3*, J. Wiley and Sons, Eds. West Sussex, England: Wiley, 2004.

[55] B. Persson, U. Tartaglino, O. Albohr, and E. Tossati, “Rubber friction on wet and dry road surfaces: The sealing effect,” *Physical review. B, Condensed matter*, vol. 71, p. 8, 2005. DOI: 10.1103/PhysRevB.71.035428. [Online]. Available: https://doi.org/10.1103/PhysRevB.71.035428.

[56] C. Venner and A. Lubrecht, “An engineering tool for the quantitative prediction of general roughness deformation in ehl contacts based on harmonic waviness attenuation.,” *Journal of Engineering Tribology*, vol. 219, pp. 303–312, 2005. DOI: 10.1243/135065005X33973. [Online]. Available: https://doi.org/10.1243/135065005X33973.

[57] C. Campaña and M. Müser, “Practical green’s function approach to the simulation of elastic semi-infinite solids.,” *Phys. Rev. B*, vol. 74, p. 075 420, 2006. DOI: 10.1103/PhysRevB.74.075420. [Online]. Available: https://link.aps.org/doi/10.1103/PhysRevB.74.075420.

[58] C. Carbonera and J. Shepherd, “A constructive approach to constrained hexahedral mesh generation,” vol. 26, Jan. 2006, pp. 435–452, ISBN: 978-3-540-34957-0. DOI: 10.1007/978-3-540-34958-7_25.

[59] A. Chapkov, C. Venner, and A. Lubrecht, “Roughness amplitude reduction under non-newtonian ehd lubrication conditions.,” *Journal of tribology*, vol. 128, pp. 753–760, 2006. DOI: 10.1016/S0167-8922(05)80065-3. [Online]. Available: https://doi.org/10.1016/S0167-8922(05)80065-3.

[60] J. Greenwood, “A simplified elliptic model of rough surface contact,” *Wear*, vol. 261, no. 2, pp. 191–200, 2006. DOI: 10.1016/j.wear.2005.09.031. [Online]. Available: https://doi.org/10.1016/j.wear.2005.09.031.

[61] K. Hofstetter, C. Grohs, J. Eberhardsteiner, and H. Mang, “Sliding behaviour of simplified tire tread patterns investigated by means of fem,” *Computers & Structures*, vol. 84, no. 17, pp. 1151–1163, 2006, Formulations and Computational Models for Finite Strains. DOI: https://doi.org/10.1016/j.compstruc.2006.01.010. [Online]. Available: https://www.sciencedirect.com/science/article/pii/S0045794906000812.

[62] W. Manners and J. Greenwood, “Some observations on persson’s diffusion theory of elastic contact,” *Wear*, vol. 261, no. 5, pp. 600–610, 2006. DOI: 10.1016/j.wear.2006.01.007. [Online]. Available: https://doi.org/10.1016/j.wear.2006.01.007.

[63] B. N. J. Persson, “Rubber friction: Role of the flash temperature,” *Journal of Physics: Condensed Matter*, vol. 18, no. 32, pp. 7789–7823, 2006. DOI: 10.1088/0953-8984/18/32/025. [Online]. Available: https://doi.org/10.1088/0953-8984/18/32/025.

[64] B. N. J. Persson and A. I. Volokitin, “Rubber friction on smooth surfaces,” *The European Physical Journal E*, vol. 21, pp. 69–80, 2006.

[65] B. Persson, “Contact mechanics for randomly rough surfaces,” *Surface Science Reports*, vol. 61, pp. 201–227, 2006. DOI: 10.1016/j.surfrep.2006.04.001. [Online]. Available: https://doi.org/10.1016/j.surfrep.2006.04.001.

[66] P. Wriggers, *Computational Contact Mechanics*, Springer, Ed. Hannover, Germany: Springer, 2006.

[67] D. J. Benson, *Explicit Finite Element Methods for Large Deformation Problems in Solid Mechanics*, J. W.
bibinitperiod Sons, Ed. California, United States: Wiley & Sons, 2007.

[68] A. Le Gal, “Investigation and modelling of rubber stationary friction on rough surfaces,” Ph.D. dissertation, Fakultät für Maschinenbau der Gottfried Wilhelm Leibniz Universität, 2007.

[69] W. Press, S. Taukolsky, W. Vetterling, and B. Flannery, *Numerical Recipes - The Art of Scientific Computing*, L. Cowles and A. Harvey, Eds. Cambridge,New York, United States: Cambridge University Press, 2007, ISBN: 978-0-511-33555-6.

[70] G. Carbone and F. Bottiglione, "Asperity contact theories: Do they predict linearity between contact area and load?" *Journal of the Mechanics and Physics of Solids*, vol. 56, pp. 2555–2572, 2008. DOI: 10.1016/j.jmps.2008.03.011. [Online]. Available: https://doi.org/10.1016/j.jmps.2008.03.011.

[71] M. Ciavarella, J. A. Greenwood, and M. Paggi, "Inclusion of "interaction" in the greenwood and williamson contact theory," *Wear*, vol. 265, pp. 729–734, 2008.

[72] A. L. Gal and M. Klüppel, "Investigation and modelling of rubber stationary friction on rough surfaces," *Journal of Physics: Condensed Matter*, vol. 20, no. 1, p. 015 007, 2008. DOI: 10.1088/0953-8984/20/01/015007. [Online]. Available: https://doi.org/10.1088/0953-8984/20/01/015007.

[73] I. Temizer and P. Wriggers, "A multiscale contact homogenization technique for the modeling of third bodies in the contact interface," *Computer Methods in Applied Mechanics and Engineering*, vol. 198, no. 3, pp. 377–396, 2008. DOI: https://doi.org/10.1016/j.cma.2008.08.008. [Online]. Available: https://www.sciencedirect.com/science/article/pii/S0045782508003095.

[74] M. Wang, "Effect of filler-elastomer interaction on tire tread performance part iii effects on abrasion," *The Journal of Materials Science*, vol. 61, pp. 33–42, 2008.

[75] T. Huemer, W. Liu, J. Eberhardsteiner, and H. Mang, "A 3d finite element formulation describing the frictional behavior of rubber on ice and concrete surfaces," *Engineering Computations*, vol. 18, pp. 417–437, 2009. DOI: 10.1108/02644400110387109. [Online]. Available: http://doi.org/10.1108/02644400110387109.

[76] B. Persson, "Theory of powdery rubber wear," *Journal of Physics: Condensed Matter*, vol. 21, no. 48, pp. 7789–7823, 2009. DOI: 10.1088/0953-8984/21/48/485001. [Online]. Available: http://doi.org/10.1088/0953-8984/21/48/485001.

[77] P. Wriggers and J. Reinelt, "Multi-scale approach for frictional contact of elastomers on rough rigid surfaces," *Computer Methods in Applied Mechanics and Engineering*, vol. 198, no. 21, pp. 1996–2008, 2009, Advances in Simulation-Based Engineering Sciences – Honoring J. Tinsley Oden, ISSN: 0045-7825. DOI: https://doi.org/10.1016/j.cma.2008.12.021. [Online]. Available: https://www.sciencedirect.com/science/article/pii/S0045782509000267.

[78] G. Zavarise and L. De-Lorenzis, "A modified node-to-segment algorithm passing the contact patch test," *International journal for numerical methods in engineering*, vol. 79, pp. 379–416, 2009. DOI: 10.1002/nme.2559. [Online]. Available: http://doi.org/10.1002/nme.2559.

[79] M. Zechmeister and M. Kurster, "The generalised lomb-scargle periodogram - a new formalism for the floating-mean and keplerian periodograms," *Astronomy & Astrophysics*, vol. 496, pp. 577–584, 2009. DOI: 10.1051/0004-6361:200811296.

[80] O. Lopez-Pamies, "A new i1-based hyperelastic model for rubber elastic materials," *Comptes Rendus Mécanique*, vol. 338, no. 1, pp. 3–11, 2010, ISSN: 1631-0721. DOI: https://doi.org/10.1016/j.crme.2009.12.007. [Online]. Available: https://www.sciencedirect.com/science/article/pii/S1631072109002113.

[81] M. Paggi and M. Ciavarella, "The coefficient of proportionality k between real contact area and load, with new asperity models," *Wear*, vol. 268, no. 7, pp. 1020–1029, 2010. DOI: 10.1016/j.wear.2009.12.038. [Online]. Available: https://doi.org/10.1016/j.wear.2009.12.038.

[82] V. L. Popov, M. Heß, and E. Willert, *Handbook of Contact Mechanics*, Springer, Ed. Berlin, Germany: Springer, 2010.

[83] V. L. Popov, *Chapter 15*, Springer, Ed. Berlin, Germany: Springer, 2010.

[84] M. Rendek and A. Lion, “Amplitude dependence of filler-reinforced rubber: Experiments, constitutive modelling and fem – implementation,” *International Journal of Solids and Structures*, vol. 47, pp. 2918–2936, 2010. DOI: 10.1016/j.ijsolstr.2010.06.021. [Online]. Available: https://doi.org/10.1016/j.ijsolstr.2010.06.021.

[85] M. Rendek and A. Lion, “Amplitude dependence of filler-reinforced rubber: Experiments, constitutive modelling and fem – implementation,” *International Journal of Solids and Structures*, vol. 47, no. 21, pp. 2918–2936, 2010, ISSN: 0020-7683. DOI: https://doi.org/10.1016/j.ijsolstr.2010.06.021. [Online]. Available: https://www.sciencedirect.com/science/article/pii/S0020768310002428.

[86] T. Rodríguez and R. Abascal, “A 3d fem–bem rolling contact formulation for unstructured meshes,” *International Journal of Solids and Structures*, vol. 47, no. 2, pp. 330–353, 2010, ISSN: 0020-7683. DOI: https://doi.org/10.1016/j.ijsolstr.2009.10.008. [Online]. Available: https://www.sciencedirect.com/science/article/pii/S0020768309003953.

[87] P. Šperka, I. Krupka, and M. Hartl, “Experimental study of real roughness attenuation in concentrated contacts.,” *Tribology International*, vol. 43, pp. 1893–1901, 2010. DOI: 10.1016/j.triboint.2009.11.003. [Online]. Available: https://doi.org/10.1016/j.triboint.2009.11.003.

[88] B. Lorenz, B. N. J. Persson, S. Dieluweit, and T. Tada, “Rubber friction: Comparison of theory with experiment,” *European Physical Journal E*, vol. 34, pp. 1–11, 2011. DOI: 10.1140/epje/i2011-11129-1. [Online]. Available: https://doi.org/10.1140/epje/i2011-11129-1.

[89] C. Hager *et al.*, “Solving dynamic contact problems with local refinement in space and time,” *Computer Methods in Applied Mechanics and Engineering*, vol. 201-204, pp. 25–41, 2012. DOI: https://doi.org/10.1016/j.cma.2011.09.006.

[90] C. Putignano, L. Afferrante, G. Carbone, and G. Demelio, “A new efficient numerical method for contact mechanics of rough surfaces,” *International Journal of Solids and Structures*, vol. 49, no. 2, pp. 338–343, 2012. DOI: https://doi.org/10.1016/j.ijsolstr.2011.10.009. [Online]. Available: https://www.sciencedirect.com/science/article/pii/S0020768311003477.

[91] C. Putignano, L. Afferrante, G. Carbone, and G. Demelio, “The influence of the statistical properties of self-affine surfaces in elastic contacts: A numerical investigation,” *Journal of the Mechanics and Physics of Solids*, vol. 60, no. 5, pp. 973–982, 2012, ISSN: 0022-5096. DOI: https://doi.org/10.1016/j.jmps.2012.01.006. [Online]. Available: https://www.sciencedirect.com/science/article/pii/S0022509612000142.

[92] G. Carbone and C. Putignano, “A novel methodology to predict sliding and rolling friction of viscoelastic materials: Theory and experiments,” *Journal of the Mechanics and Physics of Solids*, vol. 61, no. 8, pp. 1822–1834, 2013, ISSN: 0022-5096. DOI: https://doi.org/10.1016/j.jmps.2013.03.005. [Online]. Available: https://www.sciencedirect.com/science/article/pii/S0022509613000604.

[93] W. D. and A. Lion, “Predeformation- and frequency-dependent material behaviour of filler-reinforced rubber: Experiments, constitutive modelling and parameter identification,” *International Journal of Solids and Structures*, vol. 50, pp. 1217–1225, 2013. DOI: 10.1016/j.ijsolstr.2012.12.015. [Online]. Available: http://dx.doi.org/10.1016/j.ijsolstr.2012.12.015.

[94] L. De Lorenzis and P. Wriggers, "Computational homogenization of rubber friction on rough rigid surfaces," *Computational Materials Science*, vol. 77, pp. 264–280, 2013, ISSN: 0927-0256. DOI: https://doi.org/10.1016/j.commatsci.2013.04.049. [Online]. Available: https://www.sciencedirect.com/science/article/pii/S0927025613002218.

[95] L. Pastewka *et al.*, "Finite size scaling in the interfacial stiffness of rough elastic contacts.," *Soft Condensed Matter*, vol. 87, p. 062 809, 2013. DOI: 10.1103/PhysRevE.87.062809.

[96] V. A. Yastrebov, *Numerical Methods in Contact Mechanics.* Croydon, United Kingdon: Wiley, 2013.

[97] G. Carbone and C. Putignano, "Rough viscoelastic sliding contact: Theory and experiments.," *Physical review. E, Statistical, nonlinear, and soft matter physics*, vol. 89 3, p. 032 408, 2014.

[98] W. Dapp, N. Prodanov, and M. Müser, "Systematic analysis of persson's contact mechanics theory of randomly rough elastic surfaces," *Journal of Physics: Condensed Matter*, vol. 26, no. 35, 2014. DOI: 10.1088/0953-8984/26/35/355002.

[99] S. Govindjee, T. Potter, and J. Wilkening, "Dynamic stability of spinning viscoelastic cylinders at finite deformation," *International Journal of Solids and Structures*, vol. 51, no. 21, pp. 3589–3603, 2014, ISSN: 0020-7683. DOI: https://doi.org/10.1016/j.ijsolstr.2014.06.022. [Online]. Available: https://www.sciencedirect.com/science/article/pii/S0020768314002546.

[100] M. Scaragi and B. N. J. Persson, "Friction and universal contact area law for randomly rough viscoelastic contacts.," *Condensed Matter*, vol. 27(10), p. 105 102, 2014. DOI: 10.1088/0953-8984/27/10/105102. [Online]. Available: http://doi.org/10.1088/0953-8984/27/10/105102.

[101] M. Scaragi and B. N. J. Persson, "Theory of viscoelastic lubrication," *Tribology International*, vol. 72, pp. 118–130, 2014. DOI: 10.1016/j.triboint.2013.12.011. [Online]. Available: http://dx.doi.org/10.1016/j.triboint.2013.12.011.

[102] Y. Zhang, "Friction prediction for rough surfaces in an elastohydrodynamically lubricated contact," Ph.D. dissertation, Institut National des Sciences Appliquées de Lyon, 2014.

[103] Y. R. Lorenz B. Oh, S. K. Nam, S. H. Jeon, and B. N. J. Persson, "Rubber friction on road surfaces: Experiment and theory for low sliding speeds," *The Journal of chemical physics*, vol. 142, p. 19, 2015. DOI: 10.1063/1.4919221. [Online]. Available: https://doi.org/10.1063/1.4919221.

[104] A. Ueckermann, D. Wang, M. Oeser, and B. Steinauer, "Calculation of skid resistance from texture measurements," *Journal of Traffic and Transportation Engineering (English Edition)*, vol. 2, no. 1, pp. 3–16, 2015, Special Issue: Functional Pavement Materials and Characterization, ISSN: 2095-7564. DOI: 10.1016/j.jtte.2015.01.001. [Online]. Available: https://doi.org/10.1016/j.jtte.2015.01.001.

[105] V. A. Yastrebov, G. Anciaux, and J. Molinari, "From infinitesimal to full contact between rough surfaces: Evolution of the contact area," *International Journal of Solids and Structures*, vol. 52, pp. 83–102, 2015, ISSN: 0020-7683. DOI: https://doi.org/10.1016/j.ijsolstr.2014.09.019. [Online]. Available: https://www.sciencedirect.com/science/article/pii/S0020768314003667.

[106] E. Fina, "The friction of racing tyres," Ph.D. dissertation, University of Surrey Faculty of Engineering and Physical Sciences, 2016.

[107] A. Kumar and O. Pamies, “On the two-potential constitutive modeling of rubber viscoelastic materials,” *Comptes Rendus Mécanique*, vol. 344, pp. 102–112, 2016. DOI: https://doi.org/10.1016/j.crme.2015.11.004.

[108] F. MORA, “Modélisation multiéchelles d'un contact rugueux viscoélastique lubrifié,” Ph.D. dissertation, Institut National des Sciences Appliquées de Lyon, 2016.

[109] S. Rajaei, “Pavement surface characterization for optimization of trade-off between grip and rolling resistance,” Center for Highway Pavement Preservation - Michigan State University, 2016.

[110] M. Scaraggi, D. Comingio, A. Al-Qudsi, and L. De Lorenzis, “The influence of geometrical and rheological non-linearity on the calculation of rubber friction,” *Tribology International*, vol. 101, pp. 402–413, 2016, ISSN: 0301-679X. DOI: https://doi.org/10.1016/j.triboint.2016.04.027. [Online]. Available: https://www.sciencedirect.com/science/article/pii/S0301679X16300810.

[111] M. Scaragi and B. N. J. Persson, “The effect of fnite roughness size and bulk thickness on the prediction of rubber friction and contact mechanics..,” *Journal of Mechanical Engineering Science*, vol. 230(9), pp. 1398–1409, 2016. DOI: 10.1177/0954406216642261. [Online]. Available: http://doi.org/10.1177/0954406216642261.

[112] R. Bugnicourt *et al.*, “Transient frictionless contact of a rough rigid surface on a viscoelastic half-space,” *Tribology International*, vol. 113, pp. 279–285, 2017, ISSN: 0301-679X. DOI: https://doi.org/10.1016/j.triboint.2017.01.032.

[113] M. Ciavarella, “A simplified version of persson's multiscale theory for rubber friction due to viscoelastic losses,” *The Journal of Tribology*, vol. 140, p. 1, 2017. DOI: 10.1115/1.4036917. [Online]. Available: https://doi.org/10.1115/1.4036917.

[114] G. Fortunato, V. Ciaravola, A. Furno, M. Scaraggi, B. Lorenz, and B. N. J. Persson, “Dependency of rubber friction on normal force or load: Theory and experiment,” *Tire Science and Technology*, vol. 45, pp. 25–54, 2017. DOI: 10.2346/tire.17.450103. [Online]. Available: https://doi.org/10.2346/tire.17.450103.

[115] M. Kanafi and A. Tuononen, “Top topography surface roughness power spectrum for pavement friction evaluation,” *Tribology International*, vol. 107, pp. 240–249, 2017, ISSN: 0301-679X. DOI: https://doi.org/10.1016/j.triboint.2016.11.038. [Online]. Available: https://www.sciencedirect.com/science/article/pii/S0301679X16304674.

[116] K. Matous *et al.*, “A review of predictive nonlinear theories for multiscale modeling of heterogeneous materials,” *Journal of Computational Physics*, vol. 330, pp. 192–220, 2017, ISSN: 0021-9991. DOI: https://doi.org/10.1016/j.jcp.2016.10.070. [Online]. Available: https://www.sciencedirect.com/science/article/pii/S0021999116305782.

[117] B. N. J. Persson, “Crack propagation in finite-sized viscoelastic solids with application to adhesion,” *Europhysics Letters*, vol. 119, no. 1, p. 18 002, 2017. DOI: 10.1209/0295-5075/119/18002.

[118] M. Scaraggi and D. Comingio, “Rough contact mechanics for viscoelastic graded materials: The role of small-scale wavelengths on rubber friction,” *International Journal of Solids and Structures*, vol. 125, pp. 276–296, 2017, ISSN: 0020-7683. DOI: 10.1016/j.ijsolstr.2017.06.008. [Online]. Available: https://doi.org/10.1016/j.ijsolstr.2017.06.008.

[119] M. Scaraggi, L. Dorogin, J. Angerhausen, H. Murrenhoff, and B. N. J. Persson, "Elastohydrodynamics for soft solids with surface roughness: Transient effects," *Tribology Letters*, vol. 65, pp. 65–95, 2017. DOI: 10.1007/s11249-017-0878-9. [Online]. Available: https://doi.org/10.1007/s11249-017-0878-9.

[120] J. VanderPlas, "Understanding the lomb–scargle periodogram," *The Astrophysical Journal Supplement Series*, vol. 136, p. 28, 2017. DOI: 10.3847/1538-4365/aab766. [Online]. Available: https://doi.org/10.3847/1538-4365/aab766.

[121] J. Wu, Y. Wang, B. Su, J. Dong, Z. Cui, and B. Gond, "Prediction of tread pattern block deformation in contact with road," *Polymer Testing*, vol. 58, pp. 208–218, 2017, ISSN: 0142-9418. DOI: https://doi.org/10.1016/j.polymertesting.2016.12.030. [Online]. Available: https://www.sciencedirect.com/science/article/pii/S0142941816312934.

[122] V. A. Yastrebov, G. Anciaux, and J. Molinari, "On the accurate computation of the true contact-area in mechanical contact of random rough surfaces," *Tribology International*, vol. 114, pp. 161–171, 2017, ISSN: 0301-679X. DOI: https://doi.org/10.1016/j.triboint.2017.04.023.

[123] V. A. Yastrebov, G. Anciaux, and J. Molinari, "The role of the roughness spectral breadth in elastic contact of rough surfaces," *Journal of the Mechanics and Physics of Solids*, vol. 107, pp. 469–493, 2017, ISSN: 0022-5096. DOI: 10.1016/j.jmps.2017.07.016. [Online]. Available: https://doi.org/10.1016/j.jmps.2017.07.016.

[124] T. Bhave, M. Tehrani, M. Ali, and A. Sarvestani, "Hysteresis friction and nonlinear viscoelasticity of rubber composites," *Composites Communications*, vol. 9, pp. 92–97, 2018, ISSN: 2452-2139. DOI: 10.1016/j.coco.2018.07.001. [Online]. Available: https://doi.org/10.1016/j.coco.2018.07.001.

[125] A. Emami, "Investigation on physics-based multi-scale modeling of contact, friction, and wear in viscoelastic materials with application in rubber compounds," Ph.D. dissertation, Virginia Polytechnic Institute and State University, 2018.

[126] F. Hartung, R. Kienle, T. Götz, *et al.*, "Numerical determination of hysteresis friction on different length scales and comparison to experiments," *Tribology International*, vol. 127, pp. 165–176, 2018, ISSN: 0301-679X. DOI: https://doi.org/10.1016/j.triboint.2018.05.018. [Online]. Available: https://www.sciencedirect.com/science/article/pii/S0301679X18302469.

[127] J. Persson, A. Tiwari, E. Valbahs, *et al.*, "On the use of silicon rubber replica for surface topography studies," *Tribology Letters*, vol. 66, 2018.

[128] A. Vakis *et al.*, "Modeling and simulation in tribology across scales: An overview," *Tribology International*, vol. 125, pp. 169–199, 2018. DOI: https://doi.org/10.1016/j.triboint.2018.02.005. [Online]. Available: https://www.sciencedirect.com/science/article/pii/S0301679X18300756.

[129] P. Wagner, "A multiscale fem approach for rubber friction on rough surfaces," Ph.D. dissertation, Von der Fakultät für Maschinenbau der Gottfried Wilhelm Leibniz Universität, 2018.

[130] R. Bugnicourt, "Simulation of the contact between a rough surface and a viscoelastic material with friction," Ph.D. dissertation, l'Institut National des Sciences Appliquées de Lyon, 2019.

[131] V. Popov, M. Heß, and E. Willert, *Handbook of Contact Mechanics*, Springer, Ed. Berlin, Germany: Springer, 2019.

[132] A. Al-Qudsi, "Multiscale modeling of rubber hysteretic friction on rough rigid surfaces," Ph.D. dissertation, Fakulttat Architektur Universittat, 2019.

[133] T. Tanya, W. Pyckhout-Hintzen, and B. Persson, “Linear and nonlinear viscoelastic modulus of rubber,” *Lubricants*, vol. 7, p. 22, 2019. DOI: 10.3390/lubricants7030022.

[134] J. Wang and Z. D, *Interfacial Mechanics Theories and Methods for Contact and Lubrication*, Taylor and L. Francis Group, Eds. Miami, United States: CRC Press, 2019.

[135] J. Wang and D. Zhu, *Chapter 4: Numerical Methods for Solving Contact Problems*, C. Press, Ed. London, United Kingdom: Taylor and Francis Group, 2019.

[136] G. Andrea, F. Carputo, M. Ciavarella, F. Farroni, A. Papangelo, and S. A., “Analysis of multiscale theories for viscoelastic rubber friction,” in Mar. 2020, pp. 1125–1135, ISBN: 978-3-030-41056-8. DOI: 10.1007/978-3-030-41057-5_91.

[137] L. Frérot, G. Anciaux, V. Rey, S. Pham-Ba, and J.-F. Molinari, “Tamaas: A library for elastic-plastic contact of periodic rough surfaces,” *Journal of Open Source Software*, vol. 5, no. 51, p. 2121, 2020. DOI: 10.21105/joss.02121. [Online]. Available: https://doi.org/10.21105/joss.02121.

[138] J. Hale, R. Lewis, and M. J. Carré, “Rubber friction and the effect of shape,” *Tribology International*, vol. 141, p. 105 911, 2020, ISSN: 0301-679X. DOI: https://doi.org/10.1016/j.triboint.2019.105911. [Online]. Available: https://www.sciencedirect.com/science/article/pii/S0301679X1930430X.

[139] E. Wallace, T. Chaise, and D. Nelias, “Three-dimensional rolling/sliding contact on a viscoelastic layered half-space,” *Journal of the Mechanics and Physics of Solids*, vol. 143, p. 104 067, 2020, ISSN: 0022-5096. DOI: https://doi.org/10.1016/j.jmps.2020.104067.

[140] Q. Wang *et al.*, “Fft-based methods for contact mechanics,” *Frontiers in Mechanical Engineering*, vol. 6, no. 2, pp. 320–328, 2020, ISSN: 0742-4787. DOI: 10.3389/fmech.2020.00061.

[141] E. Wiyao, V. Cerezo, Z. Zahouani H., and F. Salvatore, “Multiscale analyses of pavement texture during polishing,” *Surface Topography: Metrology and Properties*, vol. 8, 2020. DOI: 10.1088/2051-672X/ab8f1b. [Online]. Available: https://hal.archives-ouvertes.fr/hal-03594465.

[142] M. J. Cugliari, “Investigation of contact mechanics and friction of rubber compounds by experimental techniques and numerical simulations,” Ph.D. dissertation, Von der Fakultät für Maschinenbau der Gottfried Wilhelm Leibniz Universität, 2021.

[143] E. Ding, K. Wang, E. Yang, and Y. Zhan, “Influence of effective texture depth on pavement friction based on 3d texture area,” *Construction and Building Materials*, vol. 287, p. 123 002, 2021, ISSN: 0950-0618. DOI: https://doi.org/10.1016/j.conbuildmat.2021.123002. [Online]. Available: https://www.sciencedirect.com/science/article/pii/S0950061821007625.

[144] J. Löwer, P. Wagner, H. Unrau, B. Wies, and F. Gauterin, “Model for the pattern-dependent wet grip prediction of tires,” *Vehicles*, vol. 3, pp. 84–110, 2021. DOI: 10.3390/vehicles3010006. [Online]. Available: https://doi.org/10.3390/vehicles3010006.

[145] J. Plagge and R. Hentschke, “Numerical solution of the adhesive rubber-solid contact problem and friction coefficients using a scale-splitting approach,” *Tribology International*, vol. 173, p. 107 622, 2022, ISSN: 0301-679X. DOI: https://doi.org/10.1016/j.triboint.2022.107622.

[146] A. Al-Qudsi, L. De Lorenzis, and M. Scaraggi, "A hybrid multiscale approach for rubber contact," *Frontiers in Mechanical Engineering*, vol. 8, 2022. DOI: 10.3389/fmech.2022.814607. [Online]. Available: https://www.frontiersin.org/articles/10.3389/fmech.2022.814607.

[147] R. I. Taylor, "Rough surface contact modelling—a review," *Lubricants*, vol. 10, p. 98, 2022. DOI: 10.3390/lubricants10050098. [Online]. Available: https://doi.org/10.3390/lubricants10050098.

[148] D. Wang *et al.*, "A review on modelling of viscoelastic contact problems," *Lubricants*, vol. 10, no. 12, 2022, ISSN: 2075-4442. DOI: 10.3390/lubricants10120358.

[149] Z. Y., M. -E.G.E., and VennerC.H., "Aspects of modeling and numerical simulation of dry point contacts between viscoelastic solids," *Tribology International*, vol. 165, p. 107 245, 2022, ISSN: 0301-679X. DOI: https://doi.org/10.1016/j.triboint.2021.107245. [Online]. Available: https://www.sciencedirect.com/science/article/pii/S0301679X21003935.

[150] A. Ricker, M. Gierig, and P. Wriggers, "Multiplicative, non-newtonian viscoelasticity models for rubber materials and brain tissues: Numerical treatment and comparative studies," *Archives of Computational Methods in Engineering*, vol. 30, pp. 2889–2927, 2023. DOI: https://doi.org/10.1007/s11831-023-09889-x.

[151] Y. Zhao, H. Liu, G. Morales-Espejel, and C. Venner, "Response of elastic/viscoelastic layers on an elastic half-space in rolling contacts: Towards a new modeling approach for elastohydrodynamic lubrication," *Tribology International*, vol. 186, p. 108 545, 2023, ISSN: 0301-679X. DOI: https://doi.org/10.1016/j.triboint.2023.108545.

[152] *HSLFT product description*, https://altracon.com/indoor-testing/, Accessed: 2022-10-12.

[153] C. Yang and B. Tartaglino U. Persson, "A multiscale molecular dynamics approach to contact mechanics.," *Eur Phys J E Soft Matter*, vol. 19(1), pp. 47–58, DOI: 0.1140/epje/e2006-00004-9.

Appendix A - Two-Potential framework

As described in the beginning of this section, two constitutive models were used in this research. In order to avoid repetition in the development and to also contextualize mathematically the rubber characteristics considered, a structured development framework called "*Two-Potential*" (also called "*generalized standard materials*") is used.

This strategy is a powerful tool to construct thermodynamically consistent models for a wide range of phenomena, where thermodynamic state/internal variables, $\mathbf{\Lambda}$, are introduced, representing a finite number of macroscopically non-observable processes. The developments will be made within the reference configuration, but a push-forward manipulation can be applied.

The thermodynamical behaviour is assumed to be described by its past and present states and not future or stochastic processes (determinism principle). In addition, the behaviour of a material point is only affected by its near neighbourhood (local action principle) [38], [49]. Therefore, from the concepts and quantities defined in section 3.1.2, the thermomechanical processes can be described not by the set $\{\mathbf{F}, \Theta, Grad(\Theta), \mathbf{\Lambda}; \mathbf{X}, t\}$, but instead $\{\mathbf{F}, \Theta, Grad(\Theta), \mathbf{\Lambda}\}$.

Four additional constitutive relations are proposed in order to render the whole system from the general principles determined:

$$\mathbf{P} = \hat{\mathbf{P}}\left[\mathbf{F}, \Theta, Grad(\Theta), \mathbf{\Lambda}\right], \tag{8.4.1}$$

$$\mathbf{Q} = \hat{\mathbf{Q}}\left[\mathbf{F}, \Theta, Grad(\Theta), \mathbf{\Lambda}\right], \tag{8.4.2}$$

$$N = \rho_0^{-1}\hat{N}\left[\mathbf{F}, \Theta, Grad(\Theta), \mathbf{\Lambda}\right], \tag{8.4.3}$$

$$\Psi = \rho_0^{-1}\hat{\Psi}\left[\mathbf{F}, \Theta, Grad(\Theta), \mathbf{\Lambda}\right]. \tag{8.4.4}$$

Those relations are inserted in the reduced dissipation inequality from (3.1.55)

$$\left[\left(\frac{\partial\hat{\Psi}}{\partial\mathbf{F}} : \frac{\partial\mathbf{F}}{\partial t} + \frac{\partial\hat{\Psi}}{\partial\Theta}\frac{\partial\Theta}{\partial t} + \frac{\partial\hat{\Psi}}{\partial\mathbf{\Lambda}} : \frac{\partial\mathbf{\Lambda}}{\partial t} + \frac{\partial\hat{\Psi}}{\partial\mathbf{G}} \cdot \frac{\partial\mathbf{G}}{\partial t}\right) - \hat{N}\frac{\partial\Theta}{\partial t}\right] + \frac{1}{\Theta}\hat{\mathbf{Q}} \cdot \mathbf{G} - \mathbf{P} : \dot{\mathbf{F}} \leq 0. \tag{8.4.5}$$

where $\mathbf{G} = Grad(\Theta)$. Reorganizing in terms of the time derivatives

$$\left(\hat{N} + \frac{\partial \hat{\Psi}}{\partial \Theta}\right)\frac{\partial \Theta}{\partial t} - \left(\mathbf{P} - \frac{\partial \hat{\Psi}}{\partial \mathbf{F}}\right) : \frac{\partial \mathbf{F}}{\partial t} + \frac{\partial \hat{\Psi}}{\partial \mathbf{G}} \cdot \frac{\partial \mathbf{G}}{\partial t} + \frac{\partial \hat{\Psi}}{\partial \boldsymbol{\Lambda}} : \frac{\partial \boldsymbol{\Lambda}}{\partial t} + \frac{1}{\Theta}\hat{\mathbf{Q}} \cdot \mathbf{G} \leq 0. \qquad (8.4.6)$$

By imposing that the constitutive equations must depend on the internal variables, one way for equation (8.4.6) to always be satisfied is when it is assumed that

$$\begin{cases} N = -\frac{\partial \hat{\Psi}}{\partial \Theta} \\ \mathbf{P} = \frac{\partial \hat{\Psi}}{\partial \mathbf{F}} \\ \frac{\partial \hat{\Psi}}{\partial \mathbf{G}} = \mathbf{0} \\ \frac{\partial \hat{\Psi}}{\partial \boldsymbol{\Lambda}} : \frac{\partial \boldsymbol{\Lambda}}{\partial t} + \frac{1}{\Theta}\hat{\mathbf{Q}} \cdot \mathbf{G} \leq 0 \end{cases} \qquad (8.4.7)$$

Some direct implications can be observed: (1) The free energy $\hat{\Psi}$ should not depend on the temperature gradient; (2) the stress, $\mathbf{P}$ and entropy N are given by functions of $\mathbf{F}$, Θ and $\boldsymbol{\Lambda}$; (3) $\hat{\Psi}$ and $\hat{\mathbf{Q}}$ must obey the inequality. Therefore

$$\mathbf{P} = \frac{\partial \hat{\Psi}}{\partial \mathbf{F}}(\mathbf{F}, \Theta, \boldsymbol{\Lambda}) \qquad (8.4.8)$$

$$N = -\rho_0^{-1}\frac{\partial \hat{\Psi}}{\partial \Theta}(\mathbf{F}, \Theta, \boldsymbol{\Lambda}) \qquad (8.4.9)$$

$$\frac{\partial \hat{\Psi}}{\partial \boldsymbol{\Lambda}} : \frac{\partial \boldsymbol{\Lambda}}{\partial t} + \frac{1}{\Theta}\hat{\mathbf{Q}} \cdot \mathbf{G} \leq 0 \qquad (8.4.10)$$

To proceed, a dissipation potential, $\varphi := \varphi(\mathbf{F}, \Theta, \boldsymbol{\Lambda}, \dot{\boldsymbol{\Lambda}})$, is defined such that

$$\frac{\partial \varphi}{\partial \dot{\boldsymbol{\Lambda}}}(\mathbf{F}, \Theta, \boldsymbol{\Lambda}, \dot{\boldsymbol{\Lambda}}) := -\frac{\partial \hat{\Psi}}{\partial \boldsymbol{\Lambda}}(\mathbf{F}, \Theta, \boldsymbol{\Lambda}) \qquad (8.4.11)$$

where φ is convex in $\dot{\boldsymbol{\Lambda}} = \frac{d\boldsymbol{\Lambda}}{dt}$ such that $argmin_{\dot{\boldsymbol{\Lambda}}}\varphi(\mathbf{F}, \Theta, \boldsymbol{\Lambda}, \dot{\boldsymbol{\Lambda}}) = 0$ [107]. By inserting this definition in the inequality (8.4.10)

$$-\frac{\partial \varphi}{\partial \dot{\boldsymbol{\Lambda}}} : \dot{\boldsymbol{\Lambda}} + \frac{1}{\Theta}\hat{\mathbf{Q}} \cdot \mathbf{G} \leq 0 \qquad (8.4.12)$$

In the context of isothermal processes, which are of interest in this study, implicate that

$$\frac{\partial \varphi}{\partial \dot{\boldsymbol{\Lambda}}}(\mathbf{F}, \boldsymbol{\Lambda}, \dot{\boldsymbol{\Lambda}}) : \dot{\boldsymbol{\Lambda}} \geq 0, \qquad (8.4.13)$$

Appendix B - Fourier Transform of a radially symmetric function

In Chapter 7, the briefly mentioned Green function is given by

$$G_f(x,y) = \frac{1}{\sqrt{x^2+y^2}}, \tag{8.4.14}$$

with Fourier Transform in space being

$$\hat{G}_f(q_x,q_y) = \mathcal{F}_{x,y}\left\{G_f(x,y)\right\} = \iint_{-\infty}^{\infty} G_f(x,y)e^{-i(q_x x+q_y y)}dq_x dq_y. \tag{8.4.15}$$

This transform can be rewritten into its polar representation, so that

$$x = rcos(\theta)\ ;\ y = rsin(\theta)\ ;\ r^2 = x^2+y^2\ ;\ \theta = arctan\left(\frac{y}{x}\right) \tag{8.4.16}$$

$$q_x = \rho cos(\psi)\ ;\ q_y = \rho sin(\psi)\ ;\ \rho^2 = q_x^2+q_y^2\ ;\ \psi = arctan\left(\frac{q_y}{q_x}\right) \tag{8.4.17}$$

which brings the Green function to be represented as

$$G_f(r) = \frac{1}{r}. \tag{8.4.18}$$

We have

$$\mathcal{F}_{r,\theta}\left\{G_f(r)\right\} = \int_0^{\infty}\int_{-\pi}^{\pi} G_f(r)e^{-ir\rho cos(\psi-\theta)}rdrd\theta. \tag{8.4.19}$$

Since this function is independent on θ one may rewrite the integral as

$$\mathcal{F}_{r,\theta}\left\{G_f(r)\right\} = 2\pi\int_0^{\infty} G_f(r)J_0(\rho r)rdrd\theta \tag{8.4.20}$$

where J_0 is the zeroth-order Bessel function of the first kind.

Upon inspection, the two-dimensional Fourier Transform of a radially symmetric function is simply its Hankel Transform multiplied by 2π. By considering equation (8.4.18), solving (8.4.20) results in the transformation pair

$$G_f(x,y) = \frac{1}{\sqrt{x^2+y^2}} \quad \xleftrightarrow{\mathcal{FT}_{x,y}} \quad \frac{2\pi}{\sqrt{q_x^2+q_y^2}} = \hat{G}_f(q_x,q_y). \tag{8.4.21}$$

ECOLE
DOCTORALE

Titre : Approches multi-échelles de l'adhérence des pneumatiques sur route mouillées

Mots clés : friction, pneu, bande-de-roulement, viscoélasticité, non-linéaire, rugosité, multi-échelle, MEF.

Résumé :

Cette recherche présente le développement d'un modèle de contact nuancé pour analyser les interactions entre le pneu et la route, en se concentrant sur l'interaction complexe entre les sculptures du pneu, les profils de la surface de la route et les propriétés viscoélastiques du caoutchouc. L'étude intègre des efforts expérimentaux, de modélisation et numériques, soulignant les défis liés à l'étude des contacts tribologiques à plusieurs échelles.
Expérimentalement, le comportement viscoélastique des mélanges industriels de caoutchouc chargé est exploré par une analyse mécanique dynamique et des essais uniaxiaux, mettant en évidence des effets non linéaires cruciaux concernant l'amplitude de la déformation et la sensibilité à la vitesse de déformation. Ces aspects ont servi de base au développement et à la caractérisation d'un modèle de matériau viscoélastique non linéaire fini, vérifié dans un environnement d'éléments finis par rapport à des cas semi-analytiques. Ce modèle facilite l'exploration des déformations induites par l'hystérésis dans des expériences simplifiées de contact atterrissage-glissement, visant à minimiser les contributions adhésives et les effets de la température, en s'appuyant à la fois sur des modèles viscoélastiques non linéaires et classiques.
Finalement, un modèle de contact frictionnel multi-échelle est proposé pour capturer les caractéristiques géométriques du sol et celles d'un matériau viscoélastique non linéaire à géométrie complexe, ce qui permet d'obtenir une corrélation raisonnable avec les observations expérimentales et de saisir les tendances essentielles en matière de déformation au sein de la sculpture.

Title : Multi-scale approaches of tire adherence on wet roads

Keywords : friction, tire, tread-pattern, viscoelasticity, non-linear, roughness, multi-scale, FEM.

Abstract :

This research presents the development of a nuanced contact model to analyze tire-road interactions, focusing on the complex interplay of tire tread patterns, road surface profiles, and the viscoelastic properties of rubber. The study integrates experimental, modeling, and numerical efforts, highlighting the challenges of addressing tribological contacts across multiple scales.
Experimentally, viscoelastic behavior of industrial filled rubber mixes are explored through dynamic mechanical analysis and uniaxial tests, uncovering crucial non-linear effects regarding strain magnitude and strain rate sensitivity. Those aspects served as basis for the development and the characterization of a finite non-linear viscoelastic material model, verified within a Finite Element environment against semi-analytical cases. This model facilitates the exploration of hysteresis-induced deformations in simplified landing-sliding contact experiments, aimed at minimizing adhesive contributions and temperature effects, leveraging both non-linear and classical viscoelastic models.
Ultimately, a multi-scale frictional contact model is proposed capturing geometrical features of the ground and a non-linear viscoelastic material with complex geometry, yielding a reasonable correlation with experimental observations and capturing essential deformation trends within the sculpture.

Institut Polytechnique de Paris
91120 Palaiseau, France